ADVERTIMENT. La consulta d'aquesta tesi queda condicionada a l'acceptació de les següents condicions d'ús: La difusió d'aquesta tesi per mitjà del servei TDX (www.tesisenxarxa.net) ha estat autoritzada pels titulars dels drets de propietat intel·lectual únicament per a usos privats emmarcats en activitats d'investigació i docència. No s'autoritza la seva reproducció amb finalitats de lucre ni la seva difusió i posada a disposició des d'un lloc aliè al servei TDX. No s'autoritza la presentació del seu contingut en una finestra o marc aliè a TDX (framing). Aquesta reserva de drets afecta tant al resum de presentació de la tesi com als seus continguts. En la utilització o cita de parts de la tesi és obligat indicar el nom de la persona autora.

ADVERTENCIA. La consulta de esta tesis queda condicionada a la aceptación de las siguientes condiciones de uso: La difusión de esta tesis por medio del servicio TDR (www.tesisenred.net) ha sido autorizada por los titulares de los derechos de propiedad intelectual únicamente para usos privados enmarcados en actividades de investigación y docencia. No se autoriza su reproducción con finalidades de lucro ni su difusión y puesta a disposición desde un sitio ajeno al servicio TDR. No se autoriza la presentación de su contenido en una ventana o marco ajeno a TDR (framing). Esta reserva de derechos afecta tanto al resumen de presentación de la tesis como a sus contenidos. En la utilización o cita de partes de la tesis es obligado indicar el nombre de la persona autora.

WARNING. On having consulted this thesis you're accepting the following use conditions: Spreading this thesis by the TDX (www.tesisenxarxa.net) service has been authorized by the titular of the intellectual property rights only for private uses placed in investigation and teaching activities. Reproduction with lucrative aims is not authorized neither its spreading and availability from a site foreign to the TDX service. Introducing its content in a window or frame foreign to the TDX service is not authorized (framing). This rights affect to the presentation summary of the thesis as well as to its contents. In the using or citation of parts of the thesis it's obliged to indicate the name of the author

POLYTECHNIC UNIVERSITY OF CATALONIA
UPC

LAMB: a SIMULATION TOOL for AIR-COUPLED LAMB WAVE BASED ULTRASONIC NDE SYSTEMS

by

José Luís Prego-Borges

A thesis submitted to the Polytechnic University of Catalonia
for the degree of Doctor of Philosophy

Thesis advisor: Dr. Miguel J. García-Hernández
Doctorate Programme in Electronics

Department of Electronic Engineering
Polytechnic University of Catalonia
Barcelona, Spain

September 2010
Vol. 1 of 1

Series of dissertations submitted to the Deparment of Electronics
Polytechnic University of Catalonia

ISSN

UNIVERSITAT POLITÈCNICA de CATALUNYA
ACTA de QUALIFICACIÓ de la TESI DOCTORAL

Reunit el tribunal integrat pels sota signants per jutjar la tesi doctoral:

Títol de la tesi: “LAMB: a simulation tool for air-coupled Lamb wave based ultrasonic NDE systems”.

Autor de la tesi: José Luís Prego-Borges

Acorda atorgar la qualificació de:

☐ No apte
☐ Aprovat
☐ Notable
☐ Excel·lent
☐ Excel·lent Cum Laude

Barcelona, ... de .... de ....

El President	El Secretari	El vocal
....	....	....
(nom i cognoms)	(nom i cognoms)	(nom i cognoms)
El vocal	El vocal	
....	....	
(nom i cognoms)	(nom i cognoms)	

Dedicated to my beloved parents Elsa & José

Abstract

Air-coupled ultrasonic Lamb waves represent an important advance in Non-Destructive Testing and Evaluation (NDT & NDE) techniques of plate materials and structures. Examples of these advances are the characterization and quality assessment of laminate materials in manufacturing processes, the location of damaged parts in aircrafts and structure monitoring in the aerospace industry.

However the rich and complex nature of mechanical vibrations encountered in acoustics make the subject of analysis and study of these systems a very complex task. Therefore a simulation tool that permits the evaluation and testing of different configuration scenarios using the flexibility of a computer model is an invaluable aid and advantage.

The objective of this thesis is to provide the field of NDT with free open source software i.e. the LAMB Matlab®toolbox. The toolbox is capable of simulating the behaviour of Lamb wave based NDE systems for single ideal isotropic laminates using air-coupled ultrasonic arrays. The programme uses a pitch-catch type of a C-scan NDE arrangement and is composed of three integrated sections each individually modelling a feature in the system: 1) Excitation, 2) Propagation, and 3) Reception.

For assessment of the individual modules of the toolbox the thesis presents comparisons between each section simulations and the data obtained from different acoustic experiments. The validation of the complete simulator was carried out by evaluation tests on the copper and aluminium plates by use of a real hardware prototype of a Lamb wave based NDE system with air-coupled concave arrays.

The negative impact on the performance of the real air-coupled NDE system based on concave arrays was effectively confirmed by the programme. This was produced by the inherent directivity of the individual sensors as well as their concave arrangement. To emulate this behaviour the thesis introduces a simple two-dimensional geometric model for the inclusion of the spatial filtering effect of the sensors plus a group of simulations for a new proposed air-coupled plane array transducer.

The software also verified the spatial coherent nature of the Lamb wave fields emitted by a plate in air. This was demonstrated by the implementation of a delay and sum beamformer to constitute an initial signal processing stage in the reception section.

The main purpose of the present work was to contribute a working scenario for the simulation and testing of new air-coupled array designs and the development of enhanced signal processing techniques for the analysis of Lamb waves fields encountered in non-contact NDE of single isotropic systems.
Finally, although the issue related to the calibration of the programme was not attainable a reasonable degree of similarity with *real* NDE data was achieved.

Keywords: Air-coupled ultrasound, Lamb waves in single isotropic layers, pitch-catch NDE model, array signal processing, software tool.

List of publications

- Prego Borges, J. L. “Lamb: a simulation software for ideal air-coupled Lamb wave based ultrasonic NDT systems”. *Submitted to Elsevier, Ultrasonics* (Jul. 2010).
- Prego Borges, J. L. “Lamb: a simulation tool for air-coupled Lamb wave based ultrasonic NDE systems”. In *Proceedings of the* $1^{st.}$ *Barcelona Forum on Ph.D. Research in Electronic Engineering* (Oct. 2009), N°1, Universitat Politècnica de Catalunya, pp. 35-36. ISBN: 978-84-7653-398-7.
- Prego Borges, J. L. “Lamb: programa de simulación para sistemas de END mediante ondas de Lamb y ultrasonidos acoplados por aire; etapa de verificación del módulo de simulación de campos acústicos”. Tech. Rep., Ministerio de Ciencia y Educación de España, October 2009. Ph.D. stay report. Oslo, Norway.
- Prego Borges, J. L., Yañez, Y., Chávez, J. A., Salazar, J., Turó, A., and Garcia Hernandez, M. J. “On the influence of using a non-ideal element model to predict the plane wavefront generation for air-coupled concave arrays transducers used in Lamb wave NDT systems”. In *The International Congress on Ultrasonics* (April 9-13) ICU2007,Vienna).
- Prego Borges, J. L., Yañez, Y., Chávez, J. A., Salazar, J., Turó, A., and Garcia Hernandez, M. J. Plane wavefront amplitude equalization for air-coupled concave array transducers used in a Lamb waves NDT systems. In $19^{\text{th}\cdot}$*International Congress on Acoustics* (Sep. 2-7). ICA2007, Madrid.
- Prego Borges, J. L., Montero de Espinosa, F., Chávez, J. A., Turó, A., and Garcia Hernandez, M. J. “Diffraction aperture non-ideal behaviour of air-coupled transducers array elements designed for NDT”. Elsevier, Ultrasonics 44 (2006), 667-672.
- Prego Borges, J. L., Claret, Q. C., and García Hernández, M. J. “FIRST: Acoustic field impulse response software. An acoustic field simulator for arrays used in non-destructive applications with air-coupled ultrasonic Lamb waves”. Tech. Rep., Polytechnic University of Catalonia (UPC), Sensor and Systems Group, Barcelona, Spain, 2006.

Acknowledgements

I'd like to express my sincere gratitude to my advisor Dr. Miguel Jesus García Hernandez for his patient endurance and encouraging help during all these years of study and struggle to arrive to this moment.

I wish also to express my thankfulness Dr. Francisco Montero de Espinosa from CSIC (Spain) for providing the air-coupled arrays without which this thesis could not be possible and to Ms. Aurora Rubio secretary of the DEE who always help me addressing the many questions and doubts that I've had during these years. Thank you very much Aurora and God bless you.

My special thankfulness are for Dr. José Luis Gonzalez from UPC-DEE and Dr. Rafel Perez Perez from UPC-FA; both for their *invaluable* support and kindness help during my Ph.D.

I've specially own my profound appreciation to Professor Sverre Holm and also to Profs. Andreas Austeng and Fritz Albregtsen from IFI Centre for Imaging from Universitetet i Oslo (Norway) and to Profs. Michel Castaings and Bernard Hosten from Laboratoire de Mécanique Physique, Université Bordeaux (France) for their invaluable aid and support with this student.

To my dear *northmen* friends Peter Nasholm and Knut Landmark goes my sincere appreciation for their kindness help during my stay at IFI and the grate patience they had shown bearing the long... monologues about "life" that they had suffered from my part. Please forgive me once again my dears friends.

This manuscript shall not be finished without the expressing the significant help from Bonny who has withstand and correct with grate patience all the mistakes of my poor English. Thank you very much dear Bonny.

This acknowledgements will not be complete without expressing my profound appreciation and thankfulness to my dear wife *Sandra* who has accompany myself from the very beginning of this incredible adventure and who had suffered and succeeded also her own Ph.D. *You did it!*

And finally and above all, I'd wish to express *my deepest* gratitude and love to my dear and patient parents *Elsa* & *José* who have gave me their continuous faith and necessary strength to accomplish this project.

You have been in my mind and soul during all these years and before... and you will be for Ever with me in this world and *beyond*...

Contents

List of Tables

List of Figures

Nomenclature

English letter symbols

a	Radius of circular excitation region with constant pressure [m]
$2a$	Width of rectangular transducer [m]
$A_{\mathrm{L,S}}$	Amplitude of harmonic bulk $\mathrm{L}_{\pm}/\mathrm{S}_{\pm}$wave [m]
$2b$	Height of rectangular transducer [m]
c	Velocity of sound in a fluid medium [m/s]
c_{a}	Cord of a cylindrical concave array [m]
c_{ph}	Phase velocity of wave in a medium [m/s]
$c_{\mathrm{L/S}}$	Phase velocity of an L/S bulk wave in a medium [m/s]
c_{Lamb}	Phase velocity of a Lamb wave in a multilayered media [m/s]
$c_{\mathrm{I,J}}$	Abbreviated subscripts elastic stiffness dyadic ($\mathrm{c}_{ij,lk}$) in [Pa]
d	Width of material plate [m]
d_{e}	Distance between center points of array elements [mm]
$[D]$	Field matrix
D_{f}	Focal distance
E	Young modulus $= \sigma_3/\epsilon_3 = 1/s_{11}$ [Pa]
$\mathcal{E}$	Energy of a signal [J]
f	Frequency [Hz]
f_0	Central frequency in the bandwidth of a transducer [Hz]
f_{s}	Sampling frequency [Hz]
h	Impulse response function $\mathrm{h}(x, y, z, t)$ in [m/s]
H	Fourier transform of the impulse response function $h(x, y, z, t)$
$H_{\mathrm{n}}^{(1)}(\mathrm{z})$	Hankel function of the $1^{\mathrm{st.}}$ kind and order n
H_{r}	Percentage of relative humidity
i	Imaginary unit $i = \sqrt{-1}$
I, J	Subscripts for the abbreviated stress/strain tensors: $I, J = \{1, 2, ..., 6\}$
$J_{\nu}(\mathrm{z})$	Bessel function of the $1^{\mathrm{st.}}$ kind
$\Im$	Imaginary part of a function or expression
$\boldsymbol{k}$	Wavenumber vector [rad/m]
k_i	Wavenumber vector component [rad/m]
$l_{\mathrm{x}}, l_{\mathrm{y}}$	Longitude and width of a laminate excitation profile [m]
$\mathcal{L}(R)$	Longitude of an arc [m]
$[L]$	Layer matrix
N	Number of samples of a discrete signal
N_{a}	Number of an array sensors
N_{f}	Number of discrete frequencies used in a given bandwidth

p	Acoustic over pressure (with sign) added to P_0 [Pa]
p_e	Inter-element space in a real array [mm]
P	Generic coordinates (x, y, z) of point in space [m]
P_0	Atmospheric pressure [Pa]
r	Distance measured on the surface of a plate [m]
R	Radial distance or distance to a point [m]
$\Re$	Real part of a function or expression
$s_\mathrm{I,J}$	Abbreviated subscripts elastic compliance dyadic ($\mathrm{s}_{ij,lk}$) in [1/Pa]
$[S]$	Multilayer system matrix
$\mathcal{S}$	Slowness $= 1/c_{ph}$ [1/(m/s)]
t	Time variable [s]
$\boldsymbol{u}$	Medium particle displacement vector [m]
u_i	Component "i" of displacement vector $\boldsymbol{u}$ [m]
v	Velocity signal [m/s]
v_n	Normal velocity of the surface of an acoustic transducer [m/s]
w	Angular frequency [rad/s]
W	Angular frequency vector [rad/s]

Greek letter symbols

α	Longitudinal bulk wave velocity of an isotropic medium [m/s]
α_i	Generic angle [Deg.]
β	Shear bulk wave velocity of an isotropic medium [m/s]
δ	Incoming angle for the directivity pattern of an array element [Deg.]
δ_s	Steering angle of an array [Deg.]
Δ	Fractional change of a volume $= \epsilon_{xx} + \epsilon_{yy} + \epsilon_{zz}$
ϵ_ij	Strain tensor, full subscript notation
ϵ_J	Strain tensor, abbreviated subscript notation
λ	Lame constant $= \mathrm{c}_{12}$ in [Pa]
μ	Lame constant $= \mathrm{c}_{44}$ in [Pa]
∇	Gradient vectorial operator $\triangleq (\mathrm{i}\frac{\partial}{\partial x} + \mathrm{j}\frac{\partial}{\partial y} + \mathrm{k}\frac{\partial}{\partial z})$
∇^2	Laplacian scalar operator $\triangleq (\frac{\partial^2}{\partial x^2} + \frac{\partial^2}{\partial y^2} + \frac{\partial^2}{\partial z^2})$
ϕ	Helmholtz scalar potential
$\theta_\mathrm{i,r}$	Incidence/reception angles [Deg.]
ρ	Mass density [kg/m^3]
σ_ij	Stress tensor, full subscript notation in [Pa]
σ_I	Stress tensor, Abbreviated subscript notation in [Pa]
τ_i	Generic time instant [s]
υ	Poisson ratio $= -\epsilon_1/\epsilon_3 = -\epsilon_2/\epsilon_3$
ξ	Wavelength [m]
$\xi_\mathrm{L/S}$	Bulk longitudinal and shear wavelengths [m]
ξ_R	Rayleigh wavelength [m]
$\boldsymbol{\psi}$	Helmholtz vectorial potential

List of common acronyms

APES	Amplitude and Phase Estimation beamformer
ASM	Angular Spectrum Method
CW	Continuous Wave
DAS	Delay and Sum
DOA	Direction Of Arrival
dll	Data Link Library
DFT	Discrete Fourier Transform
FE/FEM	Finite Element/Finite Element Method
FFT	Fast Fourier Transform
FSF	Free Software Foundation
GMM	Global Matrix Method
GNU	The gnu wildebeest, logo of FSF
GPL	General Public License
GUI	Graphic User Interface
IDFT	Inverse Discrete Fourier Transform
IDT	Interdigital Transducer
IFFT	Inverse Fast Fourier Transform
IRM	Impulse Response Method
MB	Mega Byte/s
MV	The Minimum Variance or Capon beamformer
NDE/NDT	Nondestructive Evaluation/Nondestructive Testing
NPL	National Physical Laboratory from the United Kingdom
OS	Operating System
PVDF	Polyvinylidene Fluoride (a polymer film piezoelectric transducer)
RX/TX	Receiver/Transmitter
SNR	Signal to Noise Ratio
THS	Time Harmonic Solution
TMM	Transfer Matrix Method
WGN	White Gaussian Noise

List of thesis acronyms

BW	Bandwidth
$\bar{\mathrm{BW}}$	Fractional Bandwidth = $\frac{BW}{f_0}$
DR	Discrete Representation
ele./eles.	Element/Elements
FIRST	Field Impulse Response Software
IR	Impulse Response
mp	Multiple precision
PW	Plane Wave
PWF	Plane Wavefront
SIE	Single Ideal Element
SNIE	Single Non-Ideal Element

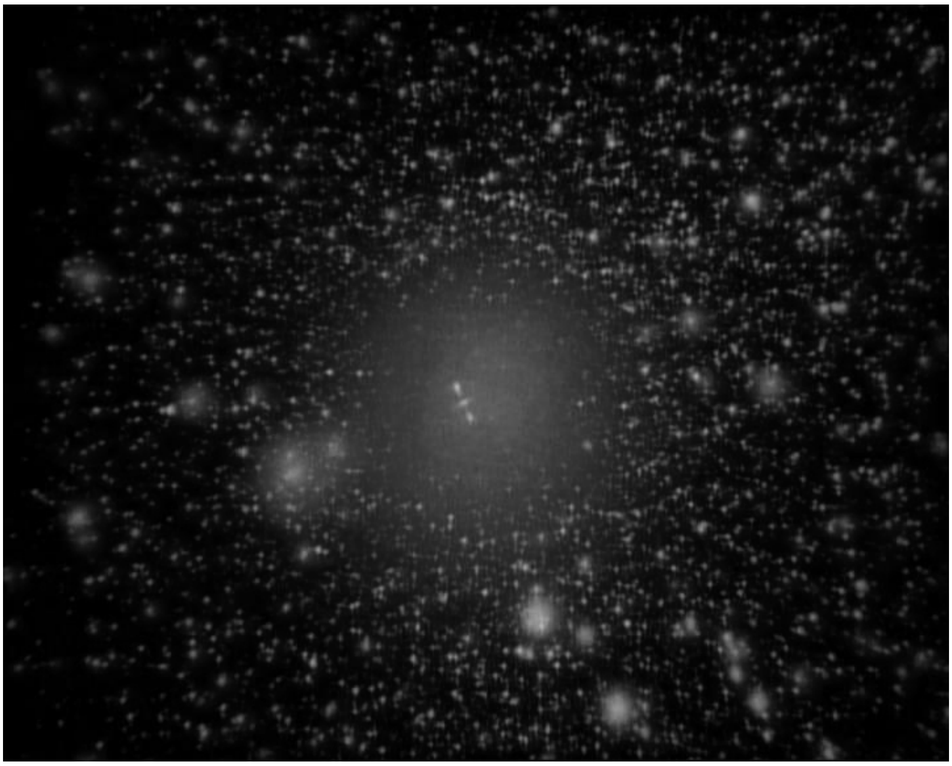

. . . There are in fact 100 billion other galaxies each of which contains something like 100 billion stars. . . Think of how many stars, planets and kinds of life there may be in this vast and awesome universe. . .

As long as there have been humans we have search for our place in the cosmos. *Where are we? Who are we?*
We find that we live on an insignificant planet of a humdrum star lost in a galaxy, tucked away in some forgotten corner of a universe in which there are far more galaxies than people. . .

We make our world significant by the courage or our questions and by the depth or our answers. We embarked on our journey to the stars with a question first framed in the childhood of our species and in each generation asked a new with undiminished wonder: "*What are the stars?*"

Exploration is in our nature. We began as wanderers and we are wanderers still. We have lingered long enough on the shores of the cosmic ocean.
We are ready at last to set sail for the stars...

Carl Sagan

Chapter 1

Introduction

1.1 Thesis motivation

The subject of non-destructive testing (NDT) and non-destructive evaluation (NDE) is not new in the field of acoustics[1]. However the topic of air-coupled ultrasound is a relatively new development and implementation.
Attempts have been made during the past 20 years to change the challenging contact coupling mode of ultrasound to a non-contact version. Then, a variety of generation/detection techniques was developed by utilizing laser, capacitive, electromagnetic (EMATs) and piezoelectric transducers. The latter is still one of the cheapest and more reliable methods available today.
The complexity of acoustic vibrations and interactions involved in the NDT of materials makes the subject of analysis, modelling and inverse problem[2] solution very challenging and research demanding.
Computer modelling aids then play a fundamental and key role in the visualization and understanding of the involved phenomena and in the determination of alternative solutions. Although to the author's knowledge, few examples of fully non-contact modelled systems have been reported in the literature[34, 112, 130, 204] so a real effort has been made in the compilation of this thesis.
The work is modest because it only involves research on ideal isotropic single laminate materials, but there are possibilities for future expansion with the inclusion of isotropic multilayer plate models[46], addition of two-dimensional arrays[3] and inclusion of improved signal processing techniques.

---

[1] The acronyms for Non-Destructive Testing (NDT), also called Non-Destructive Evaluation (NDE) or Non-Destructive Inspection (NDI), indicate that experiments and analysis on a test piece do not destroy the exemplar and they will be used interchangeably along the thesis.

[2] Inverse problems are those based on accurate elasticity theory models that compare ultrasonic measured data to numerical predictions and then infer material properties e.g. the complex viscoelastic moduli of a plate[38].

[3] The use of single circular transducers for excitation/reception is not contemplated in this thesis because these belong to two-dimensional aperture types which at present are not implemented in the programme.

1.2 Thesis objectives and contributions

The objective of the present work is to provide the NDE/NDT field with a free open source computer simulation environment for air-coupled Lamb wave based systems i.e. **The LAMB software**[4].
The programme is capable to recreate the behaviour of plane and cylindrical concave arrays[77, 299] used in NDE systems based on single ideal isotropic laminates excited by air-coupled ultrasonic Lamb waves.
The main purpose of the simulator is to identify the performance of these systems under different acoustic aperture designs and to study phased array beamforming techniques in reception. The thesis contributions include:

1.2.1 Directivity effect of individual sensors

The effective verification of the key role of the spatial directivity of individual air-coupled array sensors. Two models were proposed for the acoustic field simulation of emitting rectangular apertures: 1) SIE and 2) SNIE approaches[5]. A simple 2D directivity schema based on the reciprocity of radiation/reception diagrams of a harmonic excited SIE aperture was included in the receiver section. The influence on detected signals and the corresponding radiation diagrams produced by the geometry of the receiver was confirmed and compared with those of a proposed new plane array design.

1.2.2 Coherent nature of Lamb wave acoustic fields emitted

The spatial coherent nature of the plate radiated fields produced by the air-coupled excited Lamb waves was verified by means of several receiver radiation diagrams.
The reconstruction of the (f, k) dispersion relation maps was verified locating a simulated plane array parallel to the examined laminate. In this aspect the use of the coincidence principle with a receiver array is not recommended since the spatial information contained in the plate radiated fields is lost in the reconstruction process.

1.2.3 DAS beamforming

A first step in a signal processing block was added to the developed tool by the implementation of a Delay And Sum (DAS) beamformer. The influence of the noise and interference present in the detected signals was verified as the main source of error in the determination of the receiver radiation diagrams. Other causes of pattern modification such as the use of array with wider sensors and non-plane aperture designs were also verified.

---

[4] A beta version is available now for downloading in the author's page at the Matlab Central website: www.mathworks.com/matlabcentral/fileexchange/authors/23152 .

[5] Acronyms corresponds to the Single Ideal Element and the Single Non-Ideal Element respectively.

1.3 Lamb waves

1.3.1 Background

Lamb waves are basically two-dimensional vibrations in plates[6]. They can be classified into *symmetric* and *antisymmetric* modes[7] and they are tightly related to Rayleigh waves[121] which tend to occur on the boundary of semi-infinite half spaces[8].

They were first studied by Lord Rayleigh in 1889 in the context of geophysical phenomena while he was analysing plate vibrations in plain strain with traction-free faces[218]. Years later in 1917 the seminal work by Horace Lamb[143] set the basis for the theory of waves that later will carry his name i.e. *Lamb waves.*
Lamb developed the mode vibrations and expressions for velocity dispersion phenomena of these guided waves in an homogeneous plate in vacuum. Later between 1945 to 1955 Firestone and Ling started the Lamb wave based NDT era[64, 65].
Since then thanks to the effort of several authors beginning with the significant contributions by Mindlin[174] and Viktorov[276, 277] in 1960 and 1967 respectively the field has advanced rapidly. The last work not only covered the theory of Rayleigh and Lamb waves but also possible NDT applications for isotropic elastic media.
Others leading contributors to the field were Achenbach[1], Auld[16], Graft[85], Brekhovskikh[29], Miklowitz[173], and many others.

Because of their 2D wave propagation nature Lamb waves can travel long distances[9] with less attenuation than bulk waves[10] which are 3D waves[11]. This feature makes Lamb waves very attractive for the NDT of plates and laminated structures in the aerospace industry[39, 47, 50, 157, 222] because they can interact with a defect[12] which is produced during the manufacturing process or caused by prolonged use. These modifications apart from causing changes in the spectrum of test signals can also lead to the appearance of other Lamb modes other than the excited modes. This is a phenomenon known as mode conversion[34, 41, 60].

---

[6] They could also appear in tubes and structures because they have lower and upper boundaries with planar dimensions far greater than the thickness dimensions.

[7] This classification is made is with respect to middle plane of a plate, see Fig. 1.1.

[8] Semi-infinite half spaces actually do not exist but because of the attenuation of a wave with the depth if the plate thickness is greater than ≈ 5 wavelengths, Lamb waves cease to exist leaving only vibrations on the surface, which are in fact Rayleigh waves.

[9] This specially true for metals in which the wave attenuation is very low so they can propagate several meters.

[10] Apart from the intrinsic part produced by the material.

[11] The terms *bulk* wave and *plane* wave are commonly used interchangeable.

[12] These can be holes, cracks, rivet holes, delaminations and disbonds.

The subject of Lamb waves has evolved and branched out enormously into many areas of NDT/NDE study[13]. Current trends in research include for example:

- Modelling of wave propagation in complex (non-plane) structures[22, 42, 144, 160, 211].
- Study of the interactions of Lamb modes with defects using the Finite Element Method (FEM) or Boundary Element (BE) codes[10, 11, 41, 59, 95, 146, 206, 265].
- Development of damage monitoring systems for critical components or structures through real time analysis of acoustic emitted wave forms. This led to the concept of smart materials or smart structures[18, 19, 61, 227, 228, 252, 305].
- Determination of complex elastic constants in single and multi-layered materials (mixtures of isotropic, orthotropic and/or anisotropic[14] plates) by inverse problem procedures with reflected and transmitted ultrasonic data[13, 40, 39, 48, 49, 62, 115, 186, 232].
- Detection of corrosion in pipelines in the chemical and petro-chemical industries. This has major concern in the oil industry because most of the pipes are buried and insulated and the corrosion may be invisible even though it is on the surface[7, 56, 141, 151, 159, 162, 199, 249].
- High repeated loads and corrosive environments in aircraft structures which produce various types of fatigue damage. Because aerospace structures are principally formed by panels that act as natural wave guides Lamb waves have increasingly been studied and used and electronic monitoring systems are being integrated as part of their structures for early damage detection[24, 51, 75, 76, 129, 163, 185, 301].
- Application and study of new signal processing techniques for Lamb wave analysis and detection such as: beamforming, migration techniques, probability-based imaging, time reversal, tomography, wavelets, etc. See for example Refs. [97, 119, 140, 191, 247, 248, 241, 301, 303, 295].

---

[13] Due to the vast volume of literature in the field here we cite only some key references. For a good review on the field see please also Refs.[26, 47, 52, 197, 221, 223, 224, 225, 226].

[14] In isotropic materials, waves have the same phase speed in all directions, while in anisotropic solids this variates with the propagation direction. On the other hand orthotropic laminates are those with an isotropy plane, like unidirectional fiber composites.

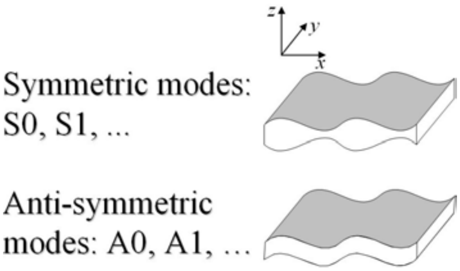

Figure 1.1: Basic types of Lamb waves on a plate.

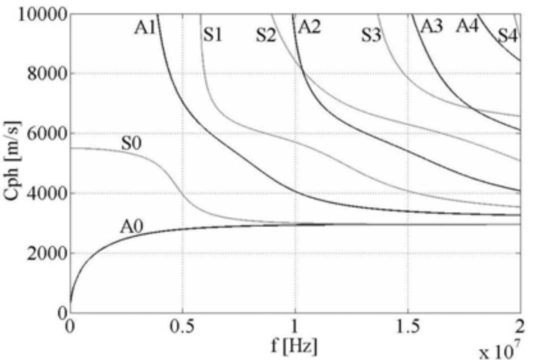

Figure 1.2: Lamb wave dispersion curves for a $d = 0.5$mm aluminium plate in air.

1.3.2 Lamb waves: main features

As mentioned before Lamb waves[15] are mainly categorized following a geometrical criterion, into *symmetric* and *anti-symmetric* modes. This principal division can be observed in the above Figure 1.1, were the common denomination of the modes is indicated[16].
The modes, which actually are the *free* or *forced* vibrations of a plate can be viewed as an internal combination[17] of successive reflections of longitudinal (or pressure waves, P) and shear vertical (SV) plane waves in the wave guide[18]. Therefore an infinite number of modes can coexist simultaneously leading to complex wave behaviour patterns.

§Dispersion

A very important characteristic of Lamb waves related to their propagation velocity in a wave guide is a phenomenon called dispersion[19]. This distinguishing feature is a non-linear relationship between the phase velocity of the waves and their frequency.

---

[15] Also known as plate waves.

[16] Here the plate deformations are enormously emphasized for the clarity of the figure.

[17] This wave coupling phenomenon strictly speaking exist in plates with free boundaries. Then for a wave propagating along the X axis the real wave vector components are: $k_{\rm x}^{\rm P} = k_{\rm x}^{\rm SV} = k_{\rm x}^{\rm Lamb}$. On a plate with other boundary conditions the P and SV waves start to lose the coupling[16] Vol.II.

[18] The P waves have their displacement field oriented towards the direction of propagation, while the SV waves are orthogonal to this direction; both of them into the XZ plane. Shear horizontal or Love waves[156] have their displacements parallel to the XY, plane and occur on the interface of two different materials coupled. Like Lamb waves Love vibrations can be further classified into symmetric and anti-symmetric modes.

[19] This is not the case for Rayleigh waves which are non-dispersive vibrations with a constant phase velocity. An approximately expression for the phase velocity in an isotropic half-space is: $c_{\rm R} = c_{\rm St}\frac{0.87+1.2\nu}{1+\nu}$. Where $c_{\rm St}$ is the phase velocity of shear transversal waves and ν the Poisson ratio.

Figure 1.2 shows a typical dispersion map[20] for an aluminium plate in air while the corresponding Lamb mode dispersion equations[143, 277] for an isotropic plate in vacuum are given by[21]

$$\frac{\tanh sd}{\tanh qd} = \frac{4k^2qs}{(k^2+s^2)^2} \tag{1.1a}$$

$$\frac{\tanh qd}{\tanh sd} = \frac{4k^2qs}{(k^2+s^2)^2} \tag{1.1b}$$

In a waveguide the physical effect that dispersion produces in the vibrations as they travel is a lengthening or *spread* of the wave packets which provokes a generalized loss in the amplitude of the signals[22]

§Excitation and reception

Because of the strong relationship of Lamb waves with P and SV waves the coupling of Lamb waves onto a plate can be carried out by many forms of excitation (see Figure 1.3). Some of them are for example[23]:

- Concentrated normal or shear perturbations over the surface of a plate.
- Periodically distributed normal excitations over surface of a laminate.
- Normal perturbations distributed accordingly to a sinusoidal law on the surface of a plate. The so called *wedge method* based on the coincidence principle of Snell law: $\sin\theta_i = \frac{\xi_{\text{air}}}{\xi_{\text{Lamb}}}$.

Similar or combined[120, 181, 285] procedures can be applied in the reception of Lamb waves specially using types a), c) and d)[24].

In the case of the present thesis which models the behaviour of an air-coupled NDT system whose excitation and reception are based on the coincidence principle the excitation is accomplish by using an arrangement of concentrated normal forces in small circular regions on the plate surface[25].

---

[20] A general approach for the determination of the Lamb mode dispersion curves in layered media is introduced in Chapter 3 with the Global Matrix Method or GMM.

[21] Here $s = \sqrt{k^2 - k_{\text{t}}^2}$; $q = \sqrt{k^2 - k_{\text{l}}^2}$ with $k_{\text{t}} = w\sqrt{\frac{\rho}{\mu}}$ and $k_{\text{l}} = w\sqrt{\frac{\rho}{\lambda+2\mu}}$.

[22] This effect of descent in the amplitudes is different from those provoked by the material attenuation or the energy leakage to the surrounding media.

[23] These types belong to the *surface* class of excitations which is different from those possibly located *inside* the plate; after I. A. Viktorov[277]. Classical ultrasonic sources/receivers used include: EMATs[8, 88, 284],capacitive[37, 187, 188] and piezoelectric polymer film (PVDF) interdigital transducers (IDTs)[100, 152, 176, 177].

[24] Non-contact excitation/detection examples of types: a) are lasers, while d) arrangements are normally employ in air-coupled systems.

[25] For more details see the Time Harmonic Solution (THS) in Chapter 4 of this thesis.

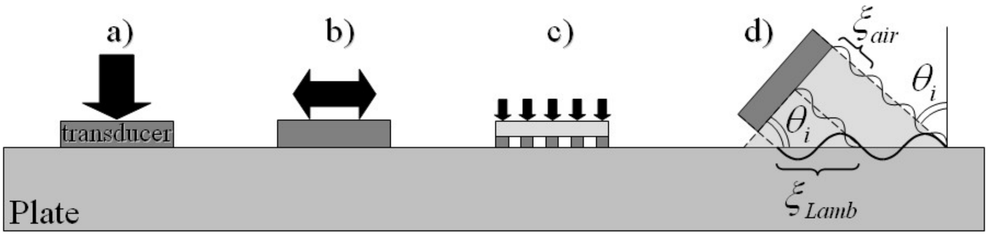

Figure 1.3: Different forms of excitation of Lamb waves: a)Normal pressure, b) Shear force, c)Normal periodically distributed pressures and d)the Wedge method.

The reception of the signals is based on the calculation of the acoustic field radiated by a selected area of the laminate[26].

1.4 Non-contact NDE with Lamb waves

1.4.1 Background

The majority of NDT methods require normally the use of couplants[27] between the material or test piece under inspection and the transducers. This is principally to enhance the pairing conditions of the transmitted and received signals and in consequence the general sensitivity of the techniques. However there are certain cases were this is not possible for any of the following reasons:

- Wood or polymer based materials such as paper and foam may be damaged by contact with couplants or be incapable of withstanding subsequent dry processes.
- Water may ingress into defects or delaminations reducing and/or changing the detectability of signals.
- Anti contamination requirements of final products. Typical examples are aerospace materials which will form part of honeycomb structures[28].

These conditions then lead to the necessity of the elimination of couplants[29] and the development of non-contact NDE methods. These can be classified into laser based[251] and air-coupled techniques[118, 165].

---

[26] This is done using the Impulse Response Method (IRM). For more details consult Chapters 2 and 5.

[27] Typical examples are: water, glycerine and a variety of water/oil based pastes.

[28] Other examples are: electronic circuit boards and in-process inspection of a fibre reinforced plastics.

[29] Dry-coupled transducers are a possible alternative solution in some cases since they use a layer of synthetic rubber with similar acoustic impedance to water to provide the coupling. A disadvantage of this approach is the requirement of significant pressures to work properly which may be incompatible or inadvisable in the case of delicate materials.

Because the present work models an array based air-coupled NDE system the subject of laser techniques will not be discuss[30] although the THS method in Chapter 4 could be apply to model laser NDT techniques.
In the area of air-coupled NDT methods[31] grate efforts had been made over the years by several researchers be it in the development of new and enhanced air-coupled transducers[90, 169, 187, 188, 189, 194, 240, 254], the improvement of the required electronics[193, 233, 272, 298, 299] or the availability of superior NDE system models[34, 38, 112, 115, 130, 153].

1.4.2 Air-coupled systems

Air-coupled NDT ultrasound has two main issues that arise in practice during evaluation tests. One is the effective amount of energy transmitted or *coupled* into a the test plate[32] and second is the attenuation of ultrasound in air. Both of these phenomena impose the main limitations on the capabilities of these techniques[33]. However with a careful system design and the application of some general rules they can be overcome. Examples are:

- Achieve the maximum acoustic power from the transmitter/s.
- Maximize the sensitivity of the receiver/s stage.
- Reduce the noise and interference in the receiver electronics as much as possible.
- Apply signal processing techniques in order to enhance the SNR[34].

§The air-coupled problem

More important than attenuation is the *coupling* effect or the efficient transference of energy to the laminate being inspected. This effect depends primarily on the difference in the acoustic impedances of air, the ultrasonic transducers used and the material being inspected.

---

[30] The advantage of optical methods is the excitation and detection in a wideband of frequencies. For more details consult Refs.[4, 117, 120, 175, 181, 191, 192, 246, 292, 297, 300, 303].

[31] For the case of water coupled NDT ultrasound see Refs.[78, 133, 171, 223, 224, 290, 304].

[32] Unless explicitly mentioned this term will be used interchangeable for single or multilayer materials laminates.

[33] Main setup arrangements for the NDE of plates include: 1) C-scan reflection, 2) C-scan transmission[133] and 3) C-scan in pitch-catch mode. This last alternative is the one used in the present model. See Figure 1.4.

[34] The most common and simple example is the use of averaging e.g. $10 \leq N_{\text{ave}} \leq 100$.

Because of an enormous mismatch of acoustic impedances between the air and the solids[35], most of the energy is not transmitted or is reflected back from the surfaces. This phenomenon can be roughly evaluated by the following wave intensity transmission coefficient[36]

$$T = 4\frac{Z_{\mathrm{air}} Z_{\mathrm{plate}}}{(Z_{\mathrm{air}} + Z_{\mathrm{plate}})^2} \tag{1.2}$$

Then to give an example for an aluminium plate immersed in water (with $Z_{\mathrm{water}} = 1.5\,\mathrm{MRayls}$) the transmission will be approximately of $T_{\mathrm{Al}}^{\mathrm{water}} \cong 29\%$, while for the same plate examined in air this will be only of $T_{\mathrm{Al}}^{\mathrm{air}} \cong 1\%$.

The fact is that in a normal non-contact NDT scenario there are four interfaces that the ultrasound must cross before being detected. Two are represented by the emitting/receiving transducer surfaces to the air (about: 35 dB + 35 dB). While the other two are form by the air to the plate interface and viceversa. These last two depend on the material being tested and could be around 50 dB to 90 dB in total. Then the global insertion loss for an air-coupled NDE system could be between from 120 dB to 160 dB.

This is a well known issue partially solved by the inclusion of $\lambda/4$ adaptation layers attached to the surface of the transducers[80, 81, 82, 83, 110, 131, 178, 179] and the use of new air-coupled composite devices[99, 250, 291].
However an advantage of air-coupled ultrasound in contrast to water-coupled techniques is the practical elimination of the loading effect on the laminate specimen. This for example has a significant influence in the attenuation of the A0 mode when a plate is immersed in a water[37].

§Attenuation of ultrasound in air

The attenuation of ultrasound with the distance is unfortunately far superior in air than in liquids. For example at a frequency of 1 MHz in air it can reach values of $\alpha \approx 164\,\mathrm{dB/m}$![38]
However for short distances of only a few centimetres it can have lower dB figures which do not constitute a significant loss.
An equation for determination[39] of the attenuation of ultrasound[272] is[40]

$$\alpha = 1.64\ 10^{-10} f^2 \ \mathrm{[dB/m]} \tag{1.3}$$

---

[35] For example for aluminium the acoustic impedance is $Z_{\mathrm{Al}} \cong 17.33\,\mathrm{MRaysl}$, while air has a value of $Z_{\mathrm{air}} \cong 427\,\mathrm{Raysl}$ @20°C, with 1 Mrayls = 10^6 kg.m^{-2}.s^{-1}

[36] This is a simplified expression[118, 133] valid only for the case at normal incidence $\theta_{\mathrm{i}} = 0$.

[37] This is mainly due the out-of-plane displacements of A0 in contrast to e.g. S0.

[38] At the same frequency in water it has an approximately value of $\alpha \approx 0.22\,\mathrm{dB/m}$ [133].

[39] An alternative expression is presented in Chapter 2 and Appendix A of this work.

[40] Then the acoustic pressure for a single frequency is: $p(\mathbf{x}, t) = p_0 e^{-\alpha \mathbf{x}} e^{\mathrm{i}(wt - \mathbf{kx})}$.

A useful relationship[41] for the estimation of the so called extinction distance or ed which is the distance where the amplitude of the pressure wave will be reduced to $1/e$ of its original value is

$$ed = \frac{5\ 10^{10}}{f^2}\ [\mathrm{m}] \tag{1.4}$$

Then for example at $f = 100\,\mathrm{kHz} \Rightarrow ed = 5\,\mathrm{m}$ and the signal will be reduced to 36.8 % of its original amplitude.

1.4.3 NDT system simulation approaches

The availability of computer models and programs that can accurate simulate the behaviour of devices or systems involved in ultrasonic NDT is a continuous and demanding research topic. Many methods and combinations are used but basically they can be classified into analytical and finite element methods (FEM).
As the their name suggests analytical techniques resolve the difficulty by implementation of available closed form formulas while FEM employs a discretization of the medium/s for solving the differential equations governing the problem. Both of these approaches have advantages and disadvantages[42] mainly related to the degree of accuracy attained for the solution and the time employed to obtained it[43].

The case of air-coupled ultrasound systems is relative new in the NDE arena although efforts can be traced back to the 80's[69, 302].
Several models and programs had been developed for different parts and/or arrangements of an NDE scheme[58, 106, 115, 122, 158, 161, 167, 182, 183, 245]. However to the author's knowledge very few models have been developed for the complete modelling an air-coupled NDT system based on Lamb waves (see Fig. 1.4). These rely alternatively in FEM[112, 130] and analytical techniques[204].

The present work contributes to the NDE field with an analytically based free Matlab simulator[44] for an air-coupled array based system like the indicated in Figure 1.4.

---

[41] This expression is valid only for $f \leq 100\,\mathrm{kHz}$. See Ref.[102].

[42] Analytical solutions usually tend to be more simple and fast at the cost of lack of flexibility while FE methods provide flexible scenarios and throughout solutions at the cost of more time consuming simulations.

[43] It is important to mention that unfortunately very few problems encountered in acoustics have a closed analytical solution available then the only alternative are FE methods.

[44] The code was verified and ran in the Matlab®versions 6.5 and 7.4.0 (R2007a).

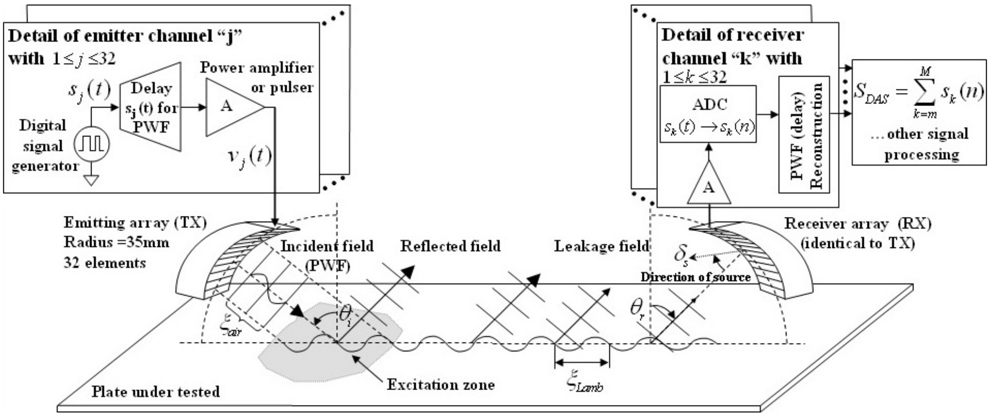

Figure 1.4: Schematic view of a C-scan pitch-catch mode developed air-coupled NDT system based on Lamb waves and cylindrical concave arrays[299].

1.5 Outline of the thesis

This section describes the organization of the thesis by summing up the methods and parts that constitute the LAMB simulator whose internal structure can be appreciated in the following Figure 1.5.

The thesis begins by presenting the generalities of Impulse Response Method or IRM for the calculation of acoustic fields. Then the particular solution for rectangular radiators derived by San Emeterio and Ullate[234] is presented. This method is implemented in the excitation block[45] of the LAMB programme and also used during the calculation of the radiated fields by the plates. A model for the attenuation of ultrasound in air is also described and included with the IRM routines[46].
Then comparisons of ultrasonic signals generated by FIRST programme are made with a well known group of acoustic simulators such as Field II, DREAM and Ultrasim[47] and the data provided from experimental measurements. The chapter finishes by including a set of simulations for a single rectangular radiator and an array composed with these elements. Conclusions are derived at the end.

The next two chapters, Chapter 3 and 4, are devoted to the programme plate propagation module.
After an introduction to the field equations for plane waves in an isotropic solid, Chapter 3 presents two methods for the computation of the Lamb wave

---

[45] This section is represented by the developed acoustic field simulator FIRST or Field Impulse Response Software.

[46] This model of the attenuation as well as the rest of the models presented on this thesis are valid only under the assumption of linear acoustics.

[47] The comparisons made with the Ultrasim software are presented in Appendix A.

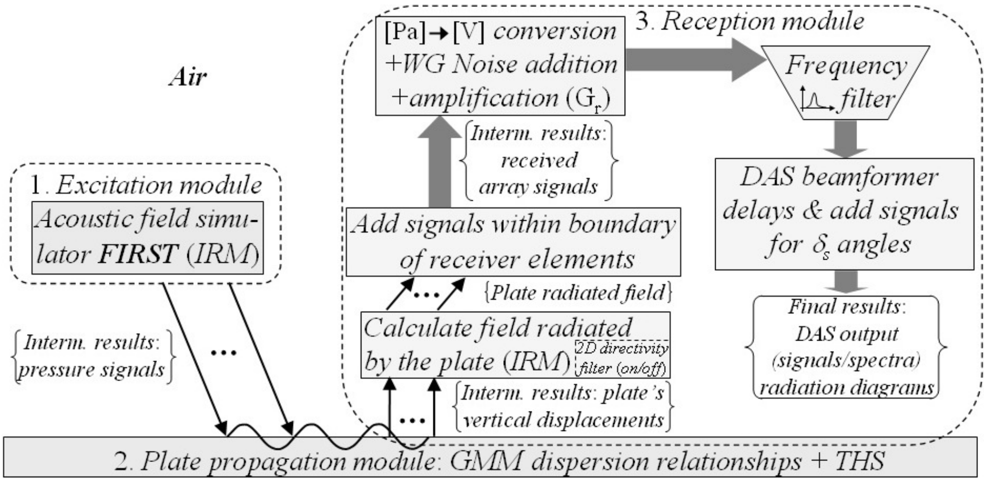

Figure 1.5: Internal block structure of the LAMB simulator programme for a Lamb wave based NDE system in ideal infinite isotropic laminates.

dispersion relationships[48] for attenuated homogeneous plane waves[49].
Here the Transfer Matrix Method (TMM) and its enhanced alternative the Global Matrix Method (GMM) are described.
Then simulation results for a GMM implementation are compared with experimental data drawn from laser vibrometer measurements in metal plates.
The chapter ends then by presenting main conclusions.

The Time Harmonic Solution method or THS is introduced in Chapter 4. This method in conjunction with the obtained dispersion data in Chapter 3 allows for the calculation of the displacement fields generated by a single circular radiator who exerts pressure on the surface of an isotropic plate.
The generalization for broadband pressure signals and arbitrary 2D excitations is then described followed by a short introduction with two other alternative approaches to THS.
A group of comparisons between THS simulations and the results obtained from FEM calculations and experimental data from impacted metal laminates are then presented for the case of a single circular radiator. Conclusions are then outline at the end of the chapter.

The internal structure of the LAMB simulator is detailed in Chapter 5. The integrating parts: 1)Excitation, 2)Propagation and 3)Reception are then described with special emphasis on the reception module of the software.
In this section of the programme the appropriate size of the plate emission

---

[48] The (f, k) maps. See Figure 1.2

[49] These are solutions with real frequency w_{Re} and a complex wavenumber $k = k_{\mathrm{Re}} + \mathrm{i}k_{\mathrm{Im}}$.

elements is discussed[50] followed by a description of a two-dimensional model used for the inclusion of the directivity characteristic of the receiving array sensors.
Then after an examination of array signal processing key concepts related to the NDE in air-coupled systems[51] a group of comparisons of LAMB programme simulations with experimental results are presented.
The assessment tests include copper and aluminium plates[52] and were carried out with a real air-coupled Lamb wave based NDE system using concave arrays[299].
An analysis of the advantages and disadvantages of using concave shaped[53] air-coupled transducer arrays is also presented.
Then a group of programme simulations for three different locations of a new proposed plane array[54] are introduced followed by the chapter conclusions.

Finally Chapter 6 makes a review of the thesis followed by the summary of findings of the work. The main conclusions are presented plus a list of suggestions for future investigation topics related to the NDE with Lamb waves using air-coupled array systems. These are grouped into: 1) LAMB software improvements and 2) Hardware system improvements.

---

[50] This is done here because the IRM field emission calculations for the plate are included into the reception module.

[51] These are related to the addition of a Delay And Sum (DAS) beamformer.

[52] The experiments include three tests: 1)A sweep in frequency with a single receiver sensor in $d = 0.35\,\text{mm}$ copper plate, 2)Narrowband signals in $d = 0.5\,\text{mm}$ aluminium plate (full array), and 3)Wideband signals in $d = 1.0\,\text{mm}$ aluminium laminate (full array).

[53] Here the geometry applies to cylindrical shaped air-coupled 1D arrays composed of rectangular piezoelectric sensors[178].

[54] The proposed linear transducer is composed of 48 sensors with the following dimensions: $\{2a, 2b, p_\text{e}\} = \{0.4, 15, 0\}\,\text{mm}$ for width, height and inter-element space respectively.

Chapter 2

The impulse response method

2.1 Introduction

This chapter is devoted to acoustic field calculation using the *impulse response method* or IRM. This method is the basis of the first module of the LAMB software to compute radiated acoustic fields.
The chapter begins with the historical background of IRM and related approaches to the acoustic field calculation.
Main equations of the method are then introduced, followed by a brief review of the use of IRM for rectangular radiators.
Then the mathematics for IRM of rectangular apertures is developed with special emphasis on the inclusion of air attenuation, wavelength and sampling frequency effects.
Finally a set of validation cases is presented to compare the results of the model with other software packages and conclusions are outlined.

2.2 History of the IRM

The desire to calculate generated fields produced by acoustic radiators, either by analytic expressions or by closed-form numeric formulas has long existed. Efforts can be traced back to the field of optics and to the original work by Kirchhoff[134] who in 1882 whilst working on the mathematical formulation for diffraction of light, laid the foundations for the later so-called *scalar diffraction theory*[84].
This theory although initially intended for light later came to constitute the base for modern ideas in acoustic field calculations [155].
It represents in the end nothing less than the Huygens-Fresnel principle of light wave interference first formulated analytically by Kirchhoff[134] and later revised and expanded by Sommerfeld[253].
We shall begin then our introduction to acoustic field calculation by reviewing only the main contributions to the subject since a comprehensive review of the field would doubtlessly be incomplete and beyond the scope of this thesis. The main purpose here is limited to extending the reader's familiarity with the *impulse response method* leaving aside other possible techniques.

2.2.1 The Rayleigh surface integral

The above mentioned works of Kirchhoff and Sommerfeld with the exact solution to the problem of diffraction using a reflecting half-space[253] were the starting point for acoustic field calculation.
Since then the first studies carried out to solve the baffling piston problem have made use of the Rayleigh integral solution[155].
In 1917 for example Rubinowicz[230] decomposed the Helmholtz and Kirchhoff integrals into a geometrical wave and a boundary diffraction wave. The latter was expressed as an line integral over the diffracting edge.
Years later in 1934 King[132] provided an alternative solution to the baffling piston problem for circular radiators with sinusoidal excitation (CW).
Schoch in 1941[242] basing his study on Rubinowicz's work on the Rayleigh form of Kirchhoff integral, published a solution for the field of a CW planar acoustic source of arbitrary shape with a uniform distribution of vibration amplitude.
Schoch[242] was the first to apply this method to the field of acoustics. For a comprehensive review of the historical development the reader is referred to the dissertation by Rutgers[231].
The Rayleigh integral[1] is a special case of the Huygens-Fresnell concept in which the radiating source and the boundary lie on a plane.
This is called the boundary element method or BEM[135, 136, 137, 166].

2.2.2 Nonuniform vibration amplitude distributions

The subject of nonuniform vibration amplitude distributions, evaluating the Rayleigh integral was studied in the 30's by Stenzel[255] and McLachlan[170] with Stenzel working in the farfield and McLachlan on the piston surface.
Jones[128] in 1945 published an extensive report on the Rayleigh integral tabulating results for farfield radiation patterns.
The majority of articles published during the 50's and 60's employed the Rayleigh surface integral as a basis for numerical analysis.
In 1974 Dekker[54] calculated on-axis and farfield distributions for circular disks with different types of boundary conditions. These conditions were piston like motion and radially symmetric velocity distributions for a simple supported disk and a clamped disk.
Greenspan[86, 87] wrote an extension of the King integral for an arbitrary axis-symmetric vibration amplitude distribution which was applicable in the farfield near to the piston axis.

---

[1] Formulated analytically by Helmholtz and Kirchhoff.

2.2.3 Transient excitations

Studies of transient fields produced by pulsed planar radiators in an infinite rigid baffle have been using integral transforms of time-harmonic expressions and direct time-domain solutions.
Supposedly Morse[180] was the first to derive an approximate expression for the radiation from a pulsed circular piston.
Hanish[91] and Freedman[72] have reviewed various aspects of transient field.
A general description of the transient fields produced by an arbitrarily shaped planar piston in terms of a convolution process was provided by Fischer[66] and then by Harris[93].
Harris summarised how a transient field can be determinated by convolving the surface velocity of the piston with the inverse Fourier transform of the time-harmonic radiation pattern of the piston.
This latter function is without doubt the spatial impulse response function.
In 1967 Chadwich and Tupholme[44] derived results from Oberhettinger's work[195] for a circular piston via a complementary scheme using Laplace and Hankel transform techniques.
Also Tupholme[271] in a study of pulsed fields generated by baffled plane pistons of arbitrary shape outlined how the Rayleigh integral could be obtained via the appropriate selection of Green's functions.
In the 70's Freedman published his results about transient fields[71].
Although not explicitly mentioned as a convolution process, the general scheme and conclusions incorporate ideas from the spatial impulse response method. Also Robinson et al.[220], had reported solutions on exact responses of near transient fields for circular pistons.
Perhaps the best known grouping and discussion of authors on their publications was made by Freedman[72], Stepanishen[257, 258, 259], and Harris[92] relating to the convolution integral representation of radiated fields.
Stepanishen plotted the impulse response in a similar form to that of Chadwick and Tupholme. He also was the first to do so explicitly by means of a convolution/impulse response approach.
From the preceding section it is clear that the Rayleigh integral expressions have provided the framework for numerous studies in the field radiated by pistons.
Most of the calculations of transient fields were either directly or indirectly based on the convolution/impulse response representation.
These works are so widely scattered in relevant literature that any discussion about the subject would remain interminable.

2.2.4 Other approaches

Another approach to the calculation of acoustic fields is the angular spectrum method (ASM) or acoustical holography[84, 184, 148].

This scheme is based on the formulation of the scalar diffraction theory in a structure that closely resembles the theory of linear invariant systems.

If across any plane the complex field distribution of monochromatic disturbances is Fourier-analyzed, the various spatial Fourier components can be identified as plane waves travelling in different directions away from the plane.

Then the field amplitude at any other point or on any other parallel plane can be calculated by adding these plane wave contributions, always taking into account first the individual phase shifts they have suffered during propagation[2].

A detailed study of the diffraction theory viewed through this method as well as applications related to the theory of radio-waves is referred to in the work of Ratcliffe[216].

Variations on the ASM are the nearfield acoustic holography (NAH), and the Helmholtz integral formulation implemented numerically by means of the boundary element method (BEM).

NAH is able to reconstruct radiated acoustic fields coming from vibrating objects using acoustic pressures measured on a hologram plane[286].

HELS, or the least square equation from the Helmholtz integral formulation is used to reconstruct interior and exterior regions of arbitrary radiating structures with relatively few measurements.

However, HELS seems to present problems for highly irregular bodies because of the slow convergence of solutions.

The above mentioned methods are only some of most important procedures and variations in techniques currently available in literature for the calculation of acoustic fields. For more information the reader is referred to Refs.[137, 287, 288, 293, 294].

It is significant that the angular spectrum methods, despite their apparent differences from the Rayleigh-Sommerfel solution and its different impulse response approaches, yield identical calculations of diffracted fields. This has been proved by Sherman[243].

2.3 IRM fundamental equations

To give support to following mathematical development of the impulse response method, first we shall define the acoustic properties of the medium in which waves will propagate.

The fluid medium is deemed to be linear unbounded, nondissipative, nondispersive, homogeneous, and isotropic with a wave propagation velocity of $c\,[m/s]$, and density $\rho\,[kg/m^3]$.

It is worth mentioning that despite these idealised medium properties, the conditions of the medium will later be adapted using an elementary attenu-

---

[2] See for example Refs.[67, 89, 237, 238, 261, 262, 268, 275].

ation model to support the air attenuation effect.

It is also important to understand that the following development is accurate provided that the diffracting aperture is larger than the minimum wavelength used. This last point is briefly discussed later at the end of the chapter[3].

Then according to the scalar diffraction theory the problem of calculating the acoustic field radiated by an aperture in a medium with the aforementioned properties could be described in terms of the acoustic velocity potential $\phi(P, t)$ as what is usually called a *boundary value problem*[180, 133].

This implies that an emitting aperture of area σ_S with a normal velocity distribution $\nu_n(P_0, t)$ is surrounded by a baffle (soft or rigid) with a normal velocity of zero.

In order to resolve the problem we take the acoustic field equation for a point in space $P(x, y, z)$,

$$\nabla^2\phi(P, t) = \frac{1}{c^2}\frac{\partial^2\phi(P, t)}{\partial t^2} \tag{2.1}$$

where ϕ is the time-dependent scalar velocity potential related to the medium particle velocity by

$$\nu_n(P_0, t) = -\nabla\phi(P_0, t) \tag{2.2}$$

Then the sound pressure at point $P(x, y, z)$ is given in terms of the potential by

$$p(P, t) = \rho\frac{\partial\phi(P, t)}{\partial t} \tag{2.3}$$

To solve Eq. (2.3) we recur to Green's theorem choosing first an appropriate function associated with the problem[84, 133]to reach the following expression[258, 259], for the acoustic field potential

$$\phi(P, t) = \int_0^t \int_\sigma \beta(z, t)\nu_n(P_0, t_0)g(P, t|P_0, t_0)\mathrm{d}S\mathrm{d}t_0 \tag{2.4}$$

where $g(P, t|P_0, t_0)$ is the associated Green function given by

$$g(P, t|P_0, t_0) = \frac{1}{4\pi}\frac{\delta(t - t_0 - |P - P_0|/c)}{|P - P_0|} \tag{2.5}$$

and $\beta(z, t)$ is an obliquity factor[84, 234] depending on the baffle condition of the problem,

$$\beta(z, t) = \begin{cases} 2 & \text{,for rigid baffle} \\ 2z/(ct) & \text{,for soft, or pressure released baffle} \\ 1 + [z/(ct)] & \text{,for free field.} \end{cases} \tag{2.6}$$

The integral (2.4) is basically a statement of Huygens's principle in that the field is found by summing up spherical radiated waves from all parts of the emitting aperture.

---

[3] See please § 2.4.5 on page 31.

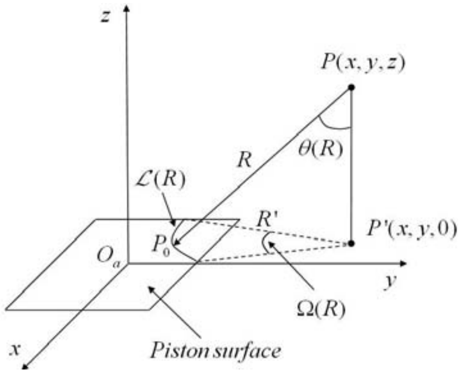

Figure 2.1: Piston schema.

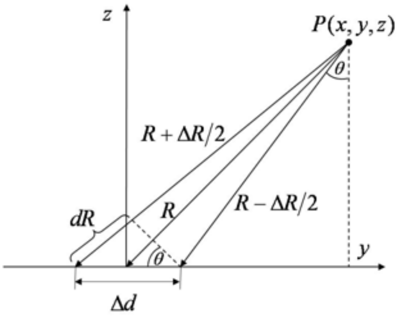

Figure 2.2: Piston schema edge on.

Furthermore, it can also be reformulated based on an acoustic reciprocity idea i.e. an emanating spherical wave[4] coming from the field point of interest P in which its expansion intersects the aperture[5] in an arc $\mathcal{L}(R)$ and where the auxiliary point P_0 lies (see Fig. 2.1). Then if we incorporate expression (2.5) for $g(P, t|P_0, t_0)$, into Eq. (2.4) we get

$$\phi(P,t) = \int_0^t \int_\sigma \nu_n(t_0) \frac{\beta(z,t)}{4\pi} \frac{\delta(t - t_0 - |P - P_0|/c)}{|P - P_0|} \mathrm{d}S\mathrm{d}t_0 \tag{2.7}$$

If we consider the vibrating element as having a uniform amplitude distribution we can further simplify Eq. (2.7) to

$$\phi(P,t) = \int_0^t \nu_n(t_0) \int_\sigma \frac{\beta(z,t)}{4\pi} \frac{\delta(t - t_0 - |P - P_0|/c)}{|P - P_0|} \mathrm{d}S\mathrm{d}t_0 \tag{2.8}$$

The evaluation of the integral (2.8) could be done by first integrating in space and then in time or viceversa initial in time and then in space. We will choose the first alternative and define $h(P, t)$ as

$$h(P,t) = \int_\sigma \frac{\beta(z,t)}{4\pi} \frac{\delta(t - t_0 - |P - P_0|/c)}{|P - P_0|} \mathrm{d}S \tag{2.9}$$

then from (2.8) and (2.9) we have expression (2.10) indicating the scalar velocity potential

$$\phi(P,t) = \int_0^t \nu_n(t_0) h(P,t) \mathrm{d}t_0 \tag{2.10}$$

or

$$\phi(P,t) = \nu_n(t) * h(P,t) \tag{2.11}$$

where the * denotes the symbol for convolution operation. We shall call $h(P, t)$ the impulse response of velocity potential for the piston-like aperture

---

[4] Dirac type impulse, see Eq. (2.5).

[5] Say at e.g. time instant t_0.

at point $P(x,y,z)$ in response to a Dirac type velocity excitation of its face. Then incorporating Eq. (2.11) into expression (2.3) which is the acoustic pressure[6] $p(P_{x,y,z},t)$, we get

$$p(P,t) = \frac{\partial[\nu_n(t) * h(P,t)]}{\partial t} \tag{2.12}$$

This can be re-expressed as

$$p(P,t) = \rho\nu_n(t) * \frac{\partial h(P,t)}{\partial t} \tag{2.13a}$$

or as

$$\begin{aligned} p(P,t) &= \rho\frac{\partial\nu_n(t)}{\partial t} * h(P,t) \\ &= \rho a(t) * h(P,t) \end{aligned} \tag{2.13b}$$

From these two alternatives we will choose the second form of equation (2.13b) including the normal acceleration[7] since it eliminates abrupt discontinuities that could arise from the derivative of Eq. (2.13a).

The idea now is to evaluate the expression (2.9) for $p(P_{x,y,z},t)$ in order to resolve the problem.

For this purpose, we have to evaluate first dS.

If we look at figure Figure 2.1 from the side and localize an auxiliary spherical coordinated system at point $P(x,y,z)$, we will see something similar to figure Figure 2.2.

In fact the contour of the aperture could have any form while it just remains flat. Then with the auxiliary system localized at P we shall define

$$R = |P - P_0| \tag{2.14}$$

as the radius of an emanating sphere from P. $\mathcal{L}(R)$ is the longitude of the arc of intersection and $\theta(R)$ is the angle formed by the arc and the normal to the surface at P. While $P'(x,y,0)$ is the projection point of P onto the plane of the aperture.

Observing Figures 2.1 and 2.2, we note that the incremental area ΔS is

$$\Delta S = \mathcal{L}(R)\Delta d \tag{2.15}$$

and

$$\Delta d = \frac{\Delta R}{\sin(\theta(R))} \tag{2.16}$$

---

[6] This is the amount of over pressure (including its sign) added to the normal ambient pressure P_0.

[7] Hereafter, we will drop the sub-index n for the normal velocity v_n and the normal acceleration a_n, meaning it's inclusion.

Then incorporating this last expression into Eq. (2.15) we get

$$\Delta S = \frac{\mathcal{L}(R)\Delta R}{\sin(\theta(R))} \tag{2.17}$$

where we observe

$$ds = \lim_{\Delta R \to 0} \Delta S \tag{2.18}$$

Then replacing the limit form of Eq. (2.17) into expression (2.9) for $h(P,t)$, it changes to

$$h(P,t) = \int_0^\infty \frac{\beta(z,t)}{4\pi} \frac{\delta(t - R/c)}{R\sin(\theta(R))} \mathcal{L}(R)\mathrm{d}R \tag{2.19}$$

With the substitution: $\tau = R/c$

$$h(P,t) = \int_0^\infty \frac{\beta(z,t)}{4\pi} \frac{\delta(t-\tau)\mathcal{L}(c\tau)}{\tau\sin(\theta(c\tau))}\mathrm{d}\tau \tag{2.20}$$

and applying the sampling property of the Dirac function, Eq. (2.20) becomes

$$h(P,t) = \beta(z,t)\frac{\mathcal{L}(ct)}{4\pi t\sin(\theta(ct))} \tag{2.21}$$

From Figure 2.1, we can observe that:

$$\begin{aligned} R &= ct \\ \sin(\theta(R)) &= \frac{R'}{R} \end{aligned} \tag{2.22}$$

Then introducing these last expressions into Eq. (2.21) we finally get

$$h(P,t) = \beta(z,t)\frac{c\Omega(ct)}{4\pi} \tag{2.23}$$

This is the departure expression for the calculation of the impulse response function for a piston-like aperture at point $P(x,y,z)$ in space.
As we can see Eq. (2.23) primarily depends on $\Omega(R)$ which in turn depends on the relative location of P, the position and form of the aperture and the propagation velocity of the medium.
It also interesting to note that these results will be a useful approximation in the case of a convexly or concave radiator (or receiver) in a baffle, as long as the dimensions and radii of the curvature are larger than the maximum wavelength over the relevant frequency band.

2.4 IRM for rectangular apertures

2.4.1 Introduction

The acoustic field of a rectangular aperture cannot be characterised as easily as that of a circular one since rectangular sources have two corresponding dimensions and they totally lack axial symmetry.
Thus, their field is dependent on the relationship between these two sides and on their respective ratios to the wavelengths present.
As a result field patterns of rectangular radiators have not been studied as extensively as those of circular pistons.
Here a brief introduction will review only the main contributions to the subject of IRM for rectangular radiators.

To the author's knowledge the first referenced work was by Stenzel[256] who in 1952 published an exact solution based on a single integration of a tabulated function for some cases of rectangular aperture.
Then in the early 70's Freedman[70, 73, 74] and Stepanichen[259, 260] both studied and found solutions for the farfield of rectangular sources while the nearfield was investigated by Lockwood and Willette[154]. Ocheltree[196] presented a method for the calculation of the continuous wave (CW) case for the rigid baffle condition.
A closed form solution for near and farfield situations was developed by Emeterio & Ullate in 1992[236, 273, 234].
It is of interest to note that this approach had been successfully used by other authors for calculations on a rectangular aperture with a cylindrically curved surface[207] and ultrasonic phased arrays under transient excitation[190].
Recently McGough[168] developed a fast method for calculating the CW excitation of nearfield rectangular transducers by removing numerical singularities in $h(P,t)$ which are caused by the use of inverse trigonometric functions.

Apart from the mentioned works on rectangular apertures, there is a vast arena of literature on the impulse response method for many other types of acoustic radiators i.e. circular, triangular, polygons, curved, radiators with non-uniform surface velocity profiles (apodized transducers) and array transducers.
A complete review of the subject is not the aim of this study, notwithstanding it would no be complete without mentioning the excellent works of A. Jensen, S. Holm and B. Piwakowski.
Jensen carried out an in depth investigation into IRM for polygon type apertures and arrays[122, 124] at various conditions with apodization[125], medium attenuation[123] and is the author of a very well know acoustic simulator software called Field II[8].

---

[8] http://server.oersted.dtu.dk/personal/jaj/field/

Next from the University of Oslo Holm et al.[105, 106, 107, 108] developed a medical imaging application called UltraSim[9].

This is a GUI[10] operated Matlab package based on the Rayleigh integral solution[259] of the discretization of the radiating surface into small piston-like sub-elements[63].

UltraSim can handle both homogeneous and layered media (without attenuation) assuming that the surface velocity of the element behaves like a separable function: $v_n(\vec{r}, t) = V(\vec{r})v(t)$.

On the other hand, B. Piwakowski developed a procedure[208, 210, 209] called discrete representation or "DR" for the calculation of the impulse response function.

This would be later implemented into a Matlab toolbox called Discrete Representation Array Modelling or DREAM[11].

DREAM is applicable to problems characterised by arbitrarily shaped Green causal functions, and lossy media with rigid, soft and free baffle condition possibilities.

In view of this scenario and bearing in mind the attainable objective of the present thesis and despite the existence of these free available packages the author preferred to develop his own routines since most of the core calculations for the impulse response in aforementioned softwares are hidden from analysis by the end user[12]. The intention is release in the near future a stable GNU[13] version of the LAMB toolbox presented on this thesis[14].

2.4.2 Definitions

Once obtained the departure expression of equation (2.23) for the calculation of the impulse response of a piston-like aperture, the following section summarises the well known work of Emeterio and Ullate[234].

This is the method which the first part of the LAMB toolbox uses.

The selection for the acoustic field simulation core of the toolbox is made on the basis that this is a relatively simple closed form solution for the near and farfield conditions which will later simplify calculations for array type aperture composed by rectangular radiators.

---

[9] http://heim.ifi.uio.no/ ultrasim/index.shtml

[10] Graphic User Interface.

[11] www.signal.uu.se/Toolbox/dream/

[12] IRM algorithms for calculation of $h(P, t)$, are hidden on private OS *dll* files.

[13] The GNU General Public License (GPL) is a widely used free software license written by Richard Stallman for the GNU project. GPL is a well known example of the type of strong copyleft license that requires derived works to be available under the same copyleft. Under this philosophy, GPL is said to grant the recipients of a computer programme the rights of the free software definition and uses copyleft to secure freedoms are preserved, even when the work is enhanced or modified.

[14] A beta version is available now for downloading in the author's page at the Matlab Central website: www.mathworks.com/matlabcentral/fileexchange/authors/23152 .

To begin with one observes that given the mirror-like symmetry of a rectangular radiator (see Fig 2.3) and assuming the medium is fluid with density ρ, speed of sound c and the above mentioned properties.
All references will be limited to the $1^{st.}$ quadrant since the rest could be referred to by taking the absolute value of corresponding coordinates. This means that the acoustic field at a point e.g. (x_1, y_1, z_1) will have a similar acoustic pressure at coordinates $(-x_1, y_1, z_1,)$, $(x_1, -y_1, z_1,)$ and $(-x_1, -y_1, z_1,)$.
Defining four regions from the $1^{st.}$ quadrant in figure Figure 2.3 and also the distances $d_i (i = 1 \ldots 4)$, from point $P'(x, y, 0)$ i.e. projection of $P(x, y, z)$ on the radiator plane to the straight lines which are the sides of the rectangle we will have

$$\begin{aligned} RegionI &= x \geq a, y \geq b \\ RegionII &= x < a, y \geq b \\ RegionIII &= x \geq a, y < b \\ RegionIV &= x < a, y < b \end{aligned}$$

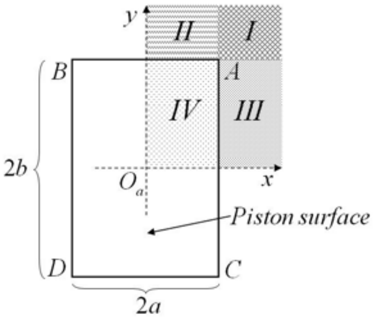

Figure 2.3: Piston zones

$$\begin{aligned} d_1 &= x - a & d_2 &= y - b \\ d_3 &= x + a & d_4 &= y + b \end{aligned} \tag{2.24}$$

Now from figures 2.4 and 2.5 and depending on the relative position of P', eight discontinuities will exist for the active arcs $\Omega(P, t)$.
The arcs are formed by the intersection of the aforementioned sphere that emanates from P and the rectangular piston surface.
These discontinuities will occur when the *active* arcs include any of the vertices of the rectangle at time instants $\tau_i (i = A \ldots D)$ or when the arcs are tangent to the rectangle boundaries at time instants $\tau_{Si} (i = 1 \ldots 4)$.
Therefore the time of flight from the signals coming from the vertices to the field point P will be

$$\begin{aligned} \tau_A &= \frac{(d_1^2 + d_2^2 + z^2)^{1/2}}{c} & \tau_B &= \frac{(d_2^2 + d_3^2 + z^2)^{1/2}}{c} \\ \tau_C &= \frac{(d_1^2 + d_4^2 + z^2)^{1/2}}{c} & \tau_D &= \frac{(d_3^2 + d_4^2 + z^2)^{1/2}}{c} \end{aligned} \tag{2.25}$$

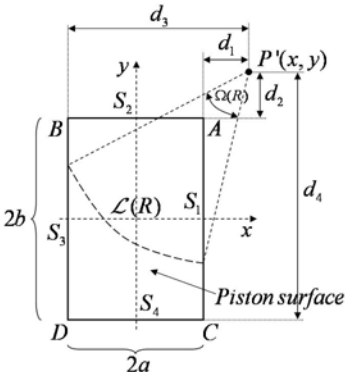

Figure 2.4: Piston dimensions

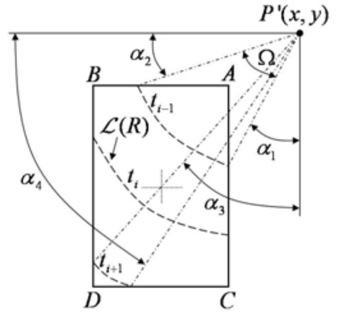

Figure 2.5: Piston angles

and when they are tangent to the borders it will be

$$\tau_{Si} = \frac{(d_i^2 + z^2)^{1/2}}{c} \qquad \forall\ i = 1,2,3,4 \tag{2.26}$$

A final discontinuity will exist in $\Omega(P,t)$ for those points whose projection $P'(x,y,0)$ lie inside the rectangular boundaries of the source. This will be at the time instant at which the upcoming sphere touches the surface for first time at $t = \tau_0$, and is given by

$$\tau_0 = \frac{z}{c} \tag{2.27}$$

With this information it may be concluded that the impulse response function $h(P,t)$ is a time limited function restricted to the time interval (τ_{min}, τ_D) with a null value outside of it and where τ_{min} is assigned to $\tau_A, \tau_2, \tau_1, \tau_0$ for the regions I, II, III and IV respectively.
Now according to[234] the functions $\alpha_i(P,t)$ that allow us to calculate $h(P,t)$ will be defined by

$$\alpha_i(P,t) = \arcsin[\frac{d_i}{\sigma(P,t)}] \tag{2.28}$$

Where $\sigma(P,t)$ is the radius of the active arc with its centre in P', it is defined by

$$\sigma(P,t) = \sqrt{(ct)^2 - z^2} \tag{2.29}$$

These α functions each corresponds to the angles α_i of Fig 2.5 and the arguments are the principal values in the interval $-\pi/2 \leq \alpha_i \leq pi/2$, for $t \geq \tau_{Si}$.

2.4.3 Determination of $h(P_{x,y,z}, t)$ expressions

Having defined the α_i functions one example of how they permit to calculate the impulse response function at a given point is seen.
Observing in Fig 2.5 the evolution of the active arcs for different time instants

t_i, from point P' and assuming that $\tau_B \leq \tau_C$ [234], Ω can be determined in the following terms

$$\Omega = \alpha_4 - \alpha_2 \qquad\qquad ; \text{ for } \tau_B \leq t \leq \tau_C$$

Then from Eq. (2.23) and assuming a rigid baffle condition with $\beta = 2$ (see Eq. 2.6) the following expression is reached

$$h(P,t) = \frac{c\Omega(ct)}{2\pi}$$

where α_i and its complementary functions $\bar{\alpha_i}$ are defined by

$$\begin{aligned} \bar{\alpha_i} &= \begin{cases} sgn(d_i)\pi/2 & \text{for } \tau_0 \leq t \leq \tau_{Si} \\ \alpha_i & \text{for } \tau_{Si} < t \leq \tau_D \end{cases} \\ \alpha_i &= arcsin[d_i/\sigma(P,t)] \end{aligned} \tag{2.30}$$

In the same manner and following the procedure described by Emeterio & Ullate in Ref. [234] it is possible to summarize in tabular form all potential cases for the active arcs $\Omega(P,t)$ at any instant in time.
These are illustrated in the following Table 2.1.

Table 2.1: Analytic expression cases of $\Omega = (2\pi/c)h(P,t)$ for a piston-like rectangular radiator in a rigid baffle condition ($\beta = 2$) where $\tau_m = min(\tau_B, \tau_C)$; $\tau_M = max(\tau_B, \tau_C)$ and $\tau_{min} = \tau_A, \tau_{S2}, \tau_{S1}, \tau_B$ for regions I, II, III and IV respectively.

$\tau_{min} \leq t \leq \tau_A$	$-$	$\pi - 2\alpha_2$	$2\bar{\alpha_3} - 2\alpha_1$	$-2\pi - 2\bar{\alpha_1} - 2\bar{\alpha_2} + 2\bar{\alpha_3} + 2\bar{\alpha_4}$
$\tau_A \leq t \leq \tau_m$	$\pi/2 - \alpha_1 - \alpha_2$	$\pi/2 - \alpha_1 - \alpha_2$	$-\pi/2 - \alpha_1 - \alpha_2 + 2\bar{\alpha_3}$	$-3\pi/2 - \alpha_1 - \alpha_2 + 2\bar{\alpha_3} + 2\bar{\alpha_4}$
$\tau_m \leq t \leq \tau_M^a$	$-\alpha_1 + \alpha_3$	$-\pi - \alpha_1 + \alpha_3 + 2\bar{\alpha_4}$	$-\alpha_1 + \alpha_3$	$-\pi - \alpha_1 + \alpha_3 + 2\bar{\alpha_4}$
$\tau_m \leq t \leq \tau_M^b$	$-\alpha_2 + \alpha_4$	$-$	$-\pi - \alpha_2 + 2\bar{\alpha_3} + \alpha_4$	$-\pi - \alpha_2 + 2\bar{\alpha_3} + \alpha_4$
$\tau_M \leq t \leq \tau_D$	$-\pi/2 + \alpha_3 + \alpha_4$	$-\pi/2 + \alpha_3 + \alpha_4$	$-\pi/2 + \alpha_3 + \alpha_4$	$-\pi/2 + \alpha_3 + \alpha_4$

'a' for $\tau_B \leq \tau_C$
'b' for $\tau_C \leq \tau_B$

Then with aid of equations (2.23) through (2.30) and Table 2.1 it is possible to build an IR core for rectangular apertures[15] that allows the calculation of acoustic fields for the LAMB toolbox.
This is based fundamentally on the superposition principle (see § 5.2.1) and is embedded in the emission block and the plate radiation part of the programme.

---

[15] The IR core it's a free subset of FIRST available for downloading in the author's page at the Matlab Central: www.mathworks.com/matlabcentral/fileexchange/authors/23152

2.4.4 Inclusion of the air attenuation effect

A fundamental characteristic of the propagation of sound in gases is the attenuation with distance of waves due to various processes that irreversibly convert the wave energy into heat.

Without entering into an unnecessary level of detail of the many and varied complex processes that take place during the attenuation phenomenon in gases[21, 20] only those concerned with the basic structure of present mechanisms involved during the attenuation phenomenon of linear acoustics will be discussed. These are enumerated in the following Table 2.2.

As can be appreciated the main division concerns spreading losses and absorption losses.

Since the main goal here is to determine the attenuation of sound in a stable atmospheric environment the effects of spreading losses[16] will be left out.

The effects of reflection and refraction are included by assumption of use of the propagation model (see § 4.3.1). Then only the absorption losses in the form of classical effects and relaxation absorption effects will be dealt with[17].

These can be taken into account by an α_{cr} coefficient plus two additional molecular resonance coefficients, $\alpha_{vib,O}$ and $\alpha_{vib,N}$ for oxygen and nitrogen gases respectively[12, 23].

Then at standard conditions of pressure and temperature ($P_0 = 1\,\mathrm{Atm.}$, $T_0 = 293.15\,\mathrm{K}$) the total attenuation coefficient of ultrasound in air α [$\mathrm{N_p/cm}$] is given by[18]

$$\alpha = \alpha_{cr} + \alpha_{vib,O} + \alpha_{vib,N} \tag{2.31}$$

and the acoustic pressure e.g. along the X axis for a single frequency w_n will be

$$p(x,t) = p_0 e^{-\alpha_\mathrm{n} x} e^{\mathrm{i}(w_\mathrm{n} t - k_\mathrm{x} x)} \tag{2.32}$$

Now to calculate the total pressure at a point $p(P,t)$ including the attenuation effects for all frequencies, equation (2.13b) will be used:

$$p(P,t) = \rho a(t) * h(P_{x,y,z}, t)$$

Since this equation depends on the normal piston acceleration $a(t)$ and the impulse response function $h(P_{x,y,z}, t)$ the attenuation factor $\alpha(w)$ can be applied to any two functions by means of a time convolution operation.

---

[16] Inverse square law and diffraction effects are already incorporated in the IRM approach.

[17] Diffusion losses contribute very little (around 0.3%) radiation losses are only important at very low frequencies and electromagnetic relaxation is significant for NO gas only at very high frequencies[21]. Absorption by ground and ground cover are not applicable

[18] For details on the determination of $\alpha(P_0, H_\mathrm{r}, T, w)$ as well as calculations of the air density and speed of sound consult Appendix A on air medium characteristics.

Table 2.2: Sound attenuation factors in gases.

a. Spreading losses	a.1 Uniform spherical spreading (inverse square law) losses.	
	a.2 Non-uniform spreading.	a.2.1 Reflection by finite boundaries. a.2.2 Refraction by nonuniform atmosphere. a.2.3 Diffraction (scattering) by nonstationary atmosphere.
b. Absorption losses	b.1 Absorption by ground and ground cover.	
	b.2 Absorption by the atmosphere (Classical absorption).	b.2.1 Viscous losses b.2.2 Heat conduction losses b.2.3 Diffusion losses b.2.4 Radiation losses
	b.3 Molecular relaxation absorption.	b.3.1 Thermal relaxation among translational energy and vibrational energy states of molecules. b.3.2 Thermal relaxation among a close vibrational resonance of two different molecules. b.3.3 Thermal relaxation among vibration of one molecule and rotation of a different molecule. b.3.4 Thermal relaxation among translational energy and rotational energy states of molecules. b.3.5 Electromagnetic relaxation between translational energy and possible electronic energy states of molecule.

Table 2.3: Acoustic wavelength values in air and element dimension ratios.

	Frequency [Hz]	**Wavelength [mm]**	$r_a = \frac{2a}{\xi/2}$ $\text{ele}_{\text{width}}=2a=1\text{mm}$	$r_b = \frac{2b}{\xi/2}$ $\text{ele}_{\text{height}}=2b=15\text{mm}$
f_{min}	$0.6\ 10^6$	0.57	3.5	52.4
f_0	$0.8\ 10^6$	0.43	4.7	69.8
f_{max}	$1.0\ 10^6$	0.34	5.8	87.3

This can be viewed from the frequency domain as a Fourier transform impulse response function $H(\mathrm{i}w)$ filtering operation.
This approach although not exact, is a fairly good approximation to the works of Jensen[123] and Piwakowski[209].
Then to include the attenuation effect in the model the corresponding filtering function $A_{\text{atte.}}(R, \mathrm{i}w)$ for the point of interest $P(x, y, z)$ at R units distant from the origin O_{a} of the acoustic radiator is calculated[19].

---

[19] See Figure 2.1. For details on the calculation of $A_{\text{atte}}(R, \mathrm{i}w)$ consult Appendix A.

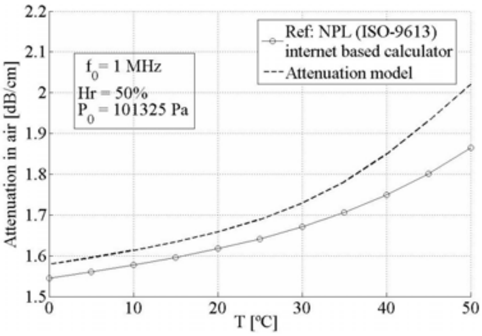

Figure 2.6: Effect of the air attenuation with temperature at $f_0 = 1\text{MHz}$, $H_{\text{r}} = 50\%$ and $P_0 = 1$ Atmosphere.

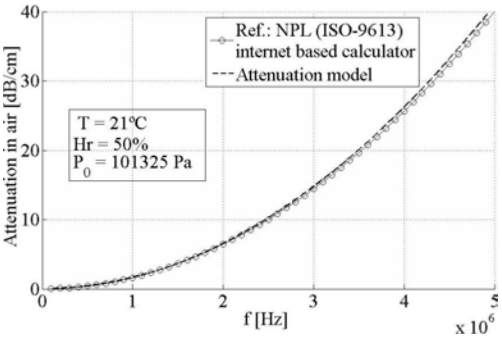

Figure 2.7: Effect of air attenuation with frequency: $T_{amb} = 21°\text{C}$, $H_{\text{r}} = 50\%$ and $P_0 = 1$ Atm. N.b. $@f_0 = 1\text{MHz} \Rightarrow atte_{air} \approx 164\,\text{dB/m}$!

The the following expression is obtained by inverse Fourier transformation of the multiplication of the frequency domain responses

$$h_a(P_{x,y,z}, t) = \frac{1}{2\pi} \int_{-\inf}^{\inf} A_{\text{atte}}(R, \text{i}w) H(\text{i}w) e^{\text{i}wt} \text{d}w \tag{2.33}$$

As a result of substitute h for h_{a} in equation (2.13b) the final attenuated acoustic pressure is given by

$$p(P_{x,y,z}, t) = \rho a(t) * h_a(P_{x,y,z}, t) \tag{2.34}$$

Figures 2.6 and 2.7 represent attenuation in function of the ambient temperature and frequency for standard conditions of pressure and relative humidity.

Here the most important and worthy case to comment is the relationship between the attenuation and the frequency since this exerts a primary and key influence on radiated acoustic fields in air. This relationship responds approximately to a square dependence law with the frequency of the form[20]

$$\alpha = af^b \Big|_{\substack{a \cong 1.732\ 10^{-12} \\ b \cong 1.996}} \quad [\text{dB/cm}] \tag{2.35}$$

Then, as the frequency of the acoustic field is higher the ultrasound almost utterly vanish in the air after a few cm.

This is a severe restriction for ultrasonic NDT/NDE since most of the time higher frequencies can carry detailed information of underlying phenomena. Nevertheless, with the availability of modern analog electronics[298] and signal processing techniques[98, 96, 121] these possibilities are now increasingly being studied.

---

[20] An alternative formula[272] is: $\alpha = 1.64\ 10^{-12} f^2$ [dB/cm].

The curves of the present attenuation model had been contrasted with available data extracted from an internet based calculator from the National Physical Laboratory[21] (NPL) in the United Kingdom. For further details please see Appendix A.

2.4.5 Wavelength and sampling frequency effects

§Wavelength effect

In any imaging system it is a well know fact that minor details or structures that need to be seen more clearly must be greater than the minimum wavelength used by a system for exploration.

In the case of acoustics and ultrasonic radiators which undergo the impulse response theory it is even more important that the size of the radiation element be greater that the maximum wavelength present in the system[133, 202].

This condition can be summed up by ensuring the parameters: $r_{\mathrm{a,b}} > 1$ (see Table 2.3).

If the parameters are not within these limit boundary conditions the baffle becomes influential and theory begins to disagree with the experiment.

This is the case for example, of small transducer elements of an ultrasonic array operating at lower frequencies.

In this case a more exact theory like the angular spectrum method mentioned in § 2.2.4, could be a more convenient approach to the problem.

For this thesis the simulation of an air-coupled NDE array based system and the low velocity value of sound propagation in air ($c \cong 343.8\ m/s\ @21^oC$) causes the wavelengths in the equation (2.35) to have submillimetre dimensions at working frequencies[22]. This in turn helps to make aperture dimension ratios greater than the unit.

$$\xi^{\downarrow} = \frac{c^{\downarrow}}{f} \tag{2.36}$$

Table 2.3 shows common wavelength values compared to typical dimensions of the rectangular elements of an array.

Problems arise when the array is operating at low frequencies and relate to the *width* of the elements because at low frequencies the ratio value almost approaches value 1. Nevertheless, simulations agree fairly well with experimental results (see e.g. § 2.5.1).

A final point to consider concerning the size of emission elements is when IRM is applied to the radiation zone of the plate (see Fig. 5.1).

Ratio parameters should be kept $r_{\mathrm{a,b}} > 1$ and at the same time corresponding

---

[21] http://resource.npl.co.uk/acoustics/techguides/absorption/

[22] The indicated values on Table 2.3 could be extended to the BW interval: [0.5−1.5]MHz in case of necessity obtaining [0.69 − 0.23] mm.

element dimensions should not exceed the minimum Lamb wavelength in the system so as not to introduce interference effects in the emission model of the plate[23]. This point is further discussed in § 5.2.3.

§Sampling frequency effect

In order to implement the impulse response method equations in a computer system the time traces must first be discretized by choosing an appropriate value of the sampling frequency f_s.
Although the sampling theorem suggest that $f_s \geq 2 f_{max}$ this may be inappropriate in this case because IRM is different in some aspects.
One way to work on of these aspects is to try to represent the maximum frequency (minimum wavelength) of the system. This can be roughly done by using 10 points per wavelength for example and then set $f_s = 10 f_{max}$.
Although ten points is generally enough for a sinusoidal wave representation, the impulse response function h may need values higher than $10 f_{max} \leq f_s$ to give acceptable results[24]. In fact, even using GHz values for f_s the "exact" solution, it still may not theoretically be possible to obtain.
Nevertheless, as Piwakowski clearly pointed out in[209], bandlimited signals fortunately no longer require this restraint.
Using then the following criteria of equation (2.37) for the sampling frequency; this should be enough to ensure later calculations and comparisons in the $0.5 - 1.5\,\mathrm{MHz}$ band for the present system[25].

$$\frac{f_{max}}{f_s} \leq 0.01 \tag{2.37}$$

This will finally result in sampling frequencies operating within the range of $100 \leq f_s \leq 500\ MHz$ always depending on the complexity of the problem, the degree of detail desired and the computing resources available.
A minimum test value assumed will be $f_s = 100\,\mathrm{MHz}$[26].

2.5 Validation of the LAMB IRM Routines

2.5.1 Simulations and experimental comparisons

In order to ensure the validity of acoustic data obtained from the developed routines, the emission section of LAMB programme[27] was checked against simulations of the aforementioned acoustic packages and compared also with experimental acoustic signals.

---

[23] This is when: $\{2a, 2b\} \leq \xi_{\min}^{\mathrm{LAMB}}/2$.

[24] See for example Ref. [209] pp. 428.

[25] See Ref.[299].

[26] If more computing power is available a more reasonable value would be $f_s = 300\ MHz$.

[27] This module is built around the Field Impulse Response Software (FIRST v0.1).

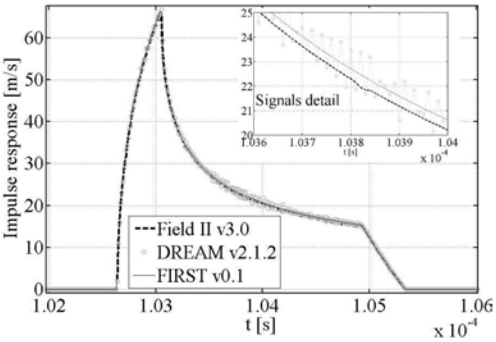

Figure 2.8: Non-attenuated impulse response functions for a rectangular aperture (width $= 1$ mm, height $= 15$ mm) at point $(5, 0, 35)$ mm. Sampling freq. $fs = 100\,\mathrm{MHz}$.

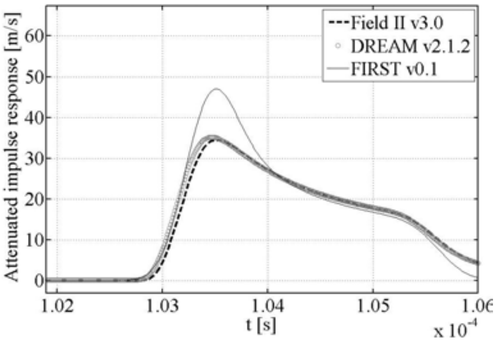

Figure 2.9: Attenuated impulse responses for the rect. aperture of Fig. 2.8. FieldII and DREAM are using a linear approximation while LAMB is using the model of Eq. (2.34).

The first validation tests is for the impulse response function $h(x, y, z, t)$ for a rectangular aperture at a given point in space for the Field II and DREAM toolboxes[28] compared with that obtained from the FIRST software.
The emitter will be a rectangular radiator or a Single Ideal Element (SIE[29]) of dimensions: $2a = 1\,\mathrm{mm}$ and $2b = 15\,\mathrm{mm}$ for width and height respectively and the point in space[30] will be $P = (5, 0, 35)$ [mm] with a sampling frequency of $f_s = 100\,\mathrm{MHz}$.
The following Figures 2.8 and 2.9 show results for cases with and without medium attenuation respectively. Close agreement is demonstrated in the case of non-attenuating media, while a medium concurrence is obtained for an attenuating medium.
This is mainly because of the different approaches used during implementation of the attenuation process. For the Field II & DREAM cases a linear model was used ($\alpha = 2.628f - 1.006$) near the central frequency ($f_0 \cong 0.8$ MHz) in the bandwidth, while for the LAMB toolbox the model of equation (2.34) was employed[31].
In order to achieve experimental comparisons of real ultrasonic signals with LAMB software simulations it is first necessary to obtain the velocity surface movement or *velocity profile* of the acoustic radiator in question.
However, since the use of a complete profile would be impractical because it would involve an unnecessary discretization of the radiator surface into piston like sub-elements[32], a single average signal obtained from the maximum vibration points on the surface will be used for this purpose.

---

[28] The Ultrasim package could not be used in this test, because it does not allow the impulse response function to be computed separately. However a group of comparisons for ultrasonic simulated signals with the FIRST programme is shown in Appendix A.

[29] For other possible apertures see also Fig. 5.3 in § 5.2.1.

[30] The rectangular radiator is located in all the cases at: $O = (0, 0, 0)$.

[31] This is the final attenuation model used in the toolbox for all the simulations.

[32] For an example of this process please see figures 5.3 and F.4 .

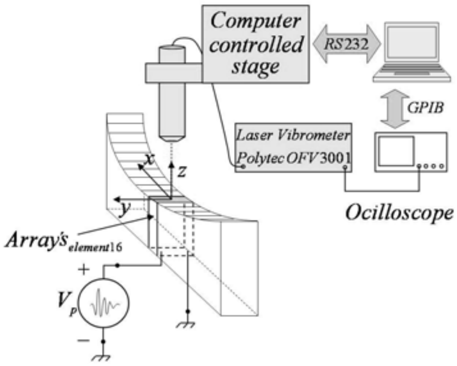

Figure 2.10: Experimental setup for determination of the average velocity signal.

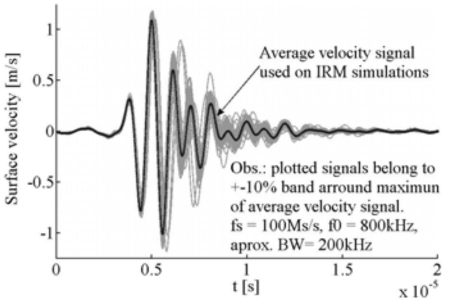

Figure 2.11: Obtained average velocity signal.

For this test a single excited element of the emission array (element 16 of 1-32) was selected and subjected to a surface vibrometer scan where it was excited with a pulsed signal. The setup for this measurement is observed in Fig.2.10.

A laser Doppler vibrometer (Polytec OFV-3001) scanned the surface of the element with a computer controlled stage capable of 10 um of minimum step size. The element was excited using the pulsed signal from circuit of Ref.[298], with an $f_0 \cong 0.8$ MHz, a signal bandwidth of $BW \cong 200$ kHz and DC level of 270 V.

The signals were captured in a 4 by 10 mm grid using 0.25 step sizes on both axes and the vibrometer was adjusted for velocity signal extraction with a constant $k_v = 0.125$ (m/s)/V.

Only part of the measured velocity signals that contribute to the average trace[33] are plotted in Fig. 2.11 and the average trace is signalled by a dark line. As can be appreciated the peak velocity is near $\approx 1\ m/s$.

An interesting phenomenon better appreciated in the full surface scans of figures 2.12 and 2.13 is the way the emission area of the array element is increased both in peak velocity amplitude and phase delay vibration profiles. This effect is mainly due to the interaction between vibrating piezoelectric bars placed underneath the air-adaptation layers which tend to extend and apodise in amplitude the active surface of the element[34].

The simulated acoustic signal can now be obtained for non-attenuating and attenuating media respectively from the time derivative of the velocity signal and equations (2.13b) or (2.33).

---

[33] The plotted signals belong to a ±10 % band around the maximum final average velocity trace.

[34] For more details on this effect and information about the arrays see Refs.[178, 214].

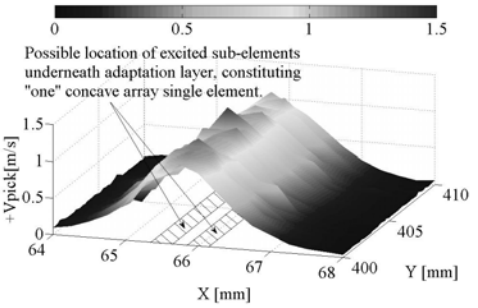

Figure 2.12: Laser scan of the central element of a concave array showing the maximum velocity signals of the surface.

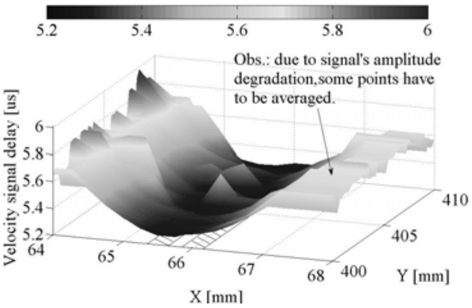

Figure 2.13: Surface velocity signal detected delays. Plotted delays were captured detecting the zero cross points after signal peak$^+$.

This is shown in figure Figure 2.14 where the measured acoustic signal for the same location in space is plotted.

The corresponding setup for this measurement is shown in Fig. 2.15, where this time the laser was replaced by a needle type hydrophone (Onda PVDF-Z44-1000 $\phi = 1$ mm) attached to a two stage amplifier and then to an oscilloscope.

Because the SNR of detected signals was low the final traces were captured 100 times by the scope to get an average response[35].

Although great care had been taken while measuring the signals a better a estimate for acoustic pressures could not be achieved.

This is because of the lack of reliable calibration data in the air for the hydrophone and the inherent difficulty associated with taking measurements in such a media.

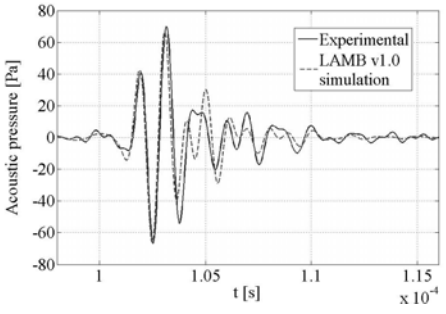

Figure 2.14: Acoustic pressure signals for a pulse type excitation: $f_0 \approx 0.8$ MHz; $BW \approx 0.2$ MHz; $f_s = 100$ MHz.

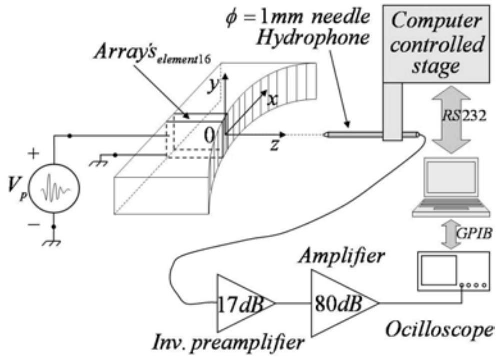

Figure 2.15: Experimental setup for measurement of the ultrasonic signals.

---

[35] More details in Ref. [214].

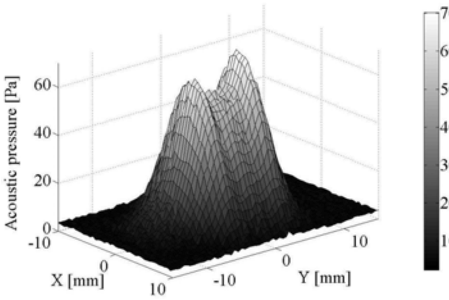

Figure 2.16: Measured values of maximum acoustic pressure in an XY plane at $z = 35$ mm, from the central excited element of the concave array (ele.16@32).

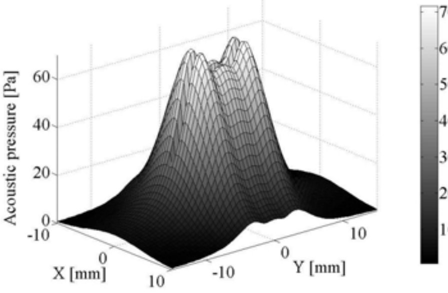

Figure 2.17: Corresponding simulation from the LAMB software for SNIE transducer of $2a = 1.6$ mm and $2b = 15$ mm.

The sensitivity of the hydrophone was assumed to be −255 dB re. 1 V/uPa. which is about ≅ 180 nV/Pa[36].
Figures 2.16 and 2.17 represent measured and simulated maximum acoustic pressure distributions respectively on an XY plane for the central element of a concave array with the same conditions as in Fig. 2.15.
Although some discrepancy in the signals can be observed, agreement in the figures is still relatively high.
This discrepancy is due to the abovementioned effect of lateral extension of the emitting surface partially caused by use of the SNIE[37] technique during simulations. Then the broader the emission surface the narrower the beam emitted. On the other hand, the small longitudinal notch observed along Y axis at the centre of Figure 2.17 is the result of a known problem not yet corrected in the IR core of the FIRST software[38].

2.5.2 Acoustic field simulations

This section is devoted to providing more examples[39] of other possible simulations achieved with the LAMB software[40]. For this purpose the SIE aperture (width = 1 mm; height = 15 mm) previously defined on page 32 will be used in all further simulations of this Chapter since this ideal piston-like

---

[36] This figure is unfortunately 3dB below the declared datasheet lower limit of sensitivity for new HNZ1000 hydrophone type (−246 ± 6dB); since the old PVDF-Z44-1000 are currently discontinued. This results in a discrepancy of about ≈ 1.4 times times below the inferior limit.

[37] The use of a single rectangular piston-like element increased this effect but was partially mitigated by the Single Non-ideal Element (SNIE) approach. More details of SNIE can be found in section §**??** and Ref.[215].

[38] This error is possibly located in calls on zone *IV* of transducer surface, see Fig. 2.3 on pp.25.

[39] For more details please see Appendix D which summarizes software capabilities.

[40] Here the acronyms LAMB and FIRST, are used interchangeably.

radiator resembles the first natural approximation of a single element of an air-coupled NDE array.

The reasons for the choice of baffle conditions for field simulations carried out for this thesis namely the rigid baffle (RB), the soft baffle (SB) and the free field (FF) are defined in the following.

The first type is, as its name implies, the rigid baffle condition and means that the radiating aperture is solidly clamped to the baffle or frame that supports and surrounds it.

When using this boundary condition the emitted fields from the apertures tend to be less of a directive than those with the soft condition. The rigid baffle condition can be directly derived from Rayleigh's integral equation[55]. On the other hand the soft baffle setting tends to be a less restrictive clamp so the Sommerfeld formulation must be employed[14] and the emitted beams are little more directive. This added directivity is however gained at the cost of losing some field amplitude.

Because of this effect the rigid baffle condition will be chosen for all acoustic field simulations carried out in this thesis. Alternatively, the behaviour of the free field condition is between that of the RB and the SB.

The effect of the three settings can be appreciated in Figures 2.18 and 2.19 which show simulated field contours for continuous wave (CW) excitation on an XZ plane[41].

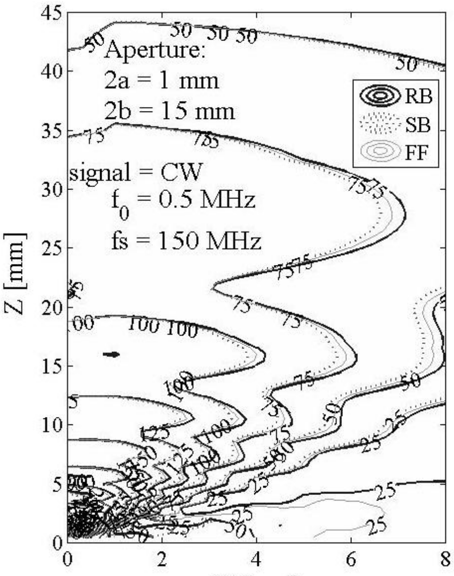

Figure 2.18: Acoustic field contours for different baffle conditions for the SIE aperture excited with a CW of 0.5 MHz.

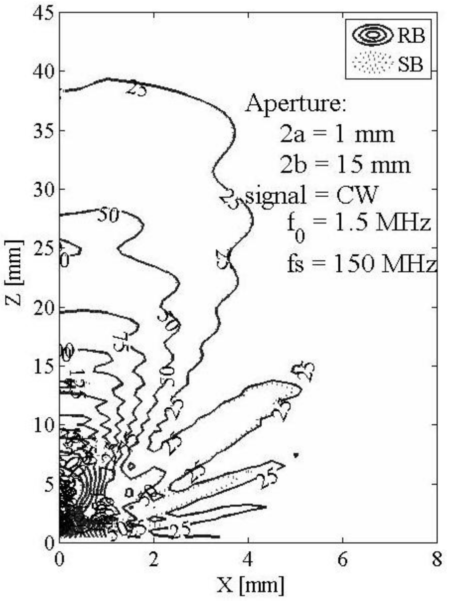

Figure 2.19: Similar settings to Fig. 2.18 but at $f = 1.5$ MHz. For clarity the FF baffle condition has been removed.

---

[41] In order to enhance the figures appearance only the right half part of the symmetric diagrams are shown here.

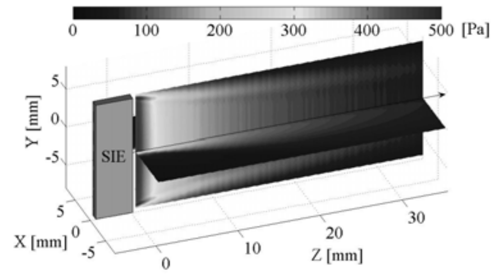

Figure 2.20: SIE's peak$^+$ acoustic pressures at the main crossover planes. Excitation is the same as in Fig. 2.11.

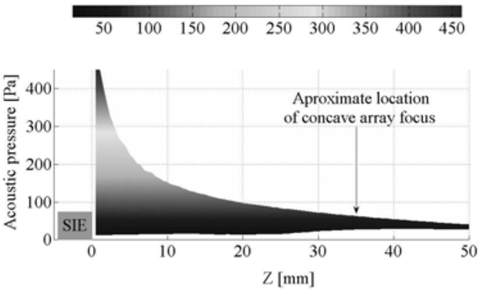

Figure 2.21: Side view, of peak acoustic pressures in the XZ plane for the rectangular SIE. The SIE drawing in the figures is merely indicative.

In the same manner, Figure 2.20 shows from a slice-like view of two crossover main acoustic planes: XZ and YZ for a pulsed excited SIE[42]. The beam is very intensive near the transducer surface and narrow on the transversal XZ plane where it rapidly loses amplitude as it moves away from the radiator. This is more clearly appreciated in Fig. 2.21 and is an important issue for air-coupled ultrasonics as pointed out at the end of § 2.4.4.

In the situation of several active elements i.e. when 1D concave array transducers of the system are used, the above Figures 2.22 and 2.23, show peak pressure simulated fields on the main plane for an array of 16 SIE emitters with and without[43] beam focalization respectively.

Another possibility for visualization is a time *instant* photo of generated acoustic fields. This is the case of Figure 2.24 which shows the acoustic wave emitted for a SIE at $t = 18$ us distant from the transducer face.

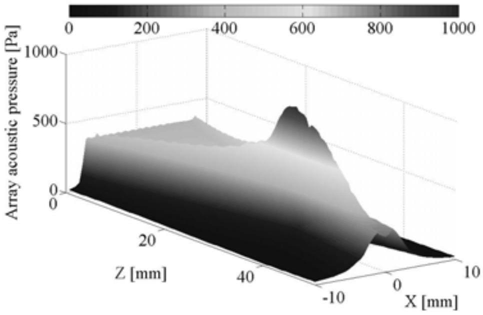

Figure 2.22: Peak$^+$ acoustic pressures in XZ plane, for a focalised concave array transducer form by 16 SIE emitters ($R \approx 35$ mm).

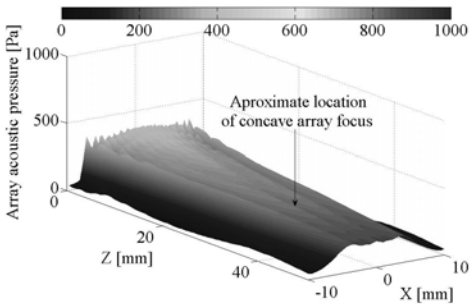

Figure 2.23: With the same conditions as in Fig. 2.22, but for a defocalised array (plane wavefront formation w/pulsed signal).

---

[42] For this figure and all the rest in this Chapter the IRM velocity excitation signal was the same as in Fig. 2.11.

[43] With plane wavefront (PWF) generation.

When several elements are active forming a PWF as in plot 2.23, the emission of defocalized fields for steering angles $\theta = 0^{\circ}$ and $\theta = 9^{\circ}$ respectively of a 16 element array are seen in Figures 2.25 and 2.26.
Notice the irregular *saw-like* amplitude distortion along the wavefront and behind it. This effect is even stronger when the beam is steered in on direction, and in fact it is a type of behaviour which departs from the usually assumed hypothesis of plane wavefront formation and excitation in NDE/NDT systems[44]. For more details see Ref.[215].

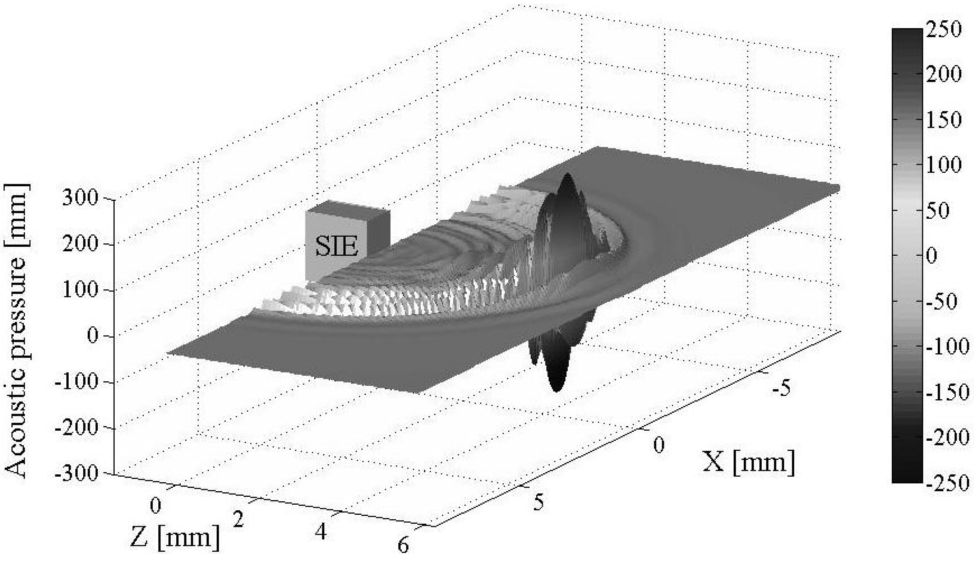

Figure 2.24: Generated acoustic pressure wave by a single ideal radiator at $t = 18$ us.

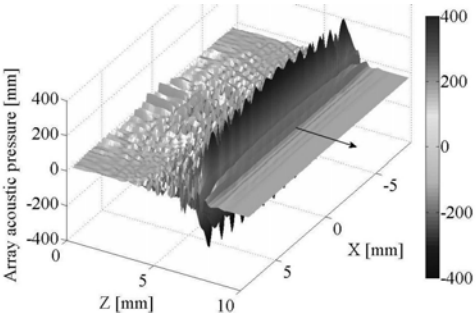

Figure 2.25: Emitted pressure wavefront by a 16 SIE array at $t = 26$ us (pulsed signal @$f_0 = 0.8$ MHz). Time&space discretization params.: $f_s = 100$ Ms/s, $x_s = 0.1$ mm and $z_s = 0.1$ mm.

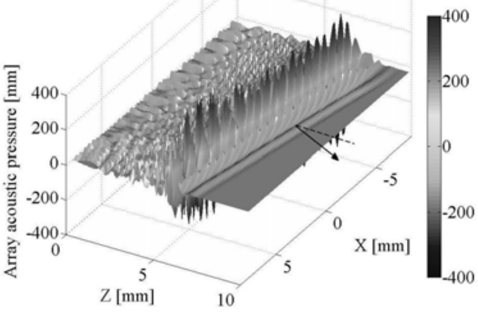

Figure 2.26: With same conditions as in Fig. 2.21, but PWF steered at 9°deg to the right.

---

[44] The ideal plane wavefront hypothesis, assumes uniform amplitude and phase across any transversal plane to the wave propagation vector $\vec{k} = \mathrm{i}\,k_x + \mathrm{j}\,k_y + \mathrm{k}\,k_z$.

2.6 Conclusions

A new acoustic Field Impulse Response Software (FIRST) has been developed for the emission part of the LAMB toolbox.
The simulator engine is freely available and has an open source model based on the GNU General Public License.
The IR core is based on the well known work of San Emeterio & Ullate[234] for rectangular apertures with special attention on the inclusion of the air attenuation effect by means of a non-linear frequency dependence model.
This attenuation model is based on the calculations of Refs.[23, 53, 79]; and was validated thanks to web available data from the National Physical Laboratory (NPL) of the United Kingdom.
Further verifications were also performed for simulated acoustic fields with the aid of a hydrophone based computer controlled system.
Although simulation and experiment agree moderately well, there is still concern about precise calibration of the system until a calibrated hydrophone stage in air is made available.
Finally, an issue discussed later on in Appendix E is the degree of detail desired and computer time required for the simulations, since an elevated number of points (in space and time) can make simulations go too slow or even become impossible to carry out[45].

---

[45] A brief guide of advice about memory fragmentation problem is given in page 141.

Chapter 3

The global matrix method

3.1 Introduction

In this chapter a modal theory for free wave propagation in a multilayered media is developed. The theory is based on the Global Matrix Method (GMM) whose roots rely on another matrix technique, the Transfer Matrix Method (TMM).

These matrix methods are introduced to allow for calculation of the Lamb wave dispersion relationships or frequency-wavenumber maps (f, k). These relationships will served as input to the Time Harmonic Solution explained later in Chapter 4 which is finally used to calculate the plate displacements in the LAMB software.

The chapter begins with a brief historical introduction to matrix techniques followed by an introduction to wave solution types and the classical theory of bulk[1] wave propagation in infinitely elastic solids.

Next the special case of wave propagation in a two-dimensional infinite space, the so called *plane strain* propagation, is considered. In this case bulk waves will be restricted to have displacements on a plane perpendicular to that of the material layer and the interaction of bulk waves with an interface is examined.

In general four plane waves will exist on each side of an interface: a longitudinal and a shear wave which come from the top and a longitudinal and a shear wave which leave the interface.

The analysis is next extended to a pile of isotropic layers or a multi-layered system by considering a sequence of rigidly connected parallel plate interfaces of a given thickness. This system will give solutions only if all boundary conditions are simultaneously satisfied at all interfaces.

For this purpose a known algorithm is employed[157] to solve the characteristic function of the system for *leaky*[2] Lamb waves and to obtain the final Lamb wave frequency-wavenumber dispersion eigensolutions.

Finally, the chapter presents a series of simulations and experimental results for dispersion curves in aluminium plates and conclusions are derived.

---

[1] Hereafter, the terms bulk wave and plane wave, will used interchangeably.

[2] This will to seek solutions with real frequency ($f = \Re\{w\}/(2\pi)$) and a complex wavenumber ($k = k' + \mathrm{i}k''$).

3.2 Historical background

Perhaps the first theory of wave propagation in a *multilayer* system was Lord Rayleigh's work[217] on waves travelling on the surface of a free semi-infinite half-space. Afterwards in 1924, a generalization of this problem for two adjoining half-spaces was presented by Stoneley[264] who analysed waves along the boundary of two elastic solids[3].

In 1917 Horace Lamb[143] added another interface to the problem with a flat layer of material or plate. He resolved the plate equation in vacuum for symmetric and anti-symmetric modes and these later became known as Lamb waves.

A previous study by Love[156] also showed that added to these modes, in-plane transversal shear modes could also exist in plates.

Later in the fifties a derivation of wave propagation into several layers for seismological applications was presented by Thomson[270] and would later be known as the current Transfer Matrix Method (TMM).

Here displacements and stresses of the last interface in a multilayered system are expressed in terms of those of the first due to the propagation of boundary conditions.

Haskell[94] later fixed a minor problem in Thomson's formulation leaving this technique currently known as the Thomson-Haskell formulation or propagator matrix method.

During the next two decades TMM received special attention to allow for the inclusion of wave attenuation during propagation and also issues related with the stability of solutions. The latter was mainly due to an ill-conditioning problem arousing from the formulation of the matrix of the system caused by the occurrence of very small numbers together with the existence of very large numbers in the matrices (number differences $< 10^{-26}$), plus limitations with computing power at that time.

Then a different approach to the problem was presented by Knopoff[138] namely the Global Matrix Method (GMM).

This technique summarized the equations of the system into a single matrix for all layers. Modal solution pairs (f, k) of decaying wave modes could then be obtained from this method without concerns about having to search for algorithms to solve the problem[157] since minor variations in the search strategy could lead to slow conversion or unstable solutions.

At the same time derivations of the GMM focuses attention on finding solutions to point source excitations[229, 282, 296]. This subject is introduced later in the next chapter with the Time Harmonic Solution (THS) since it will be engine for wave propagation in the LAMB software.

---

[3] A Stoneley wave is a free wave whose energy may propagate close to the interface between two solids without any attenuation. These types of waves appear only in materials with very similar shear bulk velocities

Further studies into matrix techniques evolved into several variations and alternatives to the GMM[36, 111, 113, 115, 269, 278, 279, 280, 281], while current areas of development include anisotropic viscoelastic stuck plates[186], layered cylindrical geometries[200] and studies on composite materials[35, 40, 50, 116].
It is interesting to mention that alternative solutions to find the roots of matrix systems are the *spectral* methods[28, 68]. These approaches are fast in solving differential equations by numerical interpolation but at the cost of inexact results. However this last point proved to be successfully overcome[4].

3.3 General considerations about waves

This section briefly discuss the typical features of different types of wave solutions in a perturbed media.
The idea is to introduce the subject in order to define the type of waves for which solutions are going to be found later with The Global Matrix Method. Here the attention is focussed on describing the distinctions among homogeneous and inhomogeneous type of waves and mainly in describing the differences between *attenuated* homogeneous and *damped* homogeneous waves.

As mentioned before a *wave* defined as perturbation in a medium that depends both on time and space could be basically classified into: *homogeneous* and *inhomogeneous* type of waves.
This division means that in an *homogeneous* wave the direction of propagation of the wave coincides with the direction of the wave attenuation. Then the field is “homogeneous” in a plane orthogonal to this unique direction.
On the contrary, in an *inhomogeneous* wave two directions are required one for the propagation (planes of constant phase) and one for the attenuation (planes of constant amplitude). These two directions could of course have any orientation in space depending on the media and the boundary conditions.

Because this thesis is dedicated to isotropic media the subject relative to inhomogeneous waves will not be discussed here[5] then the discussion will only be limited to the homogeneous phenomenon.

3.3.1 Time harmonic homogeneous plane waves

Consider the acoustic scalar wave equation:

$$\nabla^2 u = \frac{1}{c^2}\frac{\partial^2 u}{\partial t^2} \tag{3.1}$$

---

[4] See for example Refs.[7, 33].

[5] For an extended review on this topic the reader is referred to the book by M. Hayes[27]

where c is a constant and $u(\boldsymbol{x}, t)$ the particle displacement field. Then solutions for non-attenuated homogeneous harmonic waves will be of the form:

$$u = \mathrm{Re}\left\{ A e^{\mathrm{i}(\boldsymbol{k}.\boldsymbol{x} - wt)} \right\} \tag{3.2}$$

where $A = a\, e^{\mathrm{i}\phi}$ is the constant complex amplitude, $\boldsymbol{k}$ the real wavenumber vector pointing into the direction of the wave propagation and w the angular frequency of the oscillations (a real parameter).
This type of solutions describes an infinite train of waves travelling without attenuation in the direction $\boldsymbol{k}$.
Introduction of equation (3.2) into Eq. (3.1) and not considering the trivial case for $A = 0$ will lead us to obtain to the so called *dispersion relation*:

$$\boldsymbol{k}.\boldsymbol{k} = \frac{w^2}{c^2} \tag{3.3}$$

where $v = \pm c = \pm w / |\boldsymbol{k}|$ is the phase velocity of the waves and $\xi = 2\pi / |\boldsymbol{k}|$ the spatial wavelength of the oscillations.

3.3.2 Time harmonic attenuated and damped homogeneous plane waves

Now consider the following scalar wave equation, where α is a positive constant:

$$\nabla^2 u = \frac{1}{c^2}\left(\frac{\partial^2 u}{\partial t^2} + \alpha \frac{\partial u}{\partial t}\right) \tag{3.4}$$

Solutions for this equation are of two possible types. The first type is called *attenuated* time harmonic homogeneous waves. These are solutions of the form of Eq. (3.2) where in this case $\boldsymbol{k} = k\boldsymbol{n} = k_{\mathrm{Re}} + \mathrm{i}k_{\mathrm{Im}}$ is a wave bivector[6] with real direction $(\boldsymbol{n} \times \boldsymbol{n}^* = 0)$[7] and w the frequency of the oscillations (real). With this parameters equation (3.2) becomes:

$$u = e^{-k_{\mathrm{Im}} \boldsymbol{n}\boldsymbol{x}} \mathrm{Re}\left\{ A e^{\mathrm{i}(k_{\mathrm{Re}} \boldsymbol{n}.\boldsymbol{x} - wt)} \right\} \tag{3.5}$$

which describes an infinite train of vibrations travelling in direction $\boldsymbol{n}$ with an attenuation coefficient k_{Im} and a phase velocity $v = w / k_{\mathrm{Re}}$.

The second type are of solutions that expression (3.4) accepts are named *damped* homogeneous plane waves which again correspond to solutions of the form (3.2) but this time with $\boldsymbol{k} = k\boldsymbol{n}$ as a real vector and $w = w_{\mathrm{Re}} + \mathrm{i}w_{\mathrm{Im}}$ as a complex number.

---

[6] The definition of a bivector is: if $\boldsymbol{c}$ and $\boldsymbol{d}$ are vectors, then $\boldsymbol{A} = \boldsymbol{c} + \mathrm{i}\,\boldsymbol{d}$ is a bivector.

[7] Here the symbol $*$ denotes complex conjugation.

With these changes solution (3.2) will be of the form:

$$u = e^{-w_{\mathrm{Im}}t}\mathrm{Re}\left\{Ae^{\mathrm{i}(k\boldsymbol{n}.\boldsymbol{x}-w_{\mathrm{Re}}t)}\right\} \tag{3.6}$$

This expression describes waves travelling in the direction $\boldsymbol{n}$, with wave speed w_{Re}/k, and wavelength $2\pi/k$. The important point now is that the field $u(\boldsymbol{x}, t)$ is no longer periodic in time and have a time *'damping'* factor equal to w_{Im}. In view of these considerations the searching algorithm of the Global Matrix Method (see §3.6.2) will find solutions only for *attenuated* homogeneous plane waves[8] which propagate into the far field of the excitation region of the plate[9]. This is because time dependent *damped* waves are usually present into the near field of the plate excitation region.

3.4 Field equations for plane waves in isotropic solids

3.4.1 Plane waves in an infinite elastic medium

The equations for propagation of homogeneous plane waves in infinite isotropic[10] elastic solids are presented here.

The usual approximation taken in acoustic literature[16] and the development carried out by Lowe[158] is followed.

The usual approach is to take an infinitesimal cubic element of a medium with density ρ and adopt a Cartesian system with medium particle displacements u_x, u_y and u_z in the directions x, y and z respectively.

Then applying Newton's law of force the equilibrium condition of stress[11] components $\sigma_{xx}, \sigma_{xy}, ...$ requires that

$$\begin{aligned}
\frac{\partial \sigma_{xx}}{\partial x} + \frac{\partial \sigma_{xy}}{\partial y} + \frac{\partial \sigma_{xz}}{\partial z} &= \rho \frac{\partial^2 u_x}{\partial t^2} \\
\frac{\partial \sigma_{yx}}{\partial x} + \frac{\partial \sigma_{yy}}{\partial y} + \frac{\partial \sigma_{yz}}{\partial z} &= \rho \frac{\partial^2 u_y}{\partial t^2} \\
\frac{\partial \sigma_{zx}}{\partial x} + \frac{\partial \sigma_{zy}}{\partial y} + \frac{\partial \sigma_{zz}}{\partial z} &= \rho \frac{\partial^2 u_z}{\partial t^2} \qquad (3.7)
\end{aligned}$$

---

[8] Solutions with real frequency (w_{Re}) and complex wavenumber ($k = k_{\mathrm{Re}} + \mathrm{i}k_{\mathrm{Im}}$).

[9] This condition is fulfilled when the distance r from the source to the vibrating point is: $10\ \xi_{\mathrm{max}}^{\mathrm{Lamb}} < r$.

[10] The term isotropic, applies to the medium defined by two constants, the Lamé constants: λ and μ in $[Pa]$, of a maximum of 21 possible stiffness constants.

[11] Stress components σ_{ij} follow the regular convention[16], where $i \Rightarrow$ the $i^{th.}$ component of the force density, acting on the cubic element's face $+j$.

These conditions can be expressed in terms of displacements by means of the following relationships[16]:

$$\begin{aligned}
&\sigma_{xx} = \lambda\Delta + 2\mu\epsilon_{xx}, \qquad && \sigma_{yy} = \lambda\Delta + 2\mu\epsilon_{yy}, \qquad && \sigma_{zz} = \lambda\Delta + 2\mu\epsilon_{zz} \\
&\sigma_{xy} = \mu\epsilon_{xy}, && \sigma_{yz} = \mu\epsilon_{yz}, && \sigma_{xz} = \mu\epsilon_{xz} \\
&\epsilon_{xx} = \frac{\partial u_x}{\partial x}, && \epsilon_{yy} = \frac{\partial u_y}{\partial y}, && \epsilon_{zz} = \frac{\partial u_z}{\partial z} \\
&\epsilon_{xy} = \frac{\partial u_x}{\partial y} + \frac{\partial u_y}{\partial x}, && \epsilon_{yz} = \frac{\partial u_y}{\partial z} + \frac{\partial u_z}{\partial y}, && \epsilon_{xz} = \frac{\partial u_x}{\partial z} + \frac{\partial u_z}{\partial x}
\end{aligned} \tag{3.8}$$

where $\Delta = \epsilon_{xx} + \epsilon_{yy} + \epsilon_{zz}$ is the fractional change in volume or dilatation and the Lamé's constants λ and μ are defined in terms of material properties[12] by

$$\begin{aligned}
\lambda &= \frac{E\nu}{(1+\nu)(1-2\nu)} = c_{12} \\
\mu &= \frac{E}{2(1+\nu)} = c_{44}
\end{aligned} \tag{3.9}$$

Then substituting equations (3.8) into Eqs. (3.7) leads to[13]

$$\begin{aligned}
\rho\frac{\partial^2 u_x}{\partial t^2} &= (\lambda+\mu)\frac{\partial}{\partial x}(\frac{\partial u_x}{\partial x} + \frac{\partial u_y}{\partial y} + \frac{\partial u_z}{\partial z}) + \mu\nabla^2 u_x \\
\rho\frac{\partial^2 u_y}{\partial t^2} &= (\lambda+\mu)\frac{\partial}{\partial y}(\frac{\partial u_x}{\partial x} + \frac{\partial u_y}{\partial y} + \frac{\partial u_z}{\partial z}) + \mu\nabla^2 u_y \\
\rho\frac{\partial^2 u_z}{\partial t^2} &= (\lambda+\mu)\frac{\partial}{\partial z}(\frac{\partial u_x}{\partial x} + \frac{\partial u_y}{\partial y} + \frac{\partial u_z}{\partial z}) + \mu\nabla^2 u_z
\end{aligned} \tag{3.10}$$

which can be further reduced by expressing it in a vector form[14]

$$\rho\frac{\partial^2 \mathbf{u}}{\partial t^2} = (\lambda+\mu)\nabla(\nabla\mathbf{u}) + \mu\nabla^2\mathbf{u} \tag{3.11}$$

This equation accepts simultaneously two kinds of solutions, one for longitudinal waves and one for shear or transversal waves[15] and can not be resolved by direct integration.

However, a solution to this problem is to employ the Helmholtz decomposing

---

[12] The Young modulus $E = \sigma_3/\epsilon_3$, and the Poisson's ratio $\nu = -\epsilon_1/\epsilon_3 = -\epsilon_2/\epsilon_3$ are defined in terms of the abbreviated stress subscripts σ_I and strain components ϵ_J[16].

[13] The definition of the *Nabla* operator is: $\boldsymbol{\nabla} \triangleq (\mathrm{i}\frac{\partial}{\partial x} + \mathrm{j}\frac{\partial}{\partial y} + \mathrm{k}\frac{\partial}{\partial z})$, and the *Laplacian* operator is: $\nabla^2 \triangleq \frac{\partial}{\partial x^2} + \frac{\partial}{\partial y^2} + \frac{\partial}{\partial z^2}$.

[14] Assuming that there are no body forces acting, the corresponding term on the right hand side of Eq (3.11) is $\boldsymbol{F} = \mathbf{0}$.

[15] Longitudinal waves (L), are waves in which the medium particle motion takes place in the same direction as the wave propagation while for shear waves (S) the particle movement is orthogonal to the propagation direction. Both are also known as *bulk waves*.

method[133] and uncoupled the displacement field into its irrotational and equivoluminal field parts respectively[15].

With this method longitudinal (L) and transversal shear (S) waves are described by ϕ and $\boldsymbol{\psi}$, the scalar and vectorial field displacement potentials respectively. Now the potential solution can be express in terms of the wavenumber vector $\boldsymbol{k} = (k_\mathrm{x}, k_\mathrm{y}, k_\mathrm{z})$, the angular frequency w and the coordinates[16] by:

$$\begin{aligned} \phi &= A_{(\boldsymbol{L})} e^{i(\boldsymbol{k}.\bar{\boldsymbol{x}}-wt)} \\ |\boldsymbol{\psi}| &= A_{(\boldsymbol{S})} e^{i(\boldsymbol{k}.\bar{\boldsymbol{x}}-wt)} \end{aligned} \tag{3.12}$$

while the displacement fields are given by

$$\begin{aligned} \boldsymbol{u}_{(\boldsymbol{L})} &= \boldsymbol{\nabla}\phi \\ \boldsymbol{u}_{(\boldsymbol{S})} &= \boldsymbol{\nabla}\times\boldsymbol{\psi} \end{aligned} \tag{3.13}$$

Here, $A_{(\boldsymbol{L})} = A_L e^{i\varphi}$ and $A_{(\boldsymbol{S})} = A_S e^{i\varphi}$ represent the complex longitudinal and transversal wave amplitudes[17].

Because the medium is isotropic and solutions for leaky waves are required, the directions of the wavenumber vector $\boldsymbol{k}$ coincides with the direction of energy propagation. Then the wave phase velocity c_ph and wavelength ξ are given by:

$$c_\mathrm{ph} = \frac{w}{|\boldsymbol{k}|}\ , \qquad \xi = \frac{2\pi}{|\boldsymbol{k}|} \tag{3.14}$$

By introducing equations (3.12) and (3.13) into (3.11) the expressions for bulk wave phase velocities in terms of medium properties are finally achieved

$$\begin{aligned} c_\mathrm{L} &= \sqrt{\frac{\lambda + 2\mu}{\rho}} = \alpha \\ c_\mathrm{S} &= \sqrt{\frac{\mu}{\rho}} = \beta \end{aligned} \tag{3.15}$$

3.4.2 Superposition of plane waves in a layered 2D space

In order to continue with the analysis and at the same time keep solutions as simple as possible without losing generality, the previous development will be adapted to a 2D layered wave propagation space. This will be done by assuming that the $L\pm$ and $S\pm$ plane waves are propagating on an XY plane, see Fig. 3.1.

Here, downward travelling waves are denoted by $(+)$ symbol, while upward waves are denoted by the $(-)$ symbol.

---

[16] The coordinates are represented here by the vector $\bar{\boldsymbol{x}} = (x, y, z)$.

[17] Their phase at $t = 0$ and $\bar{\boldsymbol{x}} = 0$ is φ.

With this assumption the particle movement is restricted to the plane $Z = 0$ which implies a plane strain condition making all $\frac{\partial(\ldots)}{\partial z} = 0$.

Then assuming this is the case for the longitudinal and transversal waves, the displacements from Eqs. (3.13) and (3.12) can be expressed as:

$$\begin{aligned}
\boldsymbol{u_L} &= \boldsymbol{\nabla}\phi = \begin{Bmatrix} k_x \\ k_y \\ 0 \end{Bmatrix} A_{(\boldsymbol{L})} e^{i(\boldsymbol{k}.\boldsymbol{u}-wt)} \\
\boldsymbol{u_S} &= \boldsymbol{\nabla}\times\boldsymbol{\psi} = \begin{Bmatrix} \frac{\partial}{\partial x} \\ \frac{\partial}{\partial y} \\ \frac{\partial}{\partial z} \end{Bmatrix} \times \begin{Bmatrix} 0 \\ 0 \\ \psi_z \end{Bmatrix} = \begin{Bmatrix} k_x \\ -k_y \\ 0 \end{Bmatrix} A_{(\boldsymbol{S})} e^{i(\boldsymbol{k}.\boldsymbol{u}-wt)}
\end{aligned} \tag{3.16}$$

It is a well known fact in acoustics that depending on boundary conditions between two media[18], e.g. at the interface between two solid layers, the incidence of a longitudinal wave will produce two transmitted L and S waves and two reflected L and S waves (see Fig. 3.1).

Where the relationship between the incidence, reflected and transmitted angles with the wave velocities follows the generalized Snell law,

$$\frac{\sin\theta_{Li}}{\alpha_I} = \frac{\sin\theta_{Sr}}{\beta_I} = \frac{\sin\theta_{Lt}}{\alpha_{II}} = \frac{\sin\theta_{St}}{\beta_{II}} \tag{3.17}$$

in particular from figure 3.2 it is observed that

$$\sin\theta_{Li} = \frac{\alpha_I}{c_{\text{ph}}} = \frac{k_x}{k_{Li}} = \frac{\xi_{Li}}{\xi_x} \tag{3.18}$$

where c_{ph}, k_x are respectively the phase velocity and wavenumber along the X axis of induced modal waves[19].

While ξ_{Li} and ξ_x are the corresponding incidence and induced wavelengths.

Now displacements and stresses for $L\pm$ and $S\pm$ waves can be found by introducing equations (3.16) into Eqs. (3.8).

For example for longitudinal waves the expression of these quantities will be:

---

[18] In the general case of two solids[133] boundary condition requires that continuous components are: 1) normal component of longitudinal stress, 2) transverse component of shear stress and 3) the normal and transverse components of displacements.

[19] The wavenumber on the Y axis can be derived from $k^2 = k_x^2 + k_y^2$ as:

$$k_{y(L\pm)} = \pm\sqrt{w^2/\alpha^2 - k_x^2} \qquad\qquad k_{y(S\pm)} = \pm\sqrt{w^2/\beta^2 - k_x^2}$$

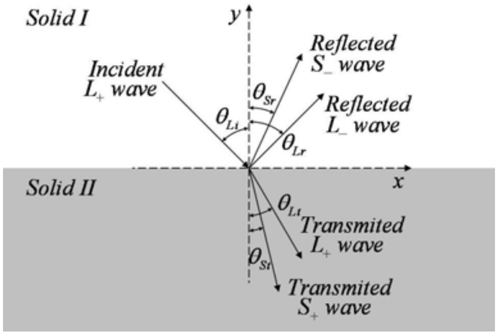

Figure 3.1: Reflection and refraction phenomena in the boundary of two solid media.

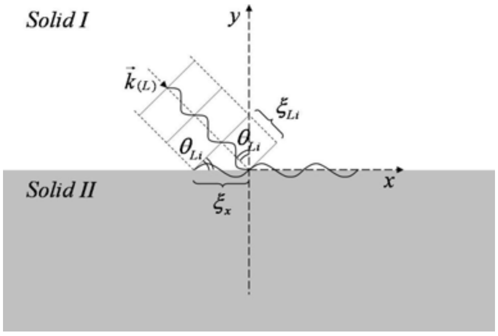

Figure 3.2: Phase velocity relationship for bulk L-waves.

$$
\begin{aligned}
u_x &= k_x A_{(L\pm)} e^{\mathrm{i}(k_x x - wt)} e^{\pm \mathrm{i}\sqrt{w^2/\alpha^2 - k_x^2}\, y} \\
u_y &= \sqrt{w^2/\alpha^2 - k_x^2} A_{(L\pm)} e^{\mathrm{i}(k_x x - wt)} e^{\pm \mathrm{i}\sqrt{w^2/\alpha^2 - k_x^2}\, y} \\
\sigma_{xx} &= (w^2 - 2\beta^2 w^2/\alpha^2 + 2\beta^2 k_x^2).\mathrm{i}\rho A_{(L\pm)} e^{\mathrm{i}(k_x x - wt)} e^{\pm \mathrm{i}\sqrt{w^2/\alpha^2 - k_x^2}\, y} \\
\sigma_{yy} &= (w^2 - 2\beta^2 k_x^2).\mathrm{i}\rho A_{(L\pm)} e^{\mathrm{i}(k_x x - wt)} e^{\pm \mathrm{i}\sqrt{w^2/\alpha^2 - k_x^2}\, y} \\
\sigma_{zz} &= (1 - 2\beta^2/\alpha^2).\mathrm{i}w^2 \rho A_{(L\pm)} e^{\mathrm{i}(k_x x - wt)} e^{\pm \mathrm{i}\sqrt{w^2/\alpha^2 - k_x^2}\, y} \\
\sigma_{xy} &= 2\beta^2 k_x \sqrt{w^2/\alpha^2 - k_x^2}.\mathrm{i}\rho A_{(L\pm)} e^{\mathrm{i}(k_x x - wt)} e^{\pm \mathrm{i}\sqrt{w^2/\alpha^2 - k_x^2}\, y} \\
\sigma_{xz} &= \sigma_{yz} = 0
\end{aligned} \tag{3.19}
$$

While for transversal waves they will be:

$$
\begin{aligned}
u_x &= \sqrt{w^2/\beta^2 - k_x^2}.A_{(S\pm)} e^{\mathrm{i}(k_x x - wt)} e^{\pm \mathrm{i}\sqrt{w^2/\beta^2 - k_x^2}\, y} \\
u_y &= -k_x A_{(S\pm)} e^{\mathrm{i}(k_x x - wt)} e^{\pm \mathrm{i}\sqrt{w^2/\beta^2 - k_x^2}\, y} \\
\sigma_{xx} &= 2\beta^2 k_x \sqrt{w^2/\beta^2 - k_x^2}.\mathrm{i}\rho A_{(S\pm)} e^{\mathrm{i}(k_x x - wt)} e^{\pm \mathrm{i}\sqrt{w^2/\beta^2 - k_x^2}\, y} \\
\sigma_{yy} &= -\sigma_{xx} \\
\sigma_{xy} &= (w^2 - 2\beta^2 k_x^2).\mathrm{i}\rho A_{(S\pm)} e^{\mathrm{i}(k_x x - wt)} e^{\pm \mathrm{i}\sqrt{w^2/\beta^2 - k_x^2}\, y} \\
\sigma_{xz} &= \sigma_{yz} = \sigma_{zz} = 0
\end{aligned} \tag{3.20}
$$

The total particle displacements and stress quantities can be determined now by adding the above contributions for L and S waves and be resumed into a single matrix $[D]$ called the field matrix:

$$\begin{Bmatrix} u_x \\ u_y \\ \sigma_{yy} \\ \sigma_{xy} \end{Bmatrix} = \underbrace{\begin{bmatrix} k_x g_\alpha & k_x/g_\alpha & C_\beta g_\beta & -C_\beta/g_\beta \\ C_\alpha g_\alpha & -C_\alpha/g_\alpha & -k_x/g_\beta & -k_x/g_\beta \\ i\rho B g_\alpha & i\rho B/g_\alpha & -2i\rho k_x \beta^2 C_\beta g_\beta & 2i\rho k_x \beta^2 C_\beta/g_\beta \\ 2i\rho k_x \beta^2 C_\alpha g_\alpha & -2i\rho k_x \beta^2 C_\alpha/g_\alpha & i\rho B g_\beta & i\rho B/g_\beta \end{bmatrix}}_{\text{[D]}} \cdot \begin{Bmatrix} A_{(L+)} \\ A_{(L-)} \\ A_{(S+)} \\ A_{(S-)} \end{Bmatrix} \tag{3.21}$$

Where the following appropriate replacements were previously introduce into the $[D]$ matrix:

$$\begin{aligned} C_\alpha &= \sqrt{w^2/\alpha^2 - k_x^2} & g_\alpha &= e^{i\sqrt{w^2/\alpha^2 - k_x^2}.x_y} \\ C_\beta &= \sqrt{w^2/\beta^2 - k_x^2} & g_\beta &= e^{i\sqrt{w^2/\beta^2 - k_x^2}.x_y} \\ B &= w^2 - 2\beta^2 k_x^2 & F &= e^{i(k_x x - wt)} \end{aligned} \tag{3.22}$$

3.5 The transfer matrix method

Since the model of wave propagation in a multilayered media involves the superposition of longitudinal and transversal bulk waves into several layers the transfer matrix method sums up this interaction by imposing corresponding boundary conditions on all layers in the system.

This is done by relating boundary conditions of the first interface to those of the last interface in the system.

For the case of a 3-layer system the corresponding nomenclature and also the origins for all the layers[20] are observed in figure 3.3.

Then if we assume that displacements and stresses are known at the first interface (i_1), the amplitude of the waves at the top of layer (l_2) could be found by inverting the corresponding $[D]_{l2,\text{top}}$ matrix to get

$$\begin{Bmatrix} A_{(L+)} \\ A_{(L-)} \\ A_{(S+)} \\ A_{(S-)} \end{Bmatrix}_{l_2} = [D]^{-1}_{l_2,top} \begin{Bmatrix} u_x \\ u_y \\ \sigma_{yy} \\ \sigma_{xy} \end{Bmatrix}_{l_2,top} \tag{3.23}$$

Now, knowing the wave amplitudes in l_2, the field parameters can be computed at interface (i_2) by introducing these values into the corresponding relationship (3.21)

$$\begin{Bmatrix} u_x \\ u_y \\ \sigma_{yy} \\ \sigma_{xy} \end{Bmatrix}_{l_2,bottom} = [D]_{l_2,bottom}.[D]^{-1}_{l_2,top} \begin{Bmatrix} u_x \\ u_y \\ \sigma_{yy} \\ \sigma_{xy} \end{Bmatrix}_{l_2,top} \tag{3.24}$$

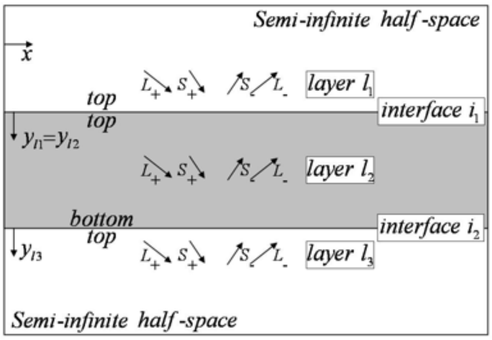

Figure 3.3: A three layer system in the Transfer Matrix Method (TMM).

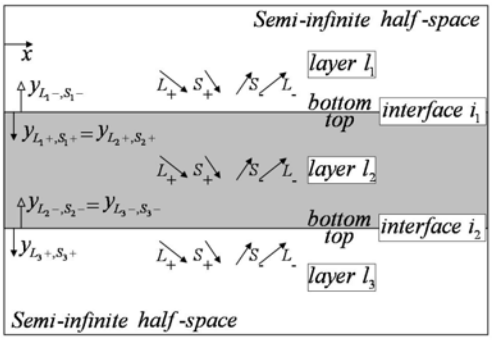

Figure 3.4: A three layer system in the Global Matrix Method (GMM).

where the layer matrix $[L]$ shall be defined as:

$$[L]_{l2} = [D]_{l2,bottom}.[D]^{-1}_{l2,top} \tag{3.25}$$

As mentioned previously boundary conditions requires that displacement and stress must be continuous through an interface of two attached layers, which in turn requires (see Fig. 3.4) that:

$$\begin{Bmatrix} u_x \\ u_y \\ \sigma_{yy} \\ \sigma_{xy} \end{Bmatrix}_{l_3,top} = \begin{Bmatrix} u_x \\ u_y \\ \sigma_{yy} \\ \sigma_{xy} \end{Bmatrix}_{l_2,bottom} = [L]_{l2} \begin{Bmatrix} u_x \\ u_y \\ \sigma_{yy} \\ \sigma_{xy} \end{Bmatrix}_{l_2,top} \tag{3.26}$$

This process can be continued further for a system with more layers arriving at the following relationships:

$$\begin{Bmatrix} u_x \\ u_y \\ \sigma_{yy} \\ \sigma_{xy} \end{Bmatrix}_{l_n,top} = [S] \begin{Bmatrix} u_x \\ u_y \\ \sigma_{yy} \\ \sigma_{xy} \end{Bmatrix}_{l_2,top} \tag{3.27}$$

with $[S]$ being the final system matrix defined by

$$[S] = [L]_{l2}.[L]_{l3}...[L]_{l(n-1)} \tag{3.28}$$

3.5.1 True mode solutions and response solutions

The idea behind true *mode solutions* (or *free modes*) and *response solutions* is that in the first case the system is in vacuum or at least with no wave

---

[20] The origins of the layers are located at the top interfaces except for the $1^{st.}$ half-space, in which case this coincides with the origin of layer 2.

excitation and no energy leakage outside it. Under these circumstances it is possible to solve the system equations to include *free modes* that propagate along the layered plates.

This is done by solving equations (3.27) with null stresses,

$$\begin{Bmatrix} u_x \\ u_y \\ 0 \\ 0 \end{Bmatrix}_{l_n,top} = [S] \begin{Bmatrix} u_x \\ u_y \\ 0 \\ 0 \end{Bmatrix}_{l_2,top} \tag{3.29}$$

which can be expand to

$$\begin{Bmatrix} 0 \\ 0 \end{Bmatrix} = \begin{bmatrix} S_{31} & S_{32} \\ S_{41} & S_{42} \end{bmatrix} \begin{Bmatrix} u_x \\ u_y \end{Bmatrix}_{l_2,top} \tag{3.30}$$

Then finding the roots (f, k) of the determinant of the system $d = S_{31}.S_{42} - S_{32}.S_{41} = 0$, the problem is resolved.

The other alternative for response solutions requires that the system be excited by (L) and/or (S) plane waves and the equations be resolved to determine the remaining wave amplitudes[21].

The system is then expressed in terms of wave amplitudes. For example for an *n-layer* system embedded in a fluid and excited from the top by a single longitudinal wave with $A_{L+} = \mathbf{1}$ this will be:

$$\begin{Bmatrix} A_{L+} \\ 0 \\ 0 \\ 0 \end{Bmatrix}_{l_n} = [D]^{-1}_{ln,top}[S][D]_{l1,top} \begin{Bmatrix} \mathbf{1} \\ A_{L-} \\ 0 \\ 0 \end{Bmatrix}_{l1} \tag{3.31}$$

However, since the present work is based on the point source excitation model and the air-influence is assumed to be rather similar to vacuum conditions for a metal plate[22], we will use the *free mode* solutions (f, k) as an approximation to the solution for the system (see § 4.3.2).

3.5.2 Addition of material attenuation and leaky waves effect

The addition of material damping can be introduced by assuming a Kelvin-Voigt viscoelastic model[36, 113, 157].

This model basically consists in a velocity-dependent damping factor (or dashpot effect) added to the equations. While the leakage effect can be

---

[21] Once these are obtained, the reflection/transmission coefficients as well displacement and stress fields can be derived from them.

[22] The mismatch in acoustic impedances for air and common metals is of the order of $\approx 4.10^4$ for *Al*, and $> 1.10^5$ for *Fe* & *Cu*.

included by converting the wavenumber into a complex number[23].
Both of these approaches can be applied replacing the Lamé constants by the following operators[24]

$$\lambda_{atte} = \lambda + \frac{\lambda^*}{w}\frac{\partial}{\partial t} \qquad , \qquad \mu_{atte} = \mu + \frac{\mu^*}{w}\frac{\partial}{\partial t} \tag{3.32}$$

Then following a similar procedure to the one mentioned above for Eqs. (3.7-3.10) a similar expression to Eq. (3.11) is arrived at

$$\rho\frac{\partial^2 \mathbf{u}}{\partial t^2} = (\lambda+\mu)\nabla(\nabla.\mathbf{u}) + \mu\nabla^2\mathbf{u} + (\frac{\lambda^*+\mu^*}{w})\nabla(\nabla.\frac{\partial \mathbf{u}}{\partial t}) + (\frac{\mu^*}{w})\nabla^2\frac{\partial \mathbf{u}}{\partial t} \tag{3.33}$$

This expression accepts similar solutions to those of Eq. (3.12) but this time with the wavenumber vector $\boldsymbol{k}$ being complex. These are[25]:

$$\phi, \psi = \boldsymbol{A}_{(\boldsymbol{L},\boldsymbol{S})} e^{i(\boldsymbol{k}_{\boldsymbol{real}}.\bar{\boldsymbol{x}} - wt)} e^{-\boldsymbol{k}_{\boldsymbol{imag}}.\bar{\boldsymbol{x}}} \tag{3.34}$$

Appropriate introductions of these equations into (3.33), lead to similar expressions of bulk wave velocities in terms of complex Lamé parameters[26].

$$\begin{aligned} c_L^* &= \sqrt{\frac{\lambda + 2\mu - i(\lambda^* + 2\mu^*)}{\rho}} = \alpha^* \\ c_S^* &= \sqrt{\frac{\mu - i\mu^*}{\rho}} = \beta^* \end{aligned} \tag{3.35}$$

3.6 The global matrix method

3.6.1 Method Equations

The main problem with the transfer matrix method (TMM) is that during the process of expressing displacement and stress of one interface in terms of the next, mixtures of very large and very small numbers[27] appear in coefficients of the layer matrix $[L]$ leading to an ill-conditioning problem[28].

---

[23] In acoustics normally the preferred choice is a complex wavenumber with a real frequency. While in seismological applications the election is more flexible depending on current work. For more details see § 3.3.1.

[24] An $*$ above a variable indicates a complex value, while the omission corresponds to a real quantity.

[25] Coordinates are represented by the vector $\bar{\boldsymbol{x}} = (x, y, z)$.

[26] A similar development could be done for the transfer matrix method without making any changes to the theory except that this time boundary conditions require at any interface that both real and imaginary parts of plate projected wavenumbers are matched (component $\mathrm{k_x} = \mathrm{k_{x,Re}} + i\mathrm{k_{x,Im}}$).

[27] This problem is also know as "the large *fd* problem".

[28] In ill-conditioning problems the addition of small perturbation to the system matrix could cause results to change severely leading to wrong solutions. A measure of the

To overcome this problem Knopoff[138] proposed a different approach in which the system matrix is assembled directly in one step leading to a system of $4(n-1)$ equations and arriving at the solution for the whole system simultaneously.

An improvement to the method was added later[204] by changing the origin of L and S waves and replacing them with those of figure 3.4 (see page 51). Here downward travelling waves (L_+, S_+) originate at the top of layers and upward travelling waves (L_-, S_-) at the *bottom.*

Then analysing interface (i_1) and applying continuity boundary conditions for displacements and stresses at layers (l_1) and (l_2) using Eq. (3.21) the following expression is obtained

$$[D]_{l1,bottom} \begin{Bmatrix} A_{(L+)} \\ A_{(L-)} \\ A_{(S+)} \\ A_{(S-)} \end{Bmatrix}_{l1} = [D]_{l2,top} \begin{Bmatrix} A_{(L+)} \\ A_{(L-)} \\ A_{(S+)} \\ A_{(S-)} \end{Bmatrix}_{l2} \tag{3.36}$$

This can be resumed in the following form

$$[D_{1b}] - [D_{2t}] \begin{Bmatrix} A_{(L+)1} \\ A_{(L-)1} \\ A_{(S+)1} \\ A_{(S-)1} \\ A_{(L+)2} \\ A_{(L-)2} \\ A_{(S+)2} \\ A_{(S-)2} \end{Bmatrix}_{l2} = \{0\} \tag{3.37}$$

where

$$[D_t] = \begin{bmatrix} k_x & k_x g_\alpha & C_\beta & -C_\beta g_\beta \\ C_\alpha & -C_\alpha g_\alpha & -k_x & -k_x g_\beta \\ i\rho B & i\rho B g_\alpha & -2i\rho k_x \beta^2 C_\beta & 2i\rho k_x \beta^2 C_\beta g_\beta \\ 2i\rho k_x \beta^2 C_\alpha & -2i\rho k_x \beta^2 C_\alpha g_\alpha & i\rho B & i\rho B g_\beta \end{bmatrix}$$

$$[D_b] = \begin{bmatrix} k_x g_\alpha & k_x & C_\beta g_\beta & -C_\beta \\ C_\alpha g_\alpha & -C_\alpha & -k_x g_\beta & -k_x \\ i\rho B g_\alpha & i\rho B & -2i\rho k_x \beta^2 C_\beta g_\beta & 2i\rho k_x \beta^2 C_\beta \\ 2i\rho k_x \beta^2 C_\alpha g_\alpha & -2i\rho k_x \beta^2 C_\alpha & i\rho B g_\beta & i\rho B \end{bmatrix} \tag{3.38}$$

As seen this process can be continued for the rest of $(n-1)$ interfaces and lead to a system matrix of $4(n-1)$ equations and $4n$ unknowns.

---

ill-condition of a problem is $\|A\| \left\|A^{-1}\right\|$, called the condition number of matrix A with respect to the inversion. This determines the loss in precision due to round off errors. The exponent of $\log_{10}(\|A\| \left\|A^{-1}\right\|)$ is an indication of the number of decimal places that a computer can lose during the round off process.

In the example of the three layer system of figure 3.4 this process will be express by:

$$\begin{bmatrix} [D_{1b}] & -[D_{2t}] & \\ & [D_{2b}] & -[D_{3t}] \end{bmatrix} \cdot \begin{Bmatrix} \{A_1\} \\ \{A_2\} \\ \{A_3\} \end{Bmatrix} = \{0\} \tag{3.39}$$

where the vectors {A$_i$} condense the layer l_i wave amplitudes $[L_+, L_-, S_+, S_-]$. This system of Eq. (3.39) as it stands can not be resolved because it has 4 more unknown than equations[29], then 4 wave amplitudes must first be defined before proceeding with the solution. Thus the idea is to solve the system via response solutions or modal solutions.

Response solutions, as previously mentioned in § 3.5.1, require previously define the excitations to the layer system and then the separation of unknown values to solve the equations.

Alternatively modal solutions require the determination of the roots (f, k) of the characteristic equation of the system i.e. $|S| = 0$.

For example introducing n = 3 into Eq. (3.31) for a layered system in a fluid excited by a single unitary amplitude longitudinal wave we have[30]

$$\begin{bmatrix} [D_{1b}^-] & -[D_{2t}] & \\ & [D_{2b}] & -[D_{3t}^+] \end{bmatrix} \cdot \begin{Bmatrix} \{A_1^-\} \\ \{A_2\} \\ \{A_3^+\} \end{Bmatrix} = \begin{bmatrix} [-D_{1b}^+] & \\ & [D_{3t}^-] \end{bmatrix} \cdot \begin{Bmatrix} \{A_1^+\} \\ \{0\} \\ \{A_3^-\} \end{Bmatrix} \tag{3.40}$$

where the symbols (±) indicate downward$^+$ and upward$^-$ travelling L/S waves, and the vectors {A$^\pm$} and matrices [D$^\pm$] respective partitions are defined by:

$$\{A^+\} = \begin{Bmatrix} A_{(L+)} \\ A_{(S+)} \end{Bmatrix} \qquad \{A^-\} = \begin{Bmatrix} A_{(L-)} \\ A_{(S-)} \end{Bmatrix}$$

$$[D^+] = \begin{bmatrix} D_{11} & D_{13} \\ D_{21} & D_{23} \\ D_{31} & D_{33} \\ D_{41} & D_{43} \end{bmatrix} \qquad [D^-] = \begin{bmatrix} D_{12} & D_{14} \\ D_{22} & D_{24} \\ D_{32} & D_{34} \\ D_{42} & D_{44} \end{bmatrix} \tag{3.41}$$

For modal solutions with no excitation the equation to resolve is $|S| = 0$ with:

$$[S] = \begin{bmatrix} [D_{1b}^-] & -[D_{2t}] & \\ & [D_{2b}] & -[D_{3t}^+] \end{bmatrix} \tag{3.42}$$

---

[29] In general there were always be four more unknowns than equations. In the above example for n = 3 layers, there are 4x3 wave amplitudes and 4x2 wave equations ($D_{i,t/b}$ is 4-by-4 matrix).

[30] In this case wave excitations are: A$_1^+$ = [1 0] and A$_3^-$ = [0 0].

3.6.2 The searching algorithm

Because *modal* solutions are used as an approximation to dispersion relationships in the next chapter, the search algorithm will look for the (f, k) pairs that resolve the characteristic equation $|S| = 0$, with real frequency $f = \Re\{w\}/(2\pi)$ and complex wavenumber $(k = k_{\text{Re}} + \text{i}k_{\text{Im}})$.
However finding the roots of such an equation for an n-layer system is not an easy task[31]. This is especially true when material damping is used and/or when roots are in close proximity e.g. near cross points of Lamb dispersion curves.
Nevertheless robust search algorithms based on a two stage search strategy have been reported in literature[157]. This method had been adapted and added to the LAMB software in order to obtain the (f, k) dispersion relationships and is briefly described here[32].

The algorithm starts looking for the initial roots of the dispersion traces by first making frequency and phase velocity sweeps on the (f, k) map. These are represented by the straight lines of figure 3.5 in which the other corresponding variable is maintained fixed while the search is performed.
Once the starting points of the dispersion curves are located the $2^{\text{nd.}}$ stage consists in steadily increasing the wavenumber in fixed steps Δk while a frequency search is performed.
Then after five new solution points are found[33] the construction of the curves switch to an extrapolation scheme seeded by the previous data (see Fig. 3.6)). This scheme continues until all the detected Lamb mode curves are plotted.

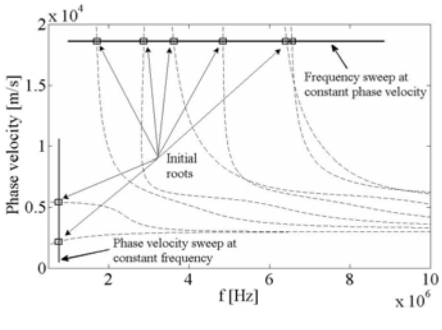

Figure 3.5: Sweeps in frequency and phase velocity of the first stage of the search algorithm.

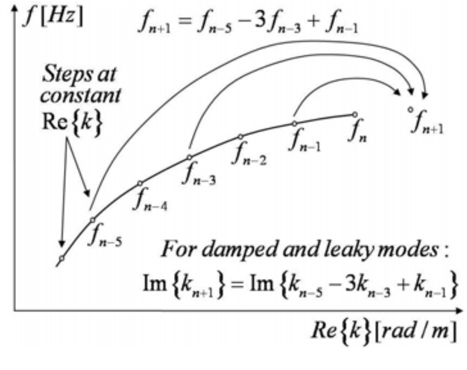

Figure 3.6: Extrapolation scheme of the dispersion curve of the algorithm.

---

[31] To visualize the process, it would be like finding the head of a pin in a kilometre high funnel with a mouth of hundreds of meters!

[32] A custom version of this algorithm is the root search engine of the commercial software *Disperse*[198].

[33] A solution is considered found when the $min\{|S|\}$ is encountered.

3.7 Dispersion curves: measurement and simulations

This section presents comparison tests between experimental and GMM simulated results for the dispersion curves for 3-layer systems[34]: *air*-Al_{plate}-*air*. These are used to validate the GMM code implemented in the LAMB software. However the programme is capable of computing the dispersion data for other layered systems too[35].

The experimental data presented here were collected from two tests in aluminium plates by use of a laser scan method combined with a two-dimensional FFT detection technique[9, 101, 145]. This arrangement permits the identification of propagating Lamb wave modes in an excited laminate.
The setup for the measurements is observed in figure 3.7, where a laser vibrometer mounted on computer controlled stage scans a line ($x_{\text{dist}} = 30\,\text{mm}$) on the surface of an aluminium plate.
For both measurements the spacing between sampling points was adjusted to $\Delta_{\text{x}} = 0.25\,\text{mm}$, while the laser vibrometer was set to measure the normal velocity of the plate with a constant of $k_{\text{laser}} = 25\,(\text{mm/s})/\text{V}$.

Example of laser detected velocity signals are presented in figures 3.8 and 3.9, for $d = 1.0$mm and $d = 0.8$mm aluminium plates respectively. The signals were previously averaged 200 times by the oscilloscope before they were stored. After that the data was processed by means of a two-dimensional Fourier transform $\mathcal{F}\{u(t,x)\}$ in order to extract the dispersion spectrum and compare with the GMM simulations.

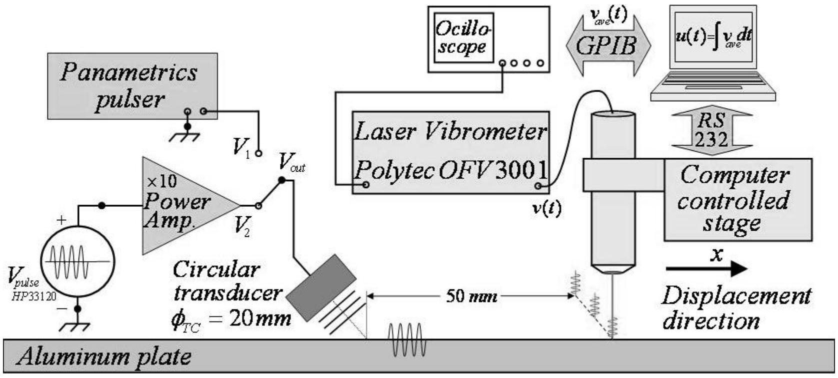

Figure 3.7: Dispersion curves measurement setup: $\text{k}_{\text{laser}} = 25$ mm/s/V, $f_0^{\text{TC}} \approx 1$ MHz, $BW_{\text{TC}} \approx 0.35$ MHz, $x_{\text{step}} = 0.25$ mm, $x_{\text{dist.}} = 30$ mm, $f_{\text{s2}} = 1/0.25$ mm.

---

[34] The majority of measurements and simulations where performed on aluminium plates (Al_{plate}) of few millimetre of width since this is a common test bench material encountered in the NDT area.

[35] See Appendix B for more details.

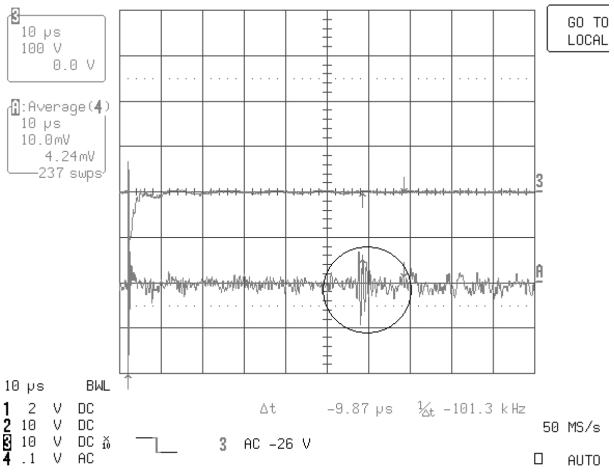

Figure 3.8: Measured pulsed signal in *Al*@1 mm plate, $f_\mathrm{s} = 50\,\mathrm{MHz}, \mathrm{V}_\mathrm{out} = \mathrm{V}_1@240\mathrm{V}_\mathrm{pp}$.

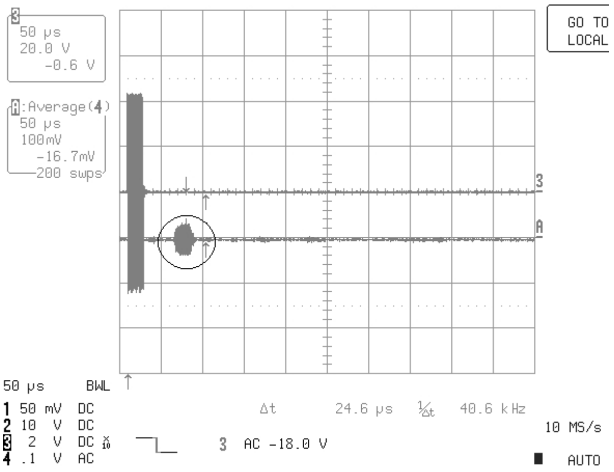

Figure 3.9: Measured burst@20 cycles signal in *Al*@0.8 mm plate, $f_\mathrm{s} = 10\,\mathrm{MHz},\ \mathrm{V}_\mathrm{out} = \mathrm{V}_2@10\mathrm{V}_\mathrm{pp} + \mathrm{x}10$ Amp.

The $|\mathcal{F}(w,k)|$ of the processed experimental data are depicted[36] in figures 3.10 and 3.11 for the mentioned plates, together with the superimposed curves from the GMM simulations[37].
A good match is clearly observed between the experimental results and the GMM simulations for the detected A0 mode, since the others modes usually have lower displacements amplitudes and are thus more difficult to detect.

---

[36] The dispersion spectrum has been transformed from (w,k) to $\rightarrow (f, c_\mathrm{ph})$.

[37] A similar example to figure 3.11 for the determination of Lamb wave propagating modes but this time using a 48 element plane array for the detection instead of a laser vibrometer is shown in figures B.8 and B.9.

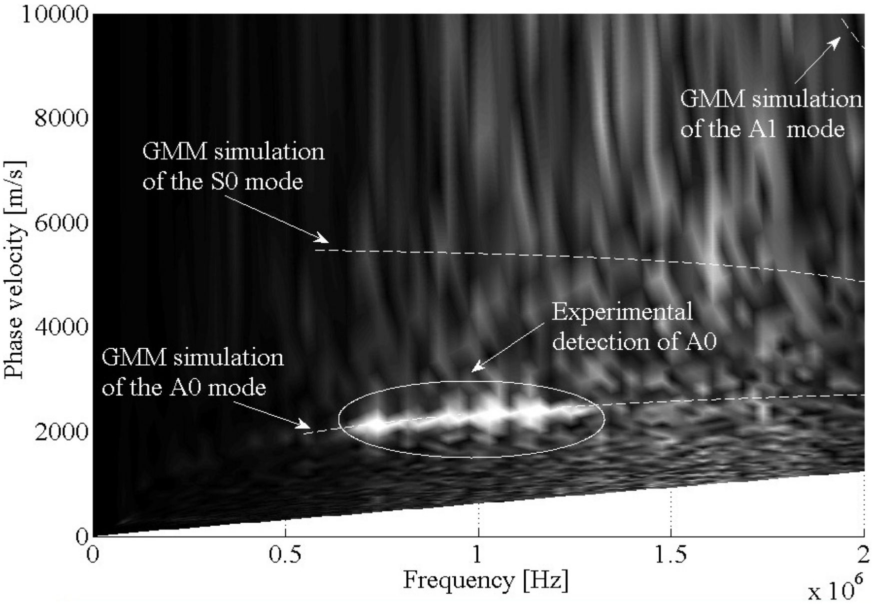

Figure 3.10: Comparison of laser vibrometer detected dispersion curve map in an aluminium plate ($d = 1\,\mathrm{mm}$) and the superimposed GMM simulations. Mode: A0, unfiltered pulsed signal,$f_0^{\mathrm{TC}} \approx 1\,\mathrm{MHz}$,$f_s = 50\,\mathrm{MHz}$,$f_{s2} = 1/0.25\,\mathrm{mm}$.

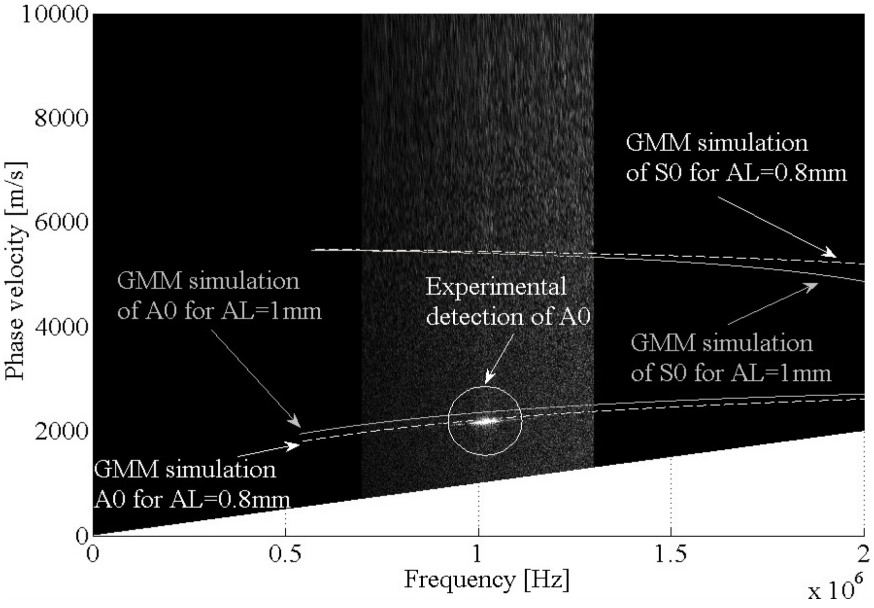

Figure 3.11: Comparison of laser vibrometer detected dispersion map in an aluminium plate ($d = 0.8\,\mathrm{mm}$) and the superimposed GMM simulations. Mode:A0, filtered sin.burst 20cycles,$f_0^{\mathrm{TC}} \approx 1\mathrm{MHz}$,$f_s = 10\mathrm{MHz}$,$f_{s2} = 1/0.25\mathrm{mm}$.

Simulation results for dispersion curves up to 20 MHz for a 0.5 mm width aluminium plate in air are depicted in figures 3.12 and 3.13.
As can be appreciated the attenuation+leakage part of the wavenumber is very small compared to the real part[38] This means that Lamb waves will travel along the plate without almost no attenuation. This is a common phenomenon in metals but not for example in plastic materials[25, 45].
An attempt was made to compute response solutions for equation (3.31) for a two layer system e.g. air-Ti excited by a single longitudinal incoming wave $A_{L+} = 1$, but with inconclusive results. These are presented in figures 3.14 and 3.15. The main reason to this unsolved problem is probably related to the solution of the equations of the system which at present is not converted to manage the quantity of digits required for matrix inversions[39].

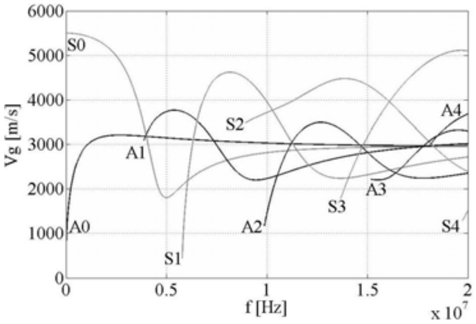

Figure 3.12: Group velocity dispersion curves for a three layers system: *air-Al*@0.5 mm-*air*.

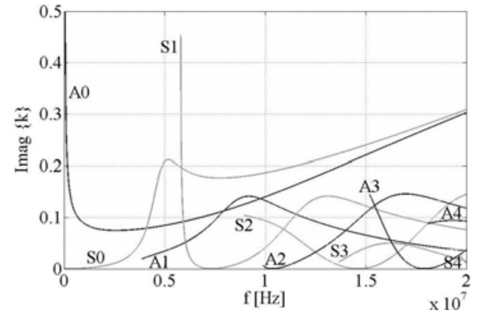

Figure 3.13: Imaginary part of wavenumber $\boldsymbol{k}$ (*attenuation+leakage*), for the same system.

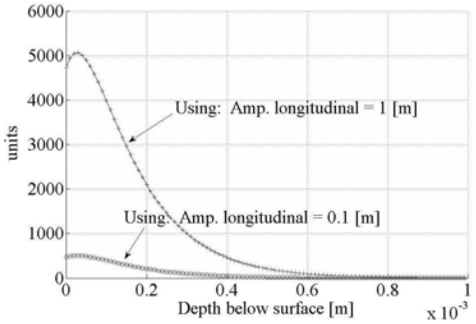

Figure 3.14: Normal displacement for a 2-layer system: *Air-Ti*@0.5 mm.

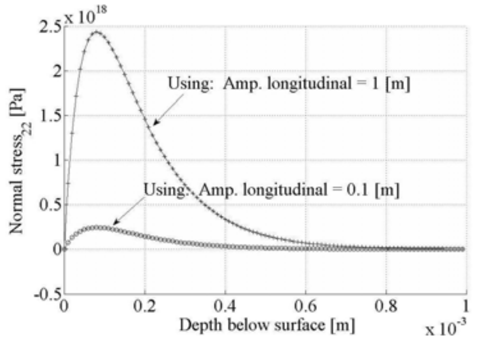

Figure 3.15: Normal stress σ_{yy} for the same *Air-Ti*@0.5 mm system.

---

[38] With $c_{\text{ph}} = w/\Re\{k\}$, e.g.: $0.1 \leq f \leq 20\,\text{MHz}$ & $c_{\text{ph}} \geq 600\,\text{m/s} \Rightarrow 1000 \leq k < 45000$.

[39] A solution to this issue partially tested by the author in GMM routines was the use of a freely available package called *mp* or Multiple Precision toolbox for Matlab. This toolbox defines a new mp class allowing for computations with arbitrary precision quantities.

3.8 Conclusions

The Transfer Matrix Method (TMM) and its improved technique the Global Matrix Method (GMM), have been introduced and presented in this chapter showing how these matrix techniques allow computations of field parameters in multilayered media systems.

A set of corresponding Matlab routines have been developed and added to the LAMB programme in order to obtain the dispersion relationship pairs (f, k) required by the propagation module based on the Time Harmonic Solution introduced in the next chapter.

Measurement results for laser detected dispersion curves in aluminium plates were presented and compared with GMM predictions from developed routines.

The single detected A0 Lamb mode demonstrated a relatively high level of agreement with the GMM simulations showing the possibilities of this technique.

However in efforts made to compute *response solutions* for the single excited wave in multilayered systems the results obtained were inconclusive. This might be resolved by carrying out a full revision and translation of the LAMB-GMM code to the Multiple Precision (mp) arithmetic.

Chapter 4

The time harmonic solution

4.1 Introduction

This chapter introduces the equations to solve the problem of a infinite ideal isotropic layer excited by a time harmonic signal exerting pressure over a circular region. The so called *time harmonic solution* or THS method which is used as the main model in the propagation module of the LAMB programme.

The chapter begins with a short historical background followed by a presentation of the approximate solution developed by Ditri et al.[57, 201] and the author's proposed generalization for the inclusion of 2D arbitrary excitation regions using broadband signals.

Then a comparison with two similar approaches to the point excitation problem solution is presented by the introduction of only final calculating expressions. To complement this point a group of trial simulations using the two alternative THS modelling cores is also presented.

Additional results obtained with the finite element method (FEM) are introduced for validation of the analytical LAMB propagation model.

Finally, experimental tests with real impacted aluminium plates are also presented for further confirmation of the models, while conclusions are outlined at the end.

4.2 Historical background

In elasticity theory there is a long tradition of study for the problem of wave propagation in an infinite elastic isotropic plates.

It was studied for the first time in 1889 by Lord Rayleigh[218] and then mainly by H. Lamb[143] who established the dispersive frequency relations of waves that nowadays bear his name i.e. Lamb waves[1].

---

[1] As well as Rayleigh, Lamb also investigated (1904) the surface vibrations in a half space produced by concentrated harmonic and impulsive loads and is now known as the Lamb problem[142].

Since then there have been several contributions most notably the plate approximate theories by Mindlin[174]; dispersion relationships by Viktorov[276, 277]; and transient solutions by Miklowitz[173].

These last three were mainly driven by the application of integral transform techniques[1] and the evaluation of results by residue calculus[172] and the method of stationary phase[2] or the method of generalized rays[3].

In the case of localised forces in a half space an alternative and more efficient solution of integrals for transient solutions was proposed by A.T. de Hoop[109] who introduced the Cagniard-de Hoop method[4] in 1960.

Expansion of the vibration field in *normal* modes[15, 16, 17] was also an approach developed and used in the literature[126, 150, 167].

This technique is applicable when the perturbations are small since it allows for expansion of the solution in a similar manner to Fourier's analysis in terms of a sum of orthogonal modes or *eigenvalues* of the system.

Apart from this brief introduction there is a vast amount of literature related to the subject[5]. Excellent reviews on the field can be found in Refs.[19, 47, 172].

4.3 The time harmonic solution

4.3.1 Formulation of the problem

This section presents the equations for the solution of the problem of an ideal infinite isotropic layer excited by a time harmonic signal which exerts pressure over a circular defined region. This is the so called *time harmonic solution* (THS) used in the propagation module of the LAMB toolbox.

THS uses the work by Ditri et al.[57] using integral transformation methods to obtain displacement solutions for Lamb waves.

The theory is approximate in the sense that it only takes into account contributions from simple poles to the solution.

Then contributions from other possible "multiple" poles that usually occur in the vicinity of cut-off frequencies ($k \rightarrow 0$) are avoided[274].

---

[2] This method (essentially for far field approximations) is based on the fact that when R is a long distance ($R >> d$ or $t >> d/C_{\mathrm{ph}}$) the variation of the integrand with k is dominated by rapid oscillations of the Bessel and cosine terms. However if the wavenumber is fixed ($k = k_0$), the variations of these functions are aligned in phases and then time displacements are dominated mainly by a sum of simple harmonic functions.

[3] The theory of generalized rays[43] although being an exact method, becomes particularly cumbersome when the source-receiver distance is greater than a 10 plate thickness because of the large number of generalized ray integrals that must be calculated.

[4] This technique deforms the path of integration on the complex plane to solve the inverse Laplace transforms.

[5] This not only includes the point-source problem for isotropic plates but also anisotropic and multilayer laminates.

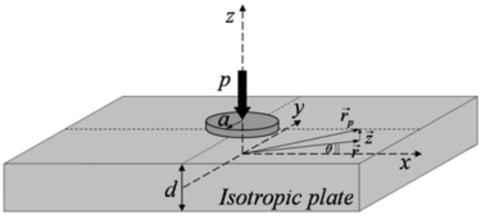

Figure 4.1: Chosen geometry for THS problem in the infinite isotropic plate.

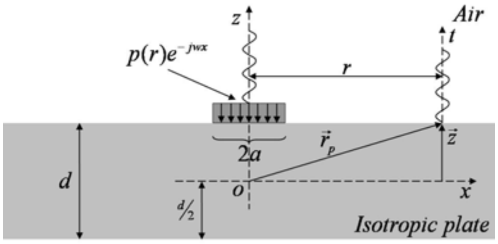

Figure 4.2: 2D view of THS geometry for the ideal plate.

This element together with the fact that only solutions for leaky Lamb waves in the (w, k) dispersion map were found in Chapter 3 proves in essence that the model is valid only in *far field* approximation, away from the excitation source.
This last statement applies to distances e.g. $r > 10\,\xi_{\max}$, where $\xi_{\max}$ is the maximum Lamb wavelength present in the signal bandwidth and r is the distance from the observation point to the source on the surface of the plate.
The development begins by considering again an infinite ideal isotropic medium[6] for vibrations as viewed in Chapter 3 equation (3.11)

$$\rho \frac{\partial^2 \mathbf{u}}{\partial t^2} = (\lambda + \mu)\nabla(\nabla \mathbf{u}) + \mu \nabla^2 \mathbf{u} \tag{4.1}$$

Because the symmetry of excitation is circular we define the cylindrical coordinates for problem resolution, in the following figures 4.1 and 4.2.
As seen from the symmetry any transversal angular stress $\sigma_{z\theta}$ is null.
Then applying boundary conditions for the rest of stress components we have

$$\begin{aligned}
\sigma_{zz|(z=d/2)} &= \begin{cases} \mathrm{f}(r)e^{-\mathrm{i}wt} & 0 < r \leq a \\ 0 & r > a \end{cases} \\
\sigma_{zz|(z=-d/2)} &= 0 \\
\sigma_{rz|(z=d/2)} &= \begin{cases} \mathrm{g}(r)e^{-\mathrm{i}wt} & 0 < r \leq a \\ 0 & r > a \end{cases} \\
\sigma_{rz|(z=-d/2)} &= 0
\end{aligned} \tag{4.2}$$

Where f(r) and g(r) are respectively the normal and transversal components of the stress applied to the laminate surface[7].

---

[6] This is also known as the elastodynamic equation. Again as mentioned in page 46, body forces are considered null.

[7] The general case with normal (σ_{zz}) and radio-transversal (σ_{rz}) stress components is obtained although only the normal components of the stress σ_{zz} are actually used.

4.3.2 Derivation of the solution

§Uncoupling the displacement equation

In the case of cylindrical coordinates Eq. (4.1) must first be uncoupled using the Helmholtz decomposition method as in the previous chapter where plate displacements were presented by

$$\boldsymbol{u} = \boldsymbol{\nabla}\phi + \boldsymbol{\nabla}\mathsf{x}\boldsymbol{\psi} \qquad , \qquad \boldsymbol{\nabla}\boldsymbol{\psi} = 0 \tag{4.3}$$

where ϕ and $\boldsymbol{\psi}$ are the scalar and vectorial displacement potentials respectively. Then incorporating the decomposition equations in (4.3) into the equations in (4.1) leads to the following relationships

$$\begin{aligned} \boldsymbol{\nabla}\left[(\lambda+\mu)\nabla^2\phi - \rho\frac{\partial^2\phi}{\partial t^2}\right] &= 0 \\ \boldsymbol{\nabla}\mathsf{x}\left[-\mu\boldsymbol{\nabla}\mathsf{x}(\boldsymbol{\nabla}\mathsf{x}\boldsymbol{\psi}) - \rho\frac{\partial^2\boldsymbol{\psi}}{\partial t^2}\right] &= 0 \end{aligned} \tag{4.4}$$

Using the vectorial identity $\boldsymbol{\nabla}\mathsf{x}\boldsymbol{\nabla}\mathsf{x}\boldsymbol{\psi} = \nabla^2\boldsymbol{\psi} + \boldsymbol{\nabla}(\boldsymbol{\nabla}\boldsymbol{\psi})$ equations (4.4) can be re-expressed in the following more appropriate ways:

$$\begin{aligned} \nabla^2\phi &= \frac{1}{\alpha^2}\frac{\partial^2\phi}{\partial t^2}\ , & \alpha &= \sqrt{\frac{\lambda+2\mu}{\rho}} \\ \nabla^2\boldsymbol{\psi} &= \frac{1}{\beta^2}\frac{\partial^2\boldsymbol{\psi}}{\partial t^2}\ , & \beta &= \sqrt{\frac{\mu}{\rho}} \end{aligned} \tag{4.5}$$

where again α and β represent the longitudinal and transversal bulk wave velocities in the isotropic laminate.
Because of the axial symmetry the field component of displacement u_θ will be defined as zero and then corresponding components of vector potential ψ_r and ψ_θ will be zero. Then $\boldsymbol{\psi}$ vector potential can be further reduced to a scalar potential $\psi = \psi_z$.
Assuming then a time harmonic dependence for the potentials [g($e^{-\mathrm{i}wt}$)] equations (4.5) can be transform finally into

$$\begin{aligned} \frac{\partial^2\phi}{\partial r^2} + \frac{1}{r}\frac{\partial\phi}{\partial r} + \frac{\partial^2\phi}{\partial z^2} + \frac{w^2}{\alpha^2}\phi &= 0 \\ \frac{\partial^2\psi}{\partial r^2} + \frac{1}{r}\frac{\partial\psi}{\partial r} - \frac{\psi}{r^2} + \frac{\partial^2\psi}{\partial z^2} + \frac{w^2}{\beta^2}\psi &= 0 \end{aligned} \tag{4.6}$$

§Applying the Hankel integral transform

The idea is to resolve the above equations (4.6) applying the boundary conditions (4.2). For this purpose and because of symmetry we will employ the Hankel integral transform to resolve these equations via residue calculus.

The Hankel transforms of order n of an arbitrary function $\mathrm{h}(r)$ are defined respectively by

$$
\begin{aligned}
H^n(k) = \mathcal{H}_n\left\{\mathrm{h}(r)\right\} &= \int_0^\infty r\mathrm{h}(\mathrm{r})J_n(kr)\mathrm{d}r \\
h(r) = \mathcal{H}_n^{-1}\left\{H^n\right\} &= \int_0^\infty kH^n(k)J_n(kr)\mathrm{d}k
\end{aligned} \tag{4.7}
$$

where the symbols $\mathcal{H}_n$ and $\mathcal{H}_n^{-1}$ represent the direct and inverse Hankel transform operators and J_n the $1^{\text{st.}}$ kind of Bessel function of order n.
Then, applying the Hankel transform and its properties[8] to equations (4.6) they are re-express into the transform domain by[9]

$$
\begin{aligned}
&\frac{\mathrm{d}^2\Phi^0}{\mathrm{d}z^2} + (k_{\mathrm{L}}^2 - k)\Phi^0 = 0 \ , \qquad && k_{\mathrm{L}} = \frac{w}{\alpha} \\
&\frac{\mathrm{d}^2\Psi^1}{\mathrm{d}z^2} + (k_{\mathrm{T}}^2 - k)\Psi^1 = 0 \ , \qquad && k_{\mathrm{T}} = \frac{w}{\beta}
\end{aligned} \tag{4.8}
$$

where Φ^0 and Ψ^1 are the zero and $1^{\text{st.}}$ order transform functions of ϕ and ψ respectively. These equations have the following general solutions

$$
\begin{aligned}
\Phi^0(k,z) &= A(k)\cos(k_{\mathrm{tl}}z) + B(k)\sin(k_{\mathrm{tl}}z) \ , \qquad && k_{\mathrm{tl}}^2 = (w/\alpha)^2 - k^2 \\
\Psi^1(k,z) &= C(k)\cos(k_{\mathrm{ts}}z) + D(k)\sin(k_{\mathrm{ts}}z) \ , \qquad && k_{\mathrm{ts}}^2 = (w/\beta)^2 - k^2
\end{aligned} \tag{4.9}
$$

where $A(k), B(k), C(k)$ and $D(k)$ are the amplitudes of the wave functions.

§Satisfying the boundary conditions

Next, boundary conditions from equation (4.2) will be applied to equations (4.9), in order to find the unknown wave amplitudes.
Since boundary conditions are express in terms of stresses they must first be expressed in terms of the Helmholtz potentials.

This can be done by using Eq. (4.3) and the following relationship: $\boldsymbol{\sigma} = \lambda\boldsymbol{I}\nabla.\boldsymbol{u} + \mu(\nabla\boldsymbol{u} + \boldsymbol{u}\nabla)$. Then we get:

$$
\begin{aligned}
\sigma_{\mathrm{zz}}(r,z) &= -\lambda k_{\mathrm{L}}^2\phi + 2\mu\frac{\partial^2\phi}{\partial z^2} + \frac{2\mu}{r}\frac{\partial}{\partial r}\left(r\frac{\mathrm{d}\psi}{\mathrm{d}z}\right) \\
\sigma_{\mathrm{rz}}(r,z) &= -\mu\left\{2\frac{\partial^2\phi}{\partial r\partial z} + \frac{\partial^2\psi}{\partial r^2} + \frac{1}{r}\frac{\partial\psi}{\partial r} - \frac{\psi}{r} - \frac{\partial^2\psi}{\partial z^2}\right\}
\end{aligned} \tag{4.10}
$$

---

[8] Using integration by parts it can be shown that:
$\mathcal{H}_0\left\{\frac{\mathrm{d}^2g(r)}{\mathrm{d}r^2} + \frac{1}{r}\frac{\mathrm{d}g(r)}{\mathrm{d}r}\right\} = -k^2G^0(r)$ and $\mathcal{H}_1\left\{\frac{\mathrm{d}^2g(r)}{\mathrm{d}r^2} + \frac{1}{r}\frac{\mathrm{d}g(r)}{\mathrm{d}r} - \frac{g(r)}{r^2}\right\} = -k^2G^1(r)$

[9] As mentioned before $k_{\mathrm{L,T}}$ represent wavenumbers for *longitudinal* and *vertical-transversal* waves in the material and k the equation wavenumber.

Now on applying the direct Hankel integral to these equations we get the transform expressions of stresses

$$\begin{aligned}\Sigma^0_{\mathrm{zz}}(k,z) &= \mathcal{H}_0\left\{\sigma_{\mathrm{zz}}\right\} = -\lambda k_{\mathrm{L}}^2\Phi^0 + 2\mu\frac{\mathrm{d}^2\Phi^0}{\mathrm{d}z^2} + 2\mu k\frac{\mathrm{d}\Psi^1}{\mathrm{d}z}\\ \Sigma^1_{\mathrm{rz}}(k,z) &= \mathcal{H}_1\left\{\sigma_{\mathrm{rz}}\right\} = -\mu\left\{2k\frac{\mathrm{d}\Phi^0}{\mathrm{d}z} + k^2\Psi^1 + \frac{\mathrm{d}^2\Psi^1}{\mathrm{d}z^2}\right\}\end{aligned} \tag{4.11}$$

Next, by application of the same operations this time to boundary conditions (4.2) we obtain the following relationships:

$$\begin{aligned}\Sigma^0_{\mathrm{zz}}(k,d/2) &= \mathcal{H}_0\left\{\mathrm{f(r)}\right\} = F^0(k)\\ \Sigma^0_{\mathrm{zz}}(k,-d/2) &= 0\\ \Sigma^1_{\mathrm{rz}}(k,d/2) &= \mathcal{H}_1\left\{\mathrm{g(r)}\right\} = G^1(k)\\ \Sigma^1_{\mathrm{rz}}(k,-d/2) &= 0\end{aligned} \tag{4.12}$$

Incorporating expressions of transform potentials (4.9) into Eq. (4.11) and applying boundary conditions (4.12) leads to the following system of linear equations for the four unknown wave amplitudes $A(k), B(k), C(k)$ and $D(k)$

$$[S]\begin{bmatrix}A\\B\\C\\D\end{bmatrix} = \begin{bmatrix}F^0\\0\\G^1\\0\end{bmatrix} \tag{4.13}$$

with

$$[S] = \begin{bmatrix}-\mu(k_{\mathrm{ts}}^2-k^2)\cos(k_{\mathrm{tl}}d/2) & -\mu(k_{\mathrm{ts}}^2-k^2)\sin(k_{\mathrm{tl}}d/2) & -2\mu kk_{\mathrm{ts}}\sin(k_{\mathrm{ts}}d/2) & 2\mu kk_{\mathrm{ts}}\cos(k_{\mathrm{ts}}d/2)\\ -\mu(k_{\mathrm{ts}}^2-k^2)\cos(k_{\mathrm{tl}}d/2) & \mu(k_{\mathrm{ts}}^2-k^2)\sin(k_{\mathrm{tl}}d/2) & 2\mu kk_{\mathrm{ts}}\sin(k_{\mathrm{ts}}d/2) & 2\mu kk_{\mathrm{ts}}\cos(k_{\mathrm{ts}}d/2)\\ 2\mu kk_{\mathrm{tl}}\sin(k_{\mathrm{tl}}d/2) & -2\mu kk_{\mathrm{tl}}\cos(k_{\mathrm{tl}}d/2) & \mu(k_{\mathrm{ts}}^2-k^2)\cos(k_{\mathrm{ts}}d/2) & \mu(k_{\mathrm{ts}}^2-k^2)\sin(k_{\mathrm{ts}}d/2)\\ -2\mu kk_{\mathrm{tl}}\sin(k_{\mathrm{tl}}d/2) & -2\mu kk_{\mathrm{tl}}\cos(k_{\mathrm{tl}}d/2) & \mu(k_{\mathrm{ts}}^2-k^2)\cos(k_{\mathrm{ts}}d/2) & -\mu(k_{\mathrm{ts}}^2-k^2)\sin(k_{\mathrm{ts}}d/2)\end{bmatrix} \tag{4.14}$$

Then the determinant for the matrix $[S]$ can be found by

$$\|A\| = 4\mu^4\Delta_{\mathrm{a}}\Delta_{\mathrm{s}} \tag{4.15}$$

where

$$\begin{aligned}\Delta_{\mathrm{s}} &= (k_{\mathrm{ts}}^2-k^2)^2\cos(k_{\mathrm{tl}}d/2)\sin(k_{\mathrm{ts}}d/2) + 4k^2k_{\mathrm{tl}}k_{\mathrm{ts}}\sin(k_{\mathrm{tl}}d/2)\cos(k_{\mathrm{ts}}d/2)\\ \Delta_{\mathrm{a}} &= (k_{\mathrm{ts}}^2-k^2)^2\sin(k_{\mathrm{tl}}d/2)\cos(k_{\mathrm{ts}}d/2) + 4k^2k_{\mathrm{tl}}k_{\mathrm{ts}}\cos(k_{\mathrm{tl}}d/2)\sin(k_{\mathrm{ts}}d/2)\end{aligned} \tag{4.16}$$

These expressions represent respectively the dispersion relationships for straight crested symmetric and anti-symmetric Lamb waves in the ideal isotropic layer. Both can be solved for real roots values $\Re\{k\}$ by equating them to zero.

However the results derived in the previous chapter[10] will be used to take into account the material attenuation and leakage effects[11] both represented by the imaginary part of the wavenumber $\Im\{k\}$.
Now the system of equations (4.13) can be resolved by Cramer's method to obtain the following equations for the wave amplitudes

$$\begin{aligned}
A &= \frac{S_{14}(k)G^1(k) - S_{34}(k)F^0(k)}{2\mu^2\Delta_\mathrm{s}(k)} \\
B &= \frac{S_{13}(k)G^1(k) - S_{33}(k)F^0(k)}{2\mu^2\Delta_\mathrm{a}(k)} \\
C &= \frac{S_{32}(k)F^0(k) - S_{12}(k)G^1(k)}{2\mu^2\Delta_\mathrm{a}(k)} \\
D &= \frac{S_{31}(k)F^0(k) - S_{11}(k)G^1(k)}{2\mu^2\Delta_\mathrm{s}(k)}
\end{aligned} \tag{4.17}$$

where S_ij are the elements of matrix $[S]$.

§Applying the inverse Hankel transform

Development of the solution follows now by incorporation of determined amplitude expressions (4.17) into the transformed potential equations (4.11) and appropriate application of the inverse Hankel transforms.
Then solutions for the Helmholtz potentials are:

$$\begin{aligned}
\phi(r,z) &= \int_0^\infty \frac{S_{14}(k)G^1(k) - S_{34}(k)F^0(k)}{2\mu^2\Delta_\mathrm{s}(k)} \cos(k_\mathrm{tl}z)J_0(kr)k\mathrm{d}k \\
&+ \int_0^\infty \frac{S_{13}(k)G^1(k) - S_{33}(k)F^0(k)}{2\mu^2\Delta_\mathrm{a}(k)} \sin(k_\mathrm{tl}z)J_0(kr)k\mathrm{d}k \\
\psi(r,z) &= \int_0^\infty \frac{S_{32}(k)F^0(k) - S_{12}(k)G^1(k)}{2\mu^2\Delta_\mathrm{a}(k)} \cos(k_\mathrm{ts}z)J_1(kr)k\mathrm{d}k \\
&+ \int_0^\infty \frac{S_{31}(k)F^0(k) - S_{11}(k)G^1(k)}{2\mu^2\Delta_\mathrm{s}(k)} \sin(k_\mathrm{ts}z)J_1(kr)k\mathrm{d}k
\end{aligned} \tag{4.18}$$

Observing the respective denominators of equations (4.18) the potentials can be correspondingly split into their symmetric and anti-symmetrical parts as

$$\begin{aligned}
\phi(r,z) &= \phi^\mathrm{s}(r,z) + \phi^\mathrm{a}(r,z) \\
\psi(r,z) &= \psi^\mathrm{s}(r,z) + \psi^\mathrm{a}(r,z)
\end{aligned} \tag{4.19}$$

---

[10] See Chapter 3, the Global Matrix Method at pp 56.

[11] Certainly, this is only an approximation because we are using plane wave results into the small circular excitation region.

Then by using again the Helmholtz decomposition equation (4.3) the displacement field is broken into its *in-plane* (r) and *out-of-plane* (z) components consequently obtaining:

$$\begin{aligned} u_{\mathrm{r}}^{\mathrm{s,a}}(r,z) &= \frac{\partial \phi^{\mathrm{s,a}}}{\partial r} - \frac{\partial \psi^{\mathrm{s,a}}}{\partial z} \\ u_{\mathrm{z}}^{\mathrm{s,a}}(r,z) &= \frac{\partial \phi^{\mathrm{s,a}}}{\partial z} + \frac{\psi^{\mathrm{s,a}}}{r} + \frac{\partial \psi^{\mathrm{s,a}}}{\partial z} \end{aligned} \tag{4.20}$$

Replacement of Eqs. (4.18) into above expressions (4.20) and differentiation under the integral symbols leads to final expressions of plate displacements[12]:

$$\begin{aligned} u_{\mathrm{z}}^{\mathrm{s}}(r,z) &= \int_0^\infty \frac{\Gamma_{\mathrm{zt}}^{\mathrm{s}}(k_{\mathrm{ts}},k_{\mathrm{tl}},k)G^1(k) + \Gamma_{\mathrm{zn}}^{\mathrm{s}}(k_{\mathrm{ts}},k_{\mathrm{tl}},k)F^0(k)}{2\mu\Delta_{\mathrm{s}}(k_{\mathrm{ts}},k_{\mathrm{tl}},k)} J_0(kr)k\mathrm{d}k \\ u_{\mathrm{z}}^{\mathrm{a}}(r,z) &= \int_0^\infty \frac{\Gamma_{\mathrm{zt}}^{\mathrm{a}}(k_{\mathrm{ts}},k_{\mathrm{tl}},k)G^1(k) + \Gamma_{\mathrm{zn}}^{\mathrm{a}}(k_{\mathrm{ts}},k_{\mathrm{tl}},k)F^0(k)}{2\mu\Delta_{\mathrm{a}}(k_{\mathrm{ts}},k_{\mathrm{tl}},k)} J_0(kr)k\mathrm{d}k \\ u_{\mathrm{r}}^{\mathrm{s}}(r,z) &= \int_0^\infty \frac{\Gamma_{\mathrm{rt}}^{\mathrm{s}}(k_{\mathrm{ts}},k_{\mathrm{tl}},k)G^1(k) + \Gamma_{\mathrm{rn}}^{\mathrm{s}}(k_{\mathrm{ts}},k_{\mathrm{tl}},k)F^0(k)}{2\mu\Delta_{\mathrm{s}}(k_{\mathrm{ts}},k_{\mathrm{tl}},k)} J_1(kr)k\mathrm{d}k \\ u_{\mathrm{r}}^{\mathrm{a}}(r,z) &= \int_0^\infty \frac{\Gamma_{\mathrm{rt}}^{\mathrm{a}}(k_{\mathrm{ts}},k_{\mathrm{tl}},k)G^1(k) + \Gamma_{\mathrm{rn}}^{\mathrm{a}}(k_{\mathrm{ts}},k_{\mathrm{tl}},k)F^0(k)}{2\mu\Delta_{\mathrm{a}}(k_{\mathrm{ts}},k_{\mathrm{tl}},k)} J_1(kr)k\mathrm{d}k \end{aligned} \tag{4.21}$$

where the functions $\Gamma_{\alpha,\beta}^{\mathrm{s,a}}$ are defined in[57] and Appendix C of this thesis.

§Defining the pressure excitation spectrum

In this section the spectrum of the normal pressure excitation is calculated[13]. The chosen excitation model will be a uniform pressure distribution in a circular region of radius a. Then we have:

$$\begin{aligned} \mathrm{f}(r) &= \begin{cases} P & , r <= a \\ 0 & , r > a \end{cases} \\ \mathrm{g}(r) &= 0 \end{aligned} \tag{4.22}$$

Now taking the direct Hankel transform of these equations[14] we get the corresponding excitation spectrum:

$$\begin{aligned} F^0(k) &= Pa\frac{J_1(ka)}{k} \\ G^1(k) &= 0 \end{aligned} \tag{4.23}$$

---

[12] From Eq. (4.9): $k_{\mathrm{tl}} = \sqrt{(w/\alpha)^2 - k^2}$, and $k_{\mathrm{ts}} = \sqrt{(w/\beta)^2 - k^2}$.

[13] Although the described model of Eq. (4.21) is valid for both, normal and radio-transversal excitations only the normal displacement expressions will be used.

[14] See equation (4.12) on page 68.

§Contour integration

In order to solve the displacement equations (4.21) the residue calculus is applied to evaluate the integrals.
This is possible only when the integrand vanish when $k \to 0$ on the large semicircle enclosing upper half complex plane. However as they stand equations (4.21) do not satisfy this required conditions. Only with aid of the following substitution:

$$\begin{aligned} J_0(z) &= [H_0^{(1)}(z) + H_0^{(1)}(z)(ze^{\mathrm{i}\pi})]/2 \\ J_1(z) &= [H_1^{(1)}(z) + H_1^{(1)}(z)(ze^{\mathrm{i}\pi})]/2 \end{aligned} \tag{4.24}$$

can integrals be transform into one of the two following forms

$$\begin{aligned} I_1 &= \int_{-\infty}^{\infty} \chi_1(k) H_0^{(1)}(kr)\mathrm{d}k \\ I_2 &= \int_{-\infty}^{\infty} \chi_2(k) H_1^{(1)}(kr)\mathrm{d} \end{aligned} \tag{4.25}$$

where $H_{\mathrm{n}}^{(1)}$ represents the Hankel function of $1^{\mathrm{st.}}$ kind of order n, and χ_1 & χ_2 are an odd and even functions of k respectively.
With this replacement contour integration is allowed and the integrands[15] behave as $e^{\mathrm{i}kr}/k^2$, for $kr \gg 1$.
Now, adding residues from the simple pole[16] the following final expression for the displacements is obtained:

$$\begin{aligned} \tilde{u}_{\mathrm{z}}^{\mathrm{s,a}}(r,z) &= \mathrm{i}\frac{\pi}{2\mu}\sum_{k_{\mathrm{s,a}}} Pa\frac{J_1(k_{\mathrm{s,a}}a)}{k_{\mathrm{s,a}}} k_{\mathrm{s,a}} \frac{\Gamma_{\mathrm{zn}}^{\mathrm{s,a}}(k_{\mathrm{s,a}})}{\Delta'_{\mathrm{s,a}}(k_{\mathrm{s,a}})} H_0^{(1)}(k_{\mathrm{s,a}}r) \quad ; \quad r > a \\ \tilde{u}_{\mathrm{r}}^{\mathrm{s,a}}(r,z) &= \mathrm{i}\frac{\pi}{2\mu}\sum_{k_{\mathrm{s,a}}} Pa\frac{J_1(k_{\mathrm{s,a}}a)}{k_{\mathrm{s,a}}} k_{\mathrm{s,a}} \frac{\Gamma_{\mathrm{rn}}^{\mathrm{s,a}}(k_{\mathrm{s,a}})}{\Delta'_{\mathrm{s,a}}(k_{\mathrm{s,a}})} H_1^{(1)}(k_{\mathrm{s,a}}r) \quad ; \quad r > a \end{aligned} \tag{4.26}$$

which can be further resumed in

$$\tilde{u}_{\mathrm{z,r}}^{\mathrm{s,a}}(r,z) = \sum_{k_{\mathrm{s,a}}} u_{\mathrm{z,r}}^{\mathrm{s,a}}(w) e^{\mathrm{i}\varphi(w)} \tag{4.27}$$

with $u_{\mathrm{z,r}}^{\mathrm{s,a}}(w)$ being the modules and $\varphi(w)$ the corresponding phases of plate harmonic vibrations. The terms $\Delta'_{\mathrm{s,a}}$ represent the derivatives of dispersion equations (4.16) with respect to the wavenumber k.

---

[15] The inclusion of the attenuation/leakage effects that are introduce with imaginary parts of $\Im(k)$ roots, ensures that poles are shifted from the negative real axis. Then solutions will correspond only to non-standing outgoing waves.

[16] The roots of the Rayleigh-Lamb equations are all simple poles except when cut-off frequencies are approached ($k \to 0$) then Hankel functions behalf as: $H_0^{(1)} \approx \mathrm{i}\frac{2}{\pi}\log(kr)$ and $H_1^{(1)} \approx \mathrm{i}\frac{2}{\pi}(\frac{2}{kr})$, and singularities may not be simple poles.

On this subject it is important to point out that these *partial* derivatives must be carefully calculated at *constant* frequency for every point on the dispersion plane[17].

4.3.3 Generalization for broadband signals and arbitrary 2D excitations

The generalization for broadband signals is made possible by summation over a finite set of harmonic excitation frequencies (N_f) and by use of the following inverse discrete Fourier transform (IDFT) relationship

$$\bar{\boldsymbol{u}}_\mathrm{z}^\mathrm{s,a}(\boldsymbol{t},\boldsymbol{r},\boldsymbol{z}) = \Re\left\{ \frac{1}{N/2} \sum_{\mathrm{n}=1}^{N_\mathrm{f}} u_\mathrm{z}^\mathrm{s,a}(w_\mathrm{n}) e^{\mathrm{i}\left[k(w_\mathrm{n})r\bar{\boldsymbol{I}} - w_\mathrm{n}\bar{\boldsymbol{t}} - \varphi(w_\mathrm{n})\bar{\boldsymbol{I}}\right]} \right\} \tag{4.28}$$

Here $\bar{\boldsymbol{I}}$ represents the unitary row vector and $\bar{\boldsymbol{t}}$ the time trace vector both of size $(1, N)$.

Then, $\bar{\boldsymbol{u}}_\mathrm{z}^\mathrm{s,a}$ is the final Lamb wave symmetric or anti-symmetric broadband mode time signal[18] at the coordinates (r, z)[19].

We observe from the above expression (4.28) that we implicitly assume that the bandwidth of interest (f_min,$f_\mathrm{max,}$) is segmented into N_f discrete frequencies.

Each contributes with a uniform amplitude spectrum and a corresponding phase in the small frequency band $\Delta w = 2\pi f_\mathrm{s}/N$; where f_s is the time sampling frequency.

Then the total normal broadband displacement $\tilde{\boldsymbol{u}}_\mathrm{z}(\boldsymbol{t},\boldsymbol{r},\boldsymbol{z})$ can be calculated by a sum over an infinite set of Lamb modes by[20]:

$$\tilde{\boldsymbol{u}}_\mathrm{z}(\boldsymbol{t},\boldsymbol{r},\boldsymbol{z}) = \sum_{\mathrm{s,a}} \bar{\boldsymbol{u}}_\mathrm{z}^\mathrm{s,a}(\boldsymbol{t},\boldsymbol{r},\boldsymbol{z}) \tag{4.29}$$

As the total broadband displacement signal for a single circular radiator is computed with the help of Eqs. (4.28) and (4.29) the generalization for an arbitrary pressure distribution is made by use of a 2D strip like approximation of the excitation field. This approach is observed in the following figures 4.3 and 4.4.

---

[17] A summary of analytical and numerical expressions for the calculation of these derivatives as well the $\Gamma_\mathrm{zn,rn}^\mathrm{s,a}$ functions are shown in Appendix C.

[18] Here and in the following the subscript 'r' for radial displacements will no longer be used since they do not affect the radiated field by the plate.

[19] Again because of the excitation symmetry here the independent coordinate θ has not been considered. Then at sufficient distance from the source in the far field ($r > 10\,\xi_\mathrm{max}$) the circular crested Lamb waves behave approximately like a plane wavefront.

[20] In this respect for practical reasons although any Lamb mode can be calculated in principle only the first four modes will be taking into account (A_0, S_0, A_1, S_1).

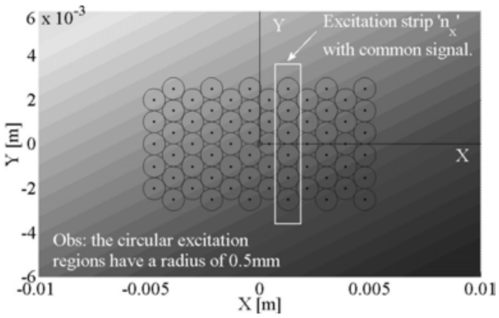

Figure 4.3: Example of an *ideal PW simulation* with a rectangular profile.

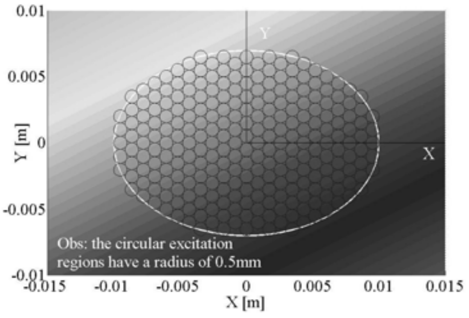

Figure 4.4: View of an *acoustic field excitation* with an elliptical profile.

As is apparent the incident acoustic field is reconstructed by a distribution of a series of parallel *excitation strips* along the Y axis[21].
Then by controlling the size and number of the pressure "points" any excitation acoustic profile can in principle be recreated.
An important aspect in this respect and closely related to computer memory issues[22] is that the software contemplates two possibilities for assigning signals to corresponding circular radiators:

1. The ideal plane wave (PW) simulation.
2. The acoustic field excitation.

The ideal PW simulation is the more simple case since it does not entirely *couple* the emission module[23] to the plate model.
Here each strip along the Y axis has a common and unique signal with fixed amplitude and given delay for all the radiators in the strip.
Then a two dimensional "ideal" finite excitation pattern can be created by a proper superposition of adjoining Y-strips applied to the laminate.

The second alternative, the *acoustic field excitation* (computationally more demanding) couples the emission module to the plate excitation region.
Then each circle on each strip has its unique pressure signal calculated by the acoustic field simulator[24].

---

[21] The distance between the center of circles along the X axis is a fixed value of $x_s = a\sqrt{3}$.

[22] This and other subjects related to memory resource use are discussed in Appendix E.

[23] The acoustic field simulator FIRST, see page 84.

[24] Because the software is not calibrated yet any issues related to the *actual* value of the pressure at a certain point on the surface of the plate are avoided.

§Effect of size of circular regions: the $\mathbf{r}_{\mathbf{atio}}$ parameter

Since the size and number of circular filling elements are completely arbitrary to choose[25] any value in principle could be selected[26].

However, some precautions are necessary so as not to produce undesired interference side effects and loose accuracy during the simulations.

In this aspect the principal variables to bear in mind are: a) the size of circles of radius 'a' and b) the minimum Lamb wavelength in the bandwidth $\xi_{\min} = \frac{c_{\text{ph,min}}}{f_{\max}}$. Both of these can be summed up into the following *ratio* parameter: $r_{\text{atio}} = \frac{2a}{\xi_{\min/2}}$ which measures the reconstruction accuracy of $\xi_{\min}$ in terms of the radius 'a'.

Then by keeping $r_{\text{atio}} \leq 1$, we have at least one circle by each half period of the minimum wavelength[27]. This in turn will help reduce interference effects across the face of circular radiators and maintain intact the high frequency components of the displacements.

To see the effect of this interference figures 4.5 and 4.6 show THS simulations of displacement signals for a single radiator (see fig 4.2) observed at a distance of 100 mm.

As the radius $a^{\uparrow}$ is increased heavy interference takes place on the radiator face and consequently the high part of the spectrum is removed. Therefore an infinite radius radiator will only excite a single frequency while an infinitesimal transducer will produce an infinite input bandwidth.

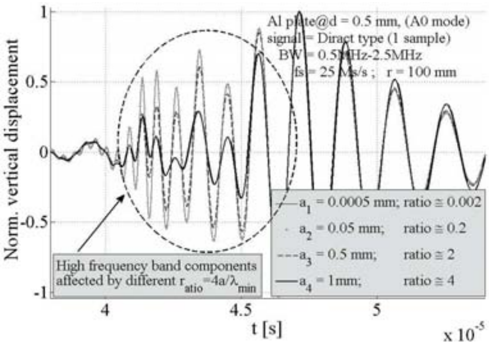

Figure 4.5: Normalised vertical displacements for A_0 mode at 0.1 m produced by a single radiator with different radius a.

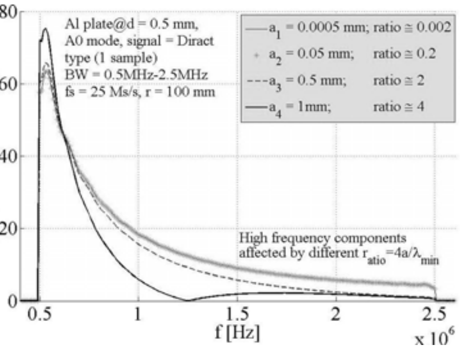

Figure 4.6: Amplitude spectra for signals in Fig. 4.5 with respect to radius and parameter $r_{\text{atio}} = \frac{2a}{\xi_{\min/2}}$, with $\xi_{\min} \approx$ 1 mm.

---

[25] Actually the user can only define the radius 'a' of filling circular elements and the type and size of incident field profile (point, line, rectangular, circular or elliptical). The number of Y-strips and circular regions is calculated automatically.

[26] Some restriction may apply if the user selects incorrect values: e.g. dimensions of excitation region $< a$.

[27] The limit figure of $r_{\text{atio}} = 1$ is an *ad hoc* value, a more typical value could be $r_{\text{atio}} =$ 0.5 or lower depending on number of *points* and computing power. For more details see Appendix E.

For an idea of possible values of ξ_{min}, Table 4.1 shows limits for the usual BW (0.5 MHz – 1.5 MHz) for the 1st four modes in a 3.2 mm Aluminium plate.

Table 4.1: Wavelength values for 1st. four Lamb modes in a 3.2 mm Al plate.

	A0	**S0**	**A1**	**S1**
ξ_{min} [mm]	2.0	2.0	2.8	3.9
ξ_{max} [mm]	5.2	10.4	16.1	10.0

All lengths are above 1 mm. Then if we assume a typical value[28] of e.g. $a = 0.5$ mm all cases will be covered by $r_{\mathrm{atio}} \leq 1$.

4.4 Comparison with other approaches

In this section we present two alternative approaches to the THS method[29] plus a set of comparisons with a finite element method (FEM) simulation programme: COMSOL Multiphysics.
The first approach taken from Ref.[246] uses the same integral transform techniques for a circular excitation region and is completely analogous to the described THS.
The second for a *point* load excitation was derived by Achenbach[5] based an orthogonal modes relationship.

4.4.1 Alternative THS derivation

This method is analogous to section § 4.3.2 for the THS derivation. It uses an similar expressions for finding solutions for plate displacements by expressing them from the start as inverse Fourier integrals and then incorporating the corresponding derivatives into Eq. (4.1).
Following Ref.[246] and after some algebraic steps taking into account boundary conditions (4.2) and solving integrals by residue calculus it is possible to obtain an analogous expression to Eq. (4.28) for the displacements[30]:

$$\bar{\boldsymbol{u}}_{\mathrm{z}}^{\mathrm{s,a}}(\boldsymbol{t}, \boldsymbol{r}, \boldsymbol{z}) = \frac{1}{4} \int_{-\infty}^{\infty} \sum_{k} F^{0} H_{\mathrm{z}}^{\mathrm{s,a}}(d, w) e^{-\mathrm{i}wt} \mathrm{d}w \tag{4.30}$$

---

[28] This will be the default value for most of the simulations throughout this thesis.

[29] For a good review on this subject see the article by Chimenti[47] and also Refs.[203, 235, 283].

[30] Here again the expressions for normal displacements is referred since they solely contribute to plate radiated fields. This is a *continuous* time version of Eq. (4.28).

were[31]

$$H_{\mathrm{z}}^{\mathrm{s}}(d,w) = \frac{\mathrm{i}\tilde{\alpha}(k^2-\tilde{\beta}^2)\sinh(\tilde{\alpha}d)\sinh(\tilde{\beta}d)}{\mu\Delta_{\mathrm{s}}^{'}}\ , \qquad \tilde{\alpha} = \sqrt{k^2 - w^2/\alpha}$$
$$H_{\mathrm{z}}^{\mathrm{a}}(d,w) = \frac{\mathrm{i}\tilde{\alpha}(k^2-\tilde{\beta}^2)\cosh(\tilde{\alpha}d)\cosh(\tilde{\beta}d)}{\mu\Delta_{\mathrm{a}}^{'}}\ , \qquad \tilde{\beta} = \sqrt{k^2 - w^2/\beta} \qquad (4.31)$$

and $F^0(k)$ is given again by equation (4.23).
The sum of equation (4.30) is carried out over a finite set of symmetric or anti-symmetric Lamb modes. As previously mentioned[32] the terms for partial derivatives $\Delta_{\mathrm{s,a}}^{'}$ are calculated with respect to $k|_{w=\mathrm{const.}}$.

4.4.2 Point load excitation

The case of a normal point load[33] in an unbounded isotropic elastic layer was studied in detail by Achenbach[5, 6].
He developed a Lamb mode orthogonality relationship based on a reciprocal identity of time-harmonic elastodynamic states[2, 3]. This procedure helps to determine plate displacements via an alternative solution to the integral transforms previously used.
Here we outline only main expressions since the complete development cover several pages[34].
The normal plate displacements can be expressed in a similar way to equation (4.26), as:

$$u_{\mathrm{z}}^{\mathrm{s,a}}(r,z) = \sum_{k_{\mathrm{s,a}}} C_{\mathrm{z}}^{\mathrm{s,a}}(d/2,z,k_{\mathrm{s,a}}) H_0^{(2)}(k_{\mathrm{s,a}}r) \qquad (4.32)$$

where[35]

$$C_{\mathrm{z}}^{\mathrm{s}}(d/2,z,k_{\mathrm{s,a}}) = D_{\mathrm{z}}^{\mathrm{s}}[s_3\sin(pz) + s_4\sin(qz)]$$
$$C_{\mathrm{z}}^{\mathrm{a}}(d/2,z,k_{\mathrm{s,a}}) = D_{\mathrm{z}}^{\mathrm{a}}[a_3\cos(pz) + a_4\cos(qz)] \qquad (4.33)$$

The reconstruction of the total wideband multi-mode signals for the above models: § 4.4.1 and § 4.4.2 can be accomplish then with help of Eq. (4.29) and equations (4.27- 4.29) respectively. This offers alternative solutions for the propagation toolbox cores[36].

---

[31] Although expressions for $\tilde{\alpha}$,$\tilde{\beta}$, differ only in the imaginary factor 'i' from those in (4.9), we prefer to introduce these new variables to retain equation forms.

[32] See bottom of page 71.

[33] Actually, this is only a mathematical abstraction for an infinitely small excitation region *of area* $\Delta(s)$ on the plate surface.

[34] For more details see Ref.[5].

[35] A summary of the remaining terms is shown in Appendix C.

[36] This is controlled upon user selection. The default propagation engine is the presented THS method, equations (4.26) through (4.29).

A comparison for single mode simulated signals for the presented models is shown in the following figures 4.7 through 4.10, for $A0$ and $S0$ modes.

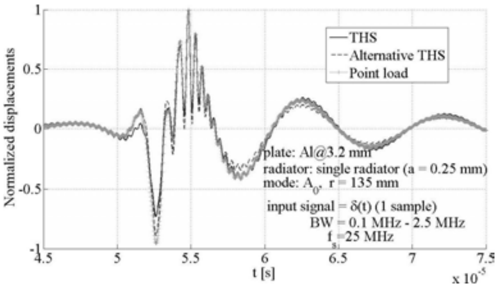

Figure 4.7: Comparison of A_0 mode normalised z-displacements for the three models in an aluminium plate@3.2 mm.

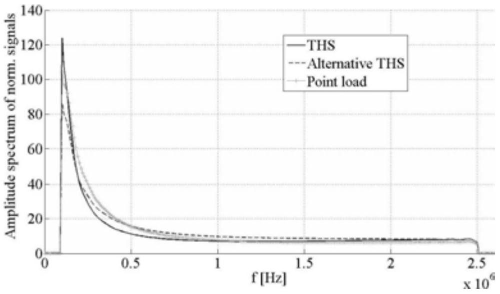

Figure 4.8: Corresponding amplitude spectra of normalised A_0 displacements for three models in Fig. 4.7.

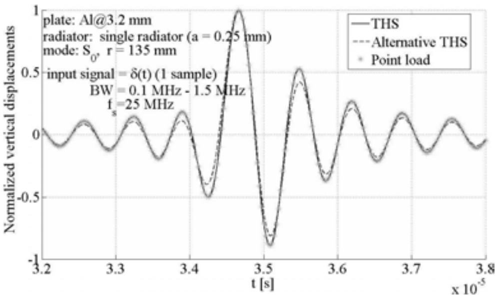

Figure 4.9: Comparison of S_0 mode normalised z-displacements for the three models in an aluminium plate@0.5 mm.

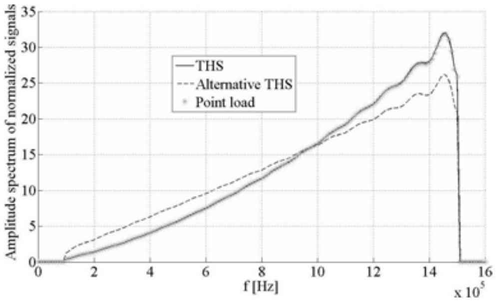

Figure 4.10: Corresponding amplitude spectra of normalised S_0 displacements for three models in Fig. 4.9.

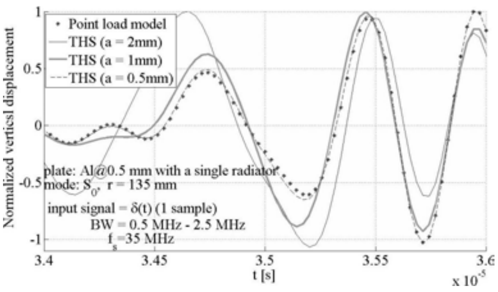

Figure 4.11: Comparison of S_0 mode norm. displacements for *point load* model and THS approach with different radii.

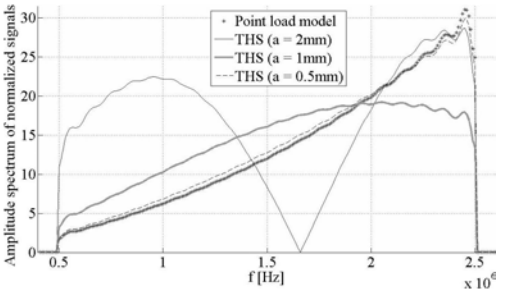

Figure 4.12: Corresponding amplitude spectra of normalised S_0 displacements for models in Fig. 4.11.

As can be observed a fairly coherent agreement is achieved[37]. A comment on the solution to chose for the single circular radiator case is, since the principal THS model and the alternative approach § 4.4.1 are complementary in principle they can be used interchangeably. However computer implementations of both can lead to some differences as can be observed in the figures. This problem has not yet been resolved.

On the other hand *point* load solution is the limit case for THS when $a \to 0$. This phenomenon is observed in figures 4.11 and 4.12, where displacements for three THS signals with decreasing radii are compared against the point load model. As observed the interference effect mentioned in § 4.3.3 is more influential as the radius of the radiator is increased.

4.4.3 Comparisons with FEM simulations

In this section a set of four cases are presented for comparison between the THS method (main core § 4.3.3) and the finite element method (FEM) from the COMSOL Multiphysics package. The normal plate displacements for THS have been changed in scale by a factor of $u_{\mathrm{z}} = 0.065\, u_{\mathrm{z}}^{\mathrm{THS}}$, in order to attain a better graphic match with FEM results.

The COMSOL simulations[38] were calculated for an ideal surround with infinite absorption properties around the *finite plate* (50x50 mm wide) so as not to receive reflections from the edges. This effect is clearly appreciated in the graphs.

In all the figures the results are view along the X axis of the plate with the location of the single circular radiator centre at $x_0 = 16$ mm.

For better adjustment the THS traces were ploted for two slightly different time instants: $t_1 = 3.45$ us, and $t_1 = 3.17$ us respectively[39].

As seen from the first three plots (Figs. 4.13-4.15) the relative matching seems to be more or less satisfactory[40].

However, as the plate width is increased as in Figure 4.16) the difference between the amplitudes unfortunately seems to increase slowly[41].

With the use of Hankel functions in the time harmonic method a singularity in the origin (at $x_0 = 16$mm) of all the figures[42] is observed in all comparisons. This is another reason to calculate the plate vibrations away from the excitation zone in the *far field.*

---

[37] Here normalised displacements have been presented since the amplitudes for the three models differ only by a multiplicative constant among them.

[38] The author would like to express his sincere gratitude to Dr. Bernard Hosten and Dr. Michel Castaings from Laboratoire de Mécanique Physique (LMP) France, for their collaboration and support in the achievement of COMSOL results.

[39] This is because the *instantaneous moment* of the COMSOL data are unknown(?), although it is believed they corresponds to the computer instant $t = 0$.

[40] This is of course including the ad hoc scaling factor $s_{\mathrm{THS}} = 65/1000$. Roughly speaking THS displacements are 15 times grater than COMSOL calculations.

[41] The author acknowledges that this point requires further investigation.

[42] The sign of the THS picks is changed as traces are plotted for different time instants.

A final observation from all the comparisons was the increased loss of phase between traces as the observer moves away from the time origin.
This effect is principally due to a mismatch in Lamb wave phase velocities for both simulation programs probably produced by a slight differences in material parameters of aluminium laminates. This causes THS vibrations to go a little slower than COMSOL waves.

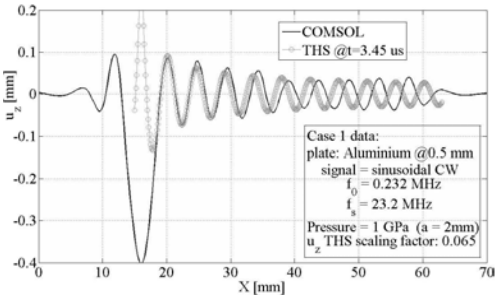

Figure 4.13: Normal displacements in an Al@0.5mm plate produced by a single radiator ($a = 2$mm) excited by a CW signal of $f_0 = 0.232$ MHz.

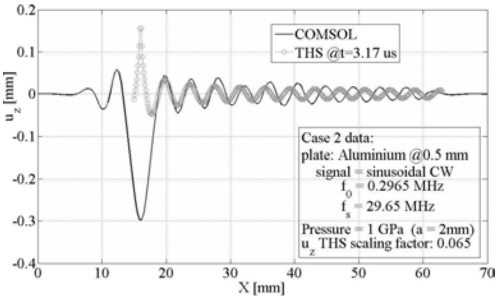

Figure 4.14: Normal displacements in an Al@0.5mm plate produced by a single radiator ($a = 2$mm) excited by a CW signal of $f_0 = 0.2965$ MHz.

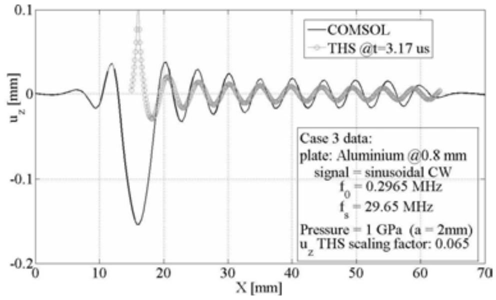

Figure 4.15: Normal displacements for an Al@0.8 mm plate produced by a single radiator ($a = 2$mm) excited by a CW signal of $f_0 = 0.2965$ MHz.

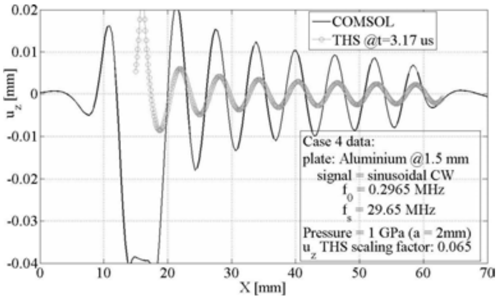

Figure 4.16: Normal displacements for an Al@1.5 mm plate produced by a single radiator ($a = 2$mm) excited by a CW signal of $f_0 = 0.2965$ MHz.

4.5 Comparisons with experimental results

In this section some experimental results are introduce for validation of the THS routines implemented in the LAMB programme. The data are drawn from real impacted aluminium plates by a circular profile colliding tip.
The tests were performed by means of the tail bit from a drill[43] dropped from a known distance above the surface onto a plate.

---

[43] The flat tail part of the drill bit (see Fig. 4.18) has an approximately and uniformly hard circular face: $\text{tip}_{\varnothing} = 1$ mm.

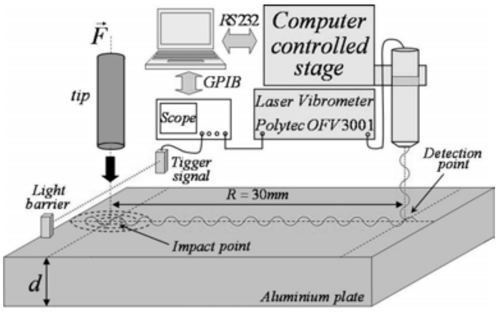

Figure 4.17: Setup for the impact experiment in *Al* plates: $k_{\text{laser}} = 0.025\,(\text{m/s})/\text{V}$.

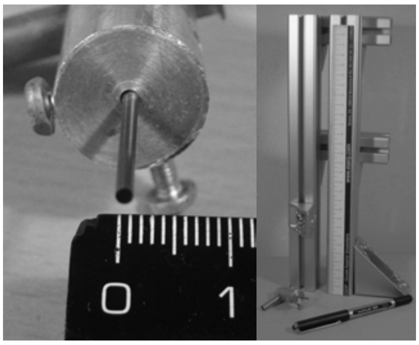

Figure 4.18: Photography of the impact *tip* (tail of a drilling tool bit) plus rail guide.

A laser vibrometer was used for detection of the plate velocity signals (see Fig. 4.17). Three aluminium plates of different widths: $d_1 = 0.3\,\text{mm}$, $d_2 = 0.5\,\text{mm}$ and $d_1 = 0.8\,\text{mm}$ were tested.

In all the experiments the distance[44] to the detection point was fixed to $r = 30\,\text{mm}$ with a velocity detection constant of $k_{\text{laser}} = 0.025\,(\text{m/s})/\text{V}$.

As pointed out before THS displacements were scaled again in order to attain a better match with the experimental data[45].

The following figures 4.19 through 4.22 depict the results.

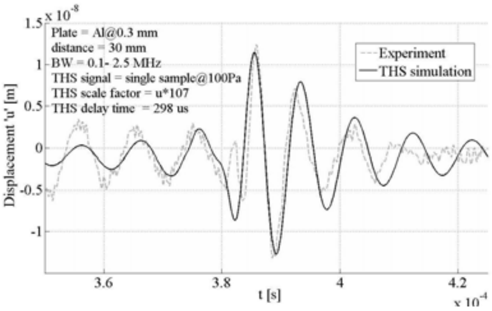

Figure 4.19: Displacement signals for the impact experiment on an *Al*@**0.3** mm plate: $\text{r} = 30\,\text{mm}, \text{tip}_{\varnothing} = 1\,\text{mm}, f_{\text{s}} = 10^8$ Hz.

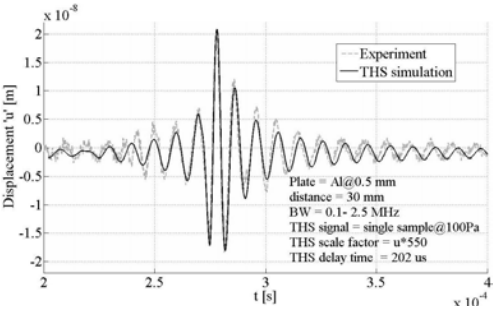

Figure 4.20: Displacement signals for the impact experiment on an *Al*@**0.5** mm plate: $\text{r} = 30\,\text{mm}, \text{tip}_{\varnothing} = 1\,\text{mm}, f_{\text{s}} = 10^8$ Hz.

---

[44] Other test for longer distances were perform with similar results but were omitted due to their increasing poor SNR. This effect can be observed in the Fig. 4.22 note the noisy aspect of the velocity signals detected.

[45] This problem remains unsolved at the moment making the LAMB programme not calibrated.

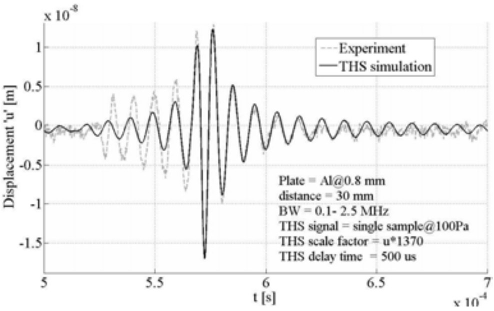

Figure 4.21: Displacement signals for the impact experiment on an Al@**0.8** mm plate: r = 30mm, $\text{tip}_\varnothing = 1$mm, $f_\text{s} = 50$MHz.

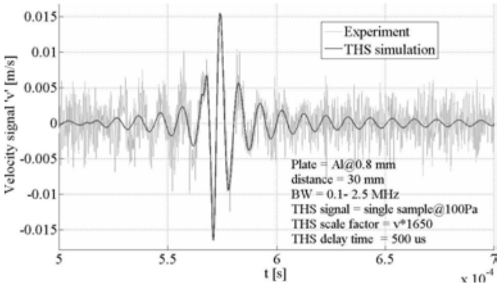

Figure 4.22: Corresponding velocity signals for impact experiment on Al@**0.8**mm plate: r = 30mm, $\text{tip}_\varnothing = 1$mm, $f_\text{s} = 50$MHz.

4.6 Conclusions

The Time Harmonic Solution method or THS had been introduced and developed for the calculation of the normal displacements on an infinite ideal isotropic laminate produced by a single circular radiator.
Three computer models were implemented in this case for the *propagation module* of the LAMB software.
The first two approaches were similar in their mathematical development and in principle interchangeable, while the third was asymptotically convergent when $a \to 0$. This method was derived by Achenbach for a *point* load problem based on the orthogonality relationships of Lamb modes.

The plate excitation of the LAMB programme was implemented by means of a strip filling method for the impact area of the acoustic field.
The filling technique entails a discretization by a series of strips each composed of small circular radiators along the Y axis of the excitation region.
Then by an adequate filling of this area of the plate any two-dimensional profile can be created.
It is important to consider the relationship between the minimum wavelength present during simulations and the size of excitation circular radiators.
This is summarized by the r_atio parameter which should be kept below ratio $r_\text{atio} \leq 1$ in order to avoid any destructive interference effects.
The assignment of signals for each radiator is based on the election of one of the two strategies.
Ones strategy assumes an ideal plane wavefront excitation which employs a common delayed signal for each individual Y strip; while the other possibility performs a full computation of the acoustic field at each desired location on the plate by the emission simulation module FIRST.

With respect to the validation of programmed routines, a group of simulation comparisons between the three propagation engines were presented.
These showed that results among them were in fact very similar although there were still some differences on the scale to resolve.
A set of validation points between the main THS core and the finite element method were also introduced.
These were carried out with help of the COMSOL Multiphysics package in order to evaluate the agreement of the plate vertical displacements with those computed with the implemented THS method.
The results had shown a relatively good match between both simulations although a scaling constant had to be added to allow the comparisons. This ad hoc factor was observed that slightly changed unfortunately, as the plate width is increased.
Nevertheless assuming it remain constant with frequency, the construction of a broadband signal can be formed by superposition of the mode vibrations.
In this respect, the comparison with a simulated FEM broadband excitation is still a point to verify in the future, as well as assessment tests with several radiators acting at the same time.
Also, a smooth increased miss-alignment between spatial phases of THS and FEM traces was observed. This undesired side effect was probably caused by a non-exact match of Lamb wave phase velocities, due to slight differences in material parameter definition of both software.
On other hand, from the experimental point of view, a set of comparisons of broadband THS simulations, against real displacement signals obtained from tip-impacted plates had been presented in order further verify the implemented model.
It was shown that a reasonable match was attained, although a scaling factor have to be introduced again in order to compare results. This is unsolved issue in the programme and makes the software be not calibrated at the moment.

Chapter 5

Description of the software system model

5.1 Introduction

This chapter summarizes previous sections by describing and integrating the constituting modules: 1)Emission, 2)Propagation, and 3)Reception, of the LAMB software; whose internal structure is detailed in Figure 5.1.
The chapter begins with an analysis of each module, highlights the main features and limitations. Special attention is paid to the receiver section since the other two, emission and propagation were previously introduced in Chapters 2 to 4.
The selection of the appropriate size of the plate radiation elements is discussed continued by the description of a simple two-dimensional geometric model for the inclusion of the directivity of the receiving array elements.
Then a brief analysis of array signal processing issues related to the NDE with air-coupled systems is discussed.

The integrity of the complete software model is evaluated then by a set experimental results drawn from a real air-coupled NDE Lamb wave system[77, 299].
The assessment tests include the use of copper and aluminium plates with burst and wideband signals for use with the principal A0 Lamb wave mode[1].
Although the programme is capable of simulating multi point receivers[2], only single point sensors were used during the simulations carried out for the chapter because of the non substantial differences with 2D patterns[3] thus avoiding time consuming calculations.
Finally, a discussion of the use of a concave aperture with simulations for a proposed new air-coupled plane array are presented while main conclusions are outlined at the end of the chapter.

---

[1] Due to limitations in the hardware caused by noise levels and bandwidth in the reception amplifiers and the laser vibrometer the upper Lamb modes S0, A1, etc. could not be detected.

[2] These are individual array sensors modelled by containing more than a single acoustic signal inside their spatial limits. See e.g. Fig. D.5 in Appendix D.

[3] This also applies to the X line type excitation/emission profiles used. For more details see Figs. D.1 and D.2 in App. D.

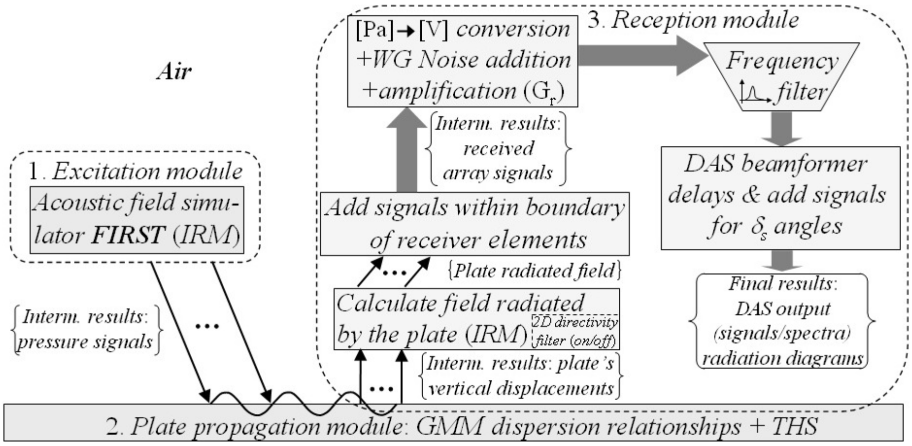

Figure 5.1: Schematic view of the LAMB programme interactive parts.

5.2 The LAMB software constituting parts

5.2.1 Emission module: the acoustic field simulator FIRST

The emission module of the software is represented by the programme FIRST[213] which is based on the impulse response method explained before in Chapter 2.
To comprehend better the operation of programme the following matlab pseudocode illustrates its internal structure:

```
main_first() {
   [first_vars] = f_input_data(user_entry)  % Define programme input data.
[ele_coords,ele_angles,ele_delay,...] = f_def_array(type,Ra,Na,[2a 2b p_e],pos,orient)
[Ps_coords,m,n] = f_cal_field_coords(reg_type,dims,orientation) % On plate surface.
             vn = f_define_velocity_signal(v_type,v_amp,fs,BW)  % For IRM
             an = diff(vn)   % Det. element's surface aceleration signal.
for k=1:Na
  a_k = f_delay_&_apodice(an,ele_delay(k),ele_apodization(k))
  %--------------------------------------------
  % Cal. pressures for array element(k)
  for j=1:m
     for i=1:n
          [x y z] = f_translate_&_rotate(Ps_coords,ele_coords,ele_angles)
  [zone,distance] = f_IRM_zone([x y z],2a,2b); % Determinate IRM-zone of point [x y z]
                A = f_construct_atte_filter(distance,BW,fs)) % BW = frequency bandwidth.
                h = f_impulse_response(t,zone,[2a 2b],[x y z])  % Cal. impulse response.
               Ha = A.*fft(h)   % '.*' -> poin by point vector multiplication.
               ha = real(ifft(Ha))
       Psk(i,j,:) = rho*conv(a_k,ha)  % rho = air density.
     end
  end
  %--------------------------------------------
  Ps = Ps + Psk;
end
Ps_lamb = f_down_sample(Ps,fs,fs_low) % Pass fs >= 100Ms/s -> 20Ms/s for Lamb programme. }
```

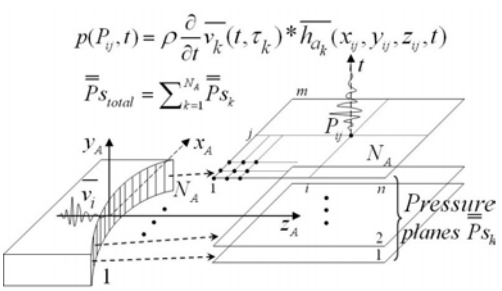

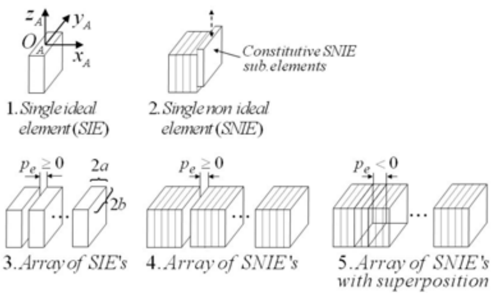

Figure 5.2: Superposition strategy of N_a acoustic *planes* for pressure calc.

Figure 5.3: List of possible acoustic sources simulated with FIRST.

After entering input variables into the programme some function calls take place in order to define the excitation aperture[4], the spatial coordinates of the field being calculated and the type of velocity signal used as excitation[5]. Then the calculation of the plate excitation field is made by means of a superposition of acoustic *planes*[6], one for each aperture element see Fig. 5.2. Here the principal aspects of the programme are: 1) the calculation of the impulse response function $h_\mathrm{a}(x, y, z, t)$ and 2) the determination of the air-attenuation filter $A(\mathrm{i}w)$; both derived previously in § 2.4.3 and § 2.4.4 respectively.

The type of acoustic apertures the programme can handle are basically plane and cylindrically concave 1D arrays composed of two types elements: 1) Single Ideal Element (SIE) and 2) Single Non-Ideal Element (SNIE), see Fig. 5.3.
This last type of emitter was introduced for modelling the broadening effect produced by the air adaptation layers[7].
With respect to the calculation speed and accuracy of the programme in contrast to other software such as Field II and Ultrasim; FIRST is about 6-7 times slower than Field II[8] and agrees well with both[212].

---

[4] This includes: arrays (plane/concave), N_a elements & dims.$\{2a,\ 2b,\ p_\mathrm{e}\}$, apodization & delays profiles (focused beam or PWF gen.@θ^o), and element location & orientation.

[5] Sinusoidal, sinusoidal burst (square/Gauss windowed), square burst (symmetric/anti-symmetric), pulse model, impact model, sinusoidal chirp, Heaviside and Dirac.

[6] This is only an abstraction to designate the associated data matrix to the spatial coordinates (point, line and grid) where the acoustic field is being calculated.

[7] See Figures 2.12, 2.13, Appendix F and Ref.[214].

[8] This test is based on 1000 free runs computing the impulse response function at a certain point. The lower performance is mainly due to C compiled feature of the Field II core (dll) in contrast to the matlab code of FIRST.

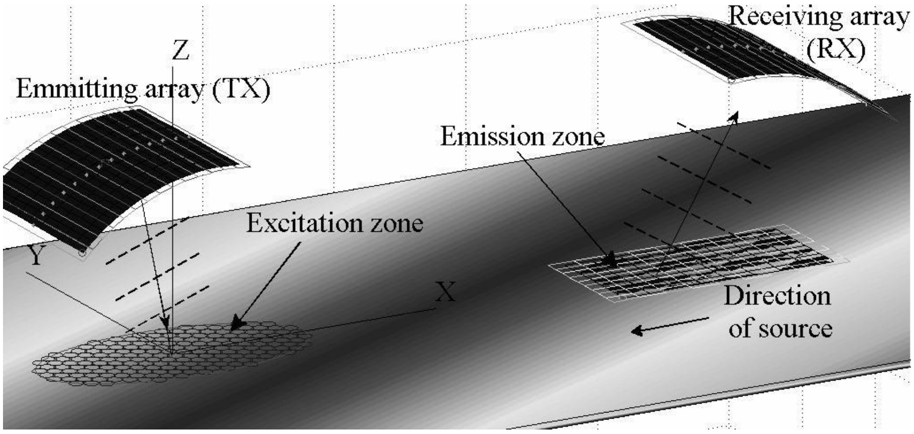

Figure 5.4: View of the LAMB simulated air-coupled NDE system with two concave arrays which indicate the excitation and emission zones on the plate.

In this respect, the intention of the programme was not to compete with excellent software programmes such as Field II and Ultrasim but rather be an open source alternative for the IRM of rectangular apertures[9].

5.2.2 The propagation module

The isotropic plate propagation module of the LAMB software was derived as an extension to the work developed by Pavlakovic *et al.* (1994)[201] for circular radiators and used a linear superposition method (see Figure 5.4). It is principally constituted by: 1) a GMM dispersion curve routine that solves the determinant of Eq. (3.42), and 2) the main core of the THS method developed in Chapter 4, equation (4.21) and equations (C.1-C.11).
In the following matlab pseudocode, once the plate width and type are selected[10], the programme loads pre-stored Lamb dispersion data[11], or calculates new with the GMM code.
Next, the definition of the plate excitation and emission regions take place. Signals and coordinates are assigned or computed depending on whether the acoustic field simulator or the ideal PWF excitation are selected in the excitation zone[12].
Then normal displacements on the plate radiation area are calculated individually from the results of pressure signals in the excitation zone and with

---

[9] The IRM core is a available for free downloading from the author's page on the Matlab Central website: http://www.mathworks.com/matlabcentral/fileexchange/authors/23152

[10] Available materials at present include: aluminium, copper, steel, gold and titanium.

[11] The data contain the dispersion relationships (f, k) for the real frequency and the complex wavenumber respectively.

[12] For more details consult pages 73 and 84.

aid of the dispersion data.
This process is repeated until all the displacement signals are computed.

```
main_propagation() {
 [plate_type,plate_width,a,...] = f_input_vars(first_data,user_entry)
 [f,k] = f_GMM(plate_type,plate_width,...)  % Cal./load plate dispersion data.
 if using_First
    % Use First calculated pressures.
    [e_coords,e_signals,Ne_points] = f_THS_load_excitation()
 else
    % Compute ideal PW excitation.
    [e_coords,e_signals,Ne_points] = f_THS_define_excitation(e_reg_type,e_dims,...)
 end
 [r_coords,Nr_points,...] = f_THS_define_emission(r_reg_type,r_dims,...)

 for j=1:Nr_points
   %-------------------------------------------
   % Sweep excitation field for emission point r(j)
   for i=1:Ne_points
     % Call LAMB main THS core.
       u_i = f_THS_displacement(plate_type,plate_width,a,W,K,e_signals,e_coords,r_coords...)
    U(j,:) = U(j,:) + u_i;  % Acumulate u_i vector in U(j,:) matrix location.
   end
   %-------------------------------------------
 end}
```

5.2.3 The reception module

The purposes of the reception section are: 1) to calculate the plate radiated acoustic field, and 2) emulate the electric signals in the receiver array.
The schematics of the reception module can be appreciated in Figure 5.1.
Once normal displacements are obtained[13] they are added[14], up-sampled[15] and space filtered[16], before the plate radiated field is calculated and further processed in the receiver unit.

§Plate radiated field calculations: size of IRM elements

Before preceding it is important to define the appropriate size of plate emission elements[17] because the coupling between plate vibrations and the final signals *received* is carried out using the impulse response method.
For this point an accurate representation of the displacements (Lamb wave sampling) at first suggest that IRM elements should be as small as possible in order to represent better any Lamb mode present and to avoid aliasing effects.

---

[13] The simulated mode displacements in module 2 can be view and analysed separately.

[14] This process detects and adds the signals “located” inside the sensor boundaries of a simulated multi-point receiver.

[15] Normal THS sampling rates are $f_{\mathrm{s}}^{\mathrm{THS}} \leq 20\,\mathrm{MHz}$, while IRM needs $f_{\mathrm{s}}^{\mathrm{IRM}} \geq 100\,\mathrm{MHz}$.

[16] The effect of the directivity filter is explained next in page 88.

[17] These are rectangular elements of dimensions $[2a_{\mathrm{r}}, 2b_{\mathrm{r}}]$

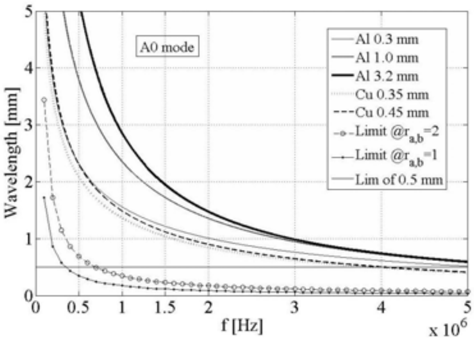

Figure 5.5: A0 mode wavelength curves showing $r_{\mathrm{a,b}}$ & 0.5 mm limits.

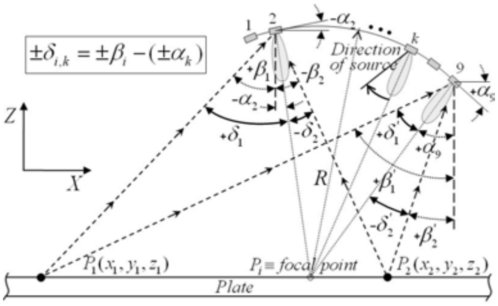

Figure 5.6: Geometric view of the 2D model for 9 element cylindrical array.

This happens when the element dimensions exceed the limit value of $\xi_{\mathrm{min}}^{\mathrm{Lamb}}/2$. However, as pointed out in § 2.4.5, the radiation parameters of any rectangular element requires that dimensions should be grater than $\xi_{\mathrm{max}}^{\mathrm{air}}/2$ in order to maintain the radiation condition $r_{\mathrm{a,b}} \geq 1$.
These opposing requirements can better be observed in the following figure 5.5 where different wavelength curves for some plates with the A0 mode are shown together with the radiation limit conditions $r_{\mathrm{a,b}} = 2$ and $r_{\mathrm{a,b}} = 1$.

It is clear that this problem requires a solution compromising both conditions. So a value that fulfils both requirements was adopted for the simulations carried out in this thesis is. This value is: $[2a_{\mathrm{r}}, 2b_{\mathrm{r}}] = 0.5\,\mathrm{mm}$ indicated by the horizontal line in the figure[18].
With these values Lamb wavelengths are sampled at least $2-4$ times in the bandwidth even under the worst conditions i.e. using copper $d = 0.35\,\mathrm{mm}$[19].

§Plate radiation field calculations: 2D directivity filter model

An important effect to consider when modelling an array aperture apart from the number of elements, their geometrical arrangement and sensitivity frequency response, is the associate directivity of its sensors.
This is a characteristic closely related with the geometry of the array since only a *punctual* receiver would have an ideal omni directional response[133, 219].
In the case of the present work aimed at the simulation of an air-coupled NDE system based on arrays composed of rectangular transducers, the inclusion of the directivity of the real sensors is a point strongly required.

---

[18] Depending on the emission/reception field complexities other values could be 0.40 mm or 0.25 mm. These may require more time or computing resources, see Appendix E.

[19] For other Lamb modes this restriction if even less significant consult Appendix B.

However this is not simple to achieve[20] but it is crucial for the correct simulation of the final aperture.

The proposed model acts as a two-dimensional *directional* filter $A_{\text{dir.}}(\text{i}w, \delta)$ for the field radiated by the plate and is included during the IRM calculations, see Fig. 5.1.
It is defined for plane and cylindrical concave arrays based on geometrical considerations of the XZ plane and simulations of the field emitted by a sinusoidal excited rectangular source.
These simulations are based on the assumption that reciprocity of the emission/receiving characteristics of an aperture are at a defined distance[21].
Figure 5.6 shows the geometric analysis for a 9 element cylindrical concave array which receives the field emitted by two plate radiators.
The incoming angle[22] $\delta_{i,k}$ to the directivity pattern is determined then by the expression:

$$\pm\delta_{i,k} = \pm\beta_i - (\pm\alpha_k) \tag{5.1}$$

This angle is used as entry point for the energy radiation pattern of Figure 5.7 to obtain the filter response by taking its square root i.e. $A^{+}_{\text{dir.}} = \sqrt{\mathcal{E}(f^{+}, \delta)}$. See the white line in the figure[23]. Next the filter response is applied to the impulse response function h_a in a similar manner to Eq. (2.32) by:

$$h(x, y, z, t) = \frac{1}{2\pi} \int_{-\inf}^{\inf} A_{\text{atte.}}(\text{i}w) A_{\text{dir.}}(\text{i}w) H(\text{i}w) e^{\text{i}wt} \text{d}w \tag{5.2}$$

This process is repeated for every plate radiator(i) and sensor(k) pair[24].
The pattern in Figure 5.7 was generated by the FIRST programme simulating a rectangular source (width, height = [2, 15] mm) with a sinusoidal excitation.
This pattern shows the energy of signals at points with a common distance of $R = 35$ mm which lie on a cross sectional plane in front the face of the radiator[25].
This R distance matches the radius of the array and was chosen as a compromised value because the radiation characteristic changes slowly in space.

---

[20] In fact each array element is made of two piezoelectric twin bars electrically connected. See for example Fig. 5.20.

[21] The directional radiation response of an individual element of the cylindrical concave array can be observed in Appendix F

[22] Positive angles δ are measured towards *direction of the source.* The *egg* like lobes in the figure are meant to imitate the directivity pattern associated to the individual sensors.

[23] The final values used are in fact an interpolation of $\sqrt{\mathcal{E}(f, \delta)}$.

[24] Here a spherical wavefront is assumed as coming from each radiator on the plate.

[25] The image was generated in angle and frequency steps of: $\Delta_\delta = 0.5^\circ$ & $\Delta_f = 10$ kHz.

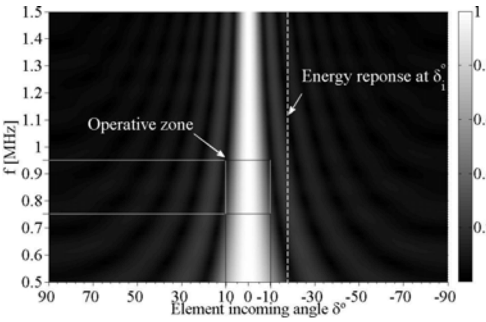

Figure 5.7: Normalized energy pattern $\mathcal{E}(f, \delta)$ for a rectangular SIE source: $2a = 2\text{mm}, 2b = 15\text{mm}$ with sinusoidal excitation and no attenuation $@R = 35\text{mm}$.

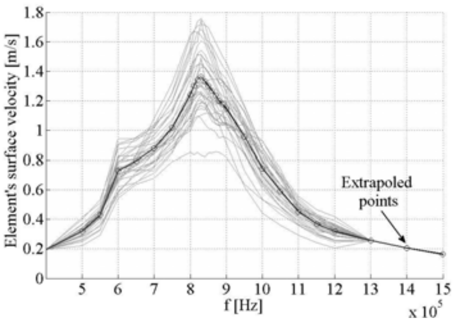

Figure 5.8: Sensitivity response in frequency of the 32 concave array elements. The dark line indicates the average response & test points.

An enhanced width of $2a = 2$ mm was used for the emulated array sensors[26] in Fig. 5.6 although "real" elements are approximately 1 mm wide, see Fig. 5.20. This is because this value is the best that matches[27] the experimental pattern produced by interaction of adaptation layers[214].

An important conclusion suggested by this elementary model is the poor omni directional characteristic that the real receiver sensors has.
Note the small operative zone in Fig. 5.7 from $-10^o \leq \delta \leq 10^o$. This will have an important effect on the *beamforming* performance of a real array transducer which detects incoming fields because the directivity of its sensors is already set[28].

§Addition, coupling and filtering of the received signals

After the plate radiated field is calculated in the receiver zone with IRM[29], the signals detected inside boundaries of each array element are added and changed from pressure to velocity with use of the following expression[30]

$$v = \frac{p}{Z_{\text{air}}} \tag{5.3}$$

Then the velocity signals are converted to electrical potentials using the conversion factor $k_{\text{r}} = 32.58\,\text{V}/(\text{m/s})$.

---

[26] Although the availability of a more accurate array element model (SNIE) the SIE approach was used for the emitter pattern of Fig. 5.7 due its simplicity and uniform surface behaviour. For details on the directivity response of SIE/SNIE models see Appendix F.

[27] Other $\mathcal{E}$ pattern simulations has been tested also for sources of $2a =$ 1-2.5 mm in steps of 0.5 mm.

[28] The global concave geometry contributes also to this phenomenon.

[29] The user may wish to include or not the spatial filter $A_{\text{dir.}}(\text{i}w, \delta)$ in the calculations.

[30] The value of the characteristic acoustic impedance for air at 20°C is $Z_{\text{air}} \cong 427$ Rayls.

This transducer value was determined from the maximum peak[31] of the average sensitivity frequency response[32] of the array elements, see Figure 5.8. This average response is normalized and used to further filter the simulated received signals. This process completes the receiver aperture *black box* model.

§Addition of signal processing: DAS beamforming

The main idea of using an array of sensors to detect signals is that this device boasts the inherit capability of distinguishing and separating fields arriving from different directions, something opposed to what occurs in a continuous aperture. However in order to perform this task an *ideal* receiver array must previously satisfy some requirements like:[33]

- Omni directional (*punctual*) narrowband sensors[34].
- Separation distance between sensors $d_{\mathrm{e}} \leq \xi/2$ (avoid spatial aliasing).
- Wider aperture size (contribute to thinner beampatterns).
- Sensor & electronics with high sensitivity and low noise (high SNR).

Nevertheless in the reality these restrictions are relaxed due mainly to hardware limitations and the particular application at hand.
In the case of the present work which involves the simulation of an ideal air-coupled array based NDE system with Lamb waves the following added difficulties are encountered:

- Inherit directivity of array sensors[35] (response between $-10^{\mathrm{o}} \leq \delta \leq 10^{\mathrm{o}}$).
- High attenuation of ultrasound in air with the frequency, specially if $f > 1\,\mathrm{MHz}$. See Figure 2.7.
- Extremely low amplitudes of Lamb vibrations (apart from A0 mode, see Fig. 5.28). The use of signal averages is common practice.
- Noise & interference in the receiver electronics (e.g. AM radio band).
- Possible need of wideband signals[36] and transducers[37].

---

[31] Near $f \approx 830\,\mathrm{kHz}$, see figure 5.8.

[32] For this measurement the setup of Fig. 2.10 was used in conjunction with a variable frequency sinusoidal tone burst @44.37 $\hat{\mathrm{V}}$, 100 cycles.

[33] This constraints are however highly application dependable.

[34] This is based on the narrowband assumption of signals which is satisfied when the *fractional bandwidth* $\bar{BW} = \frac{BW}{f_0} << 1$. This avoids the occurrence of a phenomenon known as *dispersion* in the array[164].

[35] The array geometry & the distance d_{e} is also an important issue discuss later in § 5.3.2

[36] Typical signals presented in this thesis do not fulfill the narrowband assumption $\bar{BW} << 1$, i.e. $\bar{BW} = \frac{0.2\,\mathrm{MHz}}{0.83\,\mathrm{MHz}} \cong 0.241$, see Fig. 5.8 with transducers response.

[37] Even if inspection signals are narrowband, for NDE spectrum analysis require transducers to respond in wideband of frequencies.

All of these technical aspects contribute to make the task of collecting and analysing the received information very complex.
However without entering into to the field of signal processing, which is not the subject of this thesis, the first step is to implement a simple DAS or Delay And Sum beamformer to help identify plate radiated fields.
This beamformer works by aligning the impinging signal in phase at each array sensor. It uses a corresponding delay $t_\mathrm{d}(\delta_\mathrm{s})$ which depends on the steering angle δ_s.
This method allows for a coherently addition of the signals at the DAS output and is also known as a *spatial matched filter*[164] with a SNR of:

$$\mathrm{SNR} = N_\mathrm{a}\,\mathrm{SNR}_\mathrm{ele} \tag{5.4}$$

Where N_a is the array number of sensors and $\mathrm{SNR}_\mathrm{ele}$ is the signal-to-noise ratio at a single sensor element.
This beamformer has been implemented in the last part of the reception section (see Fig. 5.1) and being used to analyse the plate emitted fields.

5.3 LAMB: programme simulations and results

5.3.1 Experimental results

This section introduces the experimental results made to validate the complete LAMB programme.
These include the following tests: 1)a sweep in frequency with a single receiver sensor in $d = 0.35\,\mathrm{mm}$ copper plate, 2)narrowband signals in $d = 0.5\,\mathrm{mm}$ aluminium laminate with a receiver array and 3)wideband signals in $d = 1.0\,\mathrm{mm}$ aluminium plate also with a receiver array.
Is is important to highlight that because the software is not calibrated, the presented comparisons have been scaled to obtain an appropriate match in the graphics.

§Experimental and simulation setups

The following Figures 5.9 and 5.10 show details of the measurement setup composed of a 16 element plane array used for the excitation[38] (left in Fig. 5.9), and a 32 element concave aperture used as a receiver (right in Fig. 5.9).
The metal plate was vertically located at an equidistant space between both transducers.
The source of emission was appropriately oriented with a goniometer and excited by a common signal (all elements in parallel) coming from a signal generator ($\hat{V_\mathrm{in}} = 3.5\,\mathrm{V_p}$) and a power amplifier with a voltage gain[39] of $V_\mathrm{g} = \times 50$.

---

[38] Unfortunately due to failure of the other concave array only 1 transducer was available.

[39] Except for the last test with Al@1 mm commented later on page 97.

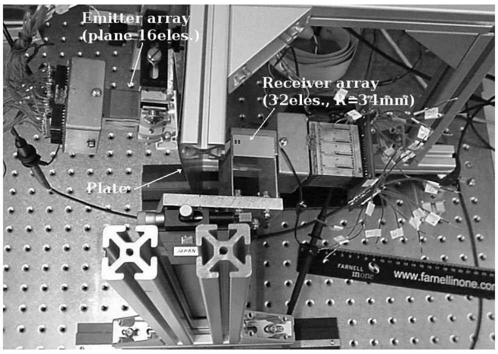

Figure 5.9: View of exp. setup. Left a 16 eles. plane array (*excitation*). Right a 32 eles. concave aperture (*receptor*).

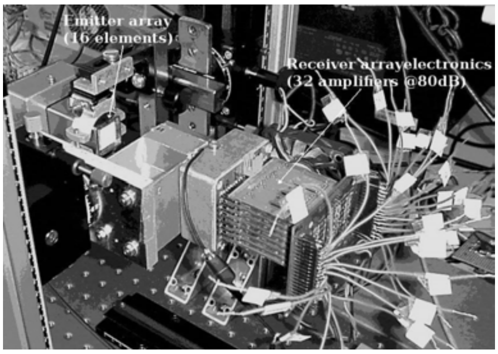

Figure 5.10: Back view of the concave array with the reception electronics: 4x8, 2-stage amplifiers @$G_v = 40\text{dB}+40\text{dB}$.

The concave receiver was connected to 32 channels with two-stage amplifiers each with a gain of $G_v = 80\,\text{dB}$. The signals were then selectively extracted with a 4 channel scope. It is important to mention that due to the array geometry only 14 sensors were actually used ($9 - 22$) and their final traces proceed from an averaging process[40].
Both apertures were correctly pointed towards the plate with the same *incidence/reception* angles θ and a common focal distance of $D_\text{f} = 35\,\text{mm}$.
For the aluminium plates the distance between focal points on the laminate surface[41] was of $r = 70\,\text{mm}$ while for copper it was of $r = 40\,\text{mm}$.
On the other hand the simulation setup was composed of a 16 SIE element plane array for the excitation and single point aperture for the receptor.
The excitation/emission zones of the plate were modelled by single *line* profiles (along X axis) with the following parameters[42]:

- Incidence & reception angles: $\theta_\text{i} = \theta_\text{r} = \theta$
- Focal distances: $D_\text{fi} = D_\text{fr} = D_\text{f} = 35\,\text{mm}$.
- Excitation zone: X axis line 20 mm long, $a = 0.5\,\text{mm}$ (see Fig. 5.23).
- Emission zone: X line 50mm & 100mm, $[2a_\text{r}, 2b_\text{r}] = 0.5\text{mm}$ (see Fig. 5.24).
- Maximum plate excitation pressure: $p_\text{max} = 1\text{Pa}$ (Normalized condition[43]).
- Excitation array: plane, 16 SIE rectangular emitters $\{2a, 2b, p\} = \{2, 15, 0\}\text{mm}$.
- Concave receiver: composed of *punctual* receivers $(1/8/10, R = 35\text{mm}, A_\text{dir} = \text{ on})$.

---

[40] Signals were averaged 100 times @$f_\text{s} = 50\,\text{MS/s}$, with a Lecroy Waverunner 2000.

[41] Some other test for other distances (90 mm and 100 mm) were performed with similar results but with less SNR.

[42] Because no significant difference was observed with multi-point receivers these were disregarded. The same can be applied with respect to the use of time consuming 2D plate profiles. More details in Appendix D.

[43] Because the programme is not calibrated this value was set for all simulations.

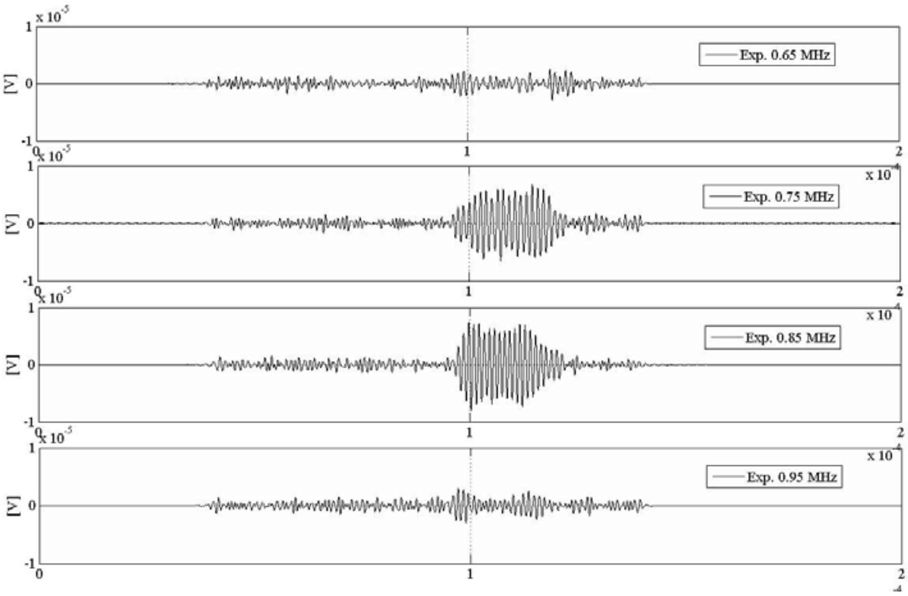

Figure 5.11: Measured signals with channel 16 for 0.35 mm copper plate.

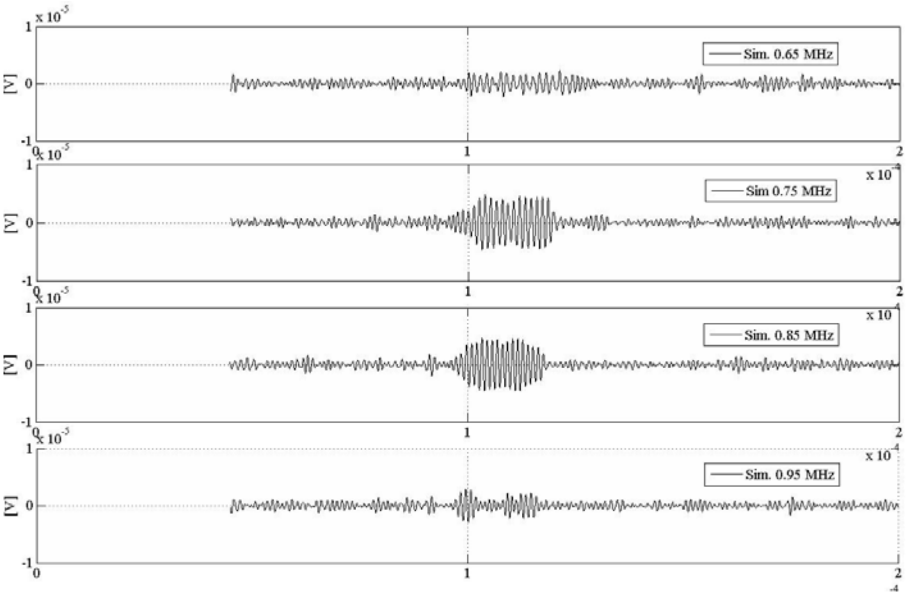

Figure 5.12: LAMB programme simulations for copper plate with a single sensor $G_\mathrm{r} = 17\,\mathrm{dB}$, $\sigma_\mathrm{n}^2 = 1\,\mathrm{pW}$. A custom delay of $\Delta t = 152.3\,\mathrm{us}$ was added for alignment.

§$1^{\text{st.}}$ test: frequency sweep with a single receiver sensor in Cu plate

The first test was carried out on a copper plate of $d = 0.35$ mm. Here a variable frequency sinusoidal burst of 15 cycles was used for the excitation with an incidence angle of $\theta \cong 15.8^{\circ}$.
The received signals were captured only with the central element of the concave array (channel 16).
Figures 5.11 and 5.12 shows respectively the experimental and simulated signals for the four tested frequencies: 650, 750, 850 and 950 kHz.
It is clearly observed how main contributions come from signals near the central frequency in the bandwidth around $f \cong 830$ kHz, see Fig. 5.8.
Then if the plate scans are required to be within a wideband of frequencies, the relationship between the amplitudes of the signals must be taken into account. Regarding the matching of the figures a reasonable degree of similarity was obtained.
In this subject two points are critical for the correct modelling: 1) the exactitude of the plate dispersion relationships (f, k) and 2) the noise model and level selected. The last of these effects is represented here by the addition of a simple Gaussian process[44] with $\sigma_{\mathrm{n}}^2 = 1$ pW.

§$2^{\text{nd.}}$ test: narrowband signals in an aluminium laminate

The next experiment was performed on a aluminium plate of $d = 0.5$ mm applying the same excitation: a rectangular windowed sinusoidal burst with $f_0 = 800$ kHz with 15 cycles and incidence/reception angles $\theta \cong 12^{\circ}$.
The received signals were captured this time with the array channels $9 - 22$.
The following Figures 5.13 and 5.14 depict the respective measured and simulated traces for the concave receiver array.

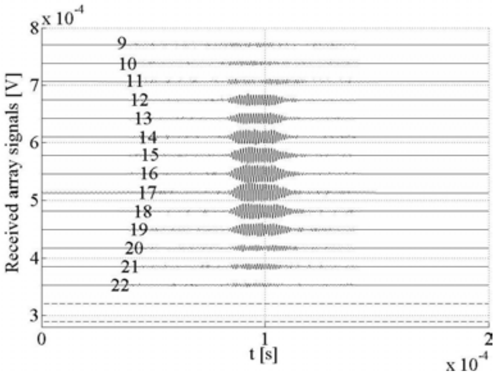

Figure 5.13: Measured signals in *Al* from concave array with channels 9–22.

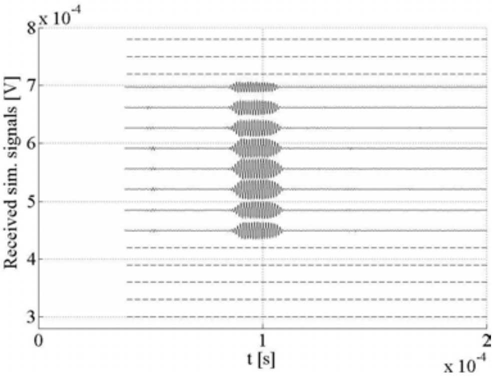

Figure 5.14: Simulated traces for the concave receiver: $G_{\mathrm{r}} = 17$ dB, $\sigma_{\mathrm{n}}^2 = 1$ pW.

---

[44] Because this might required a more complex treatment that includes dependences on the *real* receiver electronics and *present* interference it had been left as a future addition.

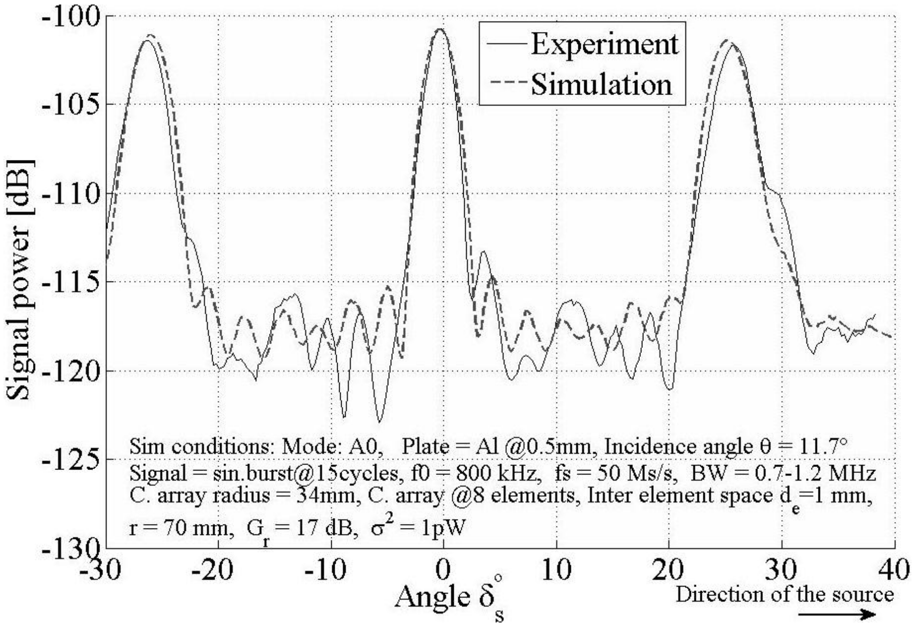

Figure 5.15: Radiation diagrams for the $d = 0.5$ mm aluminium plate with $G_{\mathrm{r}} = 17$dB, $\sigma_{\mathrm{n}}^2 = 1$pW. The maximum main lobe occurs approx. at $\theta_{\mathrm{r}} \approx 11.7^{\mathrm{o}}$.

As observed the signals decrease in amplitude as one moves away the center of the array near channel 16. This phenomenon is more pronounced in the experiment (Fig. 5.13) than in the simulation[45] and is provoked by the combined effects of receiver geometry and directivity of the elements.

Next, by properly delaying and adding signals for a range of δ_{s} input angles with the DAS beamformer the corresponding array steered response or radiation diagram can be obtained for the experiment and simulation, see Fig. 5.15.

Note the aperture grating lobes near $\pm 25^{\mathrm{o}}$ produced by aliasing effect when the inter-element space condition $d_{\mathrm{e}} \leq \xi/2$ is not respected[46].

The agreement of the diagrams were achieved not without difficulties because many aspects influence the patterns. The main factor is the added *noise+interference* model and level used.

This not only provoke changes in the diagrams but also decreases the difference between the main lobe and the sidelobes when the noise power σ_{n}^2 is increased.

Nevertheless a moderate similarity between the simulations and the experimental results was obtained[47].

---

[45] This is an issue still not solved in the model and because of this only 8 channels were used in the simulations.

[46] This also happens when elements are side by side i.e. with $p_{\mathrm{e}} = 0$, but their width $2a > \xi/2$. For further details see § 5.3.2.

[47] For the appropriate matching of all radiation diagrams a custom level in dB was added to the simulated patterns. These were in all cases below $level < 10\,dB$.

§3$^{\text{rd.}}$ test: wideband signals in an aluminium plate

The last test was for a $d = 1.0$mm aluminium plate with an incidence/reception angle of $\theta \cong 9^{\text{o}}$.

The excitation of the plane array 16 elements was a single cycle square pulse of $\hat{V_{\text{in}}} = 500\,\text{V}_{\text{p}}$, $f_0 \approx 750\,\text{kHz}$. The captured signals were again extracted from the concave array channels $9 - 22$.

An alternative set of two-stage $G_v = 80$ dB amplifiers was used this time for the receiver.

The levels in the gain factor G_{r} and noise level were adjusted to suit the new group of signal amplifiers. While the DAS measured and simulated patterns can be observed in the next Figure 5.16.

The output of the DAS beamformer for the plane wavefront (PWF) and focused conditions are shown in corresponding Figures 5.17 and 5.18.

The gain in SNR is clearly appreciated when using the array PWF conformation instead of the focused technique. However the focused technique should not be abandoned if improved signal processing methods are used[266, 267].

Another observation is the increased amplitude of the focused simulated signal in comparison to the experimental trace.

This is again a side effect of the problem commented on page 96 which refers to the programme elementary directivity model.

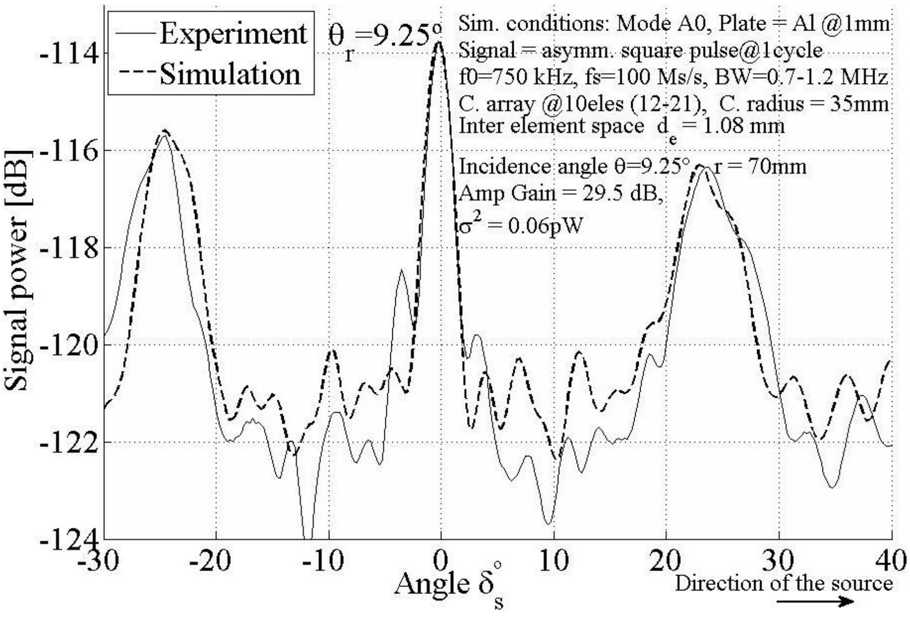

Figure 5.16: Radiation diagrams for the $d = 1$ mm Al plate were $G_{\text{r}} = 29.5$ dB, $\sigma_{\text{n}}^2 = 0.06$ pW. The maximum main lobe occurs approximately at $\theta_{\text{r}} \approx 9.25^{\text{o}}$.

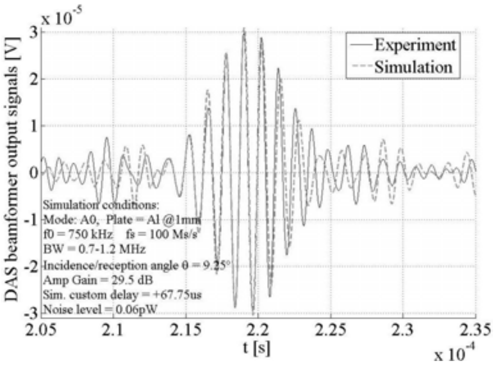

Figure 5.17: Measured and simulated PWF signals from DAS output @$\delta_{\mathrm{s}} = 0^{\mathrm{o}}$

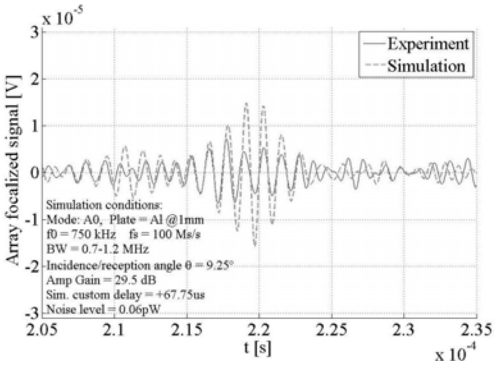

Figure 5.18: Measured and simulated *focused* signals from DAS at $\delta_{\mathrm{s}} = 0^{\mathrm{o}}$.

5.3.2 The air-coupled concave arrays

This section introduces and briefly discuss the characteristics of the air-coupled concave apertures used in an NDT system with Lamb waves[77, 299]. Figures 5.19 and 5.20 shows images of one of the 32 element concave arrays that integrate a developed NDE system used during the tests of the LAMB software[48].

The arrays are basically composed of 64 piezoelectric slabs arranged in a cylindrical shape with a radius of $R \cong 35\,\mathrm{mm}$.

The bars are connected by pairs forming 32 twin sensors with the frequency response shown in Figure 5.8. The dimensions of the bars are: $\hat{2a} = 0.3\mathrm{mm}, \hat{2b} = 15\,\mathrm{mm}$ and $\hat{p_{\mathrm{e}}} = 0.2\,\mathrm{mm}$ for width, height, and inter-element space respectively. This configuration results in the following approximate size of *final* receivers: $\{2a \approx 1\,\mathrm{mm}, 2b = 15\,\mathrm{mm}, \text{and } p_{\mathrm{e}} \approx 0\,\mathrm{mm}\} \Rightarrow d_{\mathrm{e}} \approx 1\,\mathrm{mm}$.

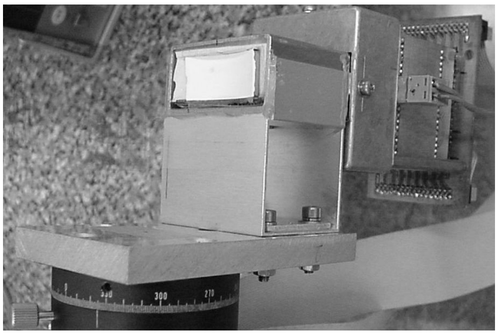

Figure 5.19: Photo a cylindrically concave array with the air-adaptation layers ($N_a = 32\,\mathrm{eles}, R \approx 35\,\mathrm{mm}$).

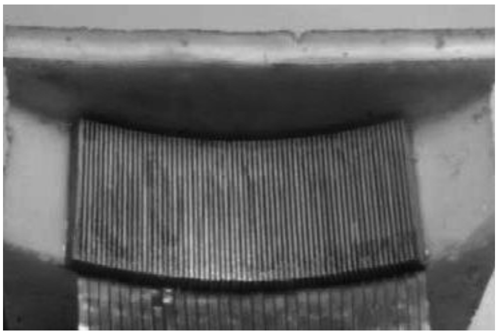

Figure 5.20: View of internal 64 piezoelectric slabs forming 32 twin elements $\{2a = 0.3\,\mathrm{mm}, 2b = 15\,\mathrm{mm}, p_{\mathrm{e}} = 0.2\,\mathrm{mm}\}$.

---

[48] For more details consult Refs.[178]

The main purpose of the concave design is to maintain the impact point fixed while the scan of the plate is performed without any mechanical rotation of the transducer. This is done by switching different sub-array sets in the aperture when the plate is insonified.

In this aspect this strategy has advantages respect other geometries because it is capable of focusing on a region with different focal depths[48, 104, 114]. The grouping scheme into twin elements was used to avoid lateral vibration modes in the piezoceramic slabs and to increased only thickness mode vibrations.

However because the spatial aliasing condition $d_\mathrm{e} > \xi^{\mathrm{air}}/2$ is not fulfilled[49] the array beampatterns showed in 5.21:P1 present the typical grating lobes[50] near ±25°and ± 65° [147, 164].

Figure 5.21 depicts also beampatterns[51] for plane arrays with $d_\mathrm{e} = \xi_0/2$ (P2) and $d_\mathrm{e} = 0.4\,\mathrm{mm}$ (P3), containing $N_\mathrm{a} = 40$, and $N_\mathrm{a} = 48$ elements respectively. In the last example the sidelobes are decreased due to the use a Hamming window creating tapering in the array[52].

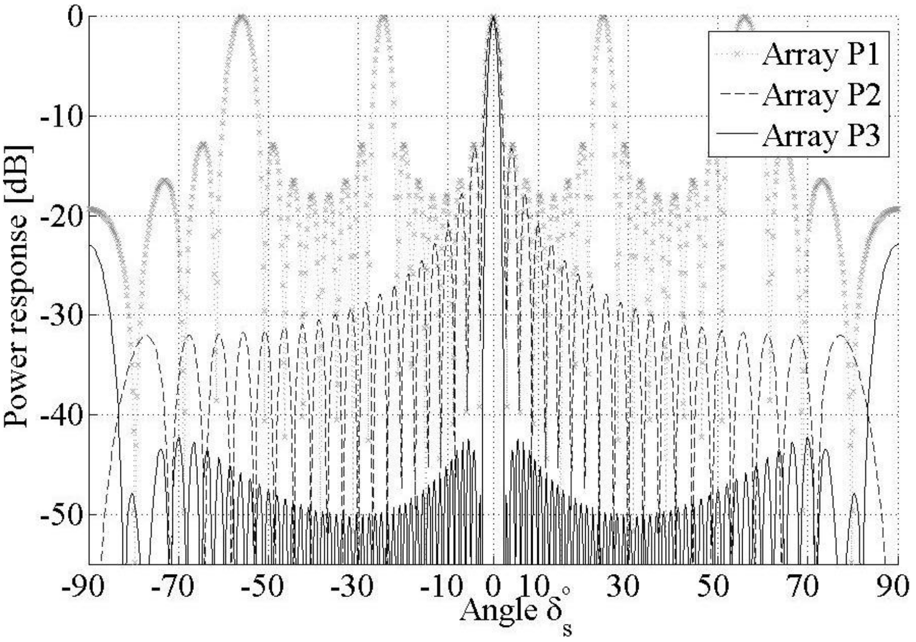

Figure 5.21: Beampatterns for different *ideal* plane (P) arrays @$f_0 = 830\,\mathrm{kHz}$: $P1\{N_a = 8\mathrm{eles.}, d = 1\mathrm{mm}\}, P2\{N_a = 40\mathrm{eles.}, d = \xi_0/2\}$ & $P3\{N_a = 48^{\mathrm{taper}}_{\mathrm{eles.}}, d = 0.4\mathrm{mm}\}$.

---

[49] In this case at $f_0 = 0.83\,\mathrm{MHz} \Rightarrow \xi_0^{\mathrm{air}} \cong 0.414\,\mathrm{mm}$, see also Table 2.3.

[50] The P1 beampattern shown in the figure does not actually correspond to a concave transducer, however with fewer elements ($N_a \leq 8$) the concavity is low and the pattern can be approximated by those of an easily calculated *ideal* plane array.

[51] Beampatterns should not be confused with the array *steered response* to a set of signals.

[52] Unfortunately this method also increase the width of the main lobe a little.

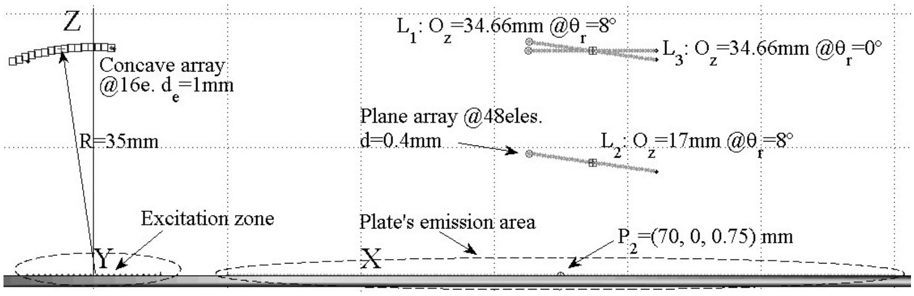

Figure 5.22: Side view of the programme simulation scenario indicating the excitation and emission zones with different receiver arrangements.

Finally we note how a wider aperture reduces the width of the main lobes which increases the resolution.
In this matter the concave silhouette represents a limitation because of the combined effect of their inherent geometry and the directivity of the sensors, see Fig. 5.6.

5.3.3 Simulations for a proposed new plane array

This section introduces a group simulations[53]. for a proposed air-coupled plane receiver composed of 48 sensors with the following dimensions $\{2a, 2b, p_\mathrm{e}\} = \{0.4, 15, 0\}$ mm.
This new design was selected among other alternatives between a wider aperture width[54] ($l_A \uparrow$) and a diminished aliasing effect condition $d_\mathrm{e} \to \xi/2$.
The simulations presented were made for a $d = 1.5$mm aluminium plate under ideal conditions ($\sigma_\mathrm{n}^2 = 0$) with different receiver arrangements: $L_1, L2$ & L_3 (see Figure 5.22).
The individual aperture sensors were emulated using ideal *point* receivers[55] either with or without the directivity filter effect ($A_\mathrm{dir.}$) presented in §5.2.3.
The emitter used in all cases was a concave array ($R = 35\,\mathrm{mm}$) made up of 16 SIE emitters $\{2a, 2b, p_\mathrm{e}\} = \{1, 15, 0\}\,\mathrm{mm}$, excited by a 1 cycle symmetric square wave with $f_0 = 830\,\mathrm{kHz}$.
The distance between focal points on the plate was $r = 70\,\mathrm{mm}$ except for the last example where $r = 100\,\mathrm{mm}$ was used.
Figures 5.22 - 5.24 show details of the simulation setup indicating the three possible receiver locations: L_1, L_2 & L_3.

---

[53] For a simulation of a dispersion map detection in $d = 0.8$ mm aluminium plate using this array see Appendix B.

[54] Details of phased array design can be found for example in Refs.[289, 244]

[55] Consult Appendix D for differences in calculations when multi-point sensors are used.

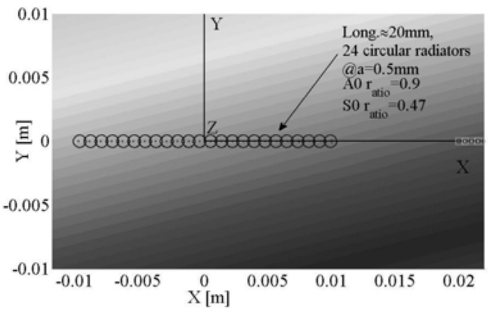

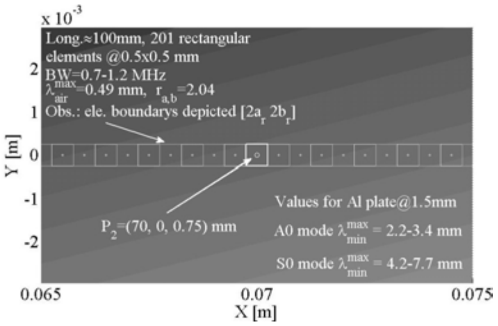

Figure 5.23: Detail of the plate excitation zone with 24 @$a = 0.5\,\mathrm{mm}$ circular radiators arranged in an X line.

Figure 5.24: Detail of the laminate emission area with 201 rectangular sources $[2a_\mathrm{r}, 2b_\mathrm{r}] = 0.5\mathrm{mm}$ along X axis.

The first comparisons were for the A0 mode with four types of receiver apertures all positioned at $L_1@\theta_\mathrm{r} = 8^\mathrm{o}$ and the following characteristics:

- C1: a 10 element concave array ($R = 35\,\mathrm{mm}, d_\mathrm{e} = 1\,\mathrm{mm}$) with $A_{\mathrm{dir.}} = \mathrm{on}$.
- P2: a 48 element linear array ($d_\mathrm{e} = 0.4\,\mathrm{mm}$) with the filter $A_{\mathrm{dir.}} = \mathrm{on}$.
- P3: a 48 element linear array ($d_\mathrm{e} = 0.4\,\mathrm{mm}$) with the filter $A_{\mathrm{dir.}} = \mathrm{off}$.
- P4: a 48 tapered-element linear array ($d_\mathrm{e} = 0.4\,\mathrm{mm}$) with $A_{\mathrm{dir.}} = \mathrm{off}$.

The respective steered responses for each of the arrays are depicted in Fig. 5.25. It is clearly appreciated that the effect of directivity of the sensors modifies the patterns whether the directivity model is included or not.
Note that the narrow main lobes of the wider plane aperture ($l_A = 19.2\,\mathrm{mm}$) and the lower grating lobes with $d_\mathrm{e} = 0.4\,\mathrm{mm}$ instead of those of the concave receptor.[56].

The next simulation was for the A0 and S0 modes using receiver P2 placed at different locations: L_1, L_2 & L_3.
Here Lamb modes were modelled as *pure* vibrations, each isolated from the others assuming ideal conditions ($\sigma_\mathrm{n}^2 = 0\,\mathrm{pW}$).
The radiation patterns for the corresponding array positions are shown in Figure 5.26. Locations L_1 and L_2 were simulated with a reception angle of $\theta = 8^\mathrm{o}$ for P2 while the angle for L_3 was $\theta = 0^\mathrm{o}$.

---

[56] In a real transducer the dimensions could be: $\{2a, 2b, p_\mathrm{e}\} = \{0.4, 15 - 30, 0\}$ mm for width, height and inter-element space respectively. Also, although not used here due to the current settings, the frequency operation band of this transducer should be close to → 0.5 MHz in order to avoid the spatial aliasing effect.

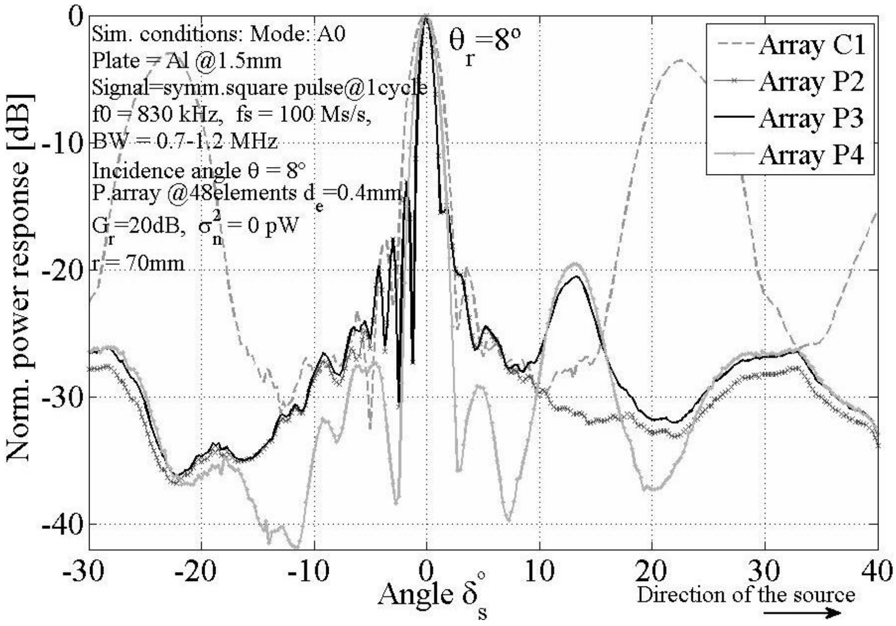

Figure 5.25: Radiation diagrams for the A0 mode on the d = 1.5 mm aluminium plate (L_1, G_r = 20 dB, σ_n^2 = 0 pW). The main lobes occurs near $\theta_\mathrm{r} \approx 8^\mathrm{o}$. A Hamming window was used for tapering the array $P4$.

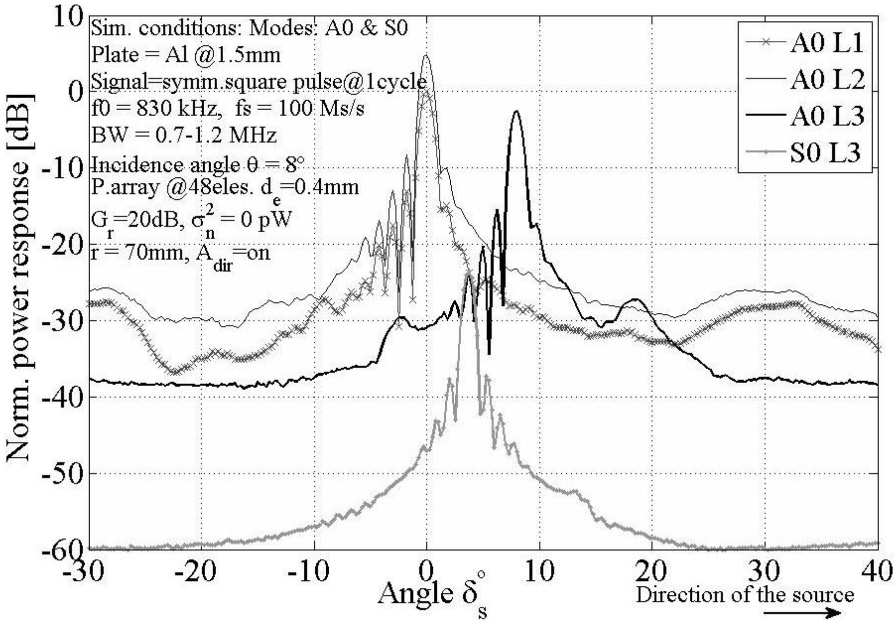

Figure 5.26: These are the radiation diagrams for the A0 and S0 modes in the d = 1.5 mm aluminium plate using array P2 in different locations (G_r = 20 dB, σ_n^2 = 0 pW). The main lobes for A0 are near $\theta_\mathrm{r} \approx 8^\mathrm{o}$, while for S0 is close to $\theta_\mathrm{r} \approx 3.85^\mathrm{o}$.

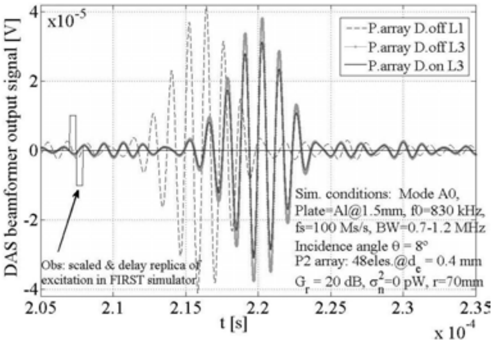

Figure 5.27: DAS output for A0 mode in Al@1.5 mm with P2 in L_1 and L_3.

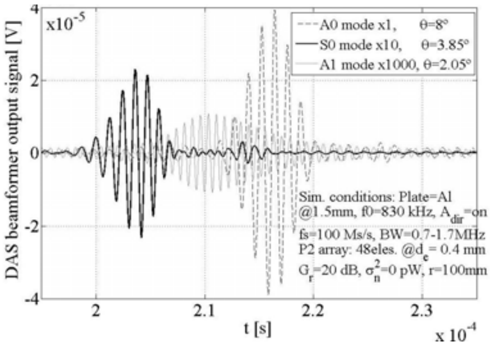

Figure 5.28: DAS output for A0, S0 & A1 modes in Al@1.5 mm with P2 array in L_1 and $r = 100$ mm.

The major effect observed is the low power of the S0 mode in contrast to those of A0 more than 20 dB.

This makes the task of identifying and isolating this mode from the others very difficult even under ideal conditions.

Note the signal gain obtained when the array is situated closer to the plate i.e. about 5 dB for position L_2.

With regard to the saw-like silhouette observed to the left of the A0 main lobes, this phenomenon also appears faintly in the experimental patterns of figures 5.15 and 5.16 and seems to be provoked by an interference effect at the receiver that degrades the output signals when the array is steered in the direction *away* the source.

The next Figure 5.27 shows respective outputs from the DAS beamformer for cases L_1 and L_3 at $\delta_s = 0^o$ with the A0 mode. While Figure 5.28 depicts final beamformer signals for the A0, S0 & A1 modes with P2 located at $L_3 : \delta_s = 0^o$ and $r = 100\,\text{mm}$[57].

Note the very low amplitudes of the S0 and A1 modes in contrast to those of A0. This is more than 1000 times for e.g. A1 mode.

However the validation of the amplitudes of these modes requires further experimental tests which unfortunately can not be addressed with the present hardware limitations.

5.4 Conclusions

This chapter have introduced the constituting parts of the LAMB software: 1)Emission, 2)Propagation and 3)Reception, describing their main characteristics and integration.

---

[57] When $\delta_s = 0^o$ is indicated we mean the DAS output at the maximum peak in the diagram of the corresponding mode.

Special emphasis was given to the reception section who simulates the receiver aperture and includes a model for the spatial response of individual sensors. This feature was implemented by means of two-dimensional directivity model based on the emission/reception reciprocity analogy and using the energy radiation pattern produced by a rectangular source at a fixed distance.

The array sensors limited directional response was effectively verified by experiments and simulations and its important influence on the global performance of an air-coupled NDE system was confirmed. This spatial effect is tightly coupled to the general geometry of the arrays and determines its final response.

Then, although the benefits of a concave receiver for maintaining fixed the focal point while the angular scan of the plate is performed, because of the strong directional response of the sensors it it suggested that this aperture should be replaced by a plane transducer. In this aspect, a new plane air-coupled receiver composed of 48 sensors with the dimensions $[2a, 2b, pe] = \{0.4, 15, 0\}$ mm was proposed[58].

This was selected as a compromised choice between a wider amplitude aperture with narrow sensors and a moderate number of receiver channels. It is also suggested, although this is highly application dependable, that the frequency operation band of the transducers should lower, around ≈ 0.5 MHz in order to not introduce much aliasing effect. This in turn will reduce the attenuation of the ultrasound in air, as well as simplify the *design* of the receiver electronics[59].

The assessment of the complete programme was made by comparisons with experimental data obtained from metal plates examined with a real prototype of an air-coupled NDE system using Lamb waves[77, 299].

A moderate degree of accuracy have been obtained during all tests with the detected A0 mode. On the other hand, the evaluation of the software with other Lamb modes i.e S0, A1, etc. still remains subject to the availability of an improved hardware. This is an important point to attain in the future in order to further verify the accuracy and usefulness of the tool.

As well, although efforts has been made to achieve the programme calibration, this was not possible to attain by the moment. This is because there are still issues relative to the GMM code and the simplified directivity model presented that possibly might require revision and further improvement.

---

[58] This dimensions corresponds to: width, height and inter-element distance. The actual value for the height is not so determinant because this is a 1D array, then it could be for example between 10 mm − 30 mm.

[59] The is a very important issue when designing a high frequency, high gain (more that 60 dB) ultra-low noise amplifier[298].

The coherent nature of the plate radiated fields produced by the Lamb waves was effectively characterized by the inclusion of a Delay And Sum (DAS) beamformer in the reception module of the programme.
The problem of identification of low energy Lamb modes (i.e $S0, A1, etc$) buried into A0 signals, was also introduced by comparisons of different radiation patterns. These clearly depict the problem of single mode separation when several modes are present in the array detected signals[60]. However with the availability of improved signal precessing techniques this might be circumvented[61].

---

[60] In this aspect attempts had been made by the author to implement a Side Lobe Canceller (SLC) for wideband signals[127, 164] in the receiver stage, although with inconclusive results.

[61] These are for example the use of wavelets[97]

Chapter 6

Conclusions and future work

6.1 Review of the Thesis

This thesis has investigated and developed of an analytically based matlab simulator i.e. **the LAMB software**.
The main objective of the programme is the analysis of the performance of new array aperture designs and the testing of signal processing techniques applicable to NDE systems which use Lamb waves in single ideal isotropic laminates.
The tool is divided into three modules: 1)Excitation, 2)Propagation and 3)Reception which use the following calculations:

- Calculation of acoustic fields: excited and radiated pressures $p(x, y, z, t)$.
- Determination of the Lamb wave dispersion relationships $(\Re\{f\}, k)$.
- Computation of displacements of an ideal isotropic plate $u_{\mathrm{z}}(x, y, z, t)$.

The theory developed in Chapter 2 explores the Impulse Response Method or IRM as a possibility for calculating acoustic fields.
Emphasis was placed on determinating the fields radiated by a rectangular aperture with use of the IRM approach which was developed by Emeterio and Ullate[234].
This technique constitutes the basic building block for the *excitation* module and the plate radiation computations.
Using this approach an acoustic field simulator FIRST[1] was build in Matlab. The programme simulations were then verified with other well known reputable tools such DREAM, Field II and Ultrasim and the results agreed well.

The basic concepts of wave propagation in multilayered media were reviewed in Chapter 3.
Matrix techniques such as the Transfer Matrix Method (TMM) and its enhanced version the Global Matrix Method (GMM) were analysed.

---

[1] The acronym stands for Field Impulse Response Software.

GMM was implemented to determine the Lamb wave dispersion relationships ($\Re\{f\}, k$). The results from the GMM code were tested using experimental data. This data was obtained from laser vibrometer detection techniques and a 2D FFT method. The GMM code was then included in the *propagation* section of the programme.

Chapter 4 investigated the role of a harmonic excited circular radiator which exerted pressure on the surface of a perfectly elastic isotropic layer. This is the so called Time Harmonic Solution (THS).

The Lamb wave dispersion data obtained in Chapter 3 were then used to calculate the THS mode vertical displacements based on the assumption that the far field approximation of circular crested Lamb waves appear as plane waves.

Then the THS was generalized for wideband signals and the *spatial* excitation of the laminate was recreated by using the following two strip based alternative techniques:

- Ideal plane wave (PW) simulation.
- Acoustic field excitation.

The first method uses an arrangement of adequately phased equal amplitude (along Y-strips) pressure signals distributed along the laminate. While the second approach uses the acoustic signals calculated with the FIRST simulator.

Both techniques construct the air-coupled excitation by a finite arrangement of radiators based on neighbouring strips along Y axis on the plate surface. An alternative formulation of the THS and the *point load* excitation method were then compared with the results of principle THS technique.

FEM[2] and plate tip impacted experimental data were also compared with THS simulations and moderate acceptable results were obtained.

The techniques discussed in previous chapters were then unified in Chapter 5 were the internal organization of the LAMB software was presented.

The validation of the programme was carried out by making tests to compare the A0 Lamb mode with data provided by a real air-coupled Lamb wave based NDT system[77, 299].

A brief analysis of concave aperture array was then made and a simple two-dimensional directivity model (XZ plane) for individual array sensors was introduced.

Finally several radiation diagrams simulations for different receiving apertures (plane and concave) with various Lamb modes were presented.

---

[2] The author would like to express his sincere gratitude to Dr. Michel Castaings and specially to the unfortunate and recently deceased Dr. Bernard Hosten from LMP in Bordeaux-France for their collaboration and support in the achievement of COMSOL data.

6.2 Summary of Findings

6.2.1 A new air-coupled Lamb wave based NDE tool

A new free and open source[3] simulator is now available for the test of array aperture designs and the implementation of signal processing techniques applicable to Lamb wave based air-coupled ultrasonic NDE systems.
The programme was built around three interactive core modules: 1)Excitation, 2)Propagation and 3)Reception and runs in the Matlab® environment simulating an ideal isotropic plate under ultrasonic test.
The programme is capable of using single and multimode Lamb waves to compute the laminate displacements, receiver trace signals and to perform simple beamforming radiation diagrams.

6.2.2 Directivity effect of individual sensors

The spatial directivity effect of air-coupled individual array sensors was effectively demonstrated and two models were proposed for IRM acoustic field simulations: 1)SIE and 2) SNIE.
A simple 2D directivity schema based on the reciprocity of radiation/reception diagrams of a harmonic excited SIE aperture was included in the receiver section of the programme.
The influence on detected signals and corresponding radiation diagrams produced by the geometry of the receiver i.e. concave array, was confirmed and compared with a those from a proposed new plane design[4].

6.2.3 Coherent nature of Lamb wave acoustic fields emitted

The spatial coherent nature of the laminate radiated fields produced by the excited Lamb waves was verified by several receiver radiation diagrams.
It was also shown that it is possible to reconstruct the (f, k) dispersion relation maps locating a plane array parallel to plate[5]. In this aspect the use of the *coincidence principle* with a receiver array is not recommended[6] since the spatial information contained in the plate radiated fields is lost.

---

[3] The LAMB programme is covered by the GNU General Public License Version 3 (29 June 2007) from the Free Software Foundation (FSF) http://www.gnu.org.

[4] The air-coupled plane receiver proposed is composed of 48 sensors with the following dimensions $\{2a, 2b, p_{\mathrm{e}}\} = \{0.4, 15, 0\}$ mm. The height dimension $(2b)$ could be widened.

[5] See figures B.8 and B.9 in Appendix B.

[6] This is applicable when a wide plane array is used to detect the (f, k) or (f, c_{ph}) dispersion spectrum instead of other apertures. In other cases the use of the coincidence principle with a *slide* sampling receiver is an alternative. See for example Refs.[97, 104, 114].

Only when the SNR ratio is low the application of this principle in conjunction with e.g. *spatial matched*[7] filter is advised.

6.2.4 DAS beamforming

The first stage of a signal processing block was added to the tool by the implementation of a simple DAS beamformer.
The influence on the radiation diagrams provoked by the noise and interference contained in the detected signals was verified as the main source of error in the diagrams.
Other causes of pattern modification such as the use of arrays with wider sensors[8] and non-plane aperture designs were also verified.

6.3 Future work

6.3.1 Individual modules

§Emission:

Future work in this software section involves fixing the problem encountered in zone IV of the IRM calculations of the FIRST simulator[9].
The addition of other types of apertures such as circular and two-dimensional array transducers is also of interest for possible inclusion in the programme. The translation of the code to C/C++ can greatly improve the speed of the programme. This will be possible as soon as the will be reorganise to obtain a stable version.

§Propagation:

The GMM code implemented to determine the Lamb wave dispersion relationships can be enhanced by: 1) revising the searching algorithm to improve its time/accuracy efficiency, 2) translate the code to the *mp* arithmetic[10].
The THS method used to calculate the plate displacements can be extended to more complex multilayer isotropic models[**?**].
A full study of the coded equations to solve *response* solutions[11] can lead to a connection of GMM with the angular spectrum method (ASM) introduced on § 2.2.4. This would be a more accurate solution than the THS and an interesting addition to the LAMB software.

---

[7] This is the simple Delay And Sum beamformer (DAS). For other types of beamformers see Ref.[164].

[8] This provokes spatial aliasing effects when $\xi^{\mathrm{air}}_{\mathrm{min}}/2 < 2a$.

[9] See e.g. the notch in Fig. 2.17.

[10] The matlab multiple precision arithmetic toolbox http://www.swox.com/gmp .

[11] These are the solutions for a multilayered system excited by plane waves[204].

§Reception:

To improve this programme module an enhanced model for the *noise+interference* effects should be added to the simulated received signals.
A revision and 3D generalization of the directivity model will enable the analysis of plate emitted fields with *two-dimensional* arrays. The implementation of other types of adaptive spatial filters and signal processing algorithms[12] apart to the DAS beamformer included is also suggested.

6.3.2 LAMB software: further assessment

Because the software is on its initial stage many are the comments and suggestions possible. The following is a list of the main for improvement:

- Programme assessment with other Lamb modes i.e. S0, A1, etc. This will require improved hardware that permits acquisition of crucial experimental data to compare with the toolbox predictions.

- Translation of the complete code to C/C++ programming language. This will reduce significantly the time required for the computations and allow for more complex simulations to be carried out.

- Programme calibration: this is the most difficult goal to attain because it involves the emulation of a complex system. However with the availability of additional measurement data this could help to identify a calibration subset for some materials and plate widths.

6.3.3 Air-coupled NDT systems: hardware improvements

A short list with suggestions for the design of new air-coupled NDT systems based on air-coupled Lamb waves is summarized here.

- Better receiver electronics design: the reduction of noise and the interference are *key* factors in the design of a successful air-coupled NDT system. This is because the received signals are often too noisy and in some cases extremely weak to detect.

- Use of plane arrays: despite the natural focusing advantages of a concave aperture the use of *small* elements and *wider* plane arrays improves the spatial discrimination feature required in NDT with Lamb waves[147, 149].

---

[12] The inclusion of the Minimum Variance (MV) or Capon beamformer[30, 32], the Amplitude and Phase Estimation beamformer (APES)[103, 263], as well Direction Of Arrival (DOA) or angle estimation techniques[164]

- Use of broadband air-coupled transducers: although some NDT applications may require only narrowband signals, the study and analysis of complex phenomena may need the operation in wideband of frequencies[194, 205, 239, 292]. For example high acoustic pressures may lead to nonlinear responses with harmonics[24, 75]. The air attenuation effect is a strong drawback in this respect and operations beyond $f > 3.5\,\mathrm{MHz}$ are not recommended. See e.g. Fig. 2.7.

Apart from these suggestions there are many others possible for a complex structure such as an air-coupled NDE system based on Lamb waves whether it be real or simulated. This is because the vibration phenomena it involves are simply enormous.
Simple questions such as: *What does this feature in this signal mean when the plate is... ?* or *How will the laminate/s respond when a crack of this... is present?* and so on... requires a profound understanding of many phenomena and diverse fields such as mechanics, electronics and signal processing.

Throughout time the efforts of many researchers have contributed to the growth of knowledge in this field both in the comprehension of the mechanics of vibrations and of its new applications in modern technology.
In recent years the NDT/NDE field has experience a tremendous expansion with the increasing addition of signal processing aids.
The present tool although modest in its scope valid for single isotropic plates offers an *approximate* simulation scenario of an air-coupled ultrasonic NDE system based on Lamb waves using 1D array transducers.
The main objective of the programme is the modelling new emitter/receiver apertures designs and the test of improved signal processing methods before implementation into a hardware prototype.
Finally, to be able to advance knowledge in this field a deep understanding of the *fundamental* mechanics and signal processing techniques is essential for successful analysis of the gathered information.

Appendix A

Calculation of the air medium characteristics

This appendix summarizes the expressions for determination of the air medium characteristics used in the LAMB programme plus a group of comparisons of simulated ultrasonic signals between the Ultrasim software and the FIRST programme.

A.1 Equations for determination of the attenuation of ultrasound in air

The frequency response attenuation function $A_{\mathrm{atte}}(R, \mathrm{i}w)$ or attenuation filter used in equation (2.33) to calculate the attenuated impulse response function $h_{\mathrm{a}}(x, y, z, t)$ at a point $P_{\mathrm{x,y,z}}$ is expressed by

$$A_{\mathrm{atte}} = 10^{-\frac{R\alpha}{20}} \tag{A.1}$$

Where R [m] is the distance between the point where the acoustic field is calculated $P_{\mathrm{x,y,z}}$ and the origin of the rectangular radiator[1].
The equations for the determination of the attenuation coefficient α [$\mathrm{N_p/m}$] were obtained from Refs.[20, 21, 23] and are:

$$\alpha = \alpha_{\mathrm{cr}} + \alpha_{\mathrm{viv,O}} + \alpha_{\mathrm{viv,N}} \tag{A.2}$$

with the classical+rotational and the vibrational oxygen and nitrogen attenuation coefficients expressed by[2]:

$$\alpha_{\mathrm{cr}} = 1.84\ 10^{-11} f^2 \left(\frac{P_0}{P_{01}}\right) \sqrt{\frac{T}{T_{01}}} \tag{A.3}$$

$$\alpha_{\mathrm{viv,O}} = f^2 \left(\frac{T_0}{T}\right)^{5/2} \left(1.278\ 10^{-2} \frac{e^{-2239.1/T}}{f_{\mathrm{r,O}} + \frac{f^2}{f_{\mathrm{r,O}}}}\right) \tag{A.4}$$

---

[1] See O_{a} in figures 2.1 and 2.3

[2] The ambient pressure is P_0 [Bar], the relative humidity H_{r}[%] and the absolute temperature T [K]. While $P_{01} = 1$ Bar, $T_0 = 293.15$ K and $T_{01} = 273.16$ K.

$$\alpha_{\mathrm{viv,N}} = f^2 \left(\frac{T_0}{T}\right)^{5/2} \left(1.068\ 10^{-1} \frac{e^{-3352/T}}{f_{\mathrm{r,N}} + \frac{f^2}{f_{\mathrm{r,N}}}}\right) \tag{A.5}$$

The oxygen $f_{\mathrm{r,O}}$ and nitrogen $f_{\mathrm{r,N}}$ relaxation frequencies in [Hz] are given by

$$f_{\mathrm{r,O}} = \left(\frac{P_0}{P_{01}}\right) \left(24 + 4.04\ 10^4 h \left(\frac{0.02 + h}{0.391 + h}\right)\right) \tag{A.6}$$

$$f_{\mathrm{r,N}} = \left(\frac{P_0}{P_{01}}\right) \sqrt{\frac{T_0}{T}} \left(9 + 280\, h\, e^{-4.17\left(\left(\frac{T_0}{T}\right)^{-1/3} - 1\right)}\right) \tag{A.7}$$

with

$$\begin{aligned} \log_{10}\left(\frac{P_{\mathrm{sat}}}{P_{01}}\right) &= 10.79586 \left(1 - \frac{T_{01}}{T}\right) - 2.2195983 \\ &+ 1.50474\ 10^{-4} \left(1 - 10^{-8.29692(T/T_{01} - 1)}\right) \\ &+ 0.42873\ 10^{-3} \left(10^{4.76955(1 - T_{01}/T)}\right) \end{aligned} \tag{A.8}$$

and the water mole fraction h [%] is:

$$h = H_{\mathrm{r}} \frac{P_{\mathrm{sat}}/P_{01}}{P_0/P_{01}} \tag{A.9}$$

A.2 Calculation of the air density

The calculation of the air density ρ[kg/m^3] was based on Refs.[31, 53, 79], with t [°C] and T [K] being the ambient and absolute temperatures respectively[3]. Then:

$$\rho = \frac{P_0 M_{\mathrm{a}} \left[1 - x_{\mathrm{v}} \left(1 - \frac{M_{\mathrm{v}}}{M_{\mathrm{a}}}\right)\right]}{ZRT} \tag{A.10}$$

with

$$Z = 1 - \frac{P_0}{T} \left[a_0 + a_1 t + a_2 t^2 + (b_0 + b_1 t)\, x_{\mathrm{v}} + (c_0 + c_1 t)\, x_{\mathrm{v}}^2\right] + \frac{P_0^2}{T^2} \left[d + e x_{\mathrm{v}}^2\right] \tag{A.11}$$

$$x_{\mathrm{v}} = \frac{H_{\mathrm{r}} f_{\mathrm{pt}} p_{\mathrm{sv}}}{100 P_0} \qquad f_{\mathrm{pt}} = \alpha + \beta P_0 + \gamma t^2 \qquad p_{\mathrm{sv}} = e^{AT^2 + BT + C + \frac{D}{T}} \tag{A.12}$$

---

[3] Here the atmospheric pressure is P_0 [Pa] and the percentage of relative humidity H_{r}.

and the following coefficients values:

$$R = 8.31441\ [\mathrm{J/(mol\,K)}] \qquad a0 = 1.62419\ 10^{-6}\ [\mathrm{K/Pa}] \tag{A.13}$$

$$Mv = 48.015\ 10^{-3}\ [\mathrm{kg/mol}] \qquad a1 = -2.8969\ 10^{-8}\ [\mathrm{1/Pa}] \tag{A.14}$$

$$Ma = 28.9635\ 10^{-3}\ [\mathrm{kg/mol}] \qquad a2 = 1.0880\ 10^{-10}\ [\mathrm{1/(K\,Pa)}] \tag{A.15}$$

$$A = 1.2811805\ 10^{-5}\ [\mathrm{K^{-2}}] \qquad b0 = 5.757\ 10^{-6}\ [\mathrm{K/Pa}] \tag{A.16}$$

$$B = -1.9509874\ 10^{-2}\ [\mathrm{K^{-1}}] \qquad b1 = -2.589\ 10^{-8}\ [\mathrm{1/Pa}] \tag{A.17}$$

$$C = 34.04626034 \qquad c0 = 1.9297\ 10^{-4}\ [\mathrm{K/Pa}] \tag{A.18}$$

$$D = -6.3536311\ 10^{3}\ [\mathrm{K}] \qquad c1 = -2.285\ 10^{-6}\ [\mathrm{1/Pa}] \tag{A.19}$$

$$\alpha = 1.00062 \qquad d = 1.73\ 10^{-11}\ [\mathrm{K^2/Pa^2}] \tag{A.20}$$

$$\beta = 3.14\ 10^{-8}\ [\mathrm{1/Pa}] \qquad e = -1.034\ 10^{-8}\ [\mathrm{K^2/Pa^2}] \tag{A.21}$$

$$\gamma = 5.6\ 10^{-7}\ [\mathrm{1/^{o}C^2}] \tag{A.22}$$

A.3 Determination of the speed of sound in air

The following equation was used for the calculation for the speed of ultrasound in air[23, 102]

$$c = c_0\sqrt{\frac{T}{T_0}} \qquad ; \qquad \text{with} \begin{cases} c_0 = 331.31\ \mathrm{m/s} \\ T_0 = 273.16\ \mathrm{K} \end{cases} \tag{A.23}$$

A.4 Comparison of ultrasonic signals with Ultrasim

This section presents a group of comparisons between simulations with the FIRST programme and the Ultrasim acoustic simulator. The simulations[4] were carried out for a single rectangular transducer or Single Ideal Element (SIE[5]) and plane and concave[6] arrays composed of 16 SIE radiators. The comparisons were made for single frequency (CW) and pulse type[7] signals without inclusion of the attenuation of sound in air[8].

---

[4] All the simulations show the maximum amplitudes of the signals normalized and expressed in dB. The simulations along the X and Y axes were carried out for segments of lines at 35 mm distant from the origin of the transducers and the focus of the array were set at infinity.

[5] All SIE used had the following dimensions: $2a = 1$ mm, $2b = 15$ mm for width and height respectively. For details on the geometry see for example figures 2.1 and 2.24.

[6] This is a cylindrical concave array with a radius $R = 35$ mm.

[7] A single cycle sinusoid signal @f_0 was used.

[8] This because Ultrasim does no includes a model for the attenuation effect, then $\alpha = 0$.

§SIE comparisons

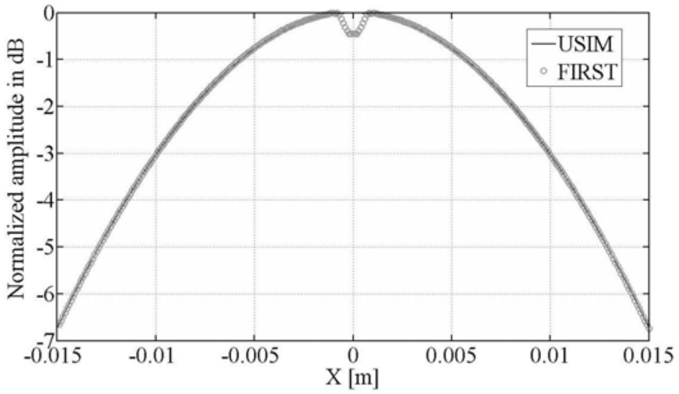

Figure A.1: SIE simulations with CW @$f_0 = 0.5\,\text{MHz}$ along an X line.

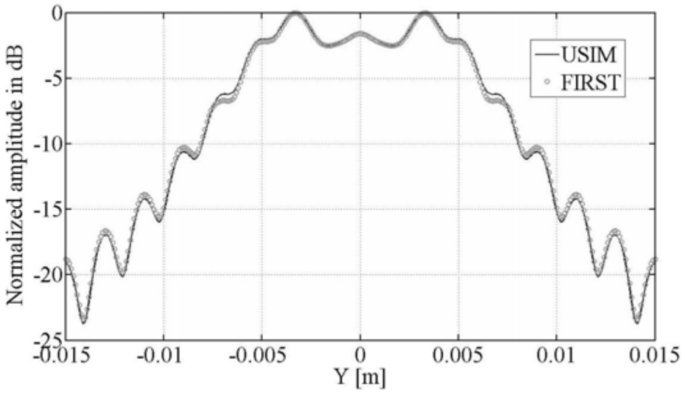

Figure A.2: SIE simulations with CW @$f_0 = 0.5\,\text{MHz}$ along an Y line.

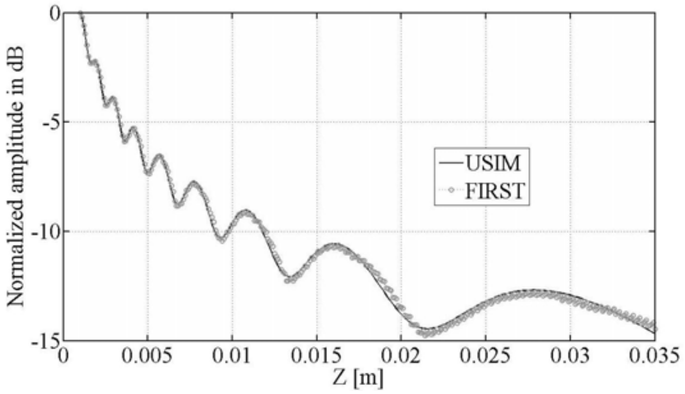

Figure A.3: SIE simulations with CW @$f_0 = 0.5\,\text{MHz}$ along an Z line.

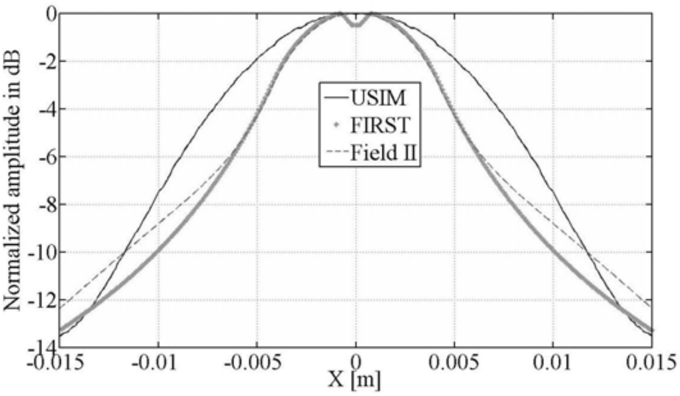

Figure A.4: SIE simulations with pulsed signal $@f_0 = 1\,\mathrm{MHz}$ along an X line.

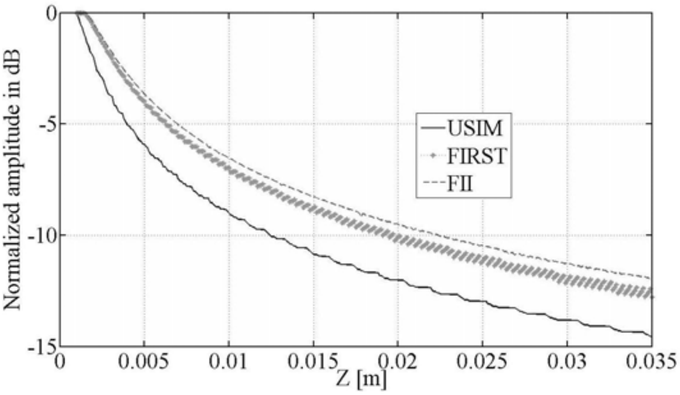

Figure A.5: SIE simulations with pulsed signal $@f_0 = 1\,\mathrm{MHz}$ along an Z line.

§Concave array comparisons: $R = 35\,\mathbf{mm}, N_\mathbf{a} = 16$ **SIE**

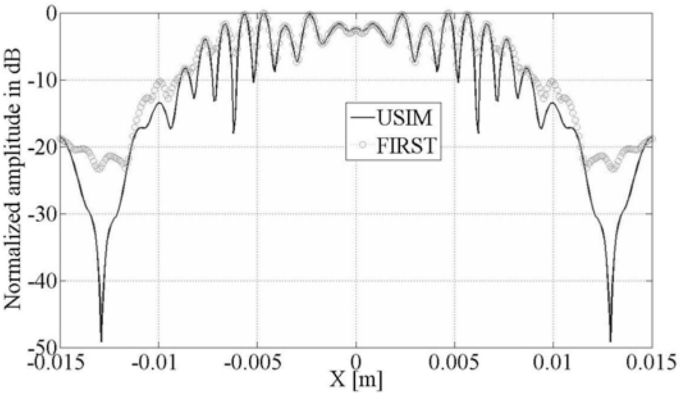

Figure A.6: Concave array CW simulations $@f_0 = 1\,\mathrm{MHz}$ along an X line.

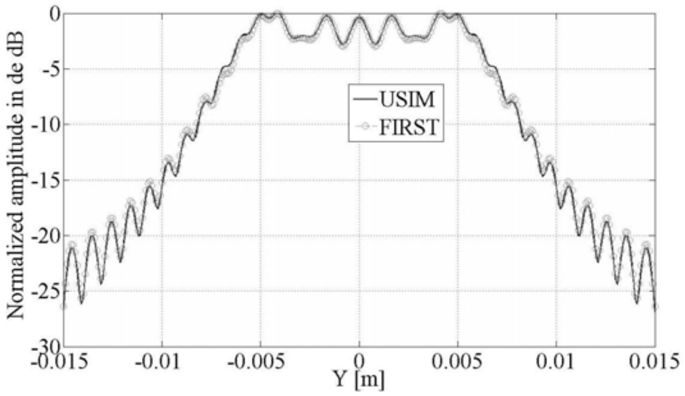

Figure A.7: Concave array CW simulations $@f_0 = 1\,\mathrm{MHz}$ along an Y line.

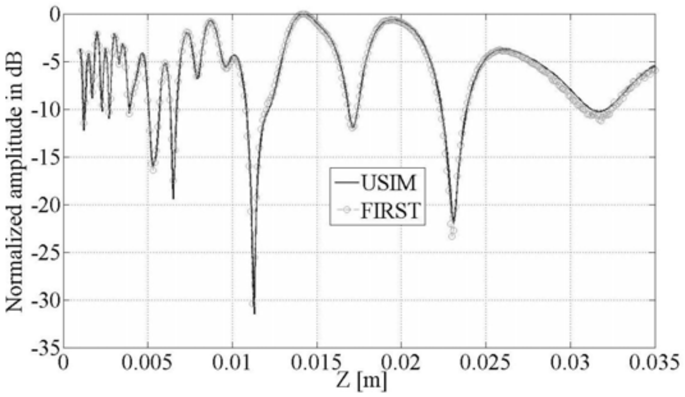

Figure A.8: Concave array CW simulations $@f_0 = 1\,\mathrm{MHz}$ along an Z line.

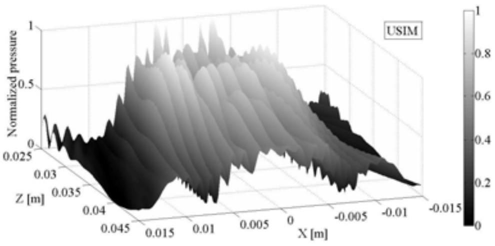

Figure A.9: Ultrasim CW simulation for a concave array generating a plane wavefront (PWF) $f_0 = 1\,\mathrm{MHz}$ in an XZ plane.

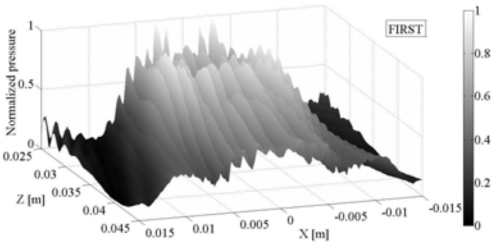

Figure A.10: FIRST CW simulation for a concave array generating a PWF (focus at infinity) $f_0 = 1\,\mathrm{MHz}$ in an XZ plane.

§Plane array comparisons: $N_\mathbf{a} = 16$ SIE

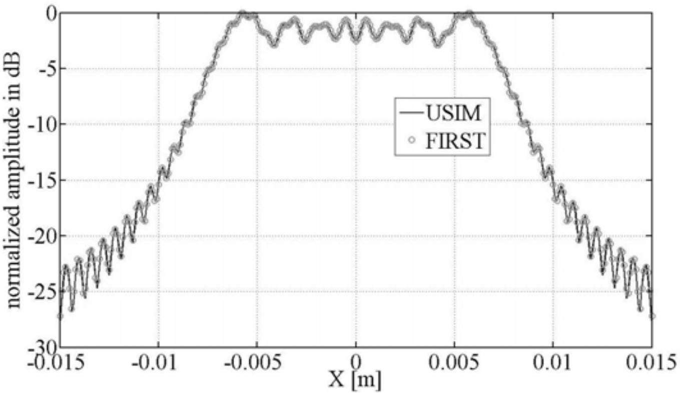

Figure A.11: Plane array CW simulations @$f_0 = 1.5\,\mathrm{MHz}$ along an X line.

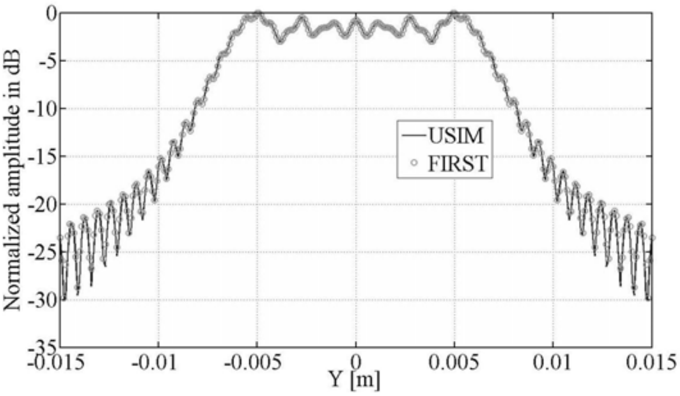

Figure A.12: Plane array CW simulations @$f_0 = 1.5\,\mathrm{MHz}$ along an Y line.

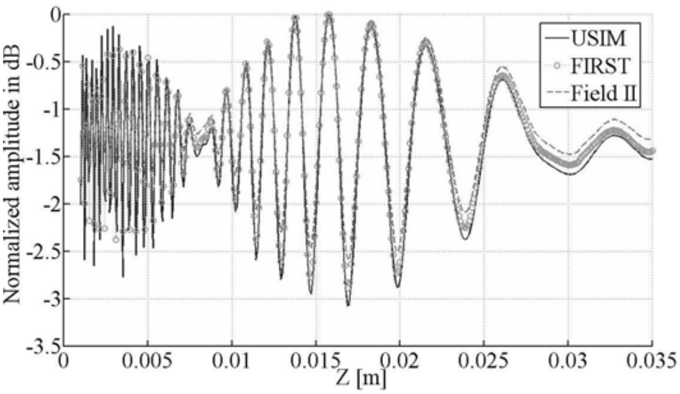

Figure A.13: Plane array CW simulations @$f_0 = 1.5\,\mathrm{MHz}$ along an Z line.

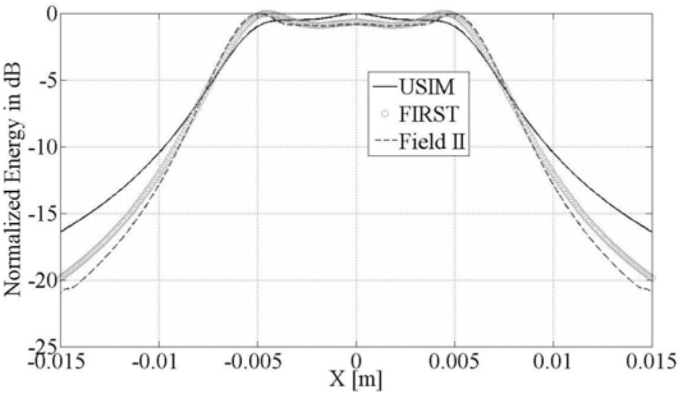

Figure A.14: Plane array pulsed simulations @$f_0 = 1.5\,\text{MHz}$ along an X line.

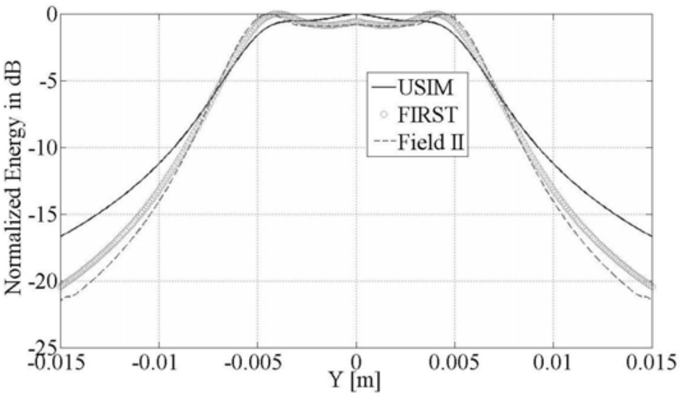

Figure A.15: Plane array pulsed simulations @$f_0 = 1.5\,\text{MHz}$ along an Y line.

Appendix B

Lamb wave dispersion curves and wavelengths

This appendix depicts Lamb wavelength values and dispersion curves for other modes and layered systems.

B.1 Lamb wavelength curves for S0 and A1 modes

The values of the Lamb wavelengths for the S0 and A1 modes in aluminium and copper plates are presented with the element radiation parameter[1] conditions $r_{\mathrm{a,b}} = 2$ and $r_{\mathrm{a,b}} = 1$ and the size of the IRM plate elements used in the simulations $[2a_{\mathrm{r}}, 2b_{\mathrm{r}}] = 0.5\,\mathrm{mm}$.

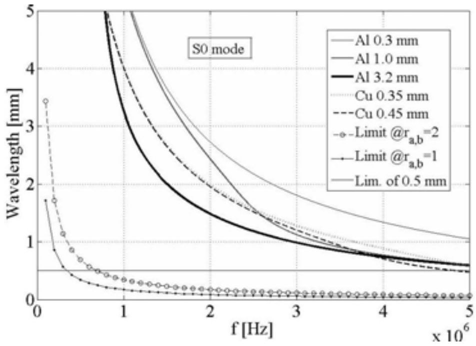

Figure B.1: Wavelength curves for S0 modes indicating the radiation conditions $r_{\mathrm{a,b}}$ and the limit of 0.5 mm.

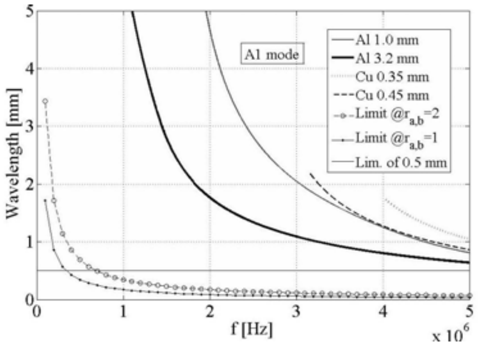

Figure B.2: Wavelength curves for A1 modes indicating the radiation conditions $r_{\mathrm{a,b}}$ and the limit of 0.5 mm.

B.2 Lamb wave dispersion curves for other systems

The dispersion curve results obtained with the implemented Global Matrix Method[158] (GMM) in the LAMB programme are presented here for two other 3-layer systems: 1)water-Titanium-water[2] and 2)air-Aluminium-air.

---

[1] For more details see Table 2.3 and Figure 5.5.

[2] This particular example had been selected in order to validate the developed routines with well known data[157]

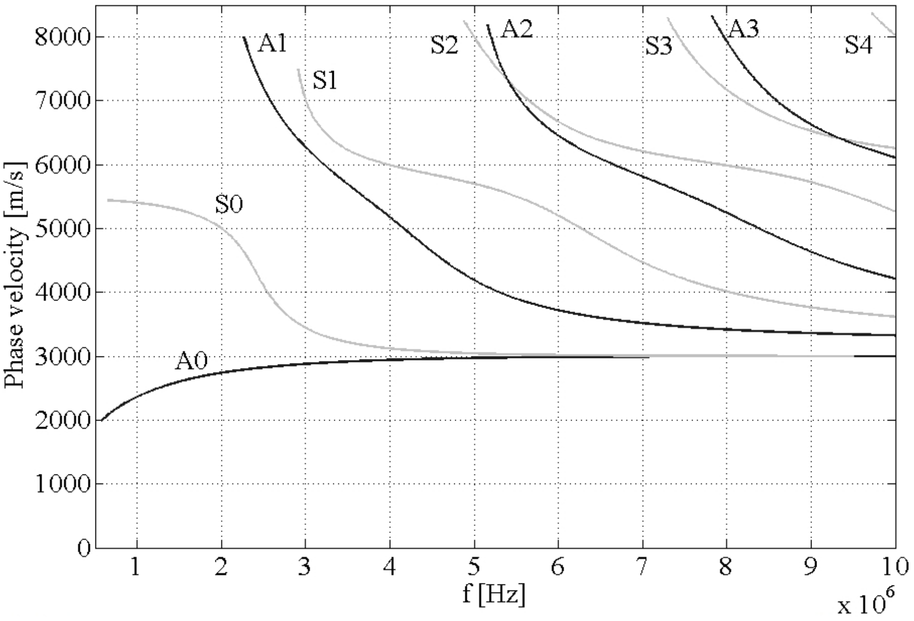

Figure B.3: Dispersion curves for 1 mm width Titanium sheet in water.

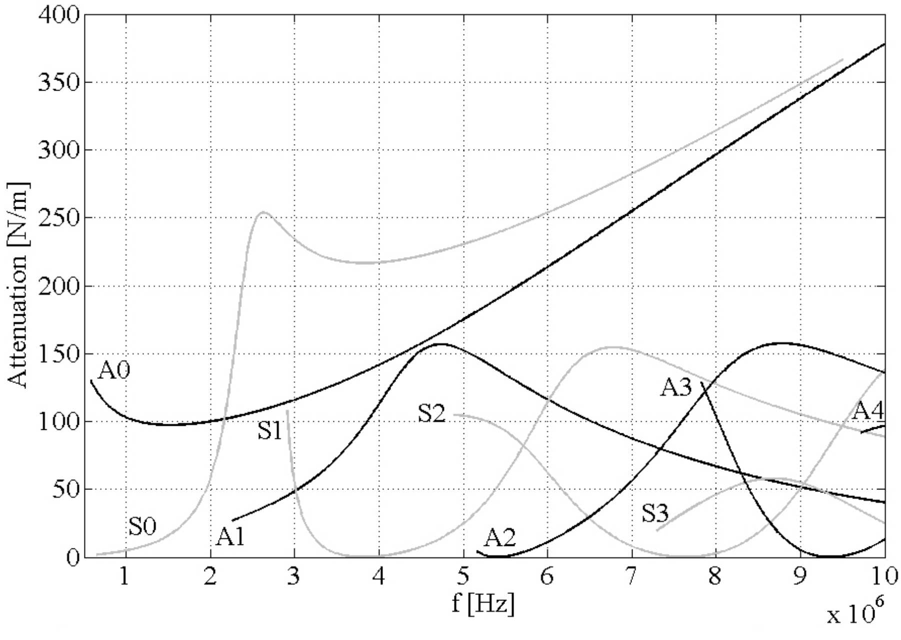

Figure B.4: Attenuation curves for the same system water-Ti@1 mm-water.

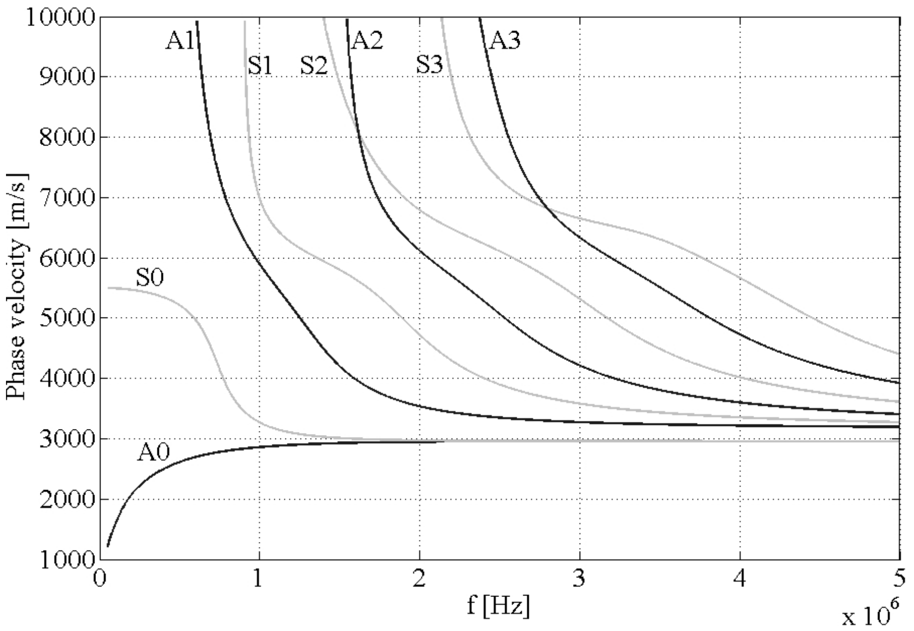

Figure B.5: Dispersion curves for 3.2 mm width Aluminium sheet in air.

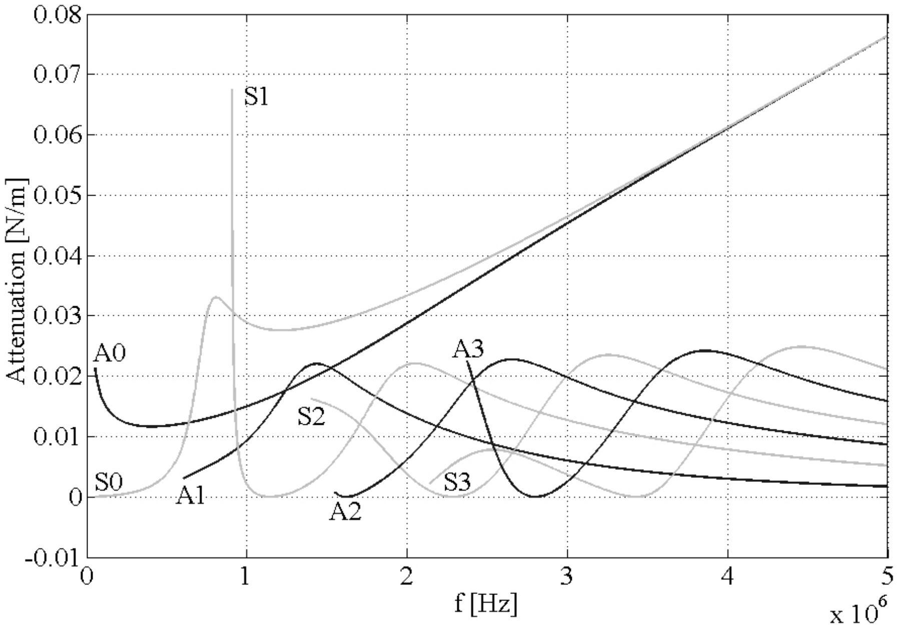

Figure B.6: Attenuation curves for the same system air-Al@3.2 mm-air.

B.3 Plane array detected dispersion maps

This section shows the Lamb wave dispersion data for an aluminium plate ($d = 0.8\,\mathrm{mm}$) generated by a two-dimensional FFT transform[9, 101, 145] of the signals received with the proposed 48 element plane array[3].
This simulation resembles the experiment carried out with the laser vibrometer in Chapter 3, Fig. 3.11.
The LAMB programme simulation setup is shown in the following figure B.7.

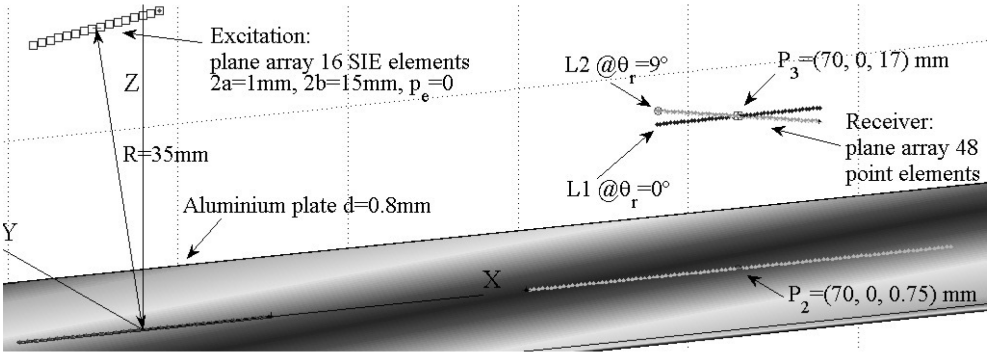

Figure B.7: View of the simulation scenario for the dispersion data detection with a 48 element plane array located at: (P_3, L_1) and (P_3, L_2).

Then observation of figures B.8 and B9 (see the next page) clearly indicate that use of the *coincidence principle* in the receiver i.e $\theta_\mathrm{r} = \theta_\mathrm{i} = 9^\circ$, destroys the Lamb waves spatial information contained in the acoustic field radiated by the plate.

In this case the positioning of the *plane* receiver oriented parallel to the laminate is a better location for this purpose.
It is of course possible to reconstruct the same map by aligning the receiver signals in location L2 with e.g $\theta_\mathrm{r} = 9^\circ$. But in multimode Lamb wave signals this process has to be done for all present modes[4], then this technique is not recommended.

---

[3] Single point elements were used to simulate this array $\{2a,\ 2b,\ p_\mathrm{e}\} = \{0,\ 0,\ 0.4\}$ mm.
[4] This depends on which modes are being simulated (?).

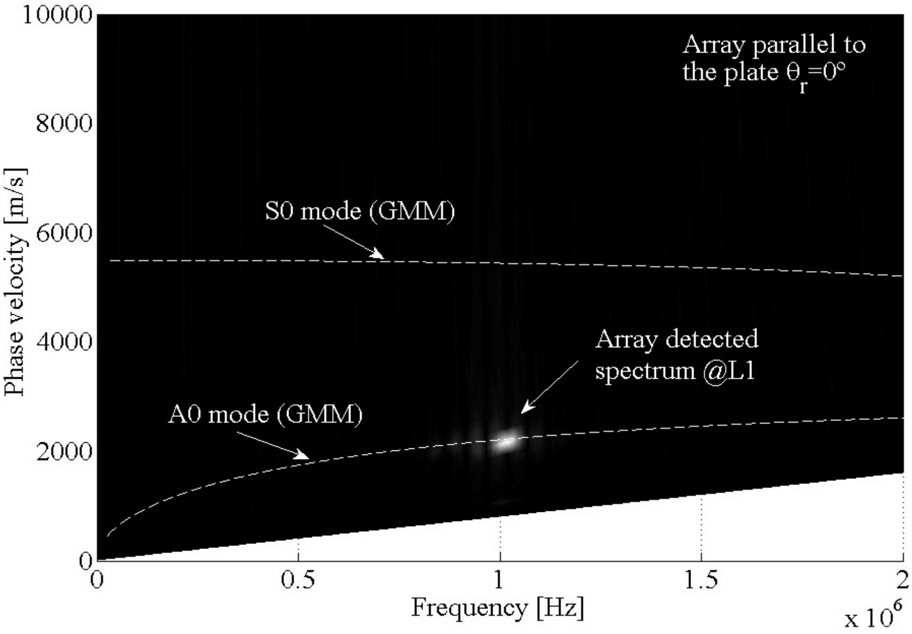

Figure B.8: Comparison of plane array ($L_1@\theta_r = 0°$) dispersion map detected in an aluminium plate ($d = 0.8$mm) and the superimposed GMM simulations. Mode: A0, sinusoidal burst @20cnt., $f_0 = 1\,\text{MHz}$, $f_s = 100\,\text{MHz}$, $f_{s2} = 1/0.4\,\text{mm}$.

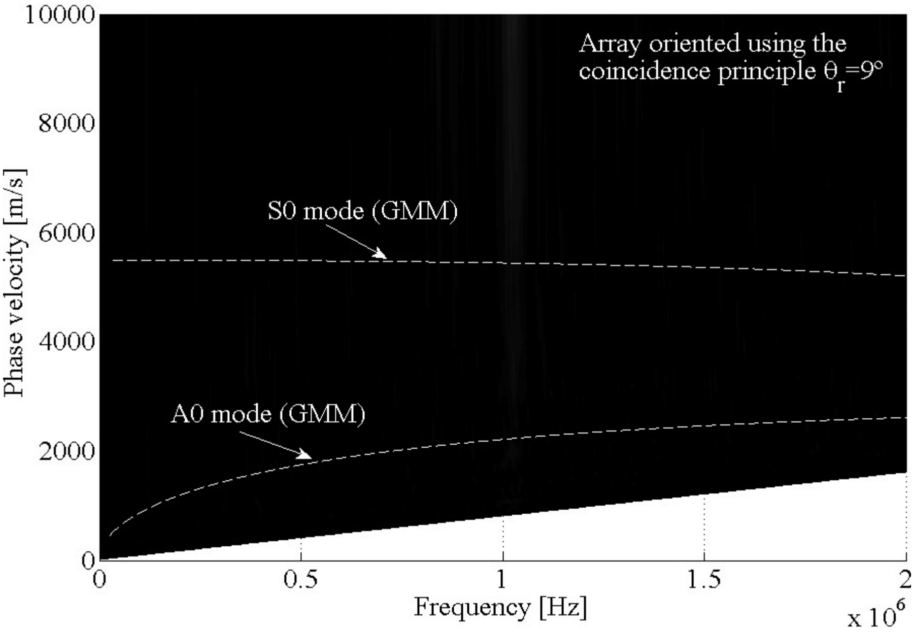

Figure B.9: Comparison of plane array ($L_2@\theta_r = 9°$) dispersion map detected in an aluminium plate ($d = 0.8$mm) and the superimposed GMM simulations. Mode: A0, sinusoidal burst @20cnt., $f_0 = 1\,\text{MHz}$, $f_s = 100\,\text{MHz}$, $f_{s2} = 1/0.4\,\text{mm}$.

Appendix C

The time harmonic equations

This appendix summarize the required equations for the Time Harmonic Solution (THS) in order to calculate the displacement fields provoked by a single circular radiator exerting a sinusoidal pressure waveform on the surface of an infinite ideal isotropic laminate of width d.

C.1 Summary of equations for the THS method

The normal and radial displacements on the plate are given by:

$$\tilde{u}_{\mathrm{z}}^{\mathrm{s,a}}(r,z) = \mathrm{i}\frac{\pi}{2\mu}\sum_{k_{\mathrm{s,a}}} F^0\left(k_{\mathrm{s,a}}\right) k_{\mathrm{s,a}} \frac{\Gamma_{\mathrm{zn}}^{\mathrm{s,a}}(k_{\mathrm{s,a}})}{\Delta'_{\mathrm{s,a}}(k_{\mathrm{s,a}})} H_0^{(1)}(k_{\mathrm{s,a}}r) \quad ; \quad r > a \tag{C.1}$$

$$\tilde{u}_{\mathrm{r}}^{\mathrm{s,a}}(r,z) = \mathrm{i}\frac{\pi}{2\mu}\sum_{k_{\mathrm{s,a}}} F^0\left(k_{\mathrm{s,a}}\right) k_{\mathrm{s,a}} \frac{\Gamma_{\mathrm{rn}}^{\mathrm{s,a}}(k_{\mathrm{s,a}})}{\Delta'_{\mathrm{s,a}}(k_{\mathrm{s,a}})} H_1^{(1)}(k_{\mathrm{s,a}}r) \quad ; \quad r > a \tag{C.2}$$

with the following equations for the $\Gamma_{\mathrm{z,r}}^{\mathrm{s,a}}\left(z,k\right)$ functions for symmetric and anti-symmetric Lamb modes[1]:

$$\Gamma_{\mathrm{zn}}^{\mathrm{s}} = k_{\mathrm{tl}}\left[2k^2\sin\left(k_{\mathrm{tl}}d/2\right)\sin\left(k_{\mathrm{ts}}z\right) + \left(k_{\mathrm{ts}}^2 - k^2\right)\sin\left(k_{\mathrm{ts}}d/2\right)\sin\left(k_{\mathrm{tl}}z\right)\right] \tag{C.3}$$

$$\Gamma_{\mathrm{rn}}^{\mathrm{s}} = k\left[-2k_{\mathrm{tl}}k_{\mathrm{ts}}\sin\left(k_{\mathrm{tl}}d/2\right)\cos\left(k_{\mathrm{ts}}z\right) + \left(k_{\mathrm{ts}}^2 - k^2\right)\sin\left(k_{\mathrm{ts}}d/2\right)\cos\left(k_{\mathrm{tl}}z\right)\right] \tag{C.4}$$

$$\Gamma_{\mathrm{zn}}^{\mathrm{a}} = k_{\mathrm{tl}}\left[-2k^2\cos\left(k_{\mathrm{tl}}d/2\right)\cos\left(k_{\mathrm{ts}}z\right) + \left(k_{\mathrm{ts}}^2 + k^2\right)\cos\left(k_{\mathrm{ts}}d/2\right)\cos\left(k_{\mathrm{tl}}z\right)\right] \tag{C.5}$$

$$\Gamma_{\mathrm{rn}}^{\mathrm{a}} = k\left[-2k_{\mathrm{tl}}k_{\mathrm{ts}}\cos\left(k_{\mathrm{tl}}d/2\right)\sin\left(k_{\mathrm{ts}}z\right) + \left(k_{\mathrm{ts}}^2 - k^2\right)\cos\left(k_{\mathrm{ts}}d/2\right)\sin\left(k_{\mathrm{tl}}z\right)\right] \tag{C.6}$$

The expression of the spatial spectrum function for the piston like harmonic pressure excitation is

$$F^0\left(k\right) = Pa\frac{J_1(ka)}{k} \tag{C.7}$$

---

[1] More details in Refs.[57, 201].

Where P in $[Pa]$ is the amplitude of the pressure and $a\,[m]$ the radius of the piston. The dispersion relationships $\Delta_{\mathrm{s,a}}$ are given by:

$$\Delta_{\mathrm{s}} = \left(k_{\mathrm{ts}}^2 - k^2\right)^2 \cos\left(k_{\mathrm{tl}} d/2\right) \sin\left(k_{\mathrm{ts}} d/2\right) + 4k^2 k_{\mathrm{tl}} k_{\mathrm{ts}} \sin\left(k_{\mathrm{tl}} d/2\right) \cos\left(k_{\mathrm{ts}} d/2\right) \tag{C.8}$$

$$\Delta_{\mathrm{a}} = \left(k_{\mathrm{ts}}^2 - k^2\right)^2 \sin\left(k_{\mathrm{tl}} d/2\right) \cos\left(k_{\mathrm{ts}} d/2\right) + 4k^2 k_{\mathrm{tl}} k_{\mathrm{ts}} \cos\left(k_{\mathrm{tl}} d/2\right) \sin\left(k_{\mathrm{ts}} d/2\right) \tag{C.9}$$

where

$$k_{\mathrm{tl}} = \sqrt{\frac{w^2}{c_{\mathrm{L}}^2} - k^2} \qquad ; \qquad c_{\mathrm{L}} = \sqrt{\frac{\lambda + 2\mu}{\rho}} \tag{C.10}$$

$$k_{\mathrm{ts}} = \sqrt{\frac{w^2}{c_{\mathrm{S}}^2} - k^2} \qquad ; \qquad c_{\mathrm{S}} = \sqrt{\frac{\mu}{\rho}} \tag{C.11}$$

§Expressions for determination of the derivatives of the dispersion equations

The analytic expressions for the derivative terms $\Delta^{'}_{\mathrm{s,a}}$ of the dispersion relationships (C.8) and (C.9) are given respectively by[2]

$$\begin{aligned}\Delta^{'}_{\mathrm{s}} = {} & -8qk \cos\left(k_{\mathrm{tl}} d/2\right) \sin\left(k_{\mathrm{ts}} d/2\right) + \frac{q^2 k}{k_{\mathrm{tl}}}(d/2) \sin\left(k_{\mathrm{tl}} d/2\right) \sin\left(k_{\mathrm{ts}} d/2\right) \\ & - \frac{q^2 k}{k_{\mathrm{ts}}}(d/2) \cos\left(k_{\mathrm{tl}} d/2\right) \cos\left(k_{\mathrm{ts}} d/2\right) + 8k_{\mathrm{tl}} k_{\mathrm{ts}} k \sin\left(k_{\mathrm{tl}} d/2\right) \cos\left(k_{\mathrm{ts}} d/2\right) \\ & - 4\frac{k_{\mathrm{ts}} k^3}{k_{\mathrm{tl}}} \sin\left(k_{\mathrm{tl}} d/2\right) \cos\left(k_{\mathrm{ts}} d/2\right) - 4\frac{k_{\mathrm{tl}} k^3}{k_{\mathrm{ts}}} \sin\left(k_{\mathrm{tl}} d/2\right) \cos\left(k_{\mathrm{ts}} d/2\right) \\ & - 4k_{\mathrm{ts}} k^3 (d/2) \cos\left(k_{\mathrm{tl}} d/2\right) \cos\left(k_{\mathrm{ts}} d/2\right) + 4k_{\mathrm{tl}} k^3 (d/2) \sin\left(k_{\mathrm{tl}} d/2\right) \sin\left(k_{\mathrm{ts}} d/2\right)\end{aligned} \tag{C.12}$$

$$\begin{aligned}\Delta^{'}_{\mathrm{a}} = {} & -8qk \sin\left(k_{\mathrm{tl}} d/2\right) \cos\left(k_{\mathrm{ts}} d/2\right) - \frac{q^2 k}{k_{\mathrm{tl}}}(d/2) \cos\left(k_{\mathrm{tl}} d/2\right) \cos\left(k_{\mathrm{ts}} d/2\right) \\ & + \frac{q^2 k}{k_{\mathrm{ts}}}(d/2) \sin\left(k_{\mathrm{tl}} d/2\right) \sin\left(k_{\mathrm{ts}} d/2\right) + 8k_{\mathrm{tl}} k_{\mathrm{ts}} k \cos\left(k_{\mathrm{tl}} d/2\right) \sin\left(k_{\mathrm{ts}} d/2\right) \\ & - 4\frac{k_{\mathrm{ts}} k^3}{k_{\mathrm{tl}}} \cos\left(k_{\mathrm{tl}} d/2\right) \sin\left(k_{\mathrm{ts}} d/2\right) - 4\frac{k_{\mathrm{tl}} k^3}{k_{\mathrm{ts}}} \cos\left(k_{\mathrm{tl}} d/2\right) \sin\left(k_{\mathrm{ts}} d/2\right) \\ & + 4k_{\mathrm{ts}} k^3 (d/2) \sin\left(k_{\mathrm{tl}} d/2\right) \sin\left(k_{\mathrm{ts}} d/2\right) - 4k_{\mathrm{tl}} k^3 (d/2) \cos\left(k_{\mathrm{tl}} d/2\right) \cos\left(k_{\mathrm{ts}} d/2\right)\end{aligned} \tag{C.13}$$

---

[2] These are calculated taking the derivative of $\Delta_{\mathrm{s,a}}$ with respect to k and maintaining the frequency fixed $\Rightarrow w = \text{const.}$

were

$$q = \sqrt{\frac{w^2}{c_{\mathrm{S}}^2} - 2k^2} \tag{C.14}$$

Alternative numerical expression for the determination of these derivatives can be also accomplish using for example the following approximation formula[139] with: $y = \mathrm{f}(x) = \Delta_{\mathrm{s,a}}(k, w)$; $w = \text{conts.}$ and $x = k$; e.g. $\Delta x = k/10000$

$$y_{\mathrm{n}}^{'} \approx \frac{1}{12\Delta x}(3y_{\mathrm{n+1}} + 10y_{\mathrm{n}} - 18y_{\mathrm{n\text{-}1}} + 6y_{\mathrm{n\text{-}2}} - y_{\mathrm{n\text{-}3}}) \tag{C.15}$$

C.2 Summary of expressions for point load excitation

A list of the remaining terms for calculation of the displacement fields for the point load solution is shown here. For more details consult Refs.[5, 6][3]:

$$u_{\mathrm{z}}^{\mathrm{s}}(r,z) = \sum_{k_{\mathrm{s}}} D_{\mathrm{n}}^{\mathrm{s}}[s_3 \sin{(pz)} + s_4 \sin{(qz)}]H_0^{(2)}(k_{\mathrm{s}}r) \tag{C.16}$$

$$u_{\mathrm{z}}^{\mathrm{a}}(r,z) = \sum_{k_{\mathrm{a}}} D_{\mathrm{n}}^{\mathrm{a}}[a_3 \cos{(pz)} + a_4 \cos{(qz)}]H_0^{(2)}(k_{\mathrm{a}}r) \tag{C.17}$$

$$u_{\mathrm{r}}^{\mathrm{s}}(r,z) = -\sum_{k_{\mathrm{s}}} D_{\mathrm{n}}^{\mathrm{s}}[s_1 \cos{(pz)} + s_2 \cos{(qz)}]H_1^{(2)}(k_{\mathrm{s}}r) \tag{C.18}$$

$$u_{\mathrm{r}}^{\mathrm{a}}(r,z) = -\sum_{k_{\mathrm{a}}} D_{\mathrm{n}}^{\mathrm{a}}[a_1 \sin{(pz)} + a_2 \sin{(qz)}]H_1^{(2)}(k_{\mathrm{a}}r) \tag{C.19}$$

where

$$D_{\mathrm{n}}^{\mathrm{s}} = \frac{kP\hat{W}_{\mathrm{s}}^{\mathrm{n}}(z)}{4\mathrm{i}\hat{I}_{\mathrm{nn}}^{\mathrm{s}}} \qquad D_{\mathrm{n}}^{\mathrm{a}} = \frac{kP\hat{W}_{\mathrm{a}}^{\mathrm{n}}(z)}{4\mathrm{i}\hat{I}_{\mathrm{nn}}^{\mathrm{a}}} \tag{C.20}$$

and

$$s_1 = 2\cos{(qh)} \qquad a_1 = 2\sin{(qh)} \tag{C.21}$$

$$s_2 = -[(k^2 - q^2)/k^2]\cos{(ph)} \qquad a_2 = -[(k^2 - q^2)/k^2]\sin{(ph)} \tag{C.22}$$

$$s_3 = -(2p/k)\cos{(qh)} \qquad a_3 = (2p/k)\sin{(qh)} \tag{C.23}$$

$$s_4 = -[(k^2 - q^2)/(qk)]\cos{(ph)} \qquad a_4 = [(k^2 - q^2)/qk]\sin{(ph)} \tag{C.24}$$

The expression for $W_{\mathrm{s,a}}^{\mathrm{n}}$ and $I_{\mathrm{nn}}^{\mathrm{s,a}}$ are:[4]

$$W_{\mathrm{s}}^{\mathrm{n}} = A_{\mathrm{n}}[s_3 \sin{(pz)} + s_4 \sin{(qz)}] \qquad W_{\mathrm{a}}^{\mathrm{n}} = B_{\mathrm{n}}[a_3 \cos{(pz)} + a_4 \cos{(qz)}] \tag{C.25}$$

$$I_{\mathrm{nn}}^{\mathrm{s}} = \mu[c_1^{\mathrm{s}} \cos^2{(ph)} + c_2^{\mathrm{s}} \cos^2{(qh)}] \qquad I_{\mathrm{nn}}^{\mathrm{a}} = \mu[c_1^{\mathrm{a}} \sin^2{(ph)} + c_2^{\mathrm{a}} \sin^2{(qh)}] \tag{C.26}$$

---

[3] Here the nomenclature of [5] is followed.

[4] The caret above the symbols in Eqs. (C.20) indicates that $A_{\mathrm{n}} = B_{\mathrm{n}} = 1$.

with

$$c_1^{\mathrm{s}} = \frac{(k^2 - q^2)(k^2 + q^2)}{2q^3k^3}[2qh(k^2 - q^2) - (k^2 + 7q^2)\sin(2qh)] \tag{C.27}$$

$$c_2^{\mathrm{s}} = \frac{(k^2 + q^2)}{pk^3}[4k^2ph + 2(k^2 - 2p^2)\sin(2ph)] \tag{C.28}$$

$$c_1^{\mathrm{a}} = \frac{(k^2 - q^2)(k^2 + q^2)}{2q^3k^3}[2qh(k^2 - q^2) + (k^2 + 7q^2)\sin(2qh)] \tag{C.29}$$

$$c_2^{\mathrm{a}} = \frac{(k^2 + q^2)}{pk^3}[4k^2ph - 2(k^2 - 2p^2)\sin(2ph)] \tag{C.30}$$

and[5]

$$p = \sqrt{\frac{w^2}{c_{\mathrm{L}}^2} - k^2} \quad ; \quad c_{\mathrm{L}} = \sqrt{\frac{\lambda + 2\mu}{\rho}} \tag{C.31}$$

$$q = \sqrt{\frac{w^2}{c_{\mathrm{S}}^2} - k^2} \quad ; \quad c_{\mathrm{S}} = \sqrt{\frac{\mu}{\rho}} \tag{C.32}$$

---

[5] The corresponding dispersion equations are the same as Eqs. (C.8) and (C.9).

Appendix D

Results for different receivers and plate profiles

The differences in simulations when using *punctual* and *multi-point* receivers in the LAMB programme are presented in this appendix. The appendix also includes comparisons results for line and two-dimensional excitations/emission plate profiles as well as simulations when the ideal plane wave (PW) excitation condition is used. The common parameters for the simulations were:

- Plate and mode: $d = 1.5\,\text{mm}$ aluminium laminate with A0 Lamb mode.
- THS zone parameters:
  - **Excitation** 1: line $\{[l_x, l_y] \cong [20, 0]\ \text{mm}\}$ & two-dimensional rectangular profiles $\{[l_x, l_y] \cong [20, 8]\text{mm}\}$. Radius of filling circles $a = 0.5\text{mm}$.
  - **Emission** 2: line $\{[l_x, l_y] \cong [40, 0]\ \text{mm}\}$ and two-dimensional rectangular profiles $\{[l_x, l_y] \cong [40, 8]\ \text{mm}\}$. Square IRM plate filling elements $\{2a_\text{r}, 2b_\text{r}\} = \{0.5, 0.5\}$ mm.
- Emitter[1]:
  - **Transducer**1: SIE concave array: $N_\text{a} = 16, R = 35\text{mm}$, tilt $\theta_\text{i} = 8^\text{o}$, cord $c_\text{a} \cong 15.87\text{mm}$. Element dimensions $\{2a, 2b, p_\text{e}\} = \{1, 15, 0\}\text{mm}$.
  - Excitation: plane wave generation (focus at infinity), with a single cycle symmetric square pulse $f_0 \cong 830\,\text{kHz}$, $BW = 0.7\text{-}1.2$ MHz.
- Receiver:
  - noise+directivity: ideal conditions $\sigma_\text{noise} = 0$, directivity $A_\text{dir} = \text{on}$.
  - **Transducer** 2**a**: concave array: $N_\text{a} = 10$, $R = 35\,\text{mm}$, $\theta_\text{r} = 8^\text{o}$, $c_\text{a} \cong 9.97\text{mm}$. Element type: single point sensors $\{2a, 2b, p_\text{e}\} = \{0, 0, 1\}\text{mm}$
  - **Transducer** 2**b**: concave array, $N_\text{a} = 10$, $R = 35\,\text{mm}$, tilt $\theta_\text{r} = 8^\text{o}$, cord $c_\text{a} \cong 9.97\,\text{mm}$. Element type: rectangular multi-point sensors $\{\text{width,height}\} \leftrightarrow \{2, 10\}$ points, dims. $\{2a, 2b, p_\text{e}\} = \{1, 10, 0\}$ mm.
- Normalization: All reception radiation diagrams are normalized and express in dB.

---

[1] This is valid for all the cases with the exception on the last two examples in which the array were replaced by the ideal PW excitation. See pp. 73.

The following figures A1-A6 detail the plate simulation conditions ($E1_{a,b}$ and $E2_{a,b}$) used in the calculation of the radiation diagrams with single ($T2_a$) and multi-point ($T2_b$) sensor arrays[2]. The comparisons were made using different combinations of receiver transducers and excitation/emission plate profiles.

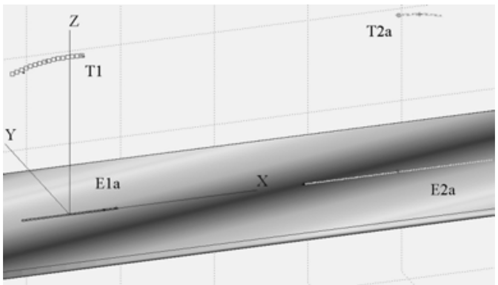

Figure D.1: View of the line profile simulation scenario with T1 and $T2_a$.

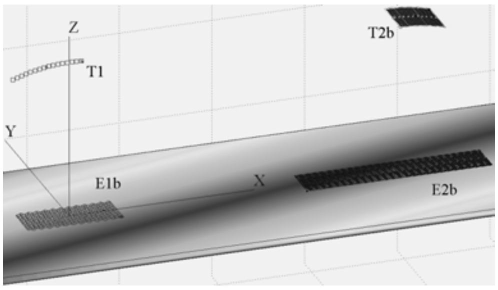

Figure D.2: View of the 2D profile simulation scenario with T1 and $T2_b$.

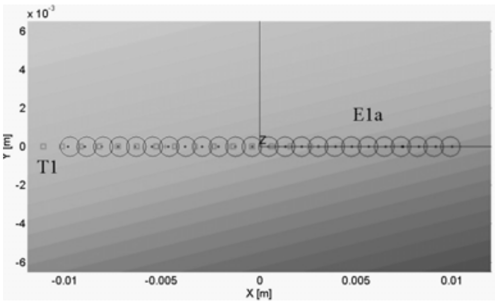

Figure D.3: Top view of the line excitation region $E1_a$.

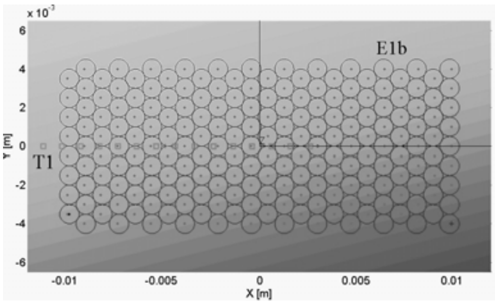

Figure D.4: Top view of the 2D excitation region $E1_b$.

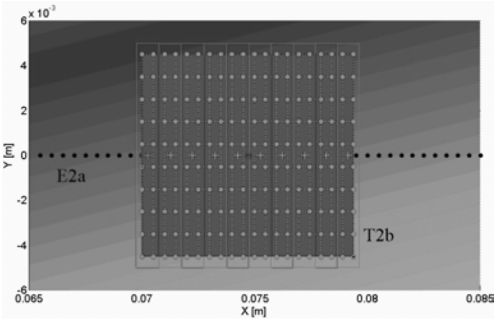

Figure D.5: Top view of the line emission zone $E2_a$ with a 10 sensors multi-point transducer $T2_b$ on top.

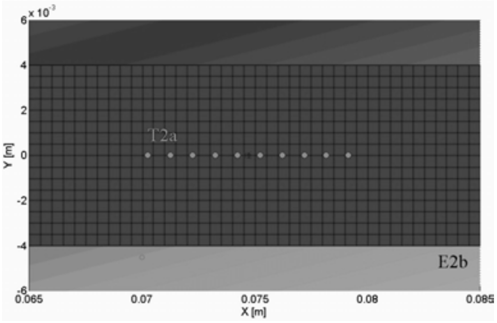

Figure D.6: Top view of the 2D plate emission area $E2_b$ with the single point 10 element transducer $T2_a$ on top.

---

[2] In figure A5 only the central points of the IRM plate radiation elements are plotted.

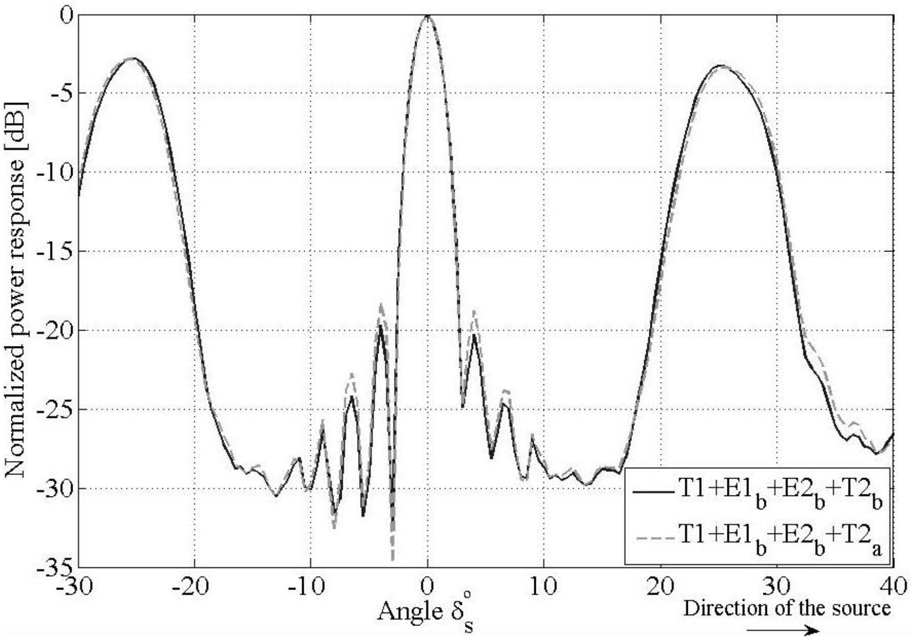

Figure D.7: Radiation diagrams for single and multi-point sensor arrays.

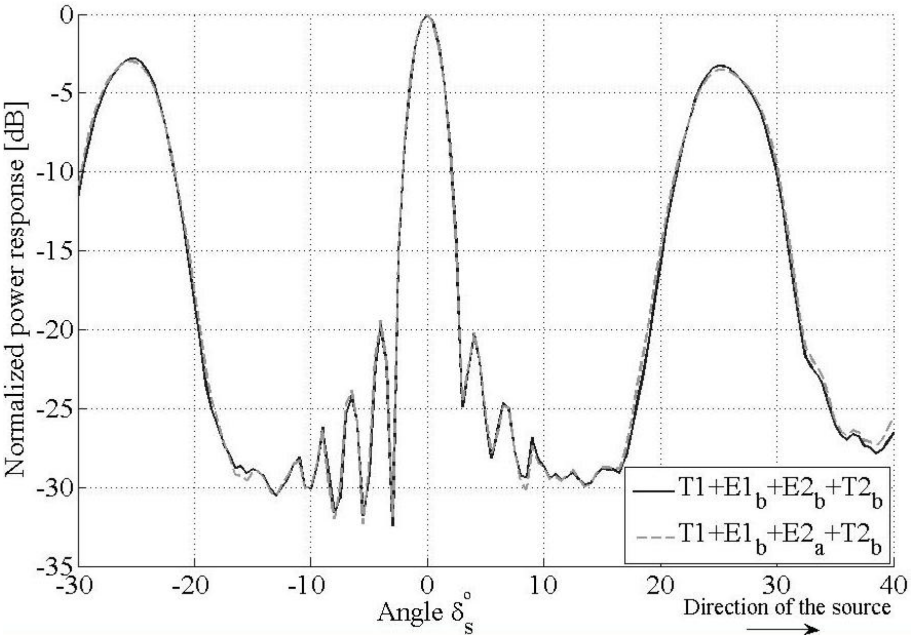

Figure D.8: Radiation diagrams with different *emission* laminate profiles.

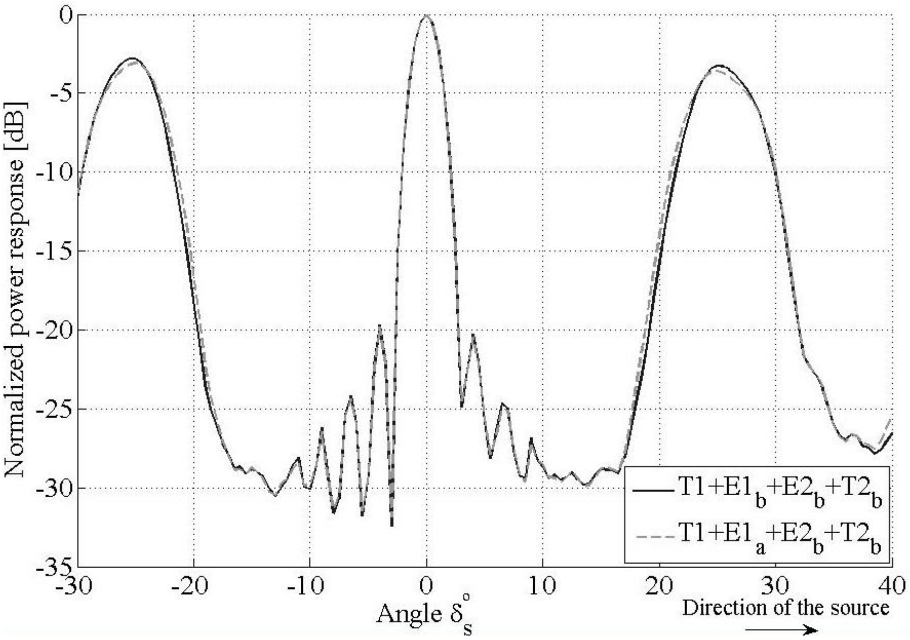

Figure D.9: Radiation diagrams with different *excitation* laminate profiles.

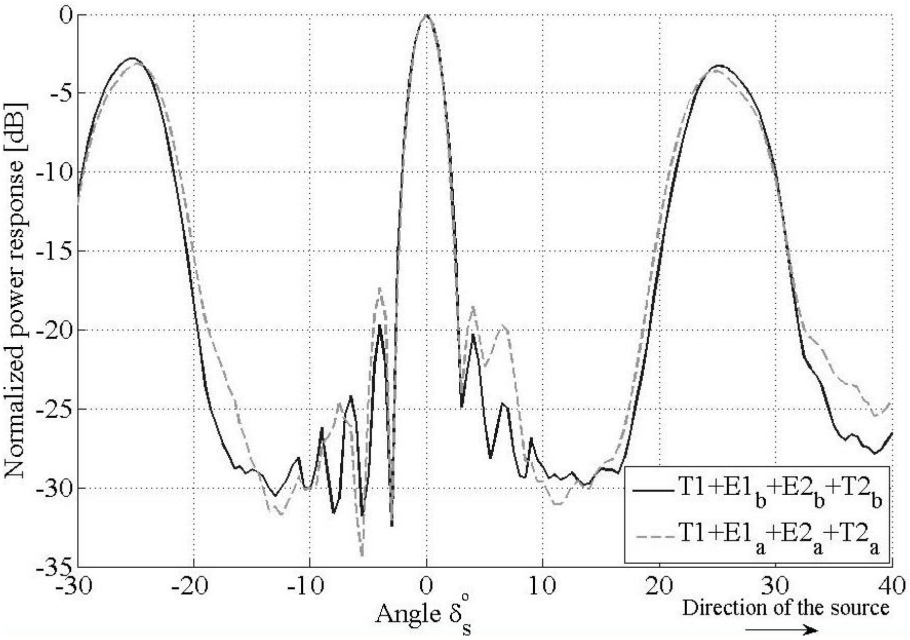

Figure D.10: Radiation diagrams for single and multi-point sensor receivers with different excitation/emission profiles.

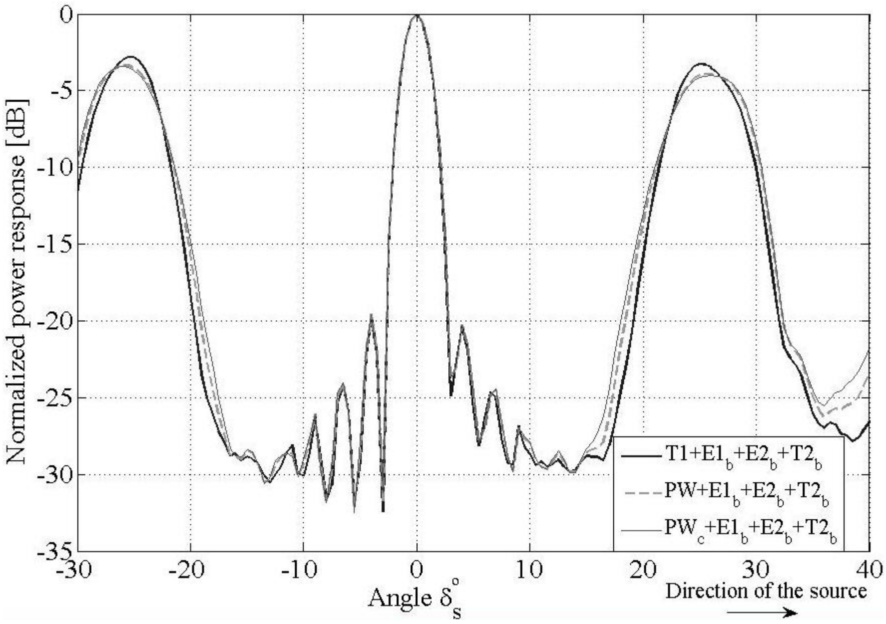

Figure D.11: Radiation diagrams for multi-point 10 sensors concave arrays with different plate excitation conditions: 1) T1 SIE@16 concave array, 2) PW or ideal plane wavefront condition $[l_x, l_y] \approx [20, 8]$ mm and 3)PW$_c$ the same as PW (see Fig. D.4) but a crossed profile $[l_x, l_y] \approx [8, 20]$ mm.

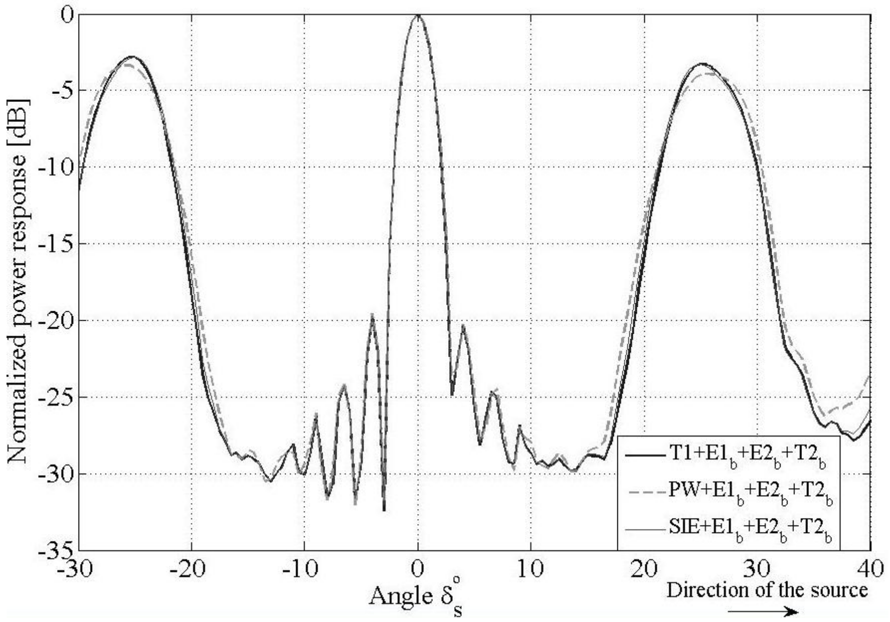

Figure D.12: Radiation diagrams for multi-point 10 sensors concave arrays with different plate excitation conditions: 1) T1 SIE@16 concave array, 2) PW $[l_x, l_y] \approx [20, 8]$ mm and 3) 1 single SIE radiator $\{2a, 2b\} = \{10, 10\}$ mm.

Appendix E

LAMB toolbox capabilities and computer issues

The software result analysis capabilities and the issues related to time consumed and memory required for the calculations of the toolbox are presented in this appendix.

E.1 Software results and analysis capabilities

The programme main results and the possibilities of their analysis are listed here. The possible calculations can be separated into three main categories with the following characteristics[1]:

1. Emission results
    (a) Pressure signals $p(t)$ on the laminate surface.
2. Propagation results
    (a) Calculation of the Lamb dispersion relationships for a given isotropic layered system by the GMM.
    (b) Determination of the displacements $u(t)$ on the plate emission area.
    (c) Calculation of the (f, k) spectrum map by 2D FFT from a discrete set of displacement traces captured along a line on the emission area.
3. Reception results[2]
    (a) Pressure signals $p(t)$ on the receiver input.
    (b) Voltage signals $v(t)$ on the receiver output.
    (c) DAS Beamforming[3]
        i. Radiation diagrams (energy or amplitude) of $v(t)$ signals.
        ii. Beamformer output signal $v_{\text{DAS}}(t)$, with or without delays.

---

[1] In all the cases were signals are available the extraction and plotting of maximum amplitude, power and signal delay profiles are available in forms a line and surface plots. Photo and movie capabilities are also available for pressure and surface displacements.

[2] The inclusion of the directivity filter $A_{\text{dir}}(\mathrm{i}w)$ is selectable by the user as well as the addition of a fixed amount [W] of white Gaussian noise to the traces.

[3] This is possible only in case of use of an array as a receiver; then a simple Delay And Sum (DAS) beamformer is available. The code for an implemented sidelobe canceller (SLC) is also available but inconclusive results at present.

E.2 Computer issues

§Time consumed in the calculations

Because of the structure of the software the time consumed during the calculations depends basically on the size and relative position of the field areas[4] defined in the following stages:

1. IRM excitation calculations
   - (a) Number of transducer excitation elements N_{ai}.
   - (b) Number of plate field "points" N_{p}.
   - (c) Distance between the transducer and the plate R_{i}.
   - (d) IRM sampling frequency $f_{\mathrm{s}}^{\mathrm{IRM}}$.
2. THS propagation calculations
   - (a) Number of plate excitation "points" N_{p}.
   - (b) Number of plate emission elements N_{e}.
   - (c) Number of Lamb modes simulated m.
   - (d) Distance between the excitation/emission areas R_{p}.
   - (e) THS sampling frequency $f_{\mathrm{s}}^{\mathrm{THS}}$.
   - (f) Number of discrete frequencies N_{f} to compute in the BW[5].
3. IRM plate emission calculations
   - (a) Number of plate emission elements N_{e}.
   - (b) Number of sensors and field points by sensor in the receiver $N_{\mathrm{ar}}, N_{\mathrm{ar}}^{\mathrm{p}}$.
   - (c) Distance between the emission area and the receiver R_{r}.
   - (d) IRM sampling frequency $f_{\mathrm{s}}^{\mathrm{IRM}}$.

These items can be summarized in the following estimated times:

$$\begin{aligned} et_1 &= \hat{t}_{\mathrm{p1}}\, N_{\mathrm{p}}\, N_{\mathrm{ai}} \\ et_2 &= \hat{t}_{\mathrm{p2}}\, m\, N_{\mathrm{f}}\, N_{\mathrm{p}}\, N_{\mathrm{e}} \\ et_3 &= \hat{t}_{\mathrm{p3}}\, N_{\mathrm{e}}\, N_{\mathrm{ar}}^{\mathrm{p}}\, N_{\mathrm{ar}} \end{aligned} \tag{E.1}$$

---

[4] These two factors in combination with the sampling frequencies chosen determine the number of points in the traces N_{1-3}. The final $N_{\mathrm{i}} = g(t_{\mathrm{max}}^{\mathrm{IRM}})$ values are selected after a $\rightarrow 2^n$ conversion process for speed up the FFT calculations.

[5] This is given by: $N_{\mathrm{f}} = \frac{BW}{\Delta_{\mathrm{f}}}$, with $\Delta_{\mathrm{f}} = f_{\mathrm{s}}^{\mathrm{THS}}/N^{\mathrm{THS}}$.

where $\hat{t}_{\mathrm{pi}}$ [s] are the corresponding estimated times[6] required to calculate a signal at a point originated from a single radiator. Then the programme total computing estimated time is given by

$$et = et_1 + et_2 + et_3 \tag{E.2}$$

Example 1:
As an example of a full computation scenario the following Table E.1 summarizes the parameter values and estimated elapsed times from the test with A0 mode[7] in Figure D.11

Table E.1: Full 2D simulation example from Figure D.11.

1)	$N_{\mathrm{ai}} = 16$	$N_{\mathrm{p}} = 204$	$m = 1$	$t_{\mathrm{p1}} = 0.0077\,\mathrm{s}$	$et_1 = 25.13\,\mathrm{s}$
2)	$N_{\mathrm{f}} = 41$	$N_{\mathrm{p}} = 204$	$N_{\mathrm{e}} = 1377$	$t_{\mathrm{p2}} = 0.00032\,\mathrm{s}$	$et_2 = 3685.5\,\mathrm{s}$
3)	$N_{\mathrm{e}} = 1377$	$N_{\mathrm{ar}}^{\mathrm{p}} = 10$	$N_{\mathrm{ar}} = 10$	$t_{\mathrm{p3}} = 0.0071\,\mathrm{s}$	$et_3 = 977.67\,\mathrm{s}$
					$et = 1:18:14$ hrs:min:sec

Example 2:
A more typical and fast example is using line excitation/reception profiles such as those from Figure D.10. Then the parameters and time are given in the following Table E.2:

Table E.2: Simplified example from Figure D.10 with line profiles (a case).

1)	$N_{\mathrm{ai}} = 16$	$N_{\mathrm{p}} = 24$	$m = 1$	$t_{\mathrm{p1}} = 0.0066\,\mathrm{s}$	$et_1 = 2.53\,\mathrm{s}$
2)	$N_{\mathrm{f}} = 41$	$N_{\mathrm{p}} = 24$	$N_{\mathrm{e}} = 81$	$t_{\mathrm{p2}} = 0.0003\,\mathrm{s}$	$et_2 = 23.91\,\mathrm{s}$
3)	$N_{\mathrm{e}} = 81$	$N_{\mathrm{ar}}^{\mathrm{p}} = 1$	$N_{\mathrm{ar}} = 10$	$t_{\mathrm{p3}} = 0.0073\,\mathrm{s}$	$et_3 = 5.91\,\mathrm{s}$
					$et = 32.4\,\mathrm{s}$

§Programme Memory Use

The programme main memory requirements (M_{i} in Bytes or Mega Bytes) are described in this section. These are highly dependant on the way the programme was coded and closely related to time calculations[8] and the matlab environment characteristics[9]. For the LAMB programme these are dived

---

[6] These are based on 10 trial calculations on dual core AMD® 6400+ Athlon machine running Windows®XP/SP2 with 3.25 GB of Ram.

[7] Other parameters for this case were: $N_{1,3} = 16384$, $N_2 = 960$, $R_{i,r} = 35\,\mathrm{mm}$, $f_{\mathrm{s}}^{IRM} = 100\,\mathrm{MHz}$, $f_{\mathrm{s}}^{THS} = 12\,\mathrm{MHz}$, $BW = 0.7$-$1.2\,\mathrm{MHz}$, $\Delta_{\mathrm{f}} = 12.5\,\mathrm{kHz}$,.

[8] When using *for...to* loops in a computer programme there is always a transaction between memory consumed and time elapsed of calculations. Then the faster the computations, the more memory is required to perform them.

[9] The multiplicative constant 2 in equations A.3 and A.5 is due to the use of an addition buffer during superposition calculations. The case equation A.4 is different because the frequency excitation matrix $[E]$ is composed of N_{f} rows and N_{p} columns includes the amplitude and phase spectrum. The number of Bytes required to storage a quantity in *double* type format in matlab is $n_{\mathrm{d}} = 8$ Bytes.

into:

1. Emission requirements:

$$M_1 = 2\, N_\mathrm{p}\, N_1\, n_\mathrm{d} \tag{E.3}$$

2. Propagation requirements:

$$M_2 = (m\, N_\mathrm{e}\, N_2 + 2\, N_\mathrm{p}\, N_\mathrm{f})\, n_\mathrm{d} \tag{E.4}$$

3. Reception requirements:

$$M_3 = 2\, N_\mathrm{ar}\, N^\mathrm{p}_\mathrm{ar}\, N_3\, n_\mathrm{d} \tag{E.5}$$

Then the total software memory requirement is given by:[10]

$$M_\mathrm{t} = M_1 + M_2 + M_3 \tag{E.6}$$

Using the data from the examples given before, the storage needs in the case of example 1 will be:

Table E.3: Memory requirements for example 1, Fig. D.11 $t^\mathrm{IRM}_\mathrm{max} = 100\,\mathrm{us}$.

1)	$N_\mathrm{p} = 204$	$N_1 = 16384$	$n_\mathrm{d} = 8$	$M_1 = 53477376$ Bytes
2)	$N_\mathrm{e} = 1377$	$N_2 = 960$	$N_\mathrm{f} = 41$	$M_2 = 10709184$ Bytes
3)	$N_\mathrm{ar} = 10$	$N_3 = 16384$	$N^\mathrm{p}_\mathrm{ar} = 10$	$M_3 = 26214400$ Bytes
				$M \cong 86.21$ MB

and for example 2 are:

Table E.4: Memory requirements for example 2, Fig. D.10 $t^\mathrm{IRM}_\mathrm{max} = 100\,\mathrm{us}$.

1)	$N_\mathrm{p} = 24$	$N_1 = 16384$	$n_\mathrm{d} = 8$	$M_1 = 6291456$ Bytes
2)	$N_\mathrm{e} = 81$	$N_2 = 960$	$N_\mathrm{f} = 41$	$M_2 = 637824$ Bytes
3)	$N_\mathrm{ar} = 10$	$N_3 = 16384$	$N^\mathrm{p}_\mathrm{ar} = 1$	$M_3 = 2621440$ Bytes
				$M \cong 9.11$ MB

An example of the $\rightarrow 2^n$ conversion process applied to number of points on the IRM traces ($N_{1,3}$) to speed up the FFT calculations are given in the following Table A.5[11]:

---

[10] This is actually an approximated expression based on principal variables only.

[11] The determination of N_2 is not described here because although its determination is more complex it has less influence in the memory required.

Table E.5: Number of points of IRM signals $N_{1,3}$ in function of the maximum time.

$t_{\mathrm{max}}^{\mathrm{IRM}}$	10 us	80 us	**100 us**	300 us	500 us	1 ms	2 ms
$\hat{N}$ @$f_{\mathrm{s}}^{\mathrm{IRM}} = 100\,\mathrm{MHz}$	4000	8000	10000	30000	50000	100000	200000
$\downarrow$	2^{12}	2^{13}	2^{14}	2^{15}	2^{16}	2^{17}	2^{18}
$N_{1,3}$	4096	8192	**16384**	32768	65536	131072	262144
$\hat{N}$ @$f_{\mathrm{s}}^{\mathrm{IRM}} = 300\,\mathrm{MHz}$	3000	24000	30000	90000	150000	300000	600000
$\downarrow$	2^{12}	2^{15}	2^{15}	2^{17}	2^{18}	2^{19}	2^{20}
$N_{1,3}$	4096	32768	32768	131072	262144	524288	1048576

§Memory fragmentation issues

A common difficulty encountered in a PC environment running Matlab is the memory fragmentation problem. This problem arouse because of a poor memory management made by the operating system (OS) and the way in what matlab stores the information.
The basic idea is although a machine can have large amounts of memory, say 4 GB the largest size of a free *continuous* block is bounded by the existence of other programs and OS process. This situation can be increased by continuous runs of a matlab programme to reduce the size of the largest free available block.
Then if a large matrix has to be stored it may not be enough *continuous* space to allocated it although there is still memory in the system. This is because matlab stores matrices in a continuous fashion[12].
A list of possible solutions to circumvent this problem are for example:

- Close all non matlab programme and process.
- Activate the /3 GB switch in the **boot.txt** file[13]
- Reallocate with a memory utility tool the OS process (dll's) that obstruct and fragment the memory space.
- Re code (if possible) the programme or routine in such a way that uses less memory at expenses of long computation times.
- Run the programme in a Linux/Unix OS.

---

[12] Tools to find out the size of the largest available block are: **dumpmemmex.dll** in matlab 6.5 and **chkmem.m** in matlab 7.x.

[13] This is for the Windows OS only. To do this enter into Control panel, System, Advance options, Start & Recovery. Then press edit and add at the end of the line (file *boot.txt*) the switch: /3GB .

Appendix F

Directional response of individual array radiators

This appendix shows the directional response of the individual elements that integrate the air-coupled concave arrays used in this thesis[1]. The response of a real single excited radiator is compared with those of two proposed models: 1)Single Ideal Element (SIE) and 2)Single Non-Ideal Element (SNIE)[2].

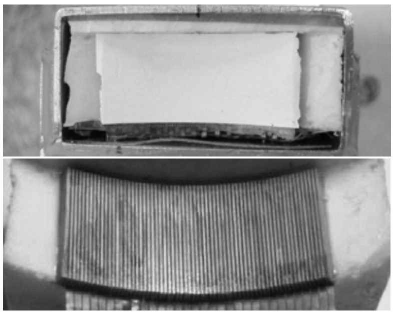

Figure F.1: Photos of an air-coupled array with and without adaptation layers.

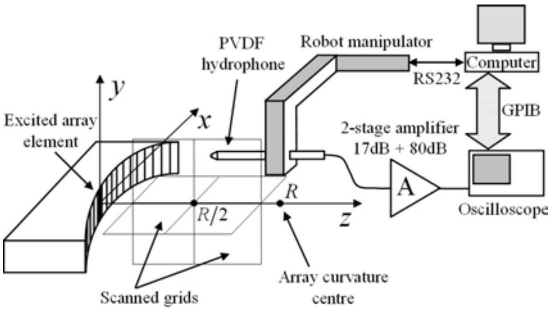

Figure F.2: View of the experimental setup.

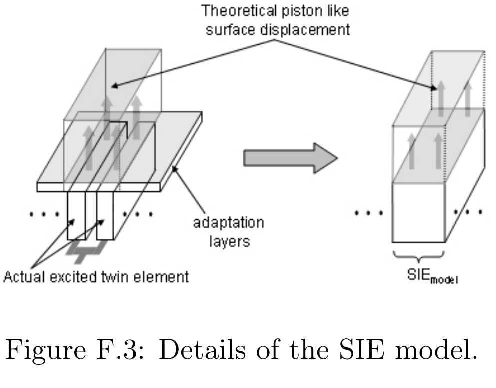

Figure F.3: Details of the SIE model.

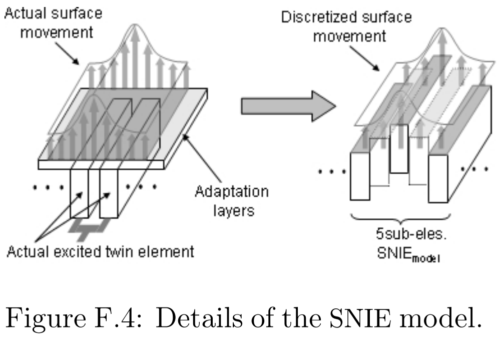

Figure F.4: Details of the SNIE model.

---

[1] See figure F.1 and Ref.[178]. The 64 piezoelectric slabs $\{2a, 2b, p_{\mathrm{e}}\} = [0.3, 15, 0.2]$ mm forms the 32 twin elements.

[2] For more details consult Ref.[214].

The setup for the measurements can be observed in figure F.2. A pulsed signal of $f_0 \cong 0.8\,\mathrm{MHz}$ and $BW \cong 0.2\,\mathrm{MHz}$ was used and the common radial distance of the measurements was $R = 17.3\,\mathrm{mm}$[3]

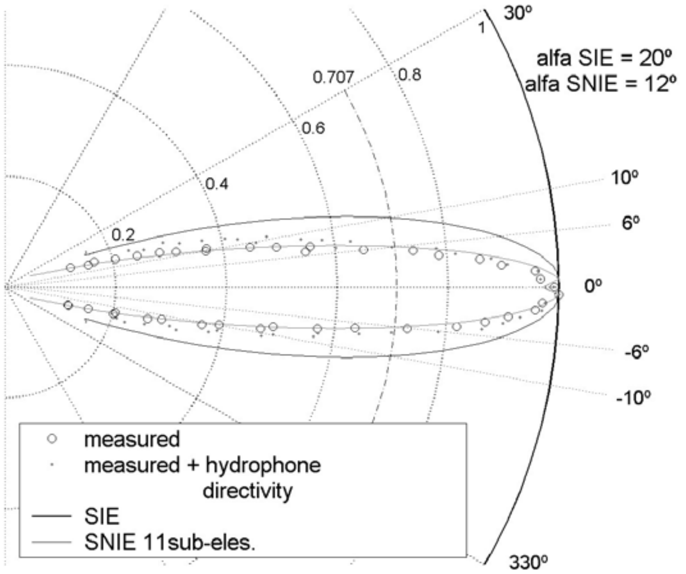

Figure F.5: Measured directivity in the XZ plane.

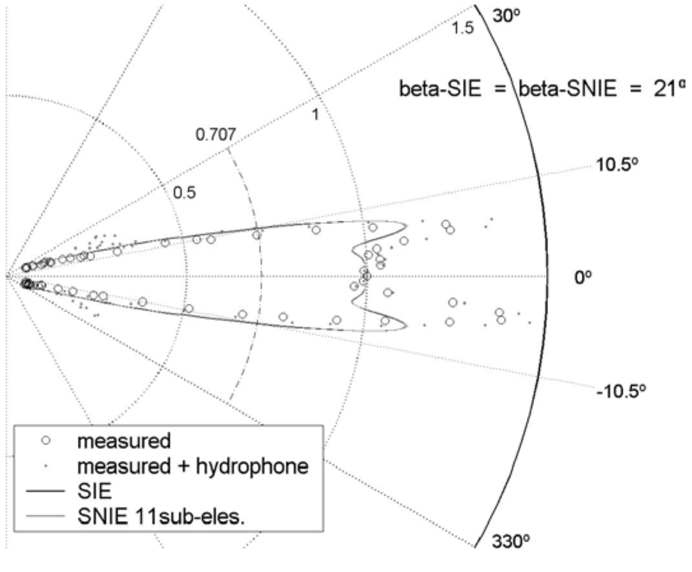

Figure F.6: Measured directivity in the YZ plane.

---

[3] This value of approximately half the curvature radius of the array ($R \cong 35\,\mathrm{mm}$) was used due the very low amplitude of the signals in air. More details in Ref.[214].

Bibliography

[1] Achenbach, J. D. *Wave propagation in elastic solids*, vol. 16. North-Holland, Amsterdam . London, 1973.

[2] Achenbach, J. D. Lamb waves as thickness vibrations superimposed on a membrane carrier wave. *J. Acoust. Soc. Am. 103*, 5 (May 1998), 2283–2286.

[3] Achenbach, J. D. Calculation of wave fields using elstodynamic reciprocity. *Elsevier, Int. J. Solids & Structures 37* (2000), 7043–7053.

[4] Achenbach, J. D. Simplifications for the calculation of surface wave pulses generated by laser-irradiation. *J. Acoust. Soc. Am. 116*, 3 (Sep. 2004), 1481–1487.

[5] Achenbach, J. D., and Xu, Y. Use of elastodynamic reciprocity to analyze point-load generated axisymmetric waves in a plate. *Elsevier, Wave Motion 30* (September 1998), 57–67.

[6] Achenbach, J. D., and Xu, Y. Wave motion in an isotropic elastic layer generated by a time-harmonic point load of arbitrary direction. *J. Acoust. Soc. Am. 106*, 1 (July 1999), 83–90.

[7] Adamou, A. T., and Craster, R. V. Spectral methods for modelling guided waves in elastic media. *J. Acoust. Soc. Am. 116*, 3 (September 2004), 1524–1535.

[8] Alers, J., and Burns, T. Emat designs for special applications. *Mater. Eval. 45* (1987), 1184–1189.

[9] Alleyne, D., and Cawley, P. A two-dimensional fourier transform method for the measurement of propagating multimode signals. *J. Acoust. Soc. Am. 89*, 3 (March 1991), 1159–1168.

[10] Alleyne, D. N. *The Nondestructive Testing of Plates Using Ultrasonic Lamb Waves.* PhD thesis, Imperial College of Science, Technology and Medicine, Feb. 1991.

[11] Alleyne, D. N., and Cawley, P. The interaction of lamb waves with defects. *IEEE Transactions on UFFC 39*, 3 (May 1992), 381–397.

[12] ANSI. Method for the calculation of the absorption of sound by the atmosphere. Tech. Rep. ANSI S1.26-1995, American National Standards Institute, (ANSI), New York, 1995.

[13] Aristégui, C., and S., B. Optimal recovery of the elasticity tensor of general anisotropic materials from ultrasonic velocity data. *J. Acoust. Soc. Am. 101*, 2 (1997), 813–833.

[14] Assaad, J., Decarpigny, J.-N., and Bruneel, C. Application of the finite elemenent method to two-dimensional radiation plroblems. *J. Acoust. Soc. Am. 94*, 1 (July 1993), 562–573.

[15] Auld, B. A. Application of microwave concepts to the theory of acoustic fields and waves in solids. *IEEE Trans. in Microwave Theory and Techniques MTT-17*, 11 (November 1969), 800–811.

[16] Auld, B. A. *Acoustic Fields and Waves in Solids*, vol. I & II. Krieger Publishing Company, Malabar, Florida, 1973. 2nd. Ed.1990.

[17] Auld, B. A., and Kino, G. Normal mode theory for acoustic waves and its application to the interdigital transducer. *IEEE Trans. on Electronic Devices ED-18*, 10 (October 1971), 898–908.

[18] Banerjee, S., and Mal, A. K. Analysis of transient lamb waves generated by dynamic surface sources in thin composite plates. *J. Acoust. Soc. Am. 115*, 5 (May 2004), 1905–1911.

[19] Banerjee, S., Prosser, W., and Mal, A. K. Calculation of the response of a composite plate to localized dynamic surface loads using a new wave number integral method. *Transactions of the ASME 72* (Jan. 2005), 18–24.

[20] Bass, E. H., Sutherland, L. C., and Evans, L. B. Atmospheric absortion of sound: Theorical predictions. *J. Acoust. Soc. Am. 51*, 5 (Part 2) (1972), 1565–1575.

[21] Bass, H. E., Bauer, H. J., and Evans, L. B. Atmospheric absortion of sound: Analytical expressions. *J. Acoust. Soc. Am. 52*, 3 (Part 2) (1972), 821–825.

[22] Beard, M. D., Lowe, M. J. S., and Cawley, P. Ultrasonic guided waves for the inspection of tendons and bolts. *J. Mater. Civ. Eng. ASCE 15* (2003), 212–218.

[23] Benny, G., and Hayward, G. Beam profile measurements and simulations for ultrasonic transducers operating in air. *J. Acoust. Soc. Am. 107*, 4 (April 2000), 2089–2100.

[24] Bermes, C., Kim, J.-Y., Qu, J., and Jacobs, L. J. Nonlinear lamb waves for the detection of material nonlinearity. *Elsevier, Mechanical Systems & Signal Processing 22* (2008), 638–646.

[25] Bernard, A., Lowe, M. J. S., and Deschamps, M. Guided waves energy velocity in absorbing and non-absorbing plates. *J. Acoust. Soc. Am. 110*, 1 (July 201), 186–196.

[26] Bhardwaj, M. *Encyclopedia of Smart Materials*. John Wiley & Sons, 2001, ch. Non-contact ultrasound: the last frontier in non-destructive testing and evaluation, pp. 1–43.

[27] Boulanger, P., and Hayes, M. *Bivectors and Waves in Mechanics and Optics*. Chapman & Hall, 1993. ISBN 0-412-464608.

[28] Boyd, J. P. *Chebyshev and Fourier Spectral Methods*. Dover, New York, NY, USA, 2001.

[29] Brekhovskikh, L. M. *Waves in Layared Media*. New York: Academic Press, 1980.

[30] Bryn, F. Optimum signal processing of three-dimensional arras operating on gaussian signals and noise. *J. Acoust. Soc. Am. 34*, 3 (Mar. 1962), 289–297.

[31] Canaves, M. J., and Pompéia, P. J. Uncertainty of the density of moist air: Gum x monte carlo. *J. of Brazilian Archives of Biology and Technology 49* (Jan. 2006), 87–95.

[32] Capon, J. High-resolution frequency-wavenumber spectrum analysis. *Proc. IEEE 57* (Aug. 1969), 1408–1418.

[33] Carcione, J. M., Herman, G. C., and Kroode ten, A. P. E. Seismic modelling. *Geophysics 67* (2002), 1304–1311.

[34] Castaings, M., and Cawley, P. The generation, propagation, and detection of lamb waves in plates using air-coupled ultrasonic transducers. *J. Acoust. Soc. Am. 100*, 5 (Nov. 1996), 3070–3077.

[35] Castaings, M., and Hosten, B. Transmission coefficient of multilayered absorbing anisotropic media. a solution to the numerical limitations of the thomson haskell method. application to composite materials. In *Ultrasonics proceedings* (Vienne, Autriche, June 1993), pp. 431–434.

[36] Castaings, M., and Hosten, B. Delta operator technique to improve the thomson-hasquell method stability for propagation in multilayered anisotropic absorbing plates. *J. Acoust. Soc. Am. 95*, 4 (April 1994), 1931–1941.

[37] Castaings, M., and Hosten, B. The use of electrostatic, ultrasonic, air-coupled transducers to generate and receive lamb waves in anisotropic, viscoelastic plates. *Elsevier, Ultrasonics 36* (1998), 361–365.

[38] Castaings, M., and Hosten, B. Air-coupled measurement of plane wave, ultrasonic plate transmission for characterising anisotropic, viscoelastic materials. *Elsevier, Ultrasonics 38* (2000), 781–786.

[39] Castaings, M., and Hosten, B. The propagation of guided waves in composite sandwich-like structures and their use for ndt. *Review of Progress in Quantum NDE 20* (2001), 999–1006. Ed. by D. O. Thompson and D. E. Chimenti.

[40] Castaings, M., Hosten, B., and Kundu, T. Inversion of ultrasonic, plane-wave transmission data in composite plates to infer viscoelastic material properties. *Elsevier, NDT&E Int. 33*, 6 (2000), 377–392.

[41] Castaings, M., Le Clezio, E., and Hosten, B. Modal decomposition method for modeling the interaction of lamb waves with cracks. *J. Acoust. Soc. Am. 112*, 6 (Dec. 2002), 2567–2582.

[42] Castaings, M., and Lowe, M. Finite element model for waves guided along solid systems of arbitrary section coupled to infinite solid media. *J. Acoust. Soc. Am. 123*, 2 (Feb. 2008), 696–708.

[43] Ceranoglu, A. N., and Pao, Y. H. Propagation of elastic pulses and acoustic emission in a plate, part i. theory, part ii. epicentral response, part iii. general responses. *ASME Journal of Applied Mechanics* (1981), 125–147.

[44] Chadwick, P., and Tupholme, G. E. In *Proc. Edinburgh Math. Soc.* (1967), vol. 15, pp. 263–277.

[45] Chan, C. W., and Cawley, P. Lamb waves in highly attenuative plastic plates. *J. Acoust. Soc. Am. 104*, 2 (August 1998), 874–881.

[46] Cheng, A., Murray, T. W., and Achenbach, J. D. Simulation of laser-generated ultrasonic waves in layered plates. *J. Acoust. Soc. Am. 110*, 2 (Aug. 2001), 848–855.

[47] Chimenti, D. E. Guided waves in plates and their use in material characterization. *J. Appl. Mech. 50*, 5 (May 1997), 247–284.

[48] Chimenti, D. E., Holland, S. D., and Dong, F. Air-coupled ultrasound and rapid elastic property characterization using focused acoustic beams. In *IEEE Ultrasonic Symposium* (2003), pp. 266–275.

[49] Chu, Y. C., and Rokhlin, S. I. A method for determination of elastic constants of a unidirectional lamina from ultrasonic bulk velocity measurements on [0/90] cross-ply composites. *J. Acoust. Soc. Am. 96*, 1 (Jul. 1994), 342–352.

[50] Cinquin, M., Castaings, M., Hosten, B., Brassier, P., and Pérès, P. Monitoring of the moisture content in carbon-epoxy plates using lamb waves. *Elsevier, NDT&E Int. 38* (June 2005), 37–44.

[51] Dalton, R. P. *The propagation of Lamb waves through metallic aircraft fuselage structure.* PhD thesis, Imperial College of Science, Technology and Medicine, January 2000.

[52] Dalton, R. P., Cawley, P., and Lowe, M. S. J. The potential of guided waves for monitoring large areas of metallic aircraft fuselage structure. *J. of Nondestructive Evaluation 20*, 1 (2001), 29–46.

[53] Davis, R. S. Equation for the determination of the density of moist air. *Metrologia 29* (1992), 67–70.

[54] Dekker, D. L., Piziali, R. L., and Dong, E. J. Effect of boundary conditions on the ultrasonic-beam characteristics of circular disks. *J. Acoust. Soc. Am. 56*, 1 (1974), 87–93.

[55] Delannoy, B., Lasota, H., Bruneel, C., Torguet, R., and Bridoux, E. The infinite planar baffles problem in acoustic radiation and its experimental verification. *J. Appl. Phys. 50* (1979), 5189–5195.

[56] Demma, A. *The interaction of guided waves with discontinuities in structures.* PhD thesis, Imperial College of Science, Technology and Medicine, January 2003.

[57] Ditri, J. J., Pilarski, A., Pavlakovic, B., and Rose, J. L. Generation of guided waves in a plate by axisymmetric normal surface loading. *Review of Progress in Quantitative NDE 13* (1994), 133–140. Ed. by D.O. Thomson and D.E. Chimenti, Plenum Press.

[58] Ditri, J. J., and Rajana, K. An experimental study of the angular dependence of lamb wave excitation amplitudes. *J. of Sound and Vibration 5* (1997), 755–768.

[59] Duflo, H., Morvan, B., and Izbicki, J. L. Interaction of lamb waves on bonded composite plates with defects. *Elsevier, Int. J. Composite Structures 79* (2007), 229–233.

[60] Eisenhardt, C., Jacobs, L. J., and Qu, J. Experimental lamb wave spectra of cracked plates. In *AIP Conf. Proc.* (2000), vol. 509A, pp. 343–349.

[61] El youbi, F., Grondel, S., and Assaad, J. Signal processing for damage detection using two different array transducers. *Elsevier, Ultrasonics 42* (2004), 803–806.

[62] Fei, D., Chimenti, D. E., and Teles, S. V. Chimenti material property estimation in thin plates using focused synthetic-aperture acoustic beams. *J. Acoust. Soc. Am. 113*, 5 (May 2003), 2599–2610.

[63] Fink, M. A., and Cardoso, J. F. Diffraction effects in pulse-echo measurements. *IEEE Trans. Son. Ultrason SU*, 31 (July 1984), 313–329.

[64] Firestone, F. A., and Ling, D. S. Propagation of waves in plates. Tech. rep., Sperry Products, Danbury, CT, USA, 1945.

[65] Firestone, F. A., and Ling, D. S. Method and means for generating and utilizing vibration waves in plates, Patent, 1954.

[66] Fischer, F. A. *Acustica 1* (1951), 35–39.

[67] Forbes, M., Lechter, S., and Stepanishen, P. R. A wave vector, time-domain method of forward projecting time-dependent pressure fields. *J. Acoust. Soc. Am. 90*, 5 (November 1991), 2782–2793.

[68] Fornberg, B. *A Practical Guide to Pseudospectral Methods.* Cambridge University Press, Cambridge, UK, 1996.

[69] Fox, J. D., Khuri-Yakub, B., and S., K. G. High frequency wave measurements in air. In *IEEE, Ultrasonics Symposium* (1983), pp. 581–592.

[70] Freedman, A. Sound field of a rectangular piston. *J. Acoust. Soc. Am. 32*, 2 (February 1960), 197–209.

[71] Freedman, A. Sound field of plane or gently curved pulsed radiators. *J. Acoust. Soc. Am. 48*, 1 (July 1970), 221–227.

[72] Freedman, A. Transient fields of acoustic radiators. *J. Acoust. Soc. Am. 48*, 1 (July 1970), 135–138.

[73] Freedman, A. Farfield of pulsed rectangular acoustic radiator. *J. Acoust. Soc. Am. 49*, 3 , part2 (1971), 738–748.

[74] Freedman, A. Reply to comments on farfield of pulsed rectangular acoustic radiator. *J. Acoust. Soc. Am. 52* (1972), 437–438.

[75] Fromme, P. *Defect detection in plates using guided waves.* PhD thesis, Swiss Federal Institute of Technology, Zürich, 2001.

[76] Fromme, P., and Sayir, M. B. Detection of cracks at rivet holes using guided waves. *Elsevier, Ultrasonics 40* (2002), 199–203.

[77] García-Hernandez, M. J., Montero de Espinosa, F., Chavez, J. A., Yañez, Y. Prego Borges, J., and Turo, A. Nde lamb waves ultrasound system using an air coupled concave array transducer. In *IEEE 16th. World Conference on Non-destructive Testing* (Montreal, Canada, September 2004).

[78] Ghosh, T., Kundu, T., and Karpur, P. Efficient use of lamb modes for detecting defects in large plates. *Elsevier, Ultrasonics 36* (1998), 791–801.

[79] Giacomo, P. Equation for the determination of the density of moist air. *Metrologia 18* (1982), 33–40.

[80] Gómez, T. E., and Montero de Espinosa, F. Bridging the gap of impedance mismatch between air and solid materials. In *Proc. 2000 IEEE Ultrasonics Symposium* (2000), pp. 1069–1072.

[81] Gómez, T. E., and Montero de Espinosa, F. Fabrication and characteriazation of silica aerogel films for air-coupled piezoelectric tranducers in the megahertz range. In *IEEE, Ultrasonic Symposium* (2002), pp. 1107–1110.

[82] Gómez, T. E., Montero de Espinosa, F., Molins, E., Moner-Girona, M., Roig, A., Rodríguez, J. R., Vargas, S., and Esteves, M. Low-impedance and low-loss customized materials for air-coupled piezoelectric transducers. In *Proc. 2001 IEEE Ultrasonics Symposium* (2000), IEEE.

[83] Gomez, T. E., Montero de Espinosa, F., and Pozas, A. P. Air-coupled ultrasonic scanner for braille. In *IEEE, Ultrasonic Symposium* (2001), pp. 591–594.

[84] Goodman, J. W. *Introduction to Fourier Optics*, 3rd. ed. Roberts & Company Publishers, 2005. 1st. Ed. 1968.

[85] Graft, K. F. *Elastic Waves in Solids.* Oxford Univ. Press, New York, 1973.

[86] Greenspan, M. *J. Acoust. Soc. Am. 40* (1966), 251–252.

[87] Greenspan, M. Piston radiator: Some extensions of the theory. *J. Acoust. Soc. Am. 65*, 3 (1979), 608–621.

[88] Guo, Z., Achenbach, J. D., and Krishnaswamy, S. Emat generation and laser detection of single lamb wave modes. *Esevier, Ultrasonics 35* (1997), 423–429.

[89] Guyomar, D., and Powers, J. A fourier approach to diffraction of pulsed ultrasonic waves in lossless media. *J. Acoust. Soc. Am. 82*, 1 (July 1987), 354–359.

[90] Haller, M., and Khuri-Yakub, T. A surface micromachined electrostatic ultrasonic air tranducer. In *Ultrasonics Symposium* (1994), IEEE, Ed., pp. 1241–1244.

[91] Hanish, S. A review of world contributions from 1945 to 1965 to the theory of acoustic radiation. Mem. Rep. 1688 1688, Naval Research Laboratory (NRL), Washingtogn, DC, U. S., March 10 1966.

[92] Harris, G. R. Review of transient field theory for a baffled planar piston. *J. Acoust. Soc. Am. 70*, 1 (July 1981), 10–20.

[93] Harris, G. R. Transient field of a baffled planar piston having an arbitrary vibration amplitude distribution. *J. Acoust. Soc. Am. 70*, 1 (July 1981), 186–204.

[94] Haskell, N. A. Dispersion of surface waves on multilayered media. *Bull. Seism. Soc. Am. 43* (1953), 17–34.

[95] Hayashi, T., and Endoh, S. Calculation and visualization of lamb wave motion. *Elsevier, Ultrasonics 38* (2000), 770–773.

[96] Hayashi, T., and Kawashima, K. Mode extraction from multimodes of lamb waves. *Review of Progress in Quantitative NDE 21* (2002), 219–224.

[97] Hayashi, T., and Kawashima, K. Single mode extraction from multiple modes of lamb wave and its application to defect detection. *JSME International Journal 46*, 4 (2003), 620–626. Series A.

[98] Hayashi, Y. e. a. Non-contact estimation of thickness and elastic properties of metallic foils by the wavelet transform of laser-generated lamb waves. *Elsevier, NDT&E Int. 32* (1999), 21–27.

[99] Hayward, G., and Gachagan, A. An evaluation of 1-3 connetivity composite tranducers for air-coupled ultrasonic applications. *J. Acoust. Soc. Am. 99*, 4 (Apr. 1996), 2148–2157.

[100] Hayward, G., Hailu, B., Farlow, R., Gachagan, A., and McNab, A. The design of embedded transducers for structural health monitoring applications. In *Proceedings of the SPIE* (2001), vol. 4327, pp. 312–323.

[101] Hayward, G., and Hyslop, J. Determination of lamb wave dispersion data in lossy anisotropic plates using time domain finite element analysis. part i: Theory and experimental verification. *IEEE Transactions on UFFC 53*, 2 (February 2006), 443–448.

[102] Hickling, R., and Marin, S. P. The use of ultrasonics for gauging and proximity sensing in air. *J. Acoust. Soc. Am. 79*, 4 (April 1986), 1151–1160.

[103] Holfort, I. K., Gran, F., and Jensen, J. A. Investigation of sound speed errors in adaptive beamforming. *Proc. IEEE Ultrason. Symp.* (2008).

[104] Holland, S. D., Teles, S. V., and Chimenti, D. E. Air-coupled, focused ultrasonic dispersion spectrum reconstruction in plates. *J. Acoust. Soc. Am. 115*, 6 (June 2004), 2866–2872.

[105] Holm, S. Analysis of worst-case phase quantization sidelobes in focused beamforming. *IEEE Transactions on UFFC 39*, 5 (September 1992), 593–599.

[106] Holm, S. Simulation of acoustic fields from medical ultrasound transducers of arbitrary shape. In *Proc. Nordic Symp. in Physical Acoustics* (Ustaoset, Norway, Jan. 1995).

[107] Holm, S. Bessel and conical beams and approximation with annular arrays. *IEEE Transactions on UFFC 45*, 3 (May. 1998), 712–718.

[108] Holm, S., Austeng, A., Iranpour, K., and Hopperstad, J. F. *Sparse sampling in array processing.* Plenum, New York, 2001.

[109] Hoop, A. T. A modification of cagniard's method for solving seismic pulse problems. *Applied Scientific Research B*, 8 (1960), 349–356.

[110] Hossack, J. A., and Auld, B. A. Multiple layer transducers for broadband applications. In *IEEE Ultrasonic Symposium* (1991), pp. 605–610.

[111] Hosten, B. Bulk heterogeneous plane waves propagation through viscoelastic plates and stratified media with large values of frequency domain. *Elsevier, Ultrasonics 29* (1991), 445–450.

[112] Hosten, B., and Biateau, C. Finite elemenent simulation of the generation and detection by air-coupled transducers of guided waves in viscoelastic and anisotropic materials. *J. Acoust. Soc. Am. 123*, 4 (April 2008), 1963–1971.

[113] Hosten, B., and Castaings, M. Transfer matrix of multilayered absorbing and anisotropic media.measurements and simulations of ultrasonic wave propagation through composite materials. *J. Acoust. Soc. Am. 94*, 3 (Sept. 1993), 1488–1495.

[114] Hosten, B., and Castaings, M. Parabolic mirror and air-coupled transducer for multimodal plate wave detection. *Review of Progress in QNDE 22* (2002), 1243–1250. AIP Press, New York.

[115] Hosten, B., and Castaings, M. Surface impedance matrices to model the propagation in multilayered media. *Elsevier, Ultrasonics 41* (June 2003), 501–507.

[116] Hosten, B., Moreau, L., and Castaings, M. Reflection and transmission coefficients for guided waves reflected by defects in viscoelastic material plates. *J. Acoust. Soc. Am. 121*, 6 (June 2007), 3409–3417.

[117] Hutchins, D. A. Ultrasonic generation by pulsed lasers. *Physical Acoustics*, 1989. Ed. by W.P. Mason and R.N. Thurston, London.

[118] Hutchins, D. A., and Schindel, D. W. Advances in non-contact and air-coupled transducers. In *IEEE, Ultrasonic Symposium* (1994), pp. 1245–1254.

[119] Ik-Keun, P., Yong-Kwon, K., Hyun-Mook, K., Houng-Kun, A., Hong-Jun, K., Woo-Sik, S., Youn-Ho, C., and Yong-Sang, C. Noncontact air-coupled guided wave mode identification using wavelet transform. Tech. rep., R. I. of NDE Technology, National Univ. of Technology, Seoul, 2004.

[120] Ing, R. K., and Fink, M. Time-reversed lamb waves. *IEEE Transactions on UFFC 45*, 4 (Jul. 1998), 1032–1043.

[121] Jenot, F., Ouaftouh, M., Xu, W. J., Duquennoy, M., and Ourak, M. Inclusions detection using lamb waves in flexible printed circuits. *Elsevier, Ultrasonics 44* (2006), 1163–1167.

[122] Jensen, J. A. A new approach to calculating spatial impulse responses. In *IEEE Ultrasonics Symposium Proceedings* (1997), IEEE, pp. 1755–1759.

[123] Jensen, J. A., Gandhi, D., and O'Brien, W. D. J. Ultrasound fields in an attenuating medium. In *IEEE Ultrasonic Symposium Proceedings* (1993), vol. 2, IEEE, pp. 943–946.

[124] Jensen, J. A., and Nikolov, S. I. Fast simulation of ultrasound images. In *IEEE Ultrasonic Symposium* (2000), IEEE, pp. 1721–1724.

[125] Jensen, J. A., and Svendsen, N. B. Calculation of pressure fields from arbitrarily shaped, apodized, and excited ultrasound transducers. *IEEE Transactions on UFFC 39*, 2 (March 1992), 262–267.

[126] Jia, X. Modal analysis of lamb wave generation in elastic plates by liquid wedge. *J. Acoust. Soc. Am. 101*, 2 (1997), 834–842.

[127] Johnson, D. H., and Dudgeon, D. E. *Array Signal Processing: Concepts and Techniques.* Prentice Hall, 1993.

[128] Jones, R. C. On the theory of the directional patterns of continuous source distributions on a plane sourface. *J. Acoust. Soc. Am. 16*, 3 (1945), 147–171.

[129] Kaczmarek, H. Lamb wave interaction with impact-induced damage in aircraft composite: Use of the a0 mode excited by air-coupled transducer. *J. of Composite Materials 37* (2003), 217–232.

[130] Ke, W., Castaings, M., and Bacon, C. 3d finite element simulations of an air-coupled ultrasonic ndt system. *NDT & E International 42* (2009), 524–533.

[131] Kelly, S. P., Hayward, G., and Gomez, T. E. An air-coupled ultrasonic matching layer employing half wavelength cavity resononce. In *IEEE, Ultrasonic Symposium* (2001), pp. 965–968.

[132] King, L. V. *Can. J. Res. 11* (1934), 135–146.

[133] Kino, G. *Acoustic waves: Devices, imaging, and analog signal processing*, corrected ed. 2000 ed. No. 602. Prentice-Hall, 2000. 1st. Ed. 1987.

[134] Kirchhoff, G. Zur theorie der lichtstrahlen. No. 2. Weidemann Ann., 1883, pp. 18–663.

[135] Kirkup, S. M. *Solution of Exterior Acoustics problems by the boundary element method.* PhD thesis, Brighton Polytechnic, Brighton, UK, 1989.

[136] Kirkup, S. M. Computational solution of the acoustic field surrounding a baffled panel by the rayleigh integral method. *Applied Mathematical Modelling 18* (1994), 403–407.

[137] Kirkup, S. M. *Computing the Acoustic Field Surrounding a Radiating Plate by the Rayleigh Integral Method: RIM3 User Manual.* Brighton Polytechnic, Brighton, UK, August 2005.

[138] Knopoff, L. A matrix method for elastic wave problems. *Bull. Seism. Soc. Am. 54* (1964), 431–438.

[139] Korn, G. A., and Korn, T. M. *Mathematical Handbook for Scientists and Engineers.* Mc. Graw Hill, 1968. 2nd. Ed.

[140] Kotte, O. Application of image processing techniques for lamb wave characterization. Master's thesis, School of Civil and Environmental Engineering Georgia Institute of Technology, Aug. 2004.

[141] Kundu, T. Recent advances of the use of lamb waves for material characteriazation. In *IUTAM Symposium on Mechanical Waves for Composite Structures Characterization* (Netherlands, 2001), Kluwer Academic Publishers, pp. 83–98.

[142] Lamb, H. On the propagation of tremors over an elastic solid. *Proc. Roy. Soc. A*, 203 (1904).

[143] Lamb, H. On waves in an elastic plate. In *Proc. Roy. Soc.* (1917), vol. 93 of *PT series A*, pp. 114–128.

[144] Lanza di Scalea, F., and Rizzo, P. Propagation of ultrasonic guided waves in lap-shear adhesive joints: Case of incident a0 lamb wave. *J. Acoust. Soc. Am. 115*, 1 (Jan. 2003), 146–156.

[145] Larose, E., Philippe, R., and Michel, C. Reconstruction of rayleigh-lamb dispersion spectrum based on noise obtained from an air-jet forcing. *J. Acoust. Soc. Am. 122*, 6 (Dec. 2007), 3437–3444.

[146] Le Clézio, E., Castaings, M., and Hosten, B. The interaction of the s0 lamb mode with vertical cracks in an aluminium plate. *Elsevier, Ultrasonics 40* (2002), 187–192.

[147] Lee, J. H., and Choi, S. W. A parametric study of ultrasonic beam profiles for a linear phased array tranducer. *IEEE Transactions on UFFC 47*, 3 (May 2000), 644–650.

[148] Leeman, S., and Healey, A. J. Field analysis witha new field simulation and propagation tecnique. In *Acoustical Imaging*, H. . Wells, Ed., vol. 25. Kluwer Academic/Plenum Publishers, 2000.

[149] Lemon, D. K., and Posakony, G. J. Linear array technology in nde applications. *Mater. Eval. 38* (Jul. 1980), 34–37.

[150] Levent Degertekin, F., and Khuri-Yakub, B. T. Lamb wave excitation by hertzian contacts with applications in nde. *IEEE Transactions on UFFC 44*, 4 (July 1997), 769–779.

[151] Li, J., and Rose, J. L. Implementing guided wave mode control by use of a phased transducer array. *IEEE Transactions on UFFC 48*, 3 (May 2001), 761–768.

[152] Lin, B., and Giurgiutiu, V. Modeling and testing of pzt and pvdf piezoelectric wafer active sensors. *Smart Materials and Structures 15* (2006), 1085–1093.

[153] Lobkis, O. I., and Chimenti, D. E. 3-d voltage model for detection of sound radiated from anisotropic materials. *Elsevier, Ultrasonics 38* (2000), 237–241.

[154] Lockwood, J. C., and Willette, J. G. High-speed method for computing the exact solution for the pressure variations in the nearfield of a baffled piston. *J. Acoust. Soc. Am. 53*, 3 (1972), 735–741.

[155] Lord Rayleigh, S. J. W. *The Theory of Sound*, vol. II. Dover, New York, 1945.

[156] Love, A. E. H. *Some Problems of Geodynamics*. London: Cambridge University Press, 1911.

[157] Lowe, M. J. S. *Plate waves for the NDT of diffusion bonded titanium.* PhD thesis, Imperial College of Science, Technology and Medicine, December 1992.

[158] Lowe, M. J. S. Matrix techniques for modelling ultrasonic waves in multilayered media. *IEEE Transactions on UFFC 42*, 4 (July 1995), 525–542.

[159] Lowe, M. J. S., Alleyne, D. N., and Cawley, P. Defect detection in pipes using guided waves. *Elsevier, Ultrasonics 36* (1998), 147–154.

[160] Lowe, M. J. S., Challis, R. E., and Chan, C. W. The transmission of lamb waves across adhesively bonded lap joints. *J. Acoust. Soc. Am. 107* (2000), 1333–1345.

[161] Lowe, M. J. S., Pavlakovic, B., and Cawley, P. A model for predicting the properties of guided ultrasonic waves, and illustration of its application to ndt. Tech. rep., Department of Mechanical Engineering, Imperial college of Science, Technology and Medicine, Exhibition Road, London SW7 2BX., 2004.

[162] Luo, W., and Rose, J. L. Phased array focusing with guided waves in a viscoelastic coated hollow cylinder. *J. Acoust. Soc. Am. 121*, 4 (April 2007), 1945–1955.

[163] Malyarenko, E. V., and Hinders, M. K. Ultrasonic lamb wave diffraction tomography. *Elsevier, Ultrasonics 39* (2001), 269–281.

[164] Manolakis, D. G., Ingle, V. K., and Kogon, S. M. *Statistical and adaptive signal processing: spectral estimation, signal modelling, adaptive filtering and array processing.* Artech House, Inc., US, 2005.

[165] Manthey, W., Kroemer, N., and Magori, V. Ultrasonic transducers and transducer arrays for operation in air. *Meas. Sci. Technol. 3*, 3 (1992), 249–261.

[166] Marchand, E. W., and Wolf, E. Boundary diffraction wave in the domain of the rayleigh kirchhoff diffraction theory. *J. Opt. Soc. Am. 52* (1962), 761–767.

[167] Marti, P. N. *Modelling of ultrasonic guided wave field generated by piezoelectric transducers.* PhD thesis, Imperial College of Science, Technology and Medicine, London, March 2002.

[168] McGough, R. J. Rapid calculations of time-harmonic nearfield pressures produced by rectangular pistons. *J. Acoust. Soc. Am. 115*, 5 (May 2004), 1934–1941.

[169] McIntosh, J. S., Hutchins, D. A., Etcheverry, G., Billson, D. R., Noble, R. A., Davies, R. R., and Koker, L. Micromachined capacitive transducer array for imaging in air. In *Proc. 2001 IEEE Ultrasonics Symposium* (2001), pp. 929–932.

[170] McLachlan, N. W. Philos. Mag. 14, 1932. 1012-1025.

[171] Merkulov, L. G. Damping of normal modes in a plate inmersed in a liquid. *Akust. Zh. 10*, 2 (1964), 206–212.

[172] Miklowitz, J. Transient compressional waves in an infinite elastic plate or elastic layer overlying a rigid half-space. *J. Appl. Mech. 29* (1962), 53–60.

[173] Miklowitz, J. *The Theory of Elastic Waves and Wave Guides.* North-Holland, Amsterdam, 1978.

[174] Mindlin, R. d. *Waves and vibrations in isotropic, elastic plates.* Structural Mechanics, Goodier J. N. and Hoff N. J., New York, 1955.

[175] Monchalin, J. P. Progress towards the application of laser ultrasonics in industry. *Review of Progress in QNDE 12* (1993), 495–506. Ed. by D.O. Thompson and D.E. Chimenti, NY.

[176] Monkhouse, R. S. C., Wilcox, P., and Cawley, P. Flexible interdigital pvdf lamb wave transducers for the development of smart structures. *Annual Review of Progress in Quantitative NDE* (1997), 877–887. Ed. Thompson and Chimenti.

[177] Monkhouse, R. S. C., Wilcox, P., and Cawley, P. Flexible interdigital pvdf transducers for the genration of lamb waves in structures. *Elsevier, Ultrasonics 35* (1997), 489–498.

[178] Montero de Espinosa, F., Chávez, J. A., Yañez, Y., Chinchurreta, F. J., and Garcia-Hernandez, M. J. Air coupled piezoelectric array transducers for ndt applications. In *16 World Conference on Non Destructive Test* (Montreal Canada, September 2004), IEEE, pp. 1–6.

[179] Montero de Espinosa, F., Gómez, T. E., Albareda, A., Rafel, P., and Casals, J. A. High sensitive piezoelectric transducers for nde air borne applications. In *Proc. 2000 IEEE Ultrasonics Symposium* (2000), IEEE, pp. 1073–1076.

[180] Morse, P. M. *Vibration and Sound*, 2nd. ed. ed. McGraw-Hill, NY, 1948.

[181] Morvan, B., Wilkie-Chancellier, N., Duflo, H., Tinel, A., and Duclos, J. Lamb wave reflection at the free edge of a plate. *J. Acoust. Soc. Am. 113*, 3 (Mar. 2003), 1417–1425.

[182] Moulin, E., Assaad, J., Delebarre, C., Grondel, S., and Balageas, D. Modeling of integrated lamb waves generation systems using a coupled finite element-normal modes expansion method. *Elsevier, Ultrasonics 38* (2000), 522–526.

[183] Moulin, E., Grondel, S., Baouahi, M., and Assaad, J. Pseudo-3d modeling of a surface-bonded lamb wave source (l). *J. Acoust. Soc. Am. 119*, 5 (May 2006), 2575–2578.

[184] Nagai, K. *Ultrasonic Holography.* Nikkan Kogyo Shinbunsha, Tokyo, Japan, 1989.

[185] Nam, K., and Mal, A. K. Characteristics of elastic waves generated by crack initiation in aluminum alloys under fatigue loading. *J. Mater. Res. 16*, 6 (Jun. 2001), 1745–1751.

[186] Neau, G. *Lamb waves in anisotropic viscoelastic plates. Study of the wave fronts and attenuation.* PhD thesis, École Doctorale Des Sciences Physiques Et De L'Ingénieur, L'Université Bordeaux I, Janvier 2003.

[187] Neild, A. *Ultrasonic air-coupled capacitive arrays.* PhD thesis, School of Engineering, University of Warwick, Coventry, UK, 2003.

[188] Neild, A., Hutchins, D. A., and Billson, D. R. Imaging using air-coupled polymer-membrane capacitive ultrasonic arrays. *Elsevier, Ultrasonics 42* (2004), 859–864.

[189] Neild, A., Hutchins, D. A., and Billson, D. R. Imaging using air-coupled polymer-membrane capacitive ultrasonic arrays. *Elsevier, Ultrasonics 42* (2004), 859–864.

[190] Neild, A., Hutchins, D. A., Robertson, T. J., Davis, L. A. J., and Billson, D. R. The radiated fields of focussing air-coupled ultrasonic phased arrays. *Elsevier, Ultrasonics in press* (April 2003), 13.

[191] Niethammer, M., and Jacobs, L. J. Time-frequency representation of lamb waves using the reassigned spectrogram. *J. Acoust. Soc. Am. 107*, 5 (May 2000), 19–24.

[192] Niethammer, M., Jacobs, L. J., Qu, J., and Jarzynski, J. Time-frequency representations of lamb waves. *J. Acoust. Soc. Am. 109*, 5 (2001), 1841–1847.

[193] Noble, R. A., Davies, R. R., Day, M. M., Koker, L., King, D. O., Brunson, K. M., Jones, A. R. D., McIntosh, J. S., Hutchins, D. A., Robertson, T. J., and Saul, P. A cost-effective and manufacturable route to the fabrication of high-density 2d micromachined ultrasonic transducer arrays and (cmos) signal conditioning electronics on the same substrate. In *IEEE Ultrasonic Symposium* (2001), pp. 941–944.

[194] Noble, R. A., Jones, A. D. R., Robertson, T. J., Hutchins, D. A., and Billson, D. R. Novel, wide bandwith, micromachined ultrasonic tranducers. *IEEE Transactions on UFFC 48* (2001), 1495–1502.

[195] Oberhettinger, F. *J. Res. Nat. Bur. Stand. 65*, B (1961), 1–6.

[196] Ocheltree, K. B., and Frizzell, L. A. Sound field calculation for rectangular sources. *IEEE Transactions on UFFC 36*, 2 (March 1989), 242–248.

[197] Paget, C. A. Active health monitoring of aerospace composite structures by embedded piezoceramic transducers. Tech. rep., Department of Aeronautics Royal Institute of Technology, Stockholm, Sweden, 2001. ISSN 0280-4646.

[198] Pavlakovic, B., Lowe, M., Alleyne, D., and Cawley, P. Disperse: A general purpose program for creating dispersion curves. *Review of Progress in Quantitative NDE 16* (1997), 185–192. In: D. Thompson and D. Chimenti (eds.).

[199] Pavlakovic, B. N. *Leaky guided ultrasonic waves in NDT.* PhD thesis, Imperial College of Science, Technology and Medicine, October 1998.

[200] Pavlakovic, B. N. *Leaky Guided Ultrasonic Waves in NDT.* PhD thesis, Imperial College of Science, Technology and Medicine, October 1998. Mechanical Engineering Deparment.

[201] Pavlakovic, B. N., and Rose, J. L. The influence of finite-size sources in acousto-ultrasonics. Unclas (NASA-CR-195374), The Pennsylvania State University, University Park, Pennsylvania, August 1994. Prepared for Lewis Research Center Under Contract NAG3-1365, National Aeronautics Space Administration.

[202] Penttinen, A., and Luukkala, M. The impulse response and pressure nearfield of a curved ultrasonics radiator. *J. Phys. D. 9* (1976), 1547–1557.

[203] Petrashen G. I., P. V. S. Nonstationary interference wave fields of sv type in a free elastic layer and the problem of ultrasonic simulation of plane seismic fields by using plate models. *J. Math. Sciences 91*, 1 (1998), 2619–2687.

[204] Pialucha, T. P. *The reflection coefficient from interface layers in NDT of adhesive joints.* PhD thesis, Imperial College of Science, Technology and Medicine, January 1992.

[205] Pierce, S., Culshaw, B., Philp, W., Lecuyer, F., and Farlow, R. Broadband lamb wave measurements in aluminium and carbon/glass fibre reinforced composite materials using non-contacting laser generation and detection. *Elsevier, Ultrasonics 35* (1997), 105–114.

[206] Pierce, S. G., Culshaw, B., Manson, G., Worden, K., and Staszewski, W. J. The application of ultrasonic lamb wave techniques to the evaluation of advanced composite structures. Tech. rep., University of Strathclyde, Dep. of Electronic & Electrical Engineering, Scotland, UK, 2005.

[207] Ping, W., and Stepinski, T. Spatial impulse response method for predicting pulse-echo fields from a linear array with cylindrically concave surface. *IEEE Transactions on UFFC 46* (September 1999), 1283–1297.

[208] Piwakowski, B., and Delannoy, B. Method for computing spatial pulse response: Time domain approach. *J. Acoust. Soc. Amer. 86*, 6 (Dec. 1989), 2422–2432.

[209] Piwakowski, B., and Sbai, K. A new approach to calculate the field radited from arbitrarily structured transducer arrays. *IEEE Transactions on UFFC 46*, 2 (March 1999), 422–440.

[210] Piwakowski, B., Sbai, K., and Delannoy, B. Computer-aided computing of acoustic field radiated from arbitrarily structured transducer arrays. In *IEEE Ultrasonic Symposium* (1994).

[211] Predoi, M. V., Castaings, M., Hosten, B., and Bacon, C. Wave propagation along transversely periodic structures. *J. Acoust. Soc. Am. 121*, 4 (April 2007), 1935–1944.

[212] Prego Borges, J. L. Lamb: Programa de simulación para sistemas de end mediante ondas de lamb y ultrasonidos acoplados por aire: etapa de verificación del módulo de simulación de campos acústicos. Tech. rep., Ministerio de Ciencia y Educación de España, Oslo, Norway, October 2009. Ph.D. stay report.

[213] Prego Borges, J. L., Claret, Q. C., and García Hernández, M. J. First: Acoustic field impulse response software. an acoustic field simulator for arrays used in non-destructive applications with air-coupled ultrasonic lamb waves. Tech. rep., Polytechnic University of Catalonia (UPC), Sensor and Systems Group, Barcelona, Spain, 2006. Unpublished.

[214] Prego Borges, J. L., Montero de Espinosa, F., Chávez, J. A., Turó, A., and Garcia-Hernandez, M. J. Diffraction aperture non-ideal behaviour of air coupled transducers array elements designed for ndt. *Elsevier, Ultrasonics 44* (2006), 667–672.

[215] Prego Borges, J. L., Yañez, Y., Chávez, J. A., Salazar, J., Turó, A., and Garcia-Hernandez, M. J. On the influence of using a non-ideal element model to predict the plane wavefront generation for air-coupled concave arrays transducers used in lamb wave ndt systems. In *The International Congress on Ultrasonics (ICU)* (Vienna, April 9-13 2007). Session R17 NDT: Modelling and simulation.

[216] Ratcliffe, J. A. Aspects of diffraction theory and their application to ionosphere. In *The Physical Society of London*, R. on Progress in Physics, Ed., vol. XIX. A. C. Strickland, 1956.

[217] Rayleigh, L. On waves propagating along the plane surface of an elastic solid. In *Proc. London Math. Soc.* (1887), vol. 17, pp. 4–11.

[218] Rayleigh, L. On the free vibrations of an infinite plate of homogeneous isotropic elastic matter. *Proc. London Roy. Math. Soc. 20* (1889), 225–234.

[219] Roberson, T., Neild, A., Hutchins, D., Mac.Intosh, J., Billson, D., Noble, R., Davies, R., and Koker, L. Radiated fields of rectangular air-coupled micromachined transducers. In *IEEE Ultrasonic Symposium* (2001), pp. pp. 891–894.

[220] Robinson, D. E., Lees, S., and Bess, L. Near field transient radiation patterns for circular pistons. *IEEE Transactions on UFFC ASSP-22*, 6 (December 1974), 395–403.

[221] Rokhlin, S. I., and Chimenti, D. E. *Review of Progress in Quantitative Nondestructive Evaluation*, vol. 9. Plenum, New York, 1990.

[222] Rose, J., Rajana, K. M., and Barshinger, J. N. Guided waves for composite patch repair of aging aircraft, in review of progress in quantitative. *Review of Progress in Quantitative NDE 15* (1996), 1291–1297.

[223] Rose, J. L. *Ultrasonic Waves in Solid Media*. Cambridge University Press, New York, 1999.

[224] Rose, J. L. Guided wave nuances for ultrasonic nondestructive evaluation. *IEEE Transactions on UFFC 47*, 3 (May 2000), 575–583.

[225] Rose, J. L. A vision of ultrasonic guided wave inspection potential. In *Proceedings of the Seventh ASME NDE Topical Conference* (2001), vol. 20 NDE.

[226] Rose, J. L. A baseline and vision of ultrasonic guided wave inspection potential. *J. of Pressure Vessel Technology 124* (Aug. 2002), 273–282.

[227] Rose, L. R. F. Mindlin plate theory for damage detection: Imaging of flexural inhomogeneities. *J. Acoust. Soc. Am. 127*, 2 (Feb. 2010), 754–763.

[228] Rose, L. R. F., and Wang, C. H. Mindlin plate theory for damage detection: Source solutions. *J. Acoust. Soc. Am. 116*, 1 (July 2004), 154–171.

[229] Rosenbaun, J. H. The long-time response of a layered elastic medium to explosive sound. *J. Geophys. Res. 65* (1960), 1577–1613.

[230] Rubinowicz, A. *Ann. Physik 53* (1917), 257–278.

[231] Rutgers, A. J. *Spatial Impulse Response of an Acoustic Line Radiator - A Study of Boundary-Diffration-Wave Phenomena and Their Experimental Detection.* PhD thesis, School of Engineering & Architecture, Catholic University of America, Washingtong, DC, 1977.

[232] Safaeinili, A., Lobkis, O., and Chimenti, D. E. Air-coupled ultrasonic estimation of viscoelastic stiffness in plates. *IEEE Transactions on UFFC 43*, 6 (1996), 1171–1180.

[233] Salazar, J., Turo, A. Chavez, J. A., Ortega, J. A., and Garcia Hernandez, M. J. High-power high-resolution pulser for air-coupled ultrasonic nde applications. *IEEE Trans. on Intrumentation and Measurements 52*, 6 (Dec. 2003), 1792–1798.

[234] San Emeterio, J. L., and Ullate, L. G. Diffraction impulse response of rectangular transducers. *J. Acoust. Soc. Am. 92*, 2 (August 1992), 651–662.

[235] Santosa, F., and Pao, Y. H. Transient axially asymmetric response of an elastic plate. *Elsevier, Wave Motion 11* (1989), 271–296.

[236] Scarano, G., Denisenko, N., Matteucci, M., and Pappalardo, M. A new approach to the derivation on the impulse response of a rectangular piston. *J. Acoust. Soc. Am. 78*, 3 (September 1985), 1109–1113.

[237] Schafer, M. E. *Transducer Characterization in Inhomogeneous Media Using the Angular Spectrum Method.* PhD thesis, Drexel University, 1988.

[238] Schafer, M. E., and Lewin, P. A. Transducer characterization using the angular spectrum method. *J. Acoust. Soc. Am. 85* (1989), 2202–2214.

[239] Schindel, D. W., and Hutchins, D. A. Application of micromachined capacitance tranducers in air-coupled ultrasonics and nondestructive evaluation. *IEEE Transactions on UFFC 42*, 1 (Jan. 1995), 51–58.

[240] Schindel, D. W., and Hutchins, D. A. The design and characteriazation of micromachined air-coupled capacitance tranducers. *IEEE Transactions on UFFC 42*, 1 (Jan. 1995), 42–50.

[241] Schmitz, V. Nondestructive acoustic imaging techniques. *Topics Appl. Phys. 84* (2002), 167–190. Springer-Verlag Berlin Heidelberg.

[242] Schooch, A. *Akust. z 6* (1941), 318–326.

[243] Sherman, G. C. Application of the convolution theorem to rayleigh's integral formulas. *J. Opt. Soc. Am. 57* (1967), 546.

[244] Shi, Y. Simulation of acoustic field of linear phased arrays. Master's thesis, Massachusetts Intitute of Thecnology, 1998.

[245] Shi, Y. *Analisys of optimim Lamb wave tuning.* PhD thesis, Department of Civil and Enviromental Engineering, Massachusetts Institute of Technology, Feb. 2002.

[246] Shi, Y., Wooh, S.-C., and Orwat, M. Laser-ultrasonic generation of lamb waves in the reaction force range. *Elsevier, Ultrasonics 41* (August 2003), 623–633.

[247] Sicard, R., Chahbaz, A., and Goyette, J. Guided lamb waves and l-saft processing technique for enhanced detection and imaging of corrosion defects in plates with small depth-to-wavelength ratio. *IEEE Transactions on UFFC 51*, 10 (Oct. 2004), 1287–1297.

[248] Sicard, R., Goyette, J., and Zellouf, D. E. A saft algorithm for lamb wave imaging of isotropic plate-like structures. *Elsevier, Ultrasonics 39* (2002), 487–494.

[249] Siqueira, M. H. S., Gatts, C. E. N., da Silva, R. R., and Rebello, J. M. A. The use of ultrasonic guided waves and wavelets analysis in pipe inspection. *Elsevier, Ultrasonics 41* (2004), 785–797.

[250] Smith, W. A., and Auld, B. A. Modelling 1-3 composite piezoelectric: thickness mode oscillations. *IEEE Transactions on UFFC 38*, 1 (1990), 40–47.

[251] Solodov, I., Pfleiderer, K., and Busse, G. Laser vibrometry of air-coupled lamb waves. *Ultrasonic Testing 47*, 3 (Jan. 2005), 123–128.

[252] Solodov, I., Wackerl, J., Pfleiderer, K., and Busse, G. Nonlinear self-modulation and subharmonic acoustic spectroscopy for damage detection and location. *Applied Physics Letters 84*, 26 (Jun. 2004), 5386–5388.

[253] Sommerfeld, A. Mathematische theorie der diffraction. *Math. Ann. 47* (1896), 317–374.

[254] Song, J., and Chimenti, D. E. Design, fabrication and characterization of a spherically focused capacitive air-coupled ultrasonic transducer. *Int. J. of App. Science and Engineering 4*, 1 (2006), 1–19.

[255] Stenzel, H. *Ann. Physik 7* (1930), 947–982.

[256] Stenzel, H. Die akustiche strahlung der recteckigen kolbenmembran. *Acustica 2* (1952), 263.

[257] Stepanishen, P. R. An approach to computing time-dependent interaction forces and mutual radiation impedances between pistons in a rigid planar baffle. *J. Acoust. Soc. Am. 49*, 1, part2 (1971), 283–292.

[258] Stepanishen, P. R. The time-dependent force and radiation impedance on a piston in a rigid infinite planar baffle. *J. Acoust. Soc. Am. 49*, 3, part2 (1971), 841–849.

[259] Stepanishen, P. R. Transient radiation from pistons in an infinite planar baffle. *J. Acoust. Soc. Am. 49*, 5, part2 (February 1971), 1629–1638.

[260] Stepanishen, P. R. Comments on 'farfield of pulsed rectangular acoustic radiator'. *J. Acoust. Soc. Am. 49* (1972), 738–748.

[261] Stepanishen, P. R., and Benjamin, K. C. Forward and backward projection of acoustic fields using fft methods. *J. Acoust. Soc. Am. 71* (1982), 803–811.

[262] Stepanishen, P. R., Forbes, M., and Lechter, S. The relationship between the impulse reponse and angular spectrum methods to evaluate acoustic transient fields. *J. Acoust. Soc. Am. 90*, 5 (Nov 1991), 2794–2798.

[263] Stoica, P., Li, H., and Li, J. A new derivation of the apes filter. *IEEE Signal Processing Letters 6*, 8 (August 1999), 205–206.

[264] Stoneley, R. Elastic waves at the surface of separation of two solids. In *Proc. London Math. Soc.* (1924), vol. 106, pp. 416–428.

[265] Su, Z., Ye, L., and Lu, Y. Guided lamb waves for identification of damage in composite structures: A review. *Elsevier, Int. J. of Sound & Vibration 295* (2006), 753–780.

[266] Synnevag, J. F., Austeng, A., and Holm, S. Adaptive beamforming applied to medical ultrasound imaging. *IEEE Transactions on UFFC 54*, 8 (August 2007), 1606–1613.

[267] SYNNEVAG, J. F., AUSTENG, A., AND HOLM, S. Benefits of minimum-variance beamforming in medical ultrasound imaging. *IEEE Transactions on UFFC 56*, 9 (September 2009), 1868–1879.

[268] TABEI, M., AND UEDA, M. On the sampling conditions for reconstruction of an acoustic field from a finite sound source. *J. Acoust. Soc. Am. 111*, 2 (Feb. 2002), 940–946.

[269] TAN, E. L. Stiffness matrix method with improved efficiency for elastic wave propagation in layered anisotropic media. *J. Acoust. Soc. Am. 118*, 6 (Dec. 2005), 3400–3403.

[270] THOMSON, W. T. Transmission of elastic waves through a stratified solid medium. *J. Appl. Phys. 21* (1950), 89–93.

[271] TUPHOLME, G. E. *Mathematica 16* (1969), 209–224.

[272] TURO, A., SALAZAR, J., CHAVEZ, J. A., GOMEZ, T. E., MONTERO DE ESPINOSA, F., AND GARCIA-HERNANDEZ, M. J. Ultra-low noise front-end electronics for air-coupled ultrasonic non-destructive evaluation. *Elsevier, NDT&E Int. 36* (2003), 93–100.

[273] ULLATE, L. G., AND SAN EMETERIO, J. L. On the impulse response of rectangular baffled pistons. In *Ultrason. Int. 89* (1989), pp. 566–571.

[274] VASUDEVAN, N., AND MAL, A. K. Response of an elastic plate to localized transient sources. *ASME Journal of Applied Mechanics 52* (1985), 356–362.

[275] VECCHIO, C. J., AND LEWIN, P. A. Finite amplitude acoustic propagation modelling using the extended angular spectrum method. *J. Acoust. Soc. Am. 95*, 5 (May. 1989), 2399–2408.

[276] VIKTOROV, I. A. Ultrasonic lamb waves. *Sov. Phys. Acoust. 11*, 1 (Jul.-Sep. 1965), 367–372.

[277] VIKTOROV, I. A. *Rayleigh and Lamb Waves: Physical Theory and Applications.* Plenum Press, 1967.

[278] WANG, L., AND ROKHLIN, S. I. Stable recursive algorithm for elastic wave propagation in layered anisotropic media: Stiffness matrix method. *J. Acoust. Soc. Am. 112*, 3 (Sep. 2001), 822–834.

[279] WANG, L., AND ROKHLIN, S. I. Stable reformulation of transfer matrix method for wave propagation in layered anisotropic media. *Elsevier, Ultrasonics 39* (2001), 413–424.

[280] Wang, L., and Rokhlin, S. I. Recursive asymptotic stiffness matrix method for analysis of surface acoustic wave devices on layered piezoelectric media. *Applied Physics Letters 81*, 21 (Nov. 2002), 4049–4051.

[281] Wang, L., and Rokhlin, S. I. Recursive impedance matrix method for wave propagation in stratified media. *Bull. Seism. Soc. Am. 92* (2002), 1129–1135.

[282] Watson, T. H. A real frequency, complex wave-number analysis of leaking modes. *Bull. Seism. Soc. Am. 62* (1972), 369–541.

[283] Weaver, R. L., and Pao, Y. H. Axisymmetric elastic waves excited by a point source in a plate. *J. Appl. Mech. 49* (December 1982), 821–836.

[284] Wilcox, P., Lowe, M., and Cawley, P. Omnidirectional guided wave inspection of large metallic plate structures using an emat array. *IEEE Transactions on UFFC 52*, 4 (2005), 653–665.

[285] Wilkie-Chancellier, N., Martinez, L., Serfaty, S., Griesmar, P., Caplain, E., Le Huérou, J. Y., and Gindre, M. Lamb mode reflections at the end of a plate loaded by a viscoelastic material. *Elsevier, Ultrasonics 44* (2006), 863–868.

[286] Williams, E. G. *Fourier Acoustics: Sound Radiation and Nearfield Acoustical Holography.* Academic, San Diego, 1999.

[287] Williams, E. G., Dardy, H. D., and Washburn, K. B. Generalized nearfield acoustical holography for cylindrical geometry: Theory and experiment. *J. Acoust. Soc. Am. 81*, 2 (February 1987), 389–407.

[288] Williams, E. G., Maynard, J. D., and Skudrzyk, E. Sound source reconstruction using a microphone array. *J. Acoust. Soc. Am. 68*, 1 (July 1980), 340–344.

[289] Wooh, S.-C., and Shi, Y. Influence of phased array element size on beam steering behaviour. *Elsevier, Ultrasonics 36* (1998), 737–749.

[290] Worlton, D. C. Experimental confirmation of lamb waves at megacycle frequencies. *J. Appl. Phys. 32*, 6 (1961), 967–971.

[291] Wright, W. M. D., Hutchins, D. A., Gachagan, A., and Hayward, G. Polymer composite material characterisation using a laser/air-transducer system. *Elsevier, Ultrasonics 34* (1996), 825–833.

[292] Wright, W. M. D., Schindel, D. W., and Hutchins, D. A. Studies of laser-generated ultrasound using micromachined silicon electrostatic tranducer in air. *J. Acoust. Soc. Am. 95*, 5 (May 1994), 2567–2575.

[293] Wu, S. F. On reconstruction of acoustic pressure fields using the helmholtz equation least squares method. *J. Acoust. Soc. Am. 107*, 5 (May 2000), 2511–2522.

[294] Wu, S. F. Hybrid near-field acoustic holography. *J. Acoust. Soc. Am. 115*, 1 (January 2004), 207–217.

[295] Xu, B., and Giurgiutiu, V. Single mode tuning effects on lamb wave time reversal with piezoelectric wafer active sensors for structural health monitoring. *J. of Nondestructive Evaluation 26* (2007), 123–134.

[296] Xu, P. C., and Mal, A. K. Calculation of the inplane green's function for a layered viscoelastic solid. *Bull. Seism. Soc. Am. 77* (1987), 1823–1837.

[297] Xu, X., Goossens, J., Shkerdin, G., and Glorieux, C. Effect of loading a plate with different liquids on the propagation of lamb-like waves studied by laser ultrasonics. *IEEE Transactions on UFFC 55*, 3 (Mar. 2008), 675–685.

[298] Yañez, Y., Chavez, J. A., Salazar, J., Turo, A., and Garcia-Hernandez, M. J. Wide dynamic range electronics for air-coupled lamb-waves ultrasonic ndt using piezoelectric transducer arrays. In *IEEE Instrumentation and Measurement Technology Conference* (Como, Italy, May. 2004), vol. 3, pp. 1926–1929.

[299] Yañez, Y. M. *Mejora del margen dinámico de sistemas de ensayos no destructivos mediante ondas de Lamb basados en agrupaciones cóncavas de transductores acoplados por aire.* PhD thesis, The Polytechnic University of Catalonia (UPC), Department of Electronics, November 2008. Barcelona, Spain.

[300] Yang, C.-H., and Tsai, Y.-C. A new optical method for the detection of in-plane motion of ultrasound propagating in metals. *Elsevier, Ultrasonics 44* (2006), 1239–1242.

[301] Yang, Z., Yu, Z., and Sun, H. On the cross correlation function amplitude vector and its application to structural damage detection. *Elsevier, Mechanical Systems & Signal Processing 21* (2007), 2918–2932.

[302] Yano, T., Tone, M., and Fukumoto, A. Range finding and surface characterization using high frequency air transducer. *IEEE Transactions on UFFC 34*, 2 (1987), 222–236.

[303] Yashiro, S., Takatsubo, J., and Toyama, N. An ndt technique for composite structures using visualized lamb-wave propagation. *Elsevier, J. Composites and Science Technology 67* (2007), 3202–3208.

[304] Zeroug, S., and Stanke, F. E. Ultrasonic pulsed beam interaction with a fluid-loaded eñastic plate: Experimental validation. *J. Acoust. Soc. Am. 100*, 3 (Sep. 1996), 1349–1356.

[305] Zhao, X., Gao, H., Zhang, G., Ayhan, B., Yan, F., Kwan, C., and Rose, J. L. Active health monitoring of an aircraft wing with embedded piezoelectric sensor/actuator network: I. defect detection, localization and growth monitoring. *Smart Materials and Structures 16* (200), 1208–1217.